Fabrication and characterization of plasmonic patch nanoantennas

Juan Uriel Esparza Villa

THÈSE DE DOCTORAT
SORBONNE UNIVERSITÉ

Spécialité : La physique, de la particule à la matière condensée

École doctorale n°564: Physique en Île-de-France

réalisée

à l'Institut des NanoSciences de Paris

sous la direction de Agnès MAITRE

présentée par

Juan Uriel ESPARZA VILLA

pour obtenir le grade de :

DOCTEUR SORBONNE UNIVERSITÉ

Sujet de la thèse :

Fabrication et caractérisation d'antennes patch plasmoniques

soutenue le 19 avril 2019

devant le jury composé de :

M.	Francois MARQUIER	Rapporteur
M.	Rafael SALAS MONTIEL	Rapporteur
M.	Gilles TESSIER	Examinateur
M.	Aloyse DEGIRON	Invité
M.	Lionel AIGOUY	Invité
Mme	Agnès MAITRE	Directrice de thèse

Contents

Remerciements

Une seule page dans cette thèse n'est pas suffisante pour remercier toutes les personnes qui m'ont offerte leur aide, leur soutien et leur encouragement pendant mon court séjour au sein de l'Institut des Nanosciences de Paris.

Durant ces travaux, j'ai été accueillie dans l'équipe de Nanostructures et Optique (NANOPT). Je voudrais d'abord remercier ma directrice de thèse Agnès Maitre, qui m'a offert la possibilité d'accomplir ce projet professionnel. Je la remercie d'avoir eu confiance en moi lors de cette mission, et de m'avoir appris la rigueur scientifique et la prudence qu'il faut maintenir dans un métier comme la recherche. Étant donné ses importantes responsabilités administratives, je lui suis reconnaissant du temps qu'elle m'a consacré, au travers d'échange de connaissances et de discussions dans un esprit ouvert.

Je voudrais également remercier chaleureusement tous les membres de l'équipe qui m'ont accueilli pour rendre mon séjour le plus agréable possible, le tout dans une formidable ambiance de travail. Merci à Jean-Marc Frigerio, François Gendron, Catherine Schwob, Laurent Coolen, Willy Daney de Marcillac, Mathieu Mivelle, Yoann Prado et à mon parrain Bruno Gallas. Pendant mon séjour, j'ai eu la chance de partager cet apprentissage côte à côte avec les doctorants et post-doctorat de l'équipe, que ce soit durant la réalisation d'une manipulation expérimentale ou au détour d'une discussion scientifique. Je voudrais donc remercier Sarra Gam Derouich, Céline Bourdillon, Guillaume Binard, Amit Raj Dhawan, Fu Feng, Thu Loan Nguyen, Ali Mcheik, Cyrine Ernandes, Pascal Djicoly Bassene, Arnaud Choux et Jiawen Liu. Dans le même esprit, c'était un grand privilège pour moi de partager quelques temps avec les stagiaires dont j'ai pu contribuer à la formation et à l'apprentissage pendant leur séjour. Merci à (par ordre chronologique) : Dmitrii Rusakov, Cyrine Ernandes, Katia Ouaret, Nishita Chowdhury, Thinhinana Aoudjit et Hajar Amyar.

Evidemment, ces remerciements seraient incomplets sans mentionner les collègues de l'Institut des Nanosciences de Paris. En premier lieu, je remercie Emmanuelle Lacaze, Hervé Cruguel pour leurs soutien lors des manipulations au microscope à force atomique. Je suis également reconnaissant à Loïc Becerra, Mélanie Escudier et Erwan Dandeu pour le temps qu'ils ont consacré à ma formations en salle blanche. Également, à Francis Breton pour sa gentillesse et sa disponibilité lorsque j'ai pu rencontrer des difficultés avec l'électroniques et l'interfaçage. Pour finir, je remercie Richard Soucek pour la formation que j'ai suivi à la salle chimie.

Je remercie l'école doctorale 564 Physique en Île-de-France pour son soutien et pour son aide dans les démarches administratives, et notamment Jean Hare, Maria Chamarro et Nadine Yassine.

Ce travail de thèse n'aurait pas pu être réalisé sans l'immense contribution de deux extraordinaires collègues de l'ESPCI : Nicolas Lequeux et Thomas Pons. Les réunions et discussions en matière de sciences chimies et de matériaux ont une part significative dans le déroulement de ce projet doctoral. Merci à vous.

Après quatre déménagements à Paris, je me suis rendu compte du dynamisme et de la richesse multiculturelle qui forme cette grande ville. Je tiens à remercier la Cité Universitaire pour m'avoir hébergé pendant une grande part de mon séjour. J'ai eu le plaisir de rencontrer et partager moments extraordinaires à la cite, merci à : Claudia Reyes, Rigel Juárez, Harold Retana et Soledad López.

Mme Canope pour m'avoir ouvert sa maison dans un moment difficile et ma tante Françoise pour toutes les discussions sur les sciences quantiques autour de la table.

Dans la série des remerciements, je ne peux pas oublier mes amies d'enfance, Ruben Hernandez, Ivan Fernandez et Viridiana Espinosa. Ces quelques années à Paris nous ont permis de découvrir de nouvelles cultures, pays et endroits inimaginables que nous garderons très précieusement dans notre mémoire pour les raconter aux générations futures.

Par ailleurs, je remercie toutes ces personnes qui ont fait partie de ma formation hors laboratoire, merci pour leur amitié et leur convivialité lors d'événements sociaux, culturels ou tout simplement de loisir, je remercie Karen, Lucie Boulin et Lorry Mongilardi.

Plus important encore, je remercie mes parents ainsi que ma sœur pour leur entier soutien, pour m'avoir supporté, compris et aimé. Je les garde en tout moment au fond de mon cœur. Merci à eux, pour tout, je les aime.

Sincèrement,
Juan Uriel Esparza

Chapter I

Light-matter interaction in plasmonic nanoantennas

I.1 Introduction

How light interacts with matter at nanoscale level is nowadays an active field of research in the development of new quantum devices oriented to quantum information and communication protocols. The progress in fabrication technologies combined with the conception of individual sources of light have led to explore light-matter interaction at individual scale using metallic or dielectric nanostructures. One of the principal advantages in such nanostructures lies in its capacity to confine the electromagnetic field in dimensions well below the incident wavelength. In particular, metallic nanostructures made of noble metals such as gold or silver present plasmonic resonances in the visible and near-infrared region of the electromagnetic spectrum.

This interaction between a single nanoemitter with respect to its environment is described by the Fermi gold rule which states that the spontaneous emission of one emitter is not dependent only of its intrinsic properties. The interaction is governed by external factors like the polarization of the incident electric field and the available local density of photonic states which modify the photon emission rate of the emitter

$$\Gamma = \frac{2\pi}{\hbar} \left| \langle \vec{d} \cdot \vec{E}(r) \rangle \right|^2 \rho(r, \omega)$$

where $\rho(r, \omega)$ is the local density of photonic states and $\vec{d}$ is the orientation of the dipole emitter. In order to quantify the strength of this interaction, it is commonly use the Purcell factor which normalize the strength of interaction with respect to an homogeneous environment

$$F_{Purcell} = \frac{\Gamma}{\Gamma_0} \propto \frac{Q}{V}$$

where Γ_0 is the total decay rate of the emitter in homogeneous environment. The Purcell

factor is proportional to the quality factor of the cavity Q divided by its mode volume V. In plasmonic resonant nanostructures, the modification of the spontaneous emission is obtained thanks to the confinement of electromagnetic field close to the metal nanostructure, reducing the mode volume of the cavity. This work thesis aims to control the spontaneous emission of a single nanocrystal by means of metallic nanostructures.

I.2 State-of-the-art for coupling single emitters with plasmonic nanoantennas

I.2.1 Not deterministic coupling

Several research groups have demonstrated the coupling of single nanoemitters with plasmonic nanoantennas. Some of them were initially conceived to probe fundamental quantum properties, like wave-particle duality in surface plasmons polaritons (SPP's). One of those works was conducted by Akimov and collegues in 2007 [1]. They showed the bosonic nature of surface plasmons by using a single colloidal CdSe quantum dot coupled to a silver nanowire. In such experiment, an acceleration of fluorescence emission of 2.5-fold was obtained when the nanocrystal was positioned in the middle of the nanowire. Two years later, Kolesov and collegues [2], achieved similar factor in acceleration of emission but using a single nitrogen-vacancy (NV) defects as single-photon source. In both experimental demonstrations, the coupling between the emitter and the nanostructure was performed in a non-deterministic way.

In 2009, Moerner and colleagues have demonstrated that, by overlapping the scattering properties of a gold bow-tie antenna with the emission properties of a single molecule, a fluorescence brightness enhancement factor f_F (defined as the ratio between the fluorescence signal of the molecule with and without nanoantenna), can reach values higher than 10^3. In such experiment, the exact position and orientation of the molecule was not known as the deposition of the molecules was random [12].

I.2.2 Deterministic coupling

In the context of deterministic coupling, several lithography techniques have been developed with the purpose of positioning single nanoemitters in deterministic fashion [5], [6]. For instance, in the group led by Niek. F. van Hulst, they have coupled single nanocrystals to a Yagi-Uda nanoantenna by using a two-step electron beam lithography technique [7]. The Yagi-Uda antenna has demonstrated the capacity to transform fluorescence emission of a single emitter into a directional light emission.

Another approach for deterministic coupling, has been performed in the group of Edo Waks using a microfluidic flow to control the position of a single quantum dots along a silver nanowire [8]. In such experiment, the enhancement of fluorescence emission has reached a value of 2-fold with an imaging accuracy of 12 nm. In a different approach for deterministic coupling, Su-Hyun Gong and colleagues have performed deterministic

coupling by selective growth of pyramidal QDs (InGaN) and thin metal film deposition [9]. The plasmonic modes excited in the apex of the pyramid nanostructure have provided an enhancement factor of 22-fold when matching the broad band spectral resonance of the plasmonic structure with the fluorescence emission of the quantum dot.

More accurate techniques have been developed using scanning near-field optical microscopy. In 2010, A. Cuche and colleagues, have showed the efficient generation of single surface plasmons using NV color centers sticked on the apex of an optical fiber tip [10]. The deterministic position of the apex tip excites single plasmons with high accuracy observed thanks to leakage radiation microscopy. The coupling of a single NV with a metallic structure by means of an Atomic Force Microscope (AFM) has been demonstrated by Andersen and colleagues in 2011 [11]. By comparing the fluorescence emission rate, before and after the coupling, they have demonstrated a Purcell factor between 2.9 to 4.6-fold of a single emitter. More recently, the coupling of quantum emitters with a metal-dielectric parabolic antenna has demonstrated large directivity and low divergence [13].

I.2.3 Some applications of optical antennas

The use of plasmonic nanoantennas covers a wide rage of applications [5], [14]. We can notably mention the use of plasmonic antennas to improve the performance of single-photon sources. Plasmonic nanostructures have been also used in photovoltaic and photodetection devices. The optical antenna increases the absorption cross-section and hence the solar light flux than arrives on the detector area. Normally, the thickness of a detector is limited by the absorption depth of the detector material. The use of metallic nanoantennas reduces the thickness of the detector area and improves performance [15], [16].

Another application of localized surface plasmons is based on the exploitation of the spectral position resonance which is very sensitive to the properties of the local dielectric environment surrounding the nanoparticle. For instance, in biological systems, the absorption of molecules on a fuctionalized metal surface can lead to significant spectral variations. The potential of highly sensitive plasmonic sensors for biological targets has been demonstrated in [17].

The scattering properties of nanoparticles is useful for labelling and detecting DNA arrays [18]. The large absorption cross-section of metallic nanoparticles can be also used for photothermal therapeutic treatment. The treatment starts with the labelling of the cancerous cell. The labelled cell is then irradiated with light which is absorbed by the particle and converted to heat. The local heating of the nanoparticle induces structural damage in the cancerous cells until destruction [19], [20], [21].

I.3 Objective of the thesis

In this thesis, the objective is to establish a protocol for in-situ lithography in order to fabricate patch nanoantennas with a single colloidal nanocrystal. Then, once several

active antennas are fabricated, we study their photon emission properties in terms of dynamics emission, spectroscopy and emission diagram in Fourier plane.

I.3.1 Plasmonic patch nanoantenna

In these systems, the confinement of surface plasmons is produced by two metal-dielectric interfaces. They are also known as Metal-Insulator-Metal structures (MIM). Such systems were firstly proposed by Bozhevolnyi in 2007 [22]. The patch nanoantenna studied in this thesis belongs to such family of nanostructures.

The patch antenna structure consists in an optically thick gold layer, below a thin dielectric layer (30-40 nm) covered by a optically thin gold patch like a nanodisk. For an active antenna, emitters are located inside the dielectric layer. Thanks to the emitter, surface plasmons are excited in both metallic-dielectric interfaces (upper thin Au nanodisk and bottom Au substrate). Therefore, the field is highly confined inside the antenna. In a plasmonic patch antenna, short-range surface plasmons are efficiently excited. These plasmons are characterized by a short propagation length and high confinement of electromagnetic field inside the insulator. Moreover, thanks to the finite size of the nano-disk a stationary plasmonic mode of the nanodisk may increase the confinement. In Figure I.1 we show the absolute value of the E_z component of the electric field of the first three modes in the patch antenna.

In 2010, Esteban and colleagues proposed the plasmonic patch nanoantenna as a novel structure to improve the photoluminescence properties of a single-photon emitter [23]. Three years later, Cherif Belacel (INSP-LPN) and colleagues have experimentally demonstrated the capacity of the patch antenna to accelerate fluorescent emission rate in small clusters of Cadmium selenide (CdSe)/Cadmium sulfide (CdS) nanocrystals up to 80-fold factor [24]. In such experimental work, the deterministic position of the nano-disk was obtained using the in-situ lithography technique reported in [25]. The first realisation of patch antennas with a single emitter deterministically located in the center of the antenna has been obtained during the thesis of Amit Raj Dhawan in 2016 [26]. The antennas have shown high Purcell factor (>72-fold) and brightness enhancement by a factor around 70 (by comparison with the same emitter on a gold layer, without the patch).

I.4 Structure of the thesis manuscript

This thesis is divided into six chapters. In the first chapter (the present one), we have discussed the physics that governs light-matter interaction in single nanoemitters. Then, we have presented the state of the art in deterministic coupling between single photon emitters with plasmonic nanostructures. We finish the chapter by describing the plasmonic properties of metal-insulator-metal structure. In Chapter 2, we will discuss the fluorescence emission properties of a single semiconductor CdSe/CdS nanocrystal. We will start by describing the core-shell heterostructure and then we will discuss the characteristic *blinking* behaviour of these nanocrystals. Later on, we will discuss the significance of the second-order autocorrelation function ($g^{(2)}(t_0, \tau)$). In the same chapter, we will discuss

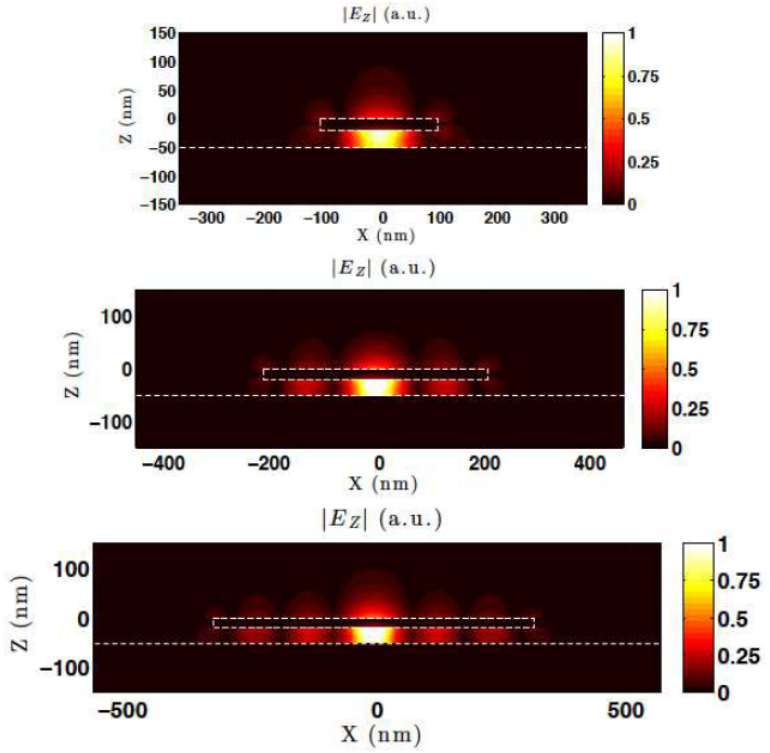

Fig. I.1 *Absolute value of the z-component of the electric field of the first three modes of the patch structure. The white dash lines represent the limits of the metallic structures. Adapted from [27].*

fluorescence dynamics and photoluminescence spectra of a single nanocrystal. We will finish by presenting a theoretical model which takes into account exciton and bi-exciton radiative recombination for describing the evolution of photon emission. In Chapter 3, we will introduce the confocal fluorescence set-up used for studying nanocrystals at individual scale. We will discuss the spectral resolution and calibration features of our spectrophotometer. Afterwards, we will discuss how to construct the decay rate curve and the second order autocorrelation function from the recording of photo-events in a row-data table. Then, we will determine the time resolution of our fluorescence experimental set-up. Finally, we will present the experiment set-up which has allowed carrying out reflectivity measurements on single passive antennas. We will show some experimental results in passive nanoantennas with different morphological characteristics. By considering the patch antenna as a system of multiple thin layers, we can recover the spectral reflectivity signature of the patch antenna. In Chapter 4, we will present the improvements of the in-situ lithography protocol mainly in development and lift-off steps. In Chapter 5, we will discuss some results of active antennas coupled to single nanocrystals. We will discuss the super-poissonian emission properties in the emission of some antennas after the application of a temporal fast filter. We will concentrate our discussion in one antenna which exhibits both super-poissonian photon distribution and coherence properties emission. Finally, in Chapter 6 we will present the general conclusions of the

thesis.

Chapter II

Spectroscopy of a single CdSe/CdS nanocrystal

II.1 Introduction

In this chapter, I will mostly discuss spectroscopic characterization of a single semiconductor Cadmium selenide (CdSe)/Cadmium sulfide (CdS) nanocrystal. The fluorescence of semiconductor nanocrystals is associated to the fundamental band-edge transition with emission of single-photons in the visible spectrum range, typically around 630 nm.

Single nanocrystals are not a simple two-level system, as they are constituted with thousands of atoms. The different excitation states can lead to the generation of one or multiple electron-hole pairs depending on excitation power. The recombination of multi-excitons can be either radiative or non-radiative. In semiconductor quantum dots, Auger mechanisms are associated to non-radiative recombination of multi-excitons, preserving their single-photon property. When Auger processes become inefficient with respect to radiative ones, multiexciton can become radiative and several photons are emitted in the recombination process.

We will present photoluminescence emission of single nanocrystals. In particular we will discuss the evolution of fluorescence emission at different conditions of excitation power. The physical characteristics of the nanocrystal studied in this chapter correspond to a core-shell structure CdSe/CdS (3.3 nm-core, 6 nm-shell thickness).

II.1.1 Structural properties

Semiconductor CdSe/CdS nanocrystals can be found in two stable crystallographic structures: wurtzite and zinc-blende. Wurtzite is an hexagonal anisotropic structure for which the crystalline axis (so-called c-axis) is not equivalent to the two remaining axis. The growth of CdSe-core layer is preferential along the c-axis [28], [29], [30]. In fact, this asymmetry in the crystal lattice may produce non spherical core/shell nanocrystals. Ellipticity of aspect ratios close to 1.3 and 1.4 has been reported based on transmission

electron microscopy [31].

On the other hand, CdSe/CdS nanocrystals can also be synthesized with a zinc-blende cubic structure. In this crystallographic structure, the three axis are equivalent. The shape of these nanocrystals is almost spherical. The nanocrystals studied in this thesis have been synthesized with a CdSe-core of zinc-blende structure as reported in [32], [33].

Composed by thousand of atoms, colloidal nanocrystals are commonly considered as "artificial atoms" or, in quantum information technologies as quantum dots. High-quality quantum dots may have exceptional photoluminescence properties including excellent photostability, high quantum yields, broad absorption bands and strong size-dependency in optical and electronic properties [34], [35], [36]. The narrow photoluminescence emission of these emitters can be tuned in the complete visible spectra by adjusting the diameter size of the nanocrystal. In the field of medicine and biology, quantum dots have been used for labelling living cells and for single particle tracking imaging.

The physical dimensions of the CdSe-core structure is normally below the Bohr exciton radius ($r_b = 5.6$ nm). For such small dimensions, the continuous electronic bands in the bulk material are reduced into discrete and quantifiable energy bands, similarly to individual atoms. In excited states, the confined electric carriers (electrons and holes) occupy discrete levels in the valence and conduction bands. The radiative recombination in then governed by the band-edge exciton transition.

The first controlled synthesis of semiconductor nanocrystals dates from 1993 by the group of M. Bawendi from MIT [37]. Consecutively, the group of P. Guyot-Sionnest [38] report the improvement of photoluminescence properties by including a ZnS capping layer to passivate the surface and protect from trapping-states of charges. Since those pioneer works, it has been significant advances in synthesis procedures and surface modification science to address the improvement of the photoluminescence properties in such confined systems.

Overcoating of the bare CdSe-core with a shell material with a larger band gap has been one effective strategy for reducing blinking emission in single quantum dots. The incorporation of a thin protective shell layer creates a potential difference. Therefore, the electric charges which are strongly confined in the spherical CdSe-core, mimic the classical "particle in a box" model of elementary quantum mechanics. In 2008, the group led by V. I. Klimov has demonstrated this improvement by encapsulating the CdSe-core in a sufficiently thick inorganic shell layer of Cd, CdS or ZnS. In these studies the reduction of blinking has been observed in core/shell and core/multishell structures [39], [40].

Beside blinking, quantum yield is another figure of merit that characterize the performance of semiconductors nanocrystals. The community of chemical science has centralized significant efforts to improve this value. In recent years, the group led by B. Dubertret has successfully synthesized nanocrystals with a composition gradient between the CdSe-core and the CdS-shell. The fluorescence emission of these quantum dots presents almost unity quantum yield for monoexciton and biexciton emission in air at room temperature

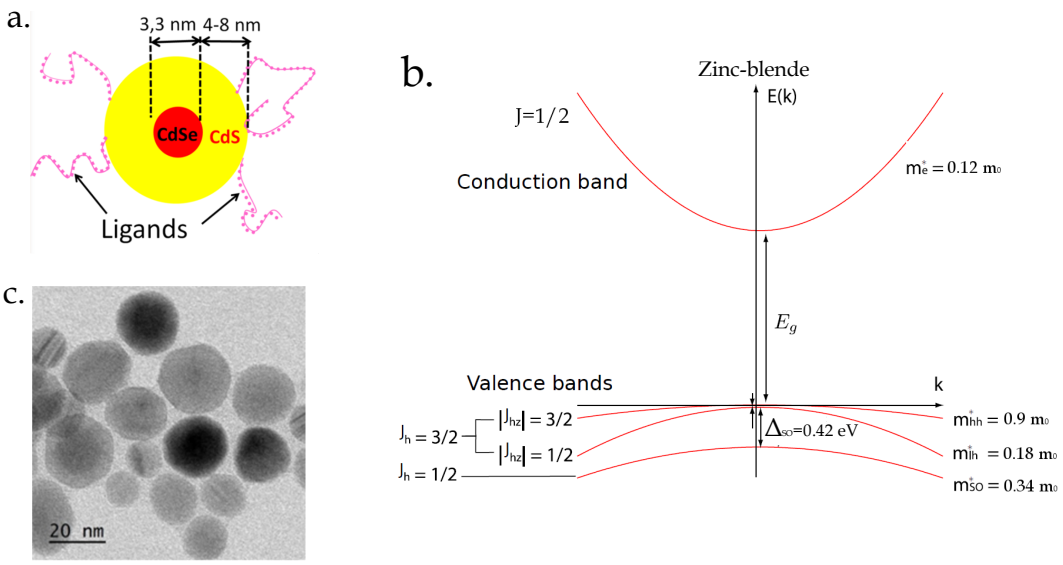

Fig. II.1 *a) Schematic design of a core/shell single nanocrystal CdSe/CdS with the organic ligands molecules surrounding the structure to provide chemical passivation of the surface and prevent nanocrystals from aggregating. b) Band diagram structure of bulk CdSe in zinc-blende crystalline structure. c) Transmission electron micrograph of CdSe/CdS quantum dots. Values of effective mass are recovered from [41].*

[33].

II.1.2 Classification of core/shell heterostructures

Commonly, core/shell heterostructures can be classified as type-I and type-II depending on the capping material and the band-offset alignments. In type-I heterostructure, the electron and hole wave functions are both localized inside the core of the heterostructure (Figure II.2a). The difference in bandgap energy between the capping material and the core layer benefit the confinement of both electrical charges. The recombination of the electrical charges is then occurring within the core. CdSe/CdS and CdSe/ZnS nanocrystals represent such kind of heterostructure. The CdSe-core has a bandgap energy of $E_g = 1.7$ eV, while ZnS-shell is around $E_g = 3.6$ eV.

CdSe/CdS nanocrystals can be classified as type-I heterostructure, according to [42]. In Figure II.2a, we show the electronic band structure of type-I heterostructure. From the Figure II.2a, we can see that the conduction band of CdSe and CdS are nearly aligned, whereas the valence band are not aligned. Therefore, the electron wave function is less confined than the hole wave function which is confined within the CdSe core. In core-shell CdSe/CdS nanocrystals, the hole remains confined inside the core while the electron is delocalized in the entire structure.

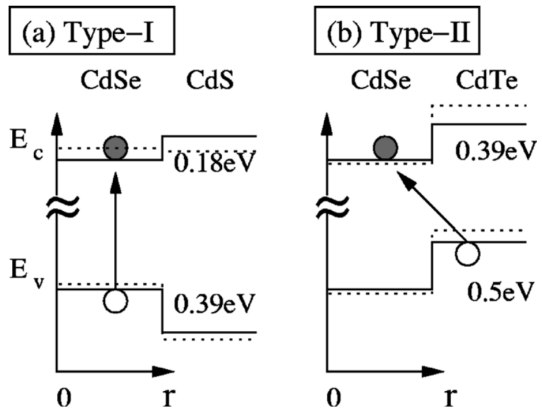

Fig. II.2 *Classification of core/shell heterostructure. a) Type-I heterostructure. b) Type-II heterostructure. In type-I, the hole remains confined inside the CdSe-core while the electron is delocalized in the whole structure. In type-II, the hole wave function is localized within the CdTe-shell and the electron wave function is confined in the CdSe-core. The solid lines represent the natural conduction and valence bands of CdSe/CdS (for type-I heterostructure) and CdSe/CdTe (for type-II heterostructure). In both classifications, the conduction bands are nearly aligned, whereas the valence bands are not aligned. The dash lines represent the theoretical electronic bands reported on [42]. In such calculations, the difference between natural and theoretical electronic bands are explained by strain effects (tensile and compressive strain). Figure adapted from [42].*

In Type-II heterostructures, the difference of energy between valence band and conduction band is large. This heterostructure is characterized by the separation of electron and hole wave functions on different sides of the heterostructure (Figure II.2b). In Type-II heterostructures, the hole wave function is localized within the shell while the electron wave function remains confined inside the core. CdTe/CdSe, CdSe/CdTe, ZnSe/CdS are examples of type-II heterostructure.

II.1.3 Types of Blinking

a) Nanocrystal blinking

Blinking is the random switching of fluorescence emission in a single nanocrystal. It is characterized by the interruption of fluorescence emission in the commutation of a bright-state (or on-state) to a dark-state (or off-state). Fluorescence blinking impacts directly the quantum yield. From all the photoluminescence characteristics of single quantum dots, blinking has been one of the most important constrains to applications.

In recent years, considerable advances in synthesis protocols has led to a new generation of single CdSe/CdS nanocrystals with reduced and almost suppressed fluorescence blinking. The solution has consisted in the incorporation of a thick-shell layer to passivate

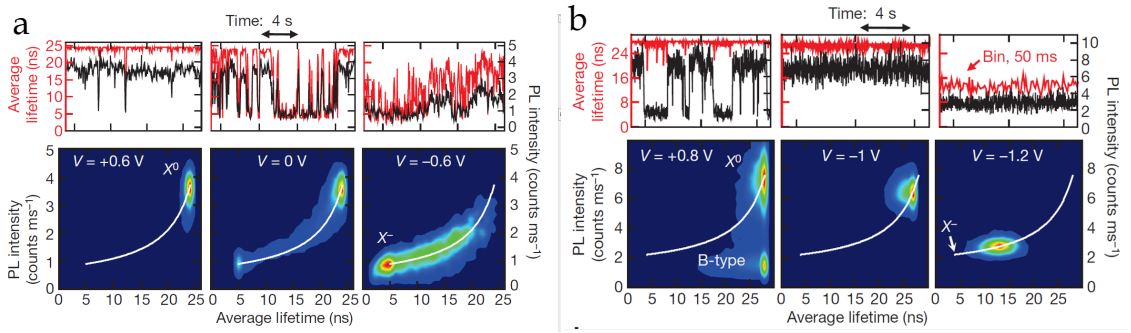

Fig. II.3 *Top images: Fluctuations in average lifetime (red line with left-axe) and photoluminescence intensity (black line with right-axe) as a function of time for a single core–shell CdSe/CdS nanocrystal exhibiting a) Type-A and b) Type-B photoluminescence blinking. The bottom images show the correlation between photoluminescence intensities and lifetimes in a two-dimensional space. The probability of occupying a given state in this 2-D representation is shown by false colours which vary from blue to red as the probability increase. Figure adapted from [45].*

the electrical charges trapped at the surface of the CdSe-core. This physical modification has improved the photoluminescence and photostability emission, exhibiting high brightness and an almost unity quantum efficiency. Nevertheless, for some core/shell nanocrystals, the growth of a thick shell layer has not completely reduced the blinking. These photoluminescence fluctuations are called flickering (switching between on-state and gray-state) [43], [44].

The origin of fluorescence blinking is directly linked with the presence of an additional electrical charge (besides the electron-hole pair). This extra charge can behave as a delocalized charge surrounding the core of the nanocrystal or, it can restrict the spatial distribution of its wave function when it is trapped by defects at the CdSe-core surface. The fluorescence dynamics of a nanocrystal in the presence of the additional charge is commonly referred to a trion-state. The fluorescence emission of a nanocrystal in a trion-state might be diminished because of the opening of non-radiative Auger channels, resulting in the decrease of photoluminescence quantum yield.

In the literature, we can identify two categories of fluorescence blinking, Type-A and Type-B [45]. Relevant aspects of the two types of blinking are described below:

b) Type-A blinking

In a type-A model, called charging model, we assume that the trapped charge leaves the core and let it charged. This process corresponds to an ionization. The nanocrystal is negatively charged. By a new excitation creating an exciton, the recombination energy of the exciton is non-radiatively via Auger effect, transferred to the delocalized electron. We have here a new non-radiative channel in competition with the radiative recombination of exciton. This competition has as a consequence a strong reduction of the quantum yield

resulting, depending on the efficiency of the Auger process, either in a dark-state or in a grey-state, for which the fluorescence is drastically reduced. The lifetime becomes much shorter as well. Indeed, the total decay rate, which is the inverse of the lifetime, is the sum of three decays corresponding to the large non-radiative Γ_{Auger} and the radiative channels of recombination of one of the two electrons with the remaining hole. The nanocrystal switches to the on-state when the hole, the trapped charge returns to the nanocrystal, which neutralizes it.

In an experimental paper [45], C. Galland and colleges demonstrated that, when applying a positive potential of $V = +0.6$ V (injection of holes), the recombination of the delocalized electrons is beneficial and blinking is strongly reduced (Figure II.3a). Reversely, when injecting electrons ($V = -0.6$ V) the nanocrystals state remains negatively charged because the electrons surrounding the nanocrystal are recombining with trapped holes at the surface which prevents the recombination of the delocalized negative charge.

c) Type-B blinking

In a type-B blinking, holes charges are trapped at each excitation cycle. Once they are trapped, they prefer to recombine non-radiatively with the delocalized charge (e^-), because the non-radiative rate is much larger than the radiative one. At the end of each cycle, the nanocrystal is neutral, and the cycle can start again. So here, on the contrary to Type A blinking, we do not have a non-radiative Auger process which competes with the radiative recombination of the exciton. Here the radiative recombination is in competition with the transfer of hole charge. Therefore, the recombination rate of exciton is not modified and the lifetime remains constant. The quantum yield is usually very low as the transfer of hole charge is usually very effective. The off-state stops when the transfer of charge becomes less efficient, for example because the trap state on the surface has changed.

In the experimental paper [45], for positive potential $V = +0.8$ V, the intensity fluctuates between two binary intensity levels but the lifetime remains constant. Switching off is due to the trapping of electrons in trap states preventing the radiative recombination of the exciton. When moderate negative potential is applied ($V = -1.0$ V), the traps states are filled with electrons and blinking is prevented. As the rate of the recombination of electrons in the band-edge is higher that the rate of electrons in the trapping states, radiative recombination is allowed. For even more negative voltage ($V = -1.2$ V), the trap states and the band-edge are filled with electrons, implying an emission from the trion state. Electrons are more likely to be trapped during B-type blinking.

From Figure II.3, we can observe that both types of blinking present a well-define switching from on-state to off-state and vice versa. The principal difference between them relies on the fact that trapping process in Type-B doesn't compete with fluorescence. In B-type blinking the average lifetime remains nearly constant independently of the nanocrystal emission.

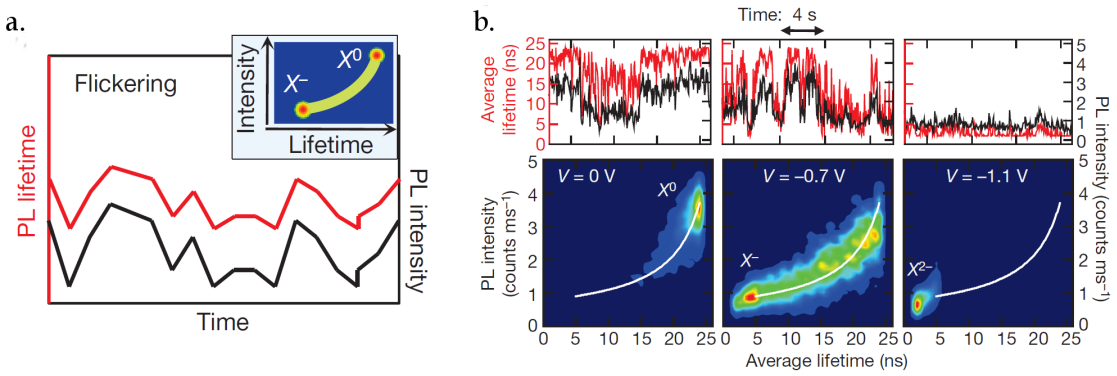

Fig. II.4 *a) Conventional model of fluorescence flickering in CdSe/CdS nanocrystals. b) Top images: Fluctuations in average lifetime (red line left-axis) and photoluminescence intensity (black line right-axis) as a function of time for a single core–shell CdSe/CdS nanocrystal. Bottom images: correlation between photoluminescence intensities and lifetimes in a two-dimensional space. Adapted from [45].*

d) Fluorescence flickering

Beside type-A and type-B blinking observed in [45], the authors differentiate another photoluminescence blinking that they named flickering. In fluorescence flickering, the photoluminescence intensity varies from on- to off- states passing through intermediate grey-states, as it is schematically showed in Figure II.4a. Because the variation of lifetime is associated with the fluctuation of intensity, fluorescence flickering can be seen as a modified type-A blinking including intermediate gray-states.

Figure II.4b displayed the photoluminescence variations of a nanocrystal exhibiting flickering. We observe that, without any voltage applied at $V = 0$ V, photoluminescence intensity and lifetime present a more continuous distribution with respect to the ordinary type-A blinking showed in Figure II.3a. The change in blinking behavior is most probably due to the shortening of the time spent by the nanocrystal in a given charge state, switching very fast between all the states.

II.1.4 Quantum efficiency

In the study of any individual fluorescence object, one of the figure of merit that accounts for the photo emission process is the quantum efficiency. We define quantum efficiency as the ratio of the number of emitted photons divided by the number of absorbed photons [46]. It determines the balance between radiative process with respect to the total relaxation mechanisms occurring in the nanocrystal. The quantum efficiency is thus the proportion

$$QE = \frac{\gamma_{rad}}{\gamma_{rad} + \gamma_{nrad}},$$

where γ_{rad} is the emission rate of a photon and γ_{nrad} accounts for the intrinsic non-radiative relaxation mechanisms of the emitter, such as thermal dissipation, vibrational phonons, residual trapped charges, etc.

II.1.5 Second-order autocorrelation function $g^{(2)}(t_0, \tau)$

Since the pioneering experiment proposed by Hanbury Brown and Twiss in 1956 to probe the correlation of photons in two coherent beams of light [47], the autocorrelation interferometer has been widely used in the scientific community. It is notably used in quantum optics to probe the single photon emission of different emitting species (individual atoms, molecules, quantum dots, color centers, etc). The first demonstration of photon anti-correlation (or commonly said anti-bunching) was performed by Kimble, Dagenais and Mandel in 1977 [48]. They observed that the fluorescence emission of an individual sodium atom displayed intensity anti-correlation, phenomena that is understandable only if considering the light as a quantum object with a quantified electromagnetic field.

Indeed, the original experiment proposed by Hanbury Brown and Twiss in 1956 was conceived to detect thermal light emission coming from stars and galaxies. After some difficulties in conceptual interpretation, they decided to test the principle of the experiment in the laboratory using a mercury arc lamp (see Figure II.5). The light emitted by a mercury lamp is originated from many different atoms. This process is known as thermal radiation and occurs when a very intense heating source (approximately T= 11 500 K, in the case of a mercury arc lamp), provides enough energy to the free electrons over the surface to break the bonding with the nuclei atom and escape into the vacuum. As each radiating atom is emitted with the same amplitude, frequency, but uncorrelated phases between all atoms, the total emitting wave will present random intensity and phase fluctuations. This is the reason why light emitting from such discharge lamps are named **chaotic light**.

At this point, it is convenient to introduce the concept of coherence in classical theory of light. The capacity of an electromagnetic wave to interfere with itself it is commonly named as coherence. We can distinguish between two types of coherence: **Temporal coherence** and **Spatial coherence**. Although both concepts are related to each other, we will concentrate our discussion in temporal coherence, since the interferometer developed by Hanbury Brown and Twiss is based on time-detection of the optical signal. The HBT interferometer provides information about the temporal distribution of light at two observation points.

The temporal coherence of a light beam is quantified by its coherence time τ_c. The coherence time is an inherent property of the source of light. It describes the duration for which the phase wave train remains stable. For instance, in the violet spectral line of a mercury lamp, the radiating light of frequency ω of an excited atom will remains constant until the the atom suffers a collision. The light emitted by a mercury lamp is originated from many different atoms.

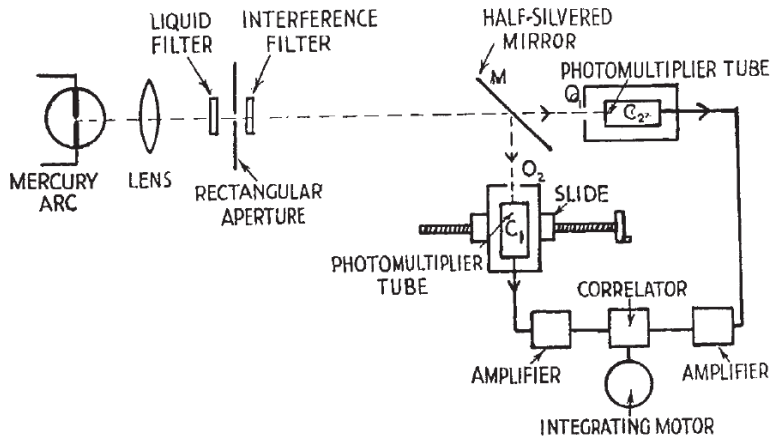

Fig. II.5 *Schemtic representation of the original autocorrelation interferometer used by Hanbury Brown-Twiss (HBT) in 1956. After [47].*

Figure II.6 shows the electric field amplitude of two wave trains emitted by a single source. The occurrence of a collision is represented by a vertical line accompanied by a random change in the phase of the wave. During a collision, the energy level of the radiating atom is slightly shifted, leading to the broadening of the radiation frequency $\Delta\omega$.

From the Figure II.6, we define τ_c as the average period of time corresponding to evolution of waves independent from collision (undisturbed light). Then, if we know the phase of the wave train at time t_0, we can know with high degree of certainty the phase of the wave train at a different time $t_0 + \tau$ at the condition that $\tau << \tau_c$. For the case of the mercury lamp, the coherence time τ_c is limited by the occurrence of collisions between

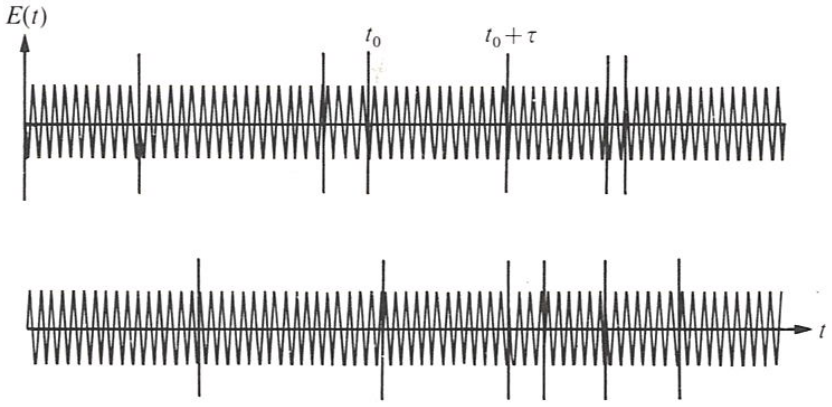

Fig. II.6 *Electric field amplitude of the wave train showing the jumps in phase due to collisions of the atoms. Adapted from [49].*

atoms. The occurrence of collision determines the width of the spectral line $\Delta\omega$. These quantities are inversely proportional

$$\tau_c \approx \frac{1}{\Delta\omega}. \tag{II.1}$$

Equation (II.1) shows that the coherence time is limited by the spectral width of the source. This implies that, in the ideal case of a perfectly monochromatic light source with $\Delta\omega = 0$, the coherence time will be infinite (perfect coherence). In practice the sources of light are characterized by a spectral width of frequencies $\gamma = \Delta\omega$ which impose limits in the interference of two electromagnetic waves.

In order to analyze quantitatively the experimental results presented by HBT, we will now introduce the second-order correlation function $g^{(2)}(t_0, \tau)$ which investigates the temporal coherence of the source based on photon statistical properties. The autocorrelation function is not only a convenient tool to probe the quantum nature of light in single nanocrystals, it also gives insight about the source depending on its photon distribution.

The second-order autocorrelation function is defined as

$$g^{(2)}(t_0, \tau) = \frac{\langle I(t_0) I(t_0 + \tau) \rangle}{\langle I(t_0) \rangle \langle I(t_0 + \tau) \rangle},$$

where $\langle\ \rangle$ denotes statistical time average. $g^{(2)}(t_0, \tau)$ is proportional to the conditional probability of detecting a second photon at time $t = \tau$, given that has been detected one at $t = t_0$. $g^{(2)}(t_0, \tau)$ is useful to prove the non-classical behaviour of fluorescence emitters. In more precise terms, the second-order autocorrelation function $g^{(2)}(t_0, \tau)$ is a tool to classify the light according to the photon statistics or, in another way, the fluctuations of the electromagnetic field. The classification is based on the value of $g^{(2)}(t_0, \tau)$ at the time $\tau = 0$. Figure II.7 illustrates the three main types of photon statistics (poissonian, super-poissonian and sub-poissonian) for $\gamma = 1$.

- $g^{(2)}(t_0, 0) > 1$. This property corresponds to a super-poissonian photon statistics. $g^{(2)}(t_0, 0) > 1$ means that the probability to detect a photon almost immediately after the first one has been detected is higher than for longer times. If we consider the poissonian distribution as reference of the random process, $g^{(2)}(t_0, 0) > 1$ means that the light is compacted in shorter intervals of time with respect to the random poissonian case. The photons arriving in such conditions are said to be bunched, they arrive in compact groups to the photodetector as it is depicted in Figure II.7a. Thermal fields radiated from black-body sources exhibit such characteristic emission. Chaotic light from electrical discharge lamps or any incandescent device in general are some other examples. In Figure II.7b we show the evolution of $g^{(2)}(t_0, \tau)$ for two forms of chaotic light: 1) Chaotic light showing a gaussian frequency distribution (orange curve) and, 2) Chaotic light showing a lorentzian frequency distribution (yellow curve).

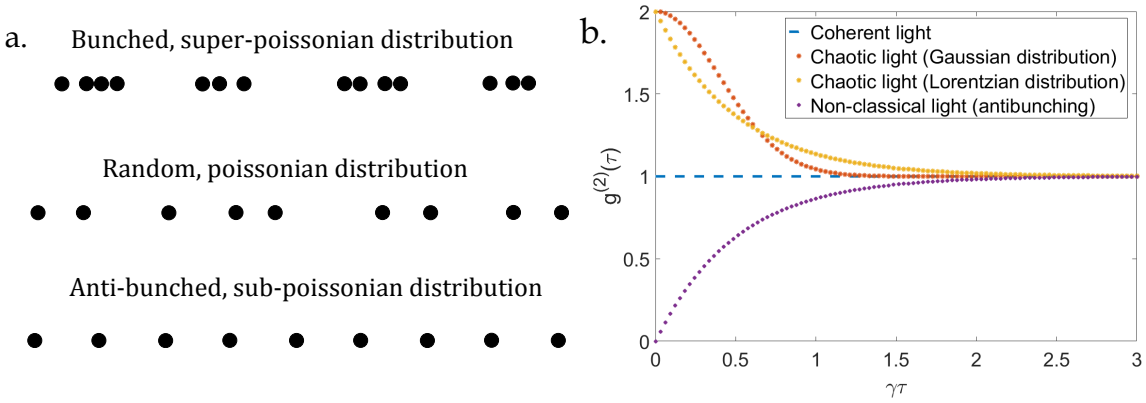

Fig. II.7 *a) Schematic representation for stream of photons showing sub-poissonian, poissonian and super-poissonian distribution. b) Second-order autocorrelation function $g^{(2)}(t_0, \tau)$ in the case of a coherent light source, chaotic light (with gaussian and lorentzian distribution) and non-classical light (antibunching) for $\Delta\omega = \gamma = 1$.*

- $g^{(2)}(t_0, 0) = 1$. This property is characteristic for a poissonian distribution. In a poissonian distribution, the events are uncorrelated and independent. The time interval between two consecutive photons is random. This implies that the probability of detecting a second photon after detecting the first one, will be the same for all values of τ. $g^{(2)}(t_0, 0) = 1$ represents the threshold between classical and quantum sources of light.

- $g^{(2)}(t_0, 0) < 1$. The source of light presents a sub-poissonian distribution. The photons arriving to the photodiode are "well ordered" in define intervals. The conditional probability of detecting a second photon, immediately after the first one, is lower than the case of a poissonian distribution. The photons are said to be antibunched. Photon antibunching represents the signature of single-photon emission. Photon antibunching is an unambiguous proof of the quantum nature of light. Sub-poissonian photon statistics has no classical theory counterpart, and it is also referred as non-classical light. Individual semiconductor nanocrystals studied in this thesis present such property of antibunching in proper conditions of excitation at room temperature.

II.1.6 Multiexcitonic Auger recombination in nanocrystals

The transfer of non-radiative energy between electrical charges is commonly referred as Auger recombination. Auger recombination takes part in direct competition with radiative recombination channels (photon emission). Auger recombination is a highly efficient process in semiconductor nanocrystals. The excited electrical charges inside the nanocrystal are proned to interact each other through Auger mechanisms occuring at some tens of picoseconds. One of these Auger mechanisms is conducted via Auger electronic thermal-

ization, which is the transfer of energy of one excited electron to one other electron. This excited electron then thermalize to the bottom level of conduction band. This model was proposed in 1995 by Al. L. Efros *et al.* for spherical CdSe nanocrystals [50].

In semiconductor quantum dots, Auger mechanisms are at the origin of single-photon emission property. During the excitation with the blue diode laser (405 nm), several electron-hole pairs are created inside the nanocrystal (multi-excitons). Because of Auger effects, most of them recombine non radiatively excluding the last exciton which may recombine radiatively emitting a single-photon.

Auger mechanisms are in competition with radiative recombination of excitons. Therefore, when many excitons have been produced by laser excitation, if the Auger processes are not infinitely efficient, some of the excitons recombine radiatively. Several studies have demonstrated that Auger recombination processes are enhanced by reducing the nanocrystal radius. Small nanocrystals are usually single photon sources whereas large nanocrystals multiexciton has a higher probability to recombine radiatively [51].

II.1.7 Bi-excitonic emission

The bi-excitonic radiative recombination in a nanocrystal can be attained when Auger mechanisms are not efficient enough to maintain single-photon emission, when radiative recombination mechanisms become predominant with respect to Auger non-radiative processes. In that case, the radiative recombination of a bi-exciton might lead to the emission of a second photon for the same excitation pulse. In this section, we are going to discuss the mechanisms that are involved during the relaxation of a bi-excitonic state.

In Figure II.8, we illustrate the situation when most of the electron-hole pairs generated during pulse excitation have recombined non-radiatively except two excitons (bi-exciton). In the figure we have used different colors (blue and red) for each excitonic charge.

There are two channels for the recombination of the bi-exciton. In the first one (left on Figure II.8), the radiative recombinations of the blue and red excitons lead to the emission of two successive photons. The first photon is emitted by the recombination of the blue exciton ($\mathbf{XX}\rightarrow\mathbf{X}$). Then, the second photon is emitted by the recombination of the red exciton ($\mathbf{X}\rightarrow\mathbf{0}$), as it is shown in Figure II.8. This cascading mechanism will contribute as one event in the zero-delay peak of the second-order autocorrelation function $g^{(2)}(t_0, 0)$.

On the right part of Figure II.8, we present the second channel for recombination of bi-exciton. The first relaxation process $\mathbf{XX}\rightarrow\mathbf{X}$ correspond to Auger non radiative recombination. The blue exciton transfers its recombination energy to the electron which reaches a higher energy state. Then, it relaxes to the fundamental band-edge transition by thermalization. In the consecutive relaxation process $\mathbf{X}\rightarrow\mathbf{0}$, there is just one exciton left. The radiative recombination of the remaining red exciton leads the emission of only one photon. In this case, thanks to the highly efficient Auger mechanism, just one single-

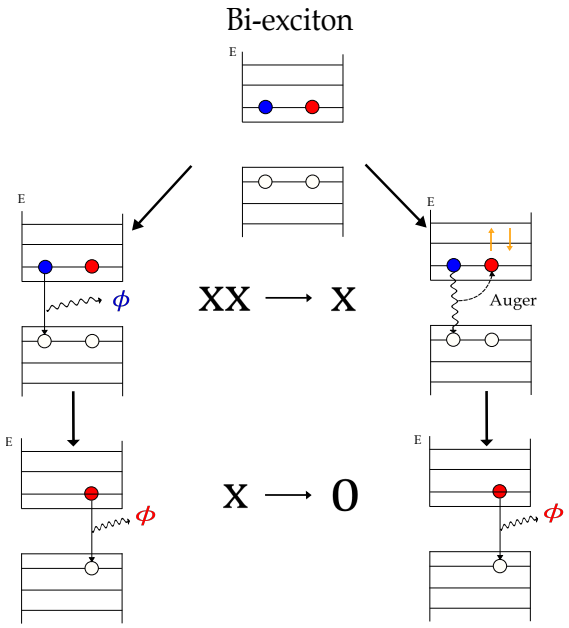

Fig. II.8 *Bi-exciton recombination in CdSe/CdS nanocrystals.*

photon is emitted by the semiconductor nanocrystal.

Until now, we have discussed the case when a single excitation pulse excites two electron-hole pairs. However, more than two excitons can be excited and could recombine radiatively. Multi-excitonic emission can occur when non-radiative channels, like Auger ones, are less efficient than radiative ones. Non-radiative Auger mechanisms are inversely proportional to the volume of the nanocrystal. Therefore, multi-excitonic emission will be more efficient for large nanocrystals than for small ones.

In the next section, we will evidence the multi-excitonic emission in single nanocrystals for different excitation power. We will show that, for a single nanocrystal, the combination of photoluminescence decay curves, the second-order correlation function ($g^{(2)}(t_0, 0)$) and photoluminescence spectra, evidence the multi-excitonic character of single quantum dots.

II.2 Photoluminescence spectra of a single CdSe/CdS nanocrystal

The photoluminescence studies of semiconductor nanocrystal at individual scale bring quantitative information different from ensemble fluorescence measurements of clusters systems. First, the fluorescence emission spectra of a single nanocrystal is not affected by the broadening of linewidth due to the size dispersion in the nanoparticles. Additionally, by dispersing the nanocrystals, there are some micrometer around each others, so that the interaction between emitters is absent. Therefore, the fundamental band-edge transition $1S_{3/2}1S_e$ and the dielectric environment will be the most relevant components for

photoluminescence emission. The emission from higher excited states is generally absent in low power excitation regime.

The possibility of creating more than one photon per excitation pulse provides additional interesting properties. Besides exciton emission (X) in quantum dots, the radiative recombination of multi-excitons (bi-exciton XX, tri-exciton XXX, etc) and charged exciton states (positive or negative trion) brings specific properties which are currently studied by the scientific community.

Several studies have been conducted to distinguish the different emission linewidths from the nanocrystals. Most of these studies have been performed in cryogenic conditions for which the coupling of phonons modes with the optical modes in the nanocrystal are significantly reduced. At cryogenic temperatures, the very thin linewidths make it possible to distinguish between exciton, bi-exciton and additional charge states emission in semiconductor nanocrystals [28], [52], [53].

II.2.1 Multiexcitonic emission of a single CdSe/CdS

In this section we will show the photon emission properties of individual nanocrystals used as source of light in the patch antenna. All the photoluminescence measurements were performed at room temperature in core-shell CdSe/CdS nanocrystals (3.3 nm-core, 6 nm-shell thickness).

We diluted 300 000 times the original batch using hexane as solvent. We spin-coated the nanocrystals in a cleaned coverslip glass assuring sufficient separation between them to distinguish the nanosources individually. When the colloidal nanocrystals are spin-coated on a glass substrate, the organic ligands (the long molecules around the nanocrystals that passivate the surface and ensure a colloidal suspension) cannot protect them from oxidation any more. We included a thin dielectric layer (2% PMMA diluted in toluene) that provides 50 nm thickness which serves as protecting layer from air and environmental contamination, reducing inherent degradation by oxidation and ageing.

We have used a laser scanning fluorescence microscope set-up together with a time-correlated single photon counting system (TCSPC) to characterize single nanocrystal fluorescence emission temporally and spectrally. The use of a variable optical density before the reflection microscope has allowed to control the optical excitation power. The complete experimental set-up is described in section III.3.

Figure II.9a shows the evolution of photoluminescence decay rate of a single nanocrystal excited with a diode laser 405 nm in pulsed mode (2.5 MHz repetition rate, 50-100 ps pulse width) when varying the excitation power. From the Figure II.9a we can observe the modification of lifetime according to the excitation power. The first two decay curves, for excitation 7 W/cm^2 (9 nW) and 12 W/cm^2 (17 nW), correspond to conditions for which the nanocrystal emits mainly single-photon (mono-excitonic emission). We can confirm this assumption by considering the zero-delay peak in the second-order autocorrelation

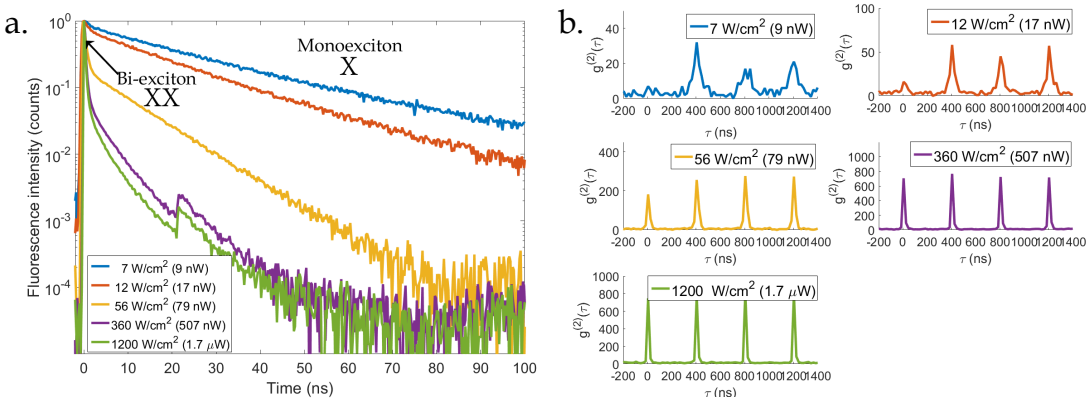

Fig. II.9 *a) Evolution of the photoluminescence decay rate in a single nanocrystal CdSe/CdS at different excitation power. b) Corresponding second-order autocorrelation function* $g^{(2)}(\tau)$.

function $g^{(2)}(\tau)$ on Figure II.9b for both excitation powers. The small difference in the slope in the decay rate could be associated to the thermal modification of the local environment due to the increase of the excitation power.

When the nanocrystal is excited with a fluence of 56 W/cm^2 (79 nW), the decay rate curve clearly shows two different decay rates, the fast decay representing the bi-excitonic recombination ($\mathbf{XX}\rightarrow\mathbf{X}$) and the slow component the mono-excitonic recombination ($\mathbf{X}\rightarrow\mathbf{0}$). For this excitation power, considering the second-order autocorrelation function on Figure II.9b, we can notice that the height of the zero-delay peak has raised up to the height of lateral peaks. This indicate that the nanocrystal doesn't emit any more single photons. In the decay curve, bi-excitonic emission presents a characteristic decay time in the order of hundreds of picoseconds, whereas excitonic emission has a characteristic time of tens of nanoseconds.

On the decay curves of Figure II.9a, we can observe that for 360 W/cm^2 (507 nW) and 1200 W/cm^2 (1.7 μW) excitation power, an increase in the quick contribution part, which corresponds to multiexcitonic recombination. The radiative recombination of multiexciton is as well demonstrated by observing the zero-delay peak in the autocorrelation $g^{(2)}(\tau)$ function which is at the same height than the neighboring peaks.

In Figure II.9a we can note that both decay curves for 360 W/cm^2 and 1200 W/cm^2 present a second peak around 21 ns. These peaks have not any physical interpretation and it is only the result of electrical rebound in the TCSPC system. The electrical saturation observed for a large rate of detection is at the origin of secondary electronic peaks in the photoluminescence decay curve.

II.2.2 Post-processing of bi-excitonic emission

Most of the multiexcitonic studies in single colloidal nanocrystals have been performed using the well-known Hanbury Brown-Twiss interferometer which provides information on the temporal distribution of the photons emitted by the quantum source. For single quantum dots, $g^{(2)}(\tau)$ can evidence the emission of a single photon for one excitation pulse (antibunching effect). In the case of multi-exciton emission at very low excitation rate, we can extract from the second-order autocorrelation function the relative efficiency between multi-exciton and exciton radiative recombination for very low excitation. The ratio of the area below the zero-delay peak and the area below neighbouring peak is equal to Q_{XX}/Q_X, where Q_{XX} is the quantum radiative efficiency for bi-exciton and Q_X the one for exciton. This relation will be demonstrated in the next section, in the model developed in II.2.3. In the case of 12 W/cm^2 excitation, we estimate the ratio between the zero-delay peak and the neighbouring peak to 0.28.

At room temperature, the spectral distinction between mono-exciton and bi-exciton emission is impossible. The linewidth emission of both transitions overlaps almost completely in the photoluminescence spectra. In this section we will discuss how we can separate bi-excitonic from mono-excitonic emission by applying a temporal filter in the decay curve.

Figure II.10a shows the intensity fluorescence lifetime for the case of bi-exciton emission. We have fitted the curve by a two-exponential function where we have obtained lifetimes of bi-exciton $\tau_{BX} = 500$ ps and mono-exciton $\tau_X = 9.8$ ns. If we now apply numerically a temporally fast filter to select only the photo-events registered after 2 ns in the complete histogram lifetime, we can process the autocorrelation $g^{(2)}(\tau)$ function exclusively for the mono-exciton recombination. Figure II.10b displays the superposition of $g^{(2)}(\tau)$ when we use the complete photoluminescence decay curve (blue line) and the one which we have removed all the photo-events recorded within the first 2 ns (red line).

From Figure II.10b we observe that the selection of the slow component retrieves the single-photon emission nature, indicating that we have unambiguously two distinctive photo emission processes, a "slow one" corresponding to exciton $\mathbf{X}\rightarrow\mathbf{0}$ recombination and a "rapid one" corresponding to bi-exciton $\mathbf{XX}\rightarrow\mathbf{X}$ recombination which is 20 times quicker than the former one. The selection of the slow component in the fluorescence histogram reduces the number of effective photo-events used for processing $g^{(2)}(t_0, t)$, therefore the height of the lateral peaks are reduced as well.

Our experimental set-up is composed of two avalanche photodiodes, as a consequence we can assure the probability of single-photon emission when $g^{(2)}(\tau) \approx 0$. In order to precisely count the quantity of photons N_ϕ emitted by the single nanocrystal for each excitation pulse, one possibility is the use of $N_\phi+1$ photodiodes. However, as the number of all possible combination events increases significantly with N_ϕ, the estimation of the quantity of photons by this method would demand an excessive integration time. For instance, including a third photodiode in order to know if we can have three photons par excitation pulse, the number of possible combinations will raise to 36 and only 6 combinations would

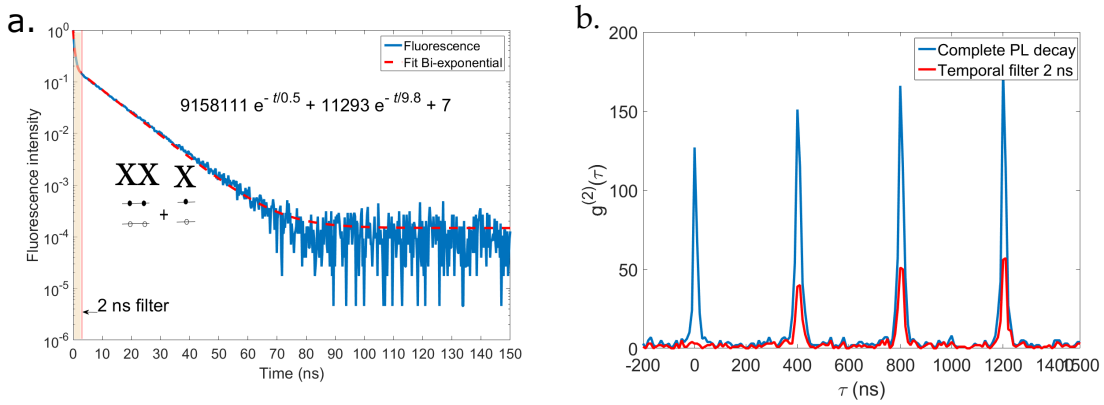

Fig. II.10 *a) Photoluminescence decay rate of a single nanocrystal exhibiting bi-excitonic emission (XX) excited at 56 W/cm^2. b) Second-order autocorrelation function $g^{(2)}(t_0, t)$ with the complete photoluminescence decay and using 2 ns temporal filter.*

contribute to the correlation function proving the recombination process of the tri-exciton.

II.2.3 Model

In this part, we will evaluate the number of photons we can extract from the fluorescence emission of a single nanocrystal excited by a pulsed laser emitting at the wavelength $\lambda_{exc} = 405$ nm, and power P_p, with a pulse width $\tau_{pulse} = 100$ ps and repetition rate $\Gamma_{rep} = 2.5$ MHz.

a) Mean number of excitons per pulse

We define the intensity of the laser as $I_p(r)$ and

$$\mathrm{P}_p = \int I_p(r) dS.$$

$I_p(r)dS$ is the local power of the laser. As the laser is a gaussian mode, $I_p(r) = I_0 e^{-2r^2/\mathrm{W}^2}$, so that the power P_p can be expressed as

$$\mathrm{P}_p = \int I_0 e^{-2r^2/\mathrm{W}^2} 2\pi r dr$$

after integration, we get $\mathrm{P}_p = I_0 \frac{\pi \mathrm{W}^2}{2}$, where W is the waist of the gaussian beam. From diffraction theory, we can approximate $\mathrm{W} \approx \frac{1.22\lambda_{exc}}{2NA}$, where NA is the numerical aperture of the objective. Therefore, we obtain

$$\mathrm{P}_p = I_0 \lambda_{exc}^2 \times \frac{0.6}{\mathrm{NA}^2}.$$

Moreover, we can consider that the nanocrystal is very small (diameter of the order of 10 nm) with respect to the size of the beam ($\approx$ 500 nm of diameter). Therefore, when the laser is centered above the nanocrystal, we can estimate that the nanocrystal sees a constant intensity equal to I_0.

We can now define the pumping rate Γ_p (in s^{-1}). This is equal to the number of exciting photons which will be absorbed by the nanocrystal and will create an exciton. In other words, Γ_p is the mean number of excitons which will be created per second thanks to the pumping laser. We can write

$$\Gamma_p = \frac{\sigma \times I_0}{hc/\lambda_{exc}},$$

where σ is the absorption cross section of the nanocrystal. The mean number of excitons which will be excited per pulse is $\bar{n} = \frac{\Gamma_p}{\Gamma_{rep}}$ (we have Γ_{rep} pulses per second)

$$\bar{n} = \frac{\sigma I_0 \lambda_{exc}}{hc} \times \frac{1}{\Gamma_{rep}}$$

b) Poissonian distribution

The absorption cross section of the nanocrystal is very low (typically $\sigma \approx 10^{-18}\ m^2$). As the consequence we can evaluate the rate of exciting photons which will be absorbed by the nanocrystal. For a laser of power P_p, the number N of laser photons is $N = \frac{\mathrm{P}_p \lambda_{exc}}{hc} = \frac{I_0 \times \lambda_{exc}^2 0.6}{\mathrm{NA}^2} \times \frac{\lambda_{exc}}{hc}$. The number of excitons is $\Gamma_p = \frac{\sigma \times I_0}{hc/\lambda_{exc}}$. We express the ratio R of absorbed photons per pump photons as

$$R = \frac{\Gamma_p}{N} = \frac{\sigma \times \mathrm{NA}^2}{0.6 \times \lambda_{exc}^2},$$

for $\lambda_{exc} = 400$ nm and NA ≈ 0.5,

$$R = \frac{10^{-17}}{2.4 \times 1.610^{-13}} = 2.6 \times 10^{-5}.$$

We need $1/R$ pump photons in order to get one exciton. The distribution of photons inside the pumping laser is generated by a Poisson law. Moreover, as the value of R is very low, the absorption by the nanocrystal is very low and random (uncorrelated events) governed also by a poissonian law. Therefore, we can consider that the mean number of excitons $\bar{n}$ follows a poissonian law.

If $\bar{n}$ is the mean number of excitons created by a pulse laser, the poissonian law indicates the probability of getting k exciton which scales as

$$P(\bar{n}, k) = \frac{\bar{n}^k}{k!} e^{-\bar{n}}$$

We will use now this law to evaluate the number of photons that will be emitted after each laser pulse.

c) Number of emitted photons N_ϕ

We consider here that the quantum efficiency for a single exciton is one. In other words, we consider that the number of photons we get for each recombining exciton is 1.

We calculate η the quantum efficiency corresponding to the first cascading recombination of a bi-exciton (**XX**→**X**). In other words, for each bi-exciton, we will get $1+\eta$ photons, where η is the photons coming from **XX**→**X** process and 1 photon coming from **X**→ 0 recombination. We consider here that the recombination of the tri-exciton (**XXX**→**XX**) is very inefficient. We will not consider any radiative recombination except **XX**→**X** and **X**→**0**.

We consider that the mean number of excitons that we can be obtained is $\bar{n}$. Then, due to the poissonian law, the probability of getting:

- Exactly 0 exciton $P(\bar{n},0) = e^{-\bar{n}}$
- Exactly 1 exciton $P(\bar{n},1) = \bar{n}e^{-\bar{n}}$
- 1 exciton or more
$$P_1 = 1 - P(\bar{n},0),$$
$$P_1 = 1 - e^{-\bar{n}}.$$
- 2 exciton or more
$$P_2 = 1 - P(\bar{n},0) - P(\bar{n},1),$$
$$P_2 = 1 - e^{-\bar{n}}(1+\bar{n}).$$

As only the **XX**→**X** and **X**→**0** transitions may be radiative, for each bi-exciton we get η photon for **XX**→**X** process, and 1 photon for the **X**→**0** process. Therefore, the total number of photons which will be emitted is

$$N_\phi = P(\bar{n},1) + P_2 \times (1+\eta),$$

by using the poissonian law, we can express N_ϕ as

$$N_\phi = \bar{n}e^{-\bar{n}} + (1+\eta)\left[1 - e^{-\bar{n}}(1+\bar{n})\right],$$

$$N_\phi = 1 + \eta + e^{-\bar{n}}\left[-(1+\eta)(1+\bar{n}) + \bar{n})\right],$$

$$N_\phi = 1 + \eta + e^{-\bar{n}}\left[-\eta\bar{n} - 1 - \eta\right]. \tag{II.2}$$

In Figure II.11 we plot as a function of $\bar{n}$ the total number of emitted photons N_ϕ with

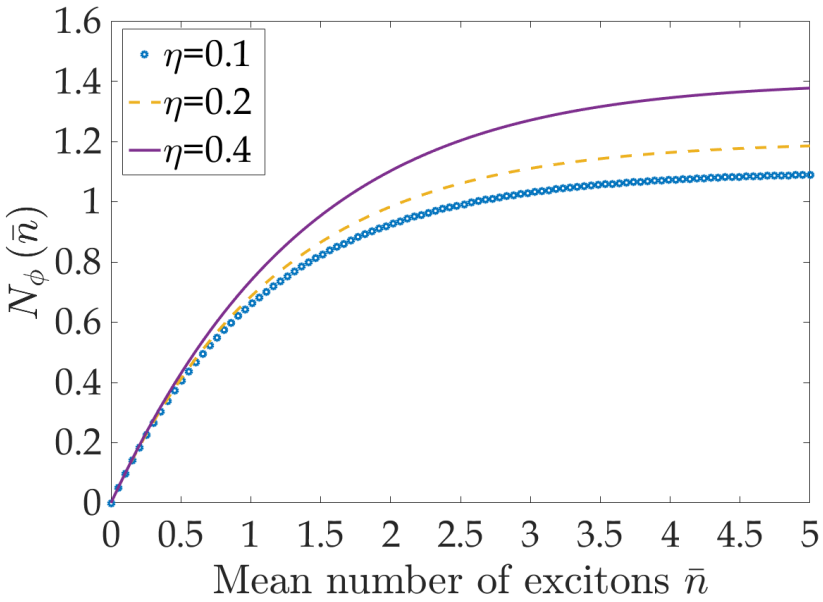

Fig. II.11 *Total number of photons emitted $N_\phi(\bar{n})$ considering three quantum efficiencies in the first cascading of bi-exciton recombination: $\eta = 0.1$, $\eta = 0.2$ and $\eta = 0.4$.*

η=0.1, 0.2 and 0.4. We can clearly see a saturation when increasing $\bar{n}$ (and P_p). This saturation is due to the fact that the recombination of tri-exciton (and more excitons) is supposed to be non-radiative. Therefore, for high pumping, there are more multiexcitons but we do not get more photons.

d) Quantum efficiency of bi-exciton

When we compute the second-order autocorrelation function $g^{(2)}(\tau)$, we consider only the events for which APD1 receives one photon before APD2 does. The only exception is the zero-delay peak, for which we consider the whole peak which is around $\tau = 0$. The zero-delay peak corresponds to the events for which both APD's receive one photon originated from the same pulse. In that case, one APD receives the photon corresponding to **XX**→**X** recombination, and the other one receives the photon corresponding to the following cascading recombination **X**→**0**. Therefore, for this specific zero-delay peak, τ can be either positive or negative.

The probability of record such events is

$$\uparrow_0 = \frac{P_2 \times \eta}{2},$$

we have to divide by 2 because we have the cases: the two photons on the same photodiode (2 cases), the **XX**→**X** on APD1 (APD2) and **X**→**0** on APD2 (resp APD1). We

pulse q	pulse $q+1$	
X	**X**	$\longrightarrow \frac{P_1^2}{4}$
XX	**X**	$\longrightarrow \frac{P_1 P_2 \eta}{4}$
X	**XX**	$\longrightarrow \frac{P_1 P_2 \eta}{4}$
XX	**XX**	$\longrightarrow \frac{P_2^2 \eta^2}{4}$

Fig. II.12 *Cases corresponding to the peak following the zero-delay peak, $q \epsilon \mathbb{N}$.*

remove the first 2 cases and keep the last 2 cases.

For the peak following the zero-delay peak (at $\tau = \tau_{rep}$), the peak is composed with the events occurring for the q^{th} pulses and $(q+1)^{th}$ pulses. The photons of the q^{th} pulse have to be detected by APD1 and the one corresponding to the $(q+1)^{th}$ by APD2. In the next lines we name **X** the events corresponding to the radiative recombination of one exciton (**X**→**0**). These events are detected by APD1 (or APD2) with a probability $\frac{P_1}{2}$.

The p^{th} peak following the zero-delay peak is constructed in a similar way by considering the q^{th} pulses and the $(q+p)^{th}$ pulses.

We focus now to the statistic of the first peak following the zero-delay. The conclusions can be easily extended to the p^{th} peak. We name **XX** the events corresponding to the radiative recombination of one bi-exciton (**XX**→**X**). These events are detected by APD1 (or APD2) with a probability $\frac{P_2 \eta}{2}$.

We can resume all the cases in Figure II.12.
To conclude, the peak following the zero-delay peak is built by 3 kind of events:

1. Photons coming both from single exciton **X**→**0** recombination. The probability is
$$\frac{P_1^2}{4}.$$
2. Photons coming one from the **XX** → **X** recombination and the other one from an excitonic recombination. The probability is
$$\frac{2P_2\eta \times P_1}{4}.$$
3. Photons coming both from **XX**→**X** recombination. The probability is
$$\frac{(P_2\eta)^2}{4}.$$

Therefore, the peak following the zero-delay peak is made with events having a probability
$$\uparrow_1 = \frac{P_1^2}{4} + \frac{2P_1P_2\eta}{4} + \frac{(P_2\eta)^2}{4}.$$

The ratio between the zero-delay peak and the peak following the zero-delay peak is

$$\frac{\uparrow_0}{\uparrow_1} = \frac{2P_2\eta}{P_1^2 + 2P_1P_2\eta + P_2^2\eta^2}, \tag{II.3}$$

with $P_2 = 1 - e^{-\bar{n}}(1+\bar{n})$ and $P_1 = 1 - e^{-\bar{n}}$.

In the limit when $\bar{n} \approx 0$, we can approximate the exponential function to $e^{-\bar{n}} = 1 - \bar{n} + \frac{\bar{n}^2}{2}$. So, the probabilities $P_1 \to \bar{n} - \frac{\bar{n}^2}{2}$ and $P_2 \to \frac{\bar{n}^2}{2}$, by neglecting the $\bar{n}^3$ term in the development. The ratio $\frac{\uparrow_0}{\uparrow_1}$ between the zero-delay peak and one of the next peak is equal to η. We can extend this result to $\boxed{\frac{\uparrow_0}{\uparrow_1} = \frac{Q_2}{Q_1}}$ where Q_2 is the quantum efficiency of bi-exciton ($\mathbf{XX} \to \mathbf{X}$) and Q_1 the quantum efficiency of exciton $\mathbf{X} \to \mathbf{0}$. Here $Q_1 = 1$ and $Q_2 = \eta$.

The area under the zero-delay peak with respect to the next ones is equal to $\frac{Q_2}{Q_1}$ in a weak excitation regime.

The Equation (II.3) can be expressed as

$$aP_1^2 + 2P_2(aP_1 - 1)\eta + aP_2^2\eta^2 = 0, \tag{II.4}$$

with $a = \frac{\uparrow_0}{\uparrow_1}$. The discriminant of the second-order equation (II.4) is $\Delta = 4P_2^2(1 - 2aP_1)$ and the two possible solutions for η are

$$\eta_{1,2} = \frac{(1 - aP_1) \pm \sqrt{1 - 2aP_1}}{aP_2}.$$

If we know experimentally the values of a and $\bar{n}$, we can extract η. We will now use this model for interpreting the experimental results.

II.2.4 Experimental spectra and intensities

In Figure II.13a, we show the photoluminescence spectra corresponding to the measurements of Figure II.9a presented before. All spectra were registered with the same integration time (20 s). In the maximum emission of the first spectrum (around 640 nm), we have drawn a continuous vertical line for reference. From Figure II.13 we can observe that the intensity and position of the maximum emission peak are modified for the different experimental conditions. In the first three excitations 7 W/cm^2, 12 W/cm^2 and 56 W/cm^2, the spectra display the emission of the fundamental peak around 640 nm. In the following two excitations 360 W/cm^2 and 1200 W/cm^2, the spectra shows a second emission peak at lower wavelengths around 560 nm.

In order to study the characteristics for each emission peak separately, we have calculated the area enclosed in the fundamental peak for each spectra. We have limited the integration range from 588 to 700 nm. The second column of Table II.1 shows the corresponding values for each experimental condition. The CCD camera of the spectrophotometer is able to register more than one photon per excitation pulse. It means that, when the nanocrystal emits more than one photon, the CCD camera is capable of registering the additional two, three or more photons at the same time. The number of photons then will be proportional to the number of counts. So, the integrated area is directly proportional to the total optical power emitted by the single nanocrystal.

If we now define $\mathbf{A}_7$ as the power collected by the single photon source for an excitation power of 7 W/cm^2. We can estimate the proportional power collected for each photoluminescence spectra $\mathbf{A}/\mathbf{A}_7$. The third column of Table II.1 shows this value for all the fluorescence spectra. For all the spectra included those with highest excitation power (360 and 1200 W/cm^2), $\mathbf{A}$ is restricted to the main peak (between 588 and 700 nm).

In the Table II.1 we can observe that, for $\mathbf{A}_{12}$, the area slightly increase to 1.33 times the area of $\mathbf{A}_7$. In the next excitation for $\mathbf{A}_{56}$, the area has increased again but we can note that the increase of emission is not proportional to the increase of excitation power. It is even saturating when the excitation power increases. In the next excitation corresponding to $\mathbf{A}_{360}$ (purple spectra in Figure II.13), we found that the nanocrystal has reached the maximum fluorescence intensity displayed in this experiment, resulting in four times the power emitted with respect to $\mathbf{A}_7$.

We present as well the emitted intensity $I(t)$ recorded by both APD's. In Figure II.14 we show the fluorescence intensity at different excitation power. The intensity was recorded during some hundreds of seconds (100 s, approximately), but the photoluminescence spectra correspond just to the first 20 s. For the first 20 s, the emission intensity has a mean value of 2.1 $Counts/ms$ for an excitation 7 W/cm^2, 2.9 $Counts/ms$ for 12 W/cm^2 and 6.8 $Counts/ms$ for 56 W/cm^2, with ratios $\frac{\mathbf{I}_{12}}{\mathbf{I}_7} = 1.38$ and $\frac{\mathbf{I}_{56}}{\mathbf{I}_7} = 3.24$ in accordance with the spectra recorded. We can notice that for an excitation power of 360 W/cm^2 and 1200 W/cm^2, in both spectra and fluorescence intensities $I(t)$ have exhibited heavy changes during the recording, as the spectras exhibit for both excitations, 2 emission peaks, one at 640 nm and other around 560 nm. For those excitation conditions, the intensity corresponding to the whole emission can not be directly linked with $\mathbf{A}$ which is associated exclusively with one peak.

Finally, for the last spectra $\mathbf{A}_{1200}$ (green spectrum in Figure II.13), we note that the fluorescence intensity of the fundamental peak has dropped and the area corresponds to 2.72 times $\mathbf{A}_7$. The reduction of the integrated area could be possible linked to photodegradation of the nanocrystal at very high excitation intensity.

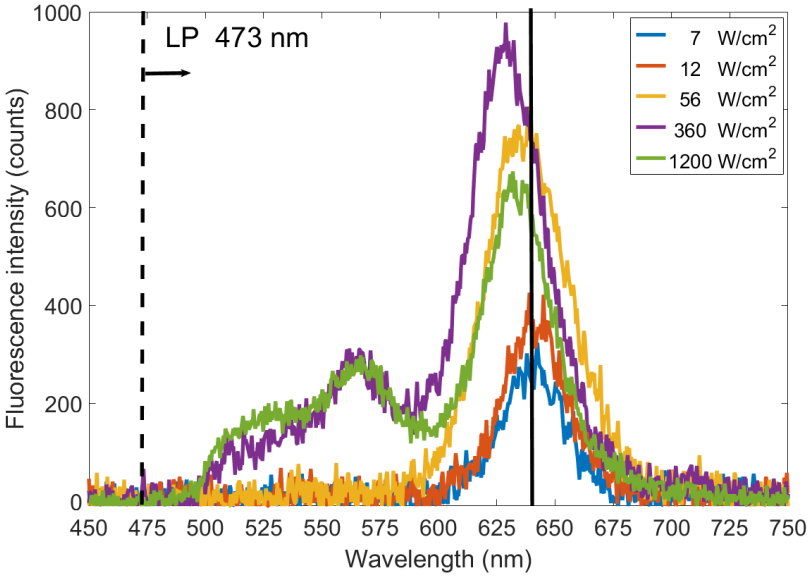

Fig. II.13 *Photoluminescence spectra of a single nanocrystal at different excitation power.*

Photoluminescence spectra	Integrated area $\times 10^4$	$\mathbf{A}/\mathbf{A}_7$
$\mathbf{A}_7$	1.05	1.00
$\mathbf{A}_{12}$	1.40	1.33
$\mathbf{A}_{56}$	3.53	3.36
$\mathbf{A}_{360}$	4.22	4.02
$\mathbf{A}_{1200}$	2.86	2.72

Table II.1: Integrated area of photoluminescence spectra (between 588 and 700 nm) as function of the excitation power.

II.2.5 Analysis of experimental results

We will restrict our analysis to the first three conditions of excitation (7 W/cm^2, 12 W/cm^2 and 56 W/cm^2). We will suppose that, in these three cases, only bi-exciton and exciton recombination occurs. If we know the excitation power, we can calculate $\bar{n}$ for each experiment, and therefore the probability of exciting exciton and bi-exciton. In Table II.2 we show the mean number of electron-hole pairs $\bar{n}$ with the probability of getting zero and one excitons exactly $P(\bar{n}, 0)$ and $P(\bar{n}, 1)$. We also include the probability of having $\mathrm{P}_1(\bar{n})$ (at least 1 exciton) and $\mathrm{P}_2(\bar{n})$ (at least one bi-exciton) for the different excitations.

From the second-order autocorrelation function of Figure II.9b, we can extract the experimental value of $\uparrow_0$ / $\uparrow_1$. Theses values are shown in the second column of Table II.3. Now, given the value of $\bar{n}$ and $\uparrow_0$ / $\uparrow_1$ for all our experimental measurements, we can use our model to extract the value of η, the quantum efficiency of the bi-excitonic

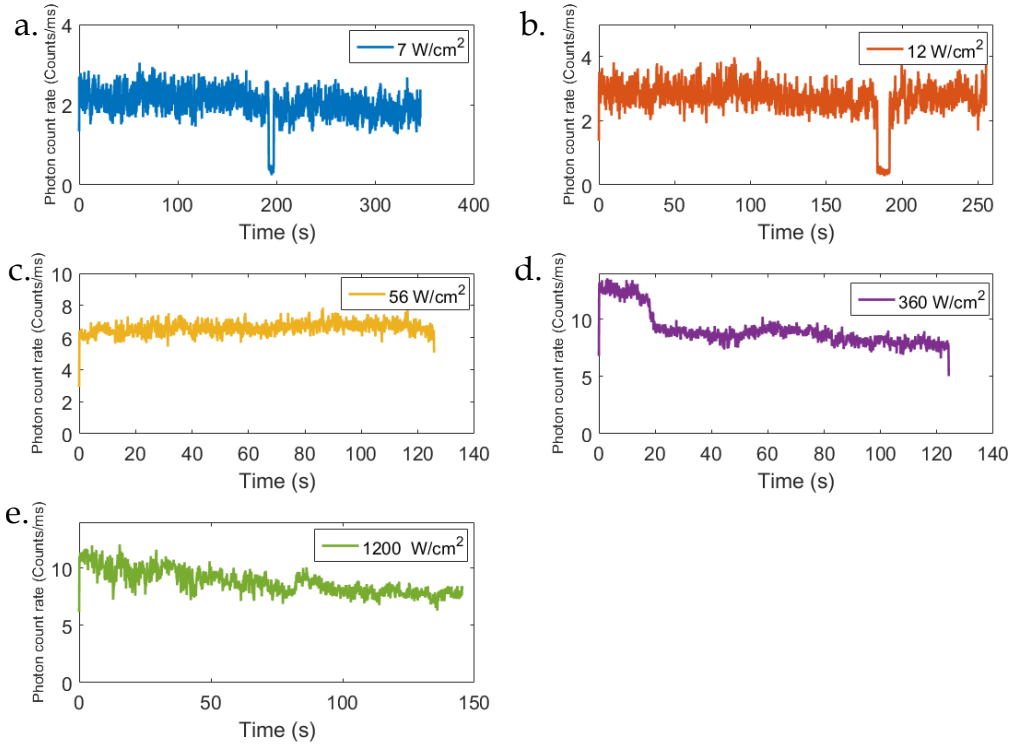

Fig. II.14 *Fluorescence intensity emitted by the single nanocrystal at different excitation power.*

Table II.2: Mean number of electron-hole pairs $\bar{n}$ for the different conditions of excitation. We have used the absorption-cross section $\sigma = 8 \times 10^{-18}\ m^2$ reported on [54].

Excitation fluence W/cm^2	Mean number of electron-hole pairs* $\bar{n}$	P($\bar{n}$,0)	P($\bar{n}$,1)	$P_1(\bar{n})$	$P_2(\bar{n})$
7	0.4	0.65	0.28	0.35	0.07
12	0.8	0.45	0.36	0.55	0.19
56	3.6	0.03	0.09	0.97	0.88
360	23.4	6.9×10^{-11}	1.6×10^{-9}	1.00	1.00
1200	78.4	8.5×10^{-35}	6.6×10^{-33}	1.00	1.00

Table II.3: Relative quantum efficiency estimated from the second order autocorrelation function $g^{(2)}(\tau)$ and the one calculated from the theoretical model.

Excitation fluence W/cm^2	$g^{(2)}(0)/g^{(2)}(\tau_{rep})$ Experiment	η Calculated from Eq. (II.3)
7	0.22	0.21
12	0.28	0.26
56	0.71	$\mathbb{C}$
360	0.92	$\mathbb{C}$
1200	0.97	$\mathbb{C}$

recombination ($\mathbf{XX} \rightarrow \mathbf{X}$). The third columns shows the calculated values of η.

We get η =21 % and η =26 % for 7 W/cm^2 and 12 W/cm^2, respectively. For 56 W/cm^2, we don't get a physical value, the solutions of Eq. (II.3) is a complex number ($\mathbb{C}$). This result is expected because of the limitations of the model which do not consider more than bi-exciton. For 56 W/cm^2 the probability of exciting 3 excitons or more is very large, $P_3(\bar{n})$=0.71, so that we can expect some limitation of our model which considers only bi-excitonic and excitonic emission.

We choose in the following $\eta = 0.21$, because we know that our model is more accurate at low power. In fact, since η is calculated from the expression (II.2) (assuming $\bar{n} \approx 0$), we can expect some disagreement even for the lowest excitation power (7 W/cm^2 or $\bar{n}$=0.4). The experimental value of $\eta = 0.21$ is probably overestimated from the real η.

We want now to validate our theoretical model with experimental values. Experimentally we do not know the absolute number of emitted photons, but we have calculated $\mathbf{A}$ which is proportional to the number of photons (or total emission power). We can calculate for each excitation $\mathbf{A}/\mathbf{A}_7$ which is equal to the number of photons emitted for this excitation divided by the number of photons emitted with the 7 W/cm^2 excitation. In Figure II.15 we plot the normalized number of emitted photons $\mathbf{A}/\mathbf{A}_7$ as a function of the normalized number of excitons $\bar{n}/\bar{n}_7$ (see Table II.1).

In the same Figure II.15, we plot the theoretical number of emission photons $N_\phi(\bar{n})$ (expression (II.2)) normalized by the value when $\bar{n}_7 = 0.4$ ($N_{\phi 7}$). From the curve we can clearly note the saturation of $N_\phi(\bar{n})/N_{\phi 7}$ when $\bar{n}/\bar{n}_7$ increases. Such behaviour is a result of the low radiative efficiency of bi-exciton combined with the nil radiative efficiency of the multi-exciton emission for a number of exciton > 2. The theoretical curve is in fairly good agreement with the experimental values obtained in Table II.1 ($\mathbf{A}_7 = 1$, $\mathbf{A}_{12}/\mathbf{A}_7 = 1.33$ and $\mathbf{A}_{56}/\mathbf{A}_7 = 3.36$). These results validate our bi-excitonic model for low excitation power.

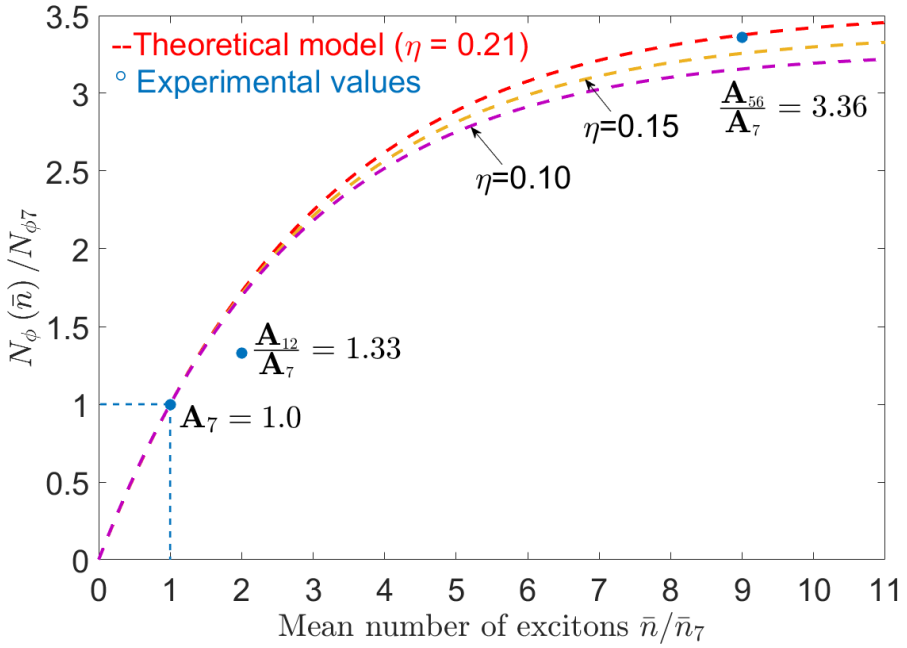

Fig. II.15 *Normalized number of photons emitted $N_\phi(\bar{n})/N_{\phi 7}$ as a function of the normalized number of exciton $\bar{n}/\bar{n}_7$ considering a quantum efficiency of bi-exciton emission equal to $\eta = 0.21$ (red dash line). We have normalized the curve using the theoretical value of N_ϕ for the excitation power of $\bar{n}_7 = 0.4$. We superpose the three experimental values corresponding to $\boldsymbol{A}_7 = 1$, $\boldsymbol{A}_{12}/\boldsymbol{A}_7 = 1.33$ and $\boldsymbol{A}_{56}/\boldsymbol{A}_7 = 3.36$ (blue points).*

II.2.6 Superposition of normalized emission spectra

In order to distinguish between lateral shifts or broadening of the emission peaks, we have normalized the fluorescence spectras and superposed them for different conditions of excitation. The normalization of the spectra to its maximum value is advantageous to visualize slight shifts in the maximum emission peak and broadening in the linewidth emission. In Figure II.16a we present the superposition spectra at 7 W/cm^2 superposed with the spectra at 56 W/cm^2. The spectra at 7 W/cm^2 presents a linewidth of 28 nm, meanwhile the spectra at 56 W/cm^2 has a linewidth of 40 nm, approximately. The difference is roughly 11 nm (or 33 meV approximately) which is attributed to the simultaneous detection of mono-exciton and bi-exciton. The probability of getting two exciton or more is close to 1 for 56 W/cm^2 and much lower for 7 W/cm^2.

In Figure II.16b we show the superposition of the spectra at 56 W/cm^2 (yellow spectra Figure II.16b) with the spectra at 360 W/cm^2 (purple spectra Figure II.16b). For high excitation power we can observe a blue-shift of around 6 nm (or 20 meV) between the fundamental emission peak. This blue-shift is accompanied by the appearance of a lateral emission peak at lower wavelengths around 560 nm, as it is indicated on Figure II.16b. This emission may be the indication either of higher order multi-exciton radiative

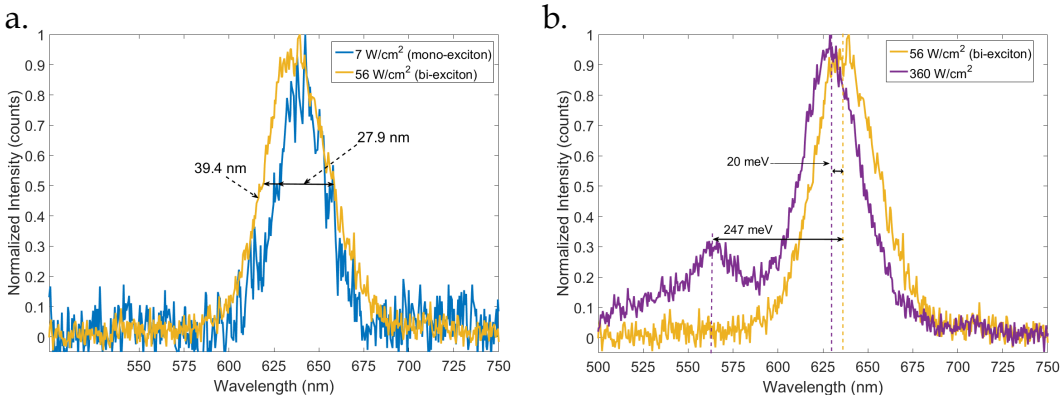

Fig. II.16 *a) Superposition of normalized spectra at 7 W/cm^2 and 56 W/cm^2 in excitation power. b) Superposition of normalized spectra at 56 W/cm^2 and 360 W/cm^2 in excitation power.*

recombination or emission from a trapping state induced by high excitation.

II.2.7 Emission in shorter wavelengths

In our studies, we have used core-shell CdSe/CdS nanocrystals with 3.3 nm-core, 6 nm-shell thickness. The photoluminescence spectra measured for a single emitter have been recorded with different excitation power. We have observed the enlargement of the fundamental band-edge transition when the radiative bi-exciton (XX) recombined. For large excitation power, we have observed a shift in the fundamental emission peak and a lateral emission peak radiative around 560 nm. This could be explained either because a multi-exciton recombination or because of a trapped recombination state (like Type-A blinking) which should achieve a quicker dynamics.

In order to characterize this lateral emission, we have carried out a similar experimental test with a different nanocrystal. We have observed similar evolution when it is excited by increasing power. Figure II.17a shows the evolution in photoluminescence emission spectra of a different nanocrystal in the sample. To characterize the emission at shorter wavelengths, we have introduced a fluorescence band-pass filter 562/40 nm when the nanocrystal it is excited at maximum optical power (260 W/cm^2), as it is shown on Figure II.17a. Figure II.17b displays the superposition of two decay curves for the same excitation condition 260 W/cm^2. The red decay curve corresponds to the complete photoluminescence spectra (without 562/40 filter) and the blue decay curve when the band-pass filter 562/40 nm is placed in the collection path of the microscope. From Figure II.17b we observe that both decay curves present a fast component of some hundreds of picoseconds, 500 ps and 300 ps for the complete spectra and partial spectra, respectively. These values found by the fitting bi-exponential model are close to the binning resolution of the decay curve, which for the measurements performed for this nanocrystal was set to 256 ps.

Nevertheless, for the low wavelength filtered emission, the proportion of the quick

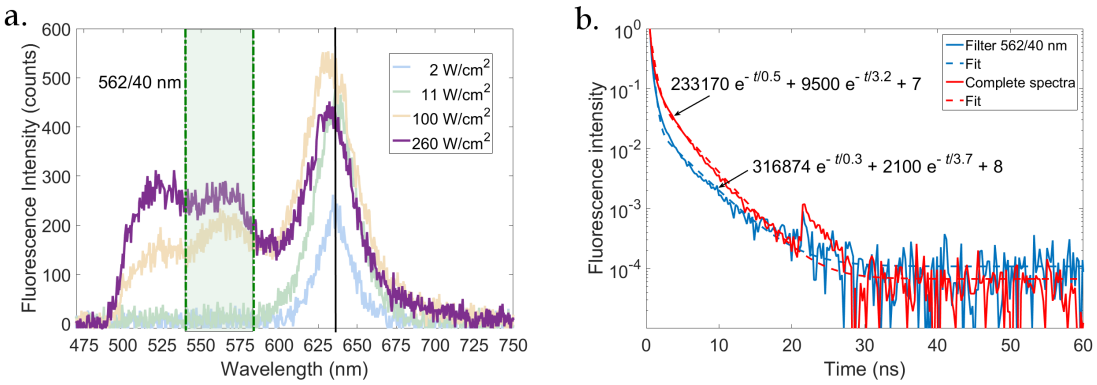

Fig. II.17 *a) Photoluminescence emission spectrum of a single nanocrystal excited at different optical power. In the maximum excitation we have introduced a band pass filter to select mostly the emission at shorter wavelengths. b) Photoluminescence decay rate when the nanocrystal is excited at 260 W/cm^2 with and without the band-pass filter 562/40 nm.*

component is a little bit longer than for the non filtered emission. Indeed, for a bi-exponential model $I = Ae^{-t/\tau_{fast}} + Be^{-t/\tau_{slow}}$, the proportion of the quick component scales as

$$\frac{A\tau_{fast}}{A\tau_{fast} + B\tau_{slow}} = C.$$

For the low wavelength filtered emission we found $C_{filtered} = 0.92$, whereas for the full emission $C_{full} = 0.79$. Therefore, as the fact that the fast component is more important for the low wavelength filtered emission, we can state the presence of higher non-radiative recombination states in the dynamics of the low wavelength part.

II.3 Conclusion

In this section we have discussed the photoluminescence properties of a single colloidal CdSe/CdS nanocrystals when it is excited at different optical power. By the combination of spectroscopic analysis and photodynamic emission, we were able to identify mono-exciton, bi-exciton and multi-exciton emission in a single nanocrystal at room temperature.

Our results showed that it is possible to identify the bi-exciton emission by observing simultaneously the fast component in the photoluminescence decay curve and the enlargement of 33 meV in the linewidth of the fundamental peak. We have demonstrated that bi-exciton emission can be separated temporally by applying a temporal post-processing filter in the photoluminescence decay curve. After the temporal filter and processing of the second-order autocorrelation function ($g^{(2)}(t_0, t)$), the characteristic of single-photon emission is recovered.

We have developed a model taking into account the mean number of excitons created by a laser pulse for describing the intensity emitted by the nanocrystal. Our model, restricted to bi-exciton radiative recombination, is in fairly good agreement with experimental results for moderate excitation power.

We have normalized the photoluminescence emission spectras to identify shift and broadening in the fundamental emission peak. We have found a broadening of the fundamental emission peak of 11 nm (33 meV) when we compared spectras at 7 W/cm^2 and 56 W/cm^2. Then, when we compared normalized spectra at 56 W/cm^2 and 360 W/cm^2, we have identified a blue-shift of the maximum emission peak of 6 nm (20 meV).

We have characterized the short wavelength emission of a single CdSe/CdS nanocrystal using a band-pass filter 562/40 nm. We have found that the lateral emission is composed of a fast and slow decay component of $\tau_f = 300$ ps and $\tau_s = 3.7$ ns, respectively. We have then compared these values with the ones obtained without any filter (complete photoluminescence spectra). We have found that the contribution of the quick component is more important for the low wavelength filtered emission. These results suggest that non-radiative recombination states are more predominant in the low wavelength emission than in the complete spectra.

Chapter III

Experimental methods

III.1 Introduction

This chapter presents different experimental methods for studying single colloidal nanocrystals in terms of fluorescence, photodynamics, spectroscopy and single-photon emission properties.

In the first part, we will describe the original experimental set-up used for photoluminescence studies in single nanocrystals. The second part is dedicated to the analysis of the acquisition data and processing of information once the Time-Correlated Single Photon Counting (TCSPC) system has registered all photo-events in order to get photoluminescence decay rate curves and second-order autocorrelation functions. We will then present the instrument response function of the experimental set-up and all different components that affect the total time resolution. We will establish the resolution of the experimental set-up for fluorescence time-resolved experiments. In the last part of this chapter, we will describe the experimental set-up to perform reflectivity measurements of individual passive nanoantennas.

III.2 Experimental set-up description

We have used a reflection optical microscope in inverted mode with an optical objective (0.80 NA) to observe nanocrystals at individual scale. To excite the fluorescent nanocrystal, we have used a picosecond pulsed diode laser emitting at λ=405 nm (3.06 eV) with a repetition rate of 2.5 MHz (400 ns separation between pulses). In time-resolved fluorescence measurements, the diode laser synchronizes the Time-Correlated Single Photon Counting System (TCSPC card) by sending an electrical signal (Sync pulse). The optical pulses are send into the microscope where a dichroic mirror (Semrock FF 605 nm) reflects the blue light from the diode laser and transmits the fluorescence light above the edge-wavelength. On the surface of the sample, a gaussian laser spot with a diameter equal to 600 nm (beam waist $\omega_0 \simeq 300$ nm) excites the individual nanocrystal.

When the intense pulse laser excites the individual nanocrystal, part of the blue light

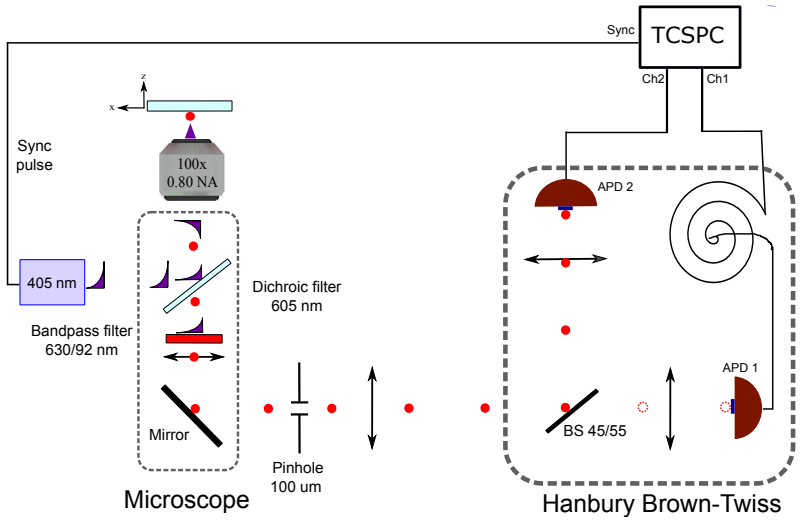

Fig. III.1 *Experimental set-up used for conventional time-resolved fluorescence measurements of single CdSe/CdS nanocrystals.*

is absorbed. Typically absorption cross-section of our CdSe/CdS nanocrystals (3.3 nm-core, 6 nm-shell thickness) is on the order of 800 Å^2 measured by saturation curve [54], [34], [55]. The nanocrystal absorbs the blue radiation, switching from a base-state to an excited-state where the electron is close to the bottom of the conduction band. After non-radiative relaxation mechanisms, bringing the electron to the lower level of the conduction band at picoseconds time scale, a single photon will be emitted by the quantum source at the nanoseconds scale. For every pulse excitation, in the case of a single exciton, the nanocrystal will emit one and only one photon which is collected by the same objective and transmitted through the FF 605 nm dichroic filter. An additional fluorescence filter 630/92 nm is introduced to remove some remaining blue excitation light reflected by the sample. It removes as well most of the background fluorescence which comes from the signal of shallow emitters. The photon is then reflected by a mirror and drives through a 100 μm pinhole (spatial filter) placed at some distance apart from the microscope in the image plane of the sample. The photon is guided to a Hanbury Brown-Twiss set-up including a beam splitter 55:45 (T:R) and 2 avalanche photodiodes (APD). After many excitation cycles, the histogram of detection times and a correlation histogram can be obtained. Figure III.1 shows the complete experimental set-up.

In photoluminescence experiments, the intervals of times should satisfy the condition $\tau_{pulse} << \tau_{lifetime} << \tau_{rep}$. That means, the duration of the pulse laser (τ_{pulse}) must be much shorter than the characteristic relaxation time of the system ($\tau_{lifetime}$) to mimic an ideal delta function generating only one absorption cycle during the excitation time. Additionally, the narrow excitation pulse has to provide sufficient power to efficiently bring the system into an excited-state. The second requirement concerns the repetition rate of the diode laser τ_{rep}. The period between 2 pulses has to be much longer than $\tau_{lifetime}$ in order to let the system returning back in ground-state before the next pulse.

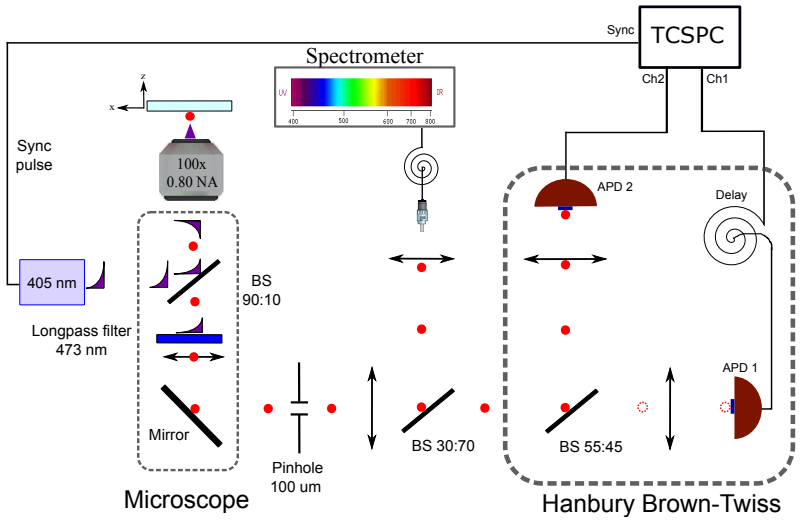

Fig. III.2 *Experimental optical set-up including the modifications implemented for measurements of saturation and transient photoluminescence spectra in a single nanocrystal.*

III.3 Spectroscopy of single emitter

Photoluminescence decay rate is one of the main quantitative property when studying fluorescence emission in single nanocrystals or any other fluorescent specimen. It provides the characteristic time in which the system evolves, depending mainly of three parameters: 1) the surrounding electromagnetic environment where the nanoemitter is located, 2) the intrinsic quantum yield taking into account radiative and non-radiative channels and 3) the excitation intensity. Additionally, spectral photoluminescence information complement the photo-emission properties of individual nanoemitters. The incorporation of the CCD spectrophotometer into the original optical set-up has allowed us to characterize photoluminescence emission of single nanocrystals, patch nanoantennas and to perform reflectivity measurements of passive plasmonic elements.

In the original set-up, we installed a 30:70 (T:R) beamsplitter before the HBT interferometer, as it is shown in Figure III.2. An optical lens couples the light through an optical fiber (Avantes FC-UV100 0.22 NA, 100 μm in diameter) who transports the light to the entrance slit of the spectrometer (Jobin Yvon HR460) equipped with a CCD camera Syncerity (http://www.horiba.com/fr/scientific/products/optical-spectroscopy/detectors/scientific-cameras-for-spectroscopy-cdd-ingaas-emccd/ccds/syncerity-details/syncerity-ccd-deep-cooled-cameras-17301). The length of the optical fiber is 15 m. The split ration 30:70 has been chosen in such a way to achieve a good compromise to detect fluorescence emission of a single nanocrystal on the spectrometer (CCD camera) and both APD's simultaneously.

For using the spectrophotometer, the Semrock FF 605 nm dichroic mirror is replaced. When exciting single emitters (or another fluorescence material), the cutting

edge-wavelength of the dichroic mirror reflects all the emission below 605 nm. It means that, along the collection path to the detectors, emission from the nanocrystal or any other specimen below 605 nm will be completely suppressed by the dichroic and not longer accessible on the CCD camera and APD's. To overcome this difficulty for spectrometric measurements, we have replaced the dichroic mirror by a second beamssplitter 90:10 (T:R) inside the optical microscope. This configuration transmits only 90 % of the fluorescence emission light but preserves the complete spectral information of the fluorescence specimen. A supplementary filter Semrock LP 473 nm has been installed which reflects light for $\lambda < 473$ nm (mostly remaining excitation laser 405 nm), and transmit almost all the spectra above.

In this configuration, we are able to perform lifetime measurements combined with spectroscopy of single CdSe/CdS nanocrystals at room temperature. Afterward, the installation of a variable optical density in the excitation path before the confocal reflection microscope will allow a higher pumping convenient for the diode laser for operation above the threshold where the laser is more stable. In addition, it provides easier control of the optical excitation power to perform photoluminescence measurements with single nanocrystals.

The complete characterization in terms of photoluminescence decay rate curve, second-order autocorrelation function $g^{(2)}(\tau)$ and emission spectra of an individual semiconductor nanocrystal CdSe/CdS is showed in Figure III.3. We have pumped the nanocrystal using the diode laser (405 nm) at 850 W/cm^2, corresponding to 1.2 μW of laser power in pulsed mode. We have measured an average photon count rate of 3 $counts/ms$ for the sum of both photodiodes. The photoluminescence spectra has been integrated during 190 seconds.

III.3.1 Spectral resolution and calibration

In this part, I will discuss the spectral resolution of the spectrophotometer used in this thesis. The spectral resolution depends of different components. We can assort most of them in three different categories:

1. **Optical grating**. This category includes the linear dispersion of the optical grating ($\frac{d\lambda}{dx}$).

2. **Slits + detector**. It corresponds to the spatial resolution limited by the width in both slits (entrance and exit). In our experimental set-up, we are able to control entrance slit, since the output slit is replaced by the array of pixels of the CCD camera. Therefore, the width of one pixel defines the exit slit size. Generally, the performance in terms of spectral resolution of the CCD camera will increase when decreasing the pixel size and slit entrance. The CCD camera contains an array of 1024×256 pixels with pixel size 26 μm$\times$ 26 μm.

3. **Optics**. It involves the optical elements which are inside the spectrometer system to compensate aberrations effects.

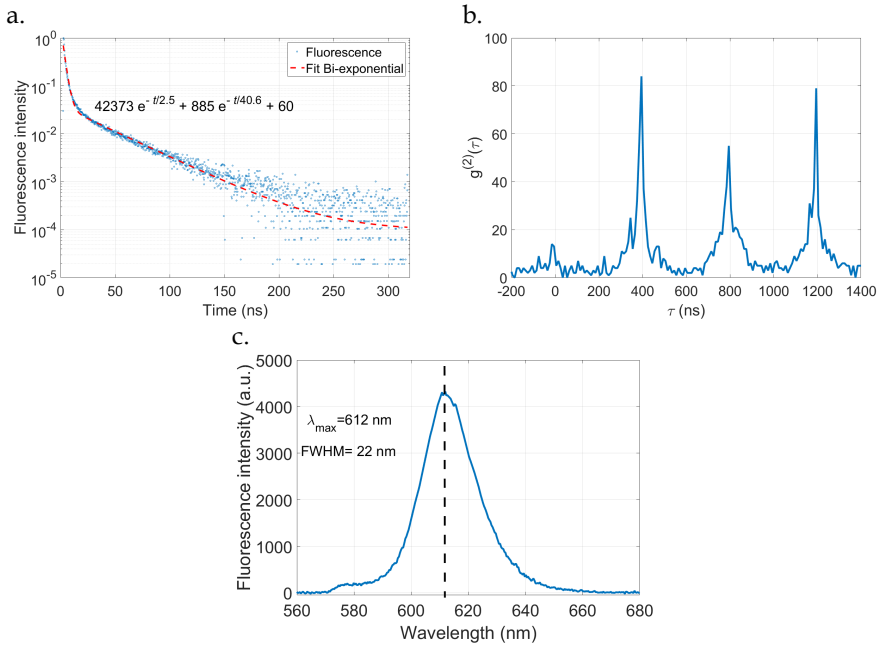

Fig. III.3 *a) Photoluminescence decay rate. b) Second-order autocorrelation function and c) Fluorescence emission spectra combined for a single CdSe/CdS nanocrystal. Integration time 190 s, excitation power 850 W/cm^2*

.

In our fluorescence spectroscopy measurements performed at room temperature, the contribution of manly two categories limit the spectral resolution: **Slits** and the **detector**. All measurements with single nanocrystals were performed with the maximum slit width in the HR 460 spectrometer to assure the maximum transmission of the fluorescence light. This slit aperture assures a resolution of 7 nm using 150 g/mm as optical grating.

We have used a spectrometer Jobin Yvon HR 460 equipped with two optical gratings: 1200 and 150 g/mm (grooves per millimeter). The higher the groove density, the higher the spectral resolution. However, the spectral range of the instrument will be limited by the number of pixels on the CCD array. In our studies, we have used 150 g/mm grating which disperse most of the 1st diffraction order of the visible spectrum on the CCD sensor area. The range of spectra is 385 nm, approximately. The spectrometer has an exit focal length of 451 mm, hence the extension of light dispersed in the focal field (linear dispersion) is $\frac{d\lambda}{dx} = 14.1$ [nm/mm]. Taking into account the physical size of the pixel we attain a resolution of 0.36 [nm/px].

The spectrometer Jobin Yvon HR 460 is composed of two entrance ports (lateral and front). The optical fiber that connects our experimental set-up makes use of the lateral entrance port. In every experimental session an internal mirror is displaced automatically depending of the pre-define entrance port (lateral for our optical fiber or front for different experimental set-up). This mechanical displacement cause a spectral misalignment between the light diffracted by the grating and the CCD detector. This constrain is

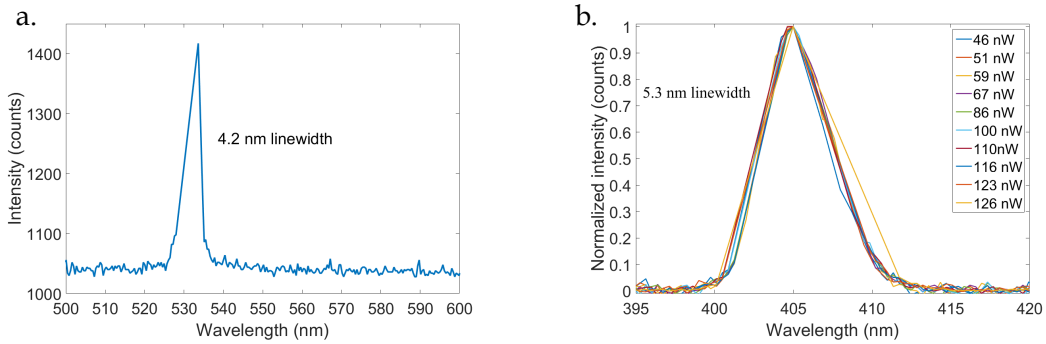

Fig. III.4 *a) Experimental spectrum of a doubled Nd:YAG green laser 532 nm used to calibrate the spectrometer. b) Emission linewidth of the diode laser 405 nm at different average optical power in pulse mode.*

overcome by performing spectral calibration in the beginning of each set of experiment. The use of narrow spectral lines, such as mercury lamp 546.1 nm or a doubled Nd:YAG green laser 532 nm can be employed equally. Figure III.4a shows the spectral line width of the green laser with a slit aperture corresponding to "7 nm resolution" in the specification of the apparatus. In that condition, the linewidth of the laser (double-frequency Nd:YAG laser) is 4.2 nm measured at Full Width Half Maximum (FWHM), which is much more than the real linewidth of this laser. Indeed, 4.2 nm linewidth corresponds to $\frac{4.2}{0.36[\mathrm{nm/px}]} = 12$ pixels, which extend to $12 \times 26\mu\mathrm{m} = 300$ μm. It means that, as the spectrometer is an 1:1 imaging system, the diameter of the beam after the fiber and its collimator at the font entrance of the spectrometer is 300 μm.

III.3.2 Spectral linewidth of diode laser

The spectroscopy studies of fluorescent nanocrystals have been performed using the diode laser as source of illumination. In the spectrometer we have used a aperture slit which provide an spectral resolution of "7 nm". In Figure III.4b we show the spectra emission of the diode laser at different excitation power in pulsed mode. From the figure we can note a constant linewidth of 5.3 nm independently of the pumping power. The value of 5.3 nm is slighly different from the one found in the technical specifications of the laser. According to PicoQuant, the spectral width of this diode laser lays around 1.47 nm [56]. We conclude then that the spectral linewidth observed in Figure III.4b is limited by the resolution of the spectrometer, mainly by the slit aperture.

III.4 Measurements and data processing

This section aims to describe the principle of operation of the Time-Correlated Single Photon Counting system (TCSPC) in order to built the decay curve and the second-order correlation function $g^{(2)}(\tau)$ from the row data collected by the Picoharp card.

Photon event	x.chan	x.time [s]	x.lifetime [ns]	Diff between x.time [us]	No. of pulses between photon-events
#1	2	0,000550784578031815	265,4720126	919,17	2298
#2	1	0,001469958841152450	85,50400406	1505,96	3765
#3	1	0,002975916674333120	87,04000413	143,60	359
#4	1	0,003119512653645700	85,76000407	487,99	1220
#5	2	0,003607498990028280	166,9120079	125,20	313
#6	2	0,003732695484526430	329,4720156	2044,74	5112
#7	2	0,005777438231729510	164,0960078	359,99	900
#8	2	0,006137428152011740	162,0480077	407,19	1018
#9	1	0,006544616750730980	271,6160129	45,60	114
#10	1	0,006590215473966730	86,01600409	322,79	807
#11	2	0,006913006435819800	163,0720077	247,99	620
#12	2	0,007160999492014220	164,6080078	762,38	1906
#13	2	0,007923378145411930	271,1040129	4,40	11
#14	2	0,007927778022215380	162,5600077	164,00	410
#15	1	0,008091773430343950	97,28000462	1723,15	4308
#16	2	0,009814925182094900	164,3520078	343,59	859
#17	1	0,010158515561564300	87,55200416	801,18	2003
#18	1	0,010959693128592400	84,99200404	563,58	1409
#19	1	0,011523277348234200	87,80800417	389,19	973
#20	2	0,011912466450939400	162,3040077		

Fig. III.5 *Row data table generated by the TCSPC system during the measurement of a single nanocrystal.*

III.4.1 Recording the photo-event

When a photon is detected by either transmission or reflection photodiode, an electrical pulse signal is sent to the TCSPC system which informs that an event has occurred. The photon-event is registered in an internal memory and after a short time in electronic processing (named deadtime, typically 90 ns) the system get ready to received the following photo-event. Hundreds, thousands or millions of photon-events can be registered in the same row data table depending of the acquisition lapse time, flux of photons and others parameters during the experimental measurement. The row data table is showed in Figure III.5. The table has three columns that are described as follows:

x.chan It indicates which photodetector has received the photon-event. The values range between 1 or 2 corresponding to APD1 (transmission) or APD2 (reflection), respectively. See Figure III.2.

x.time It corresponds to the absolute time of the laser pulse which is at the origin of the photo-event. When the measurement starts, the TCSPC system initiates an internal clock which runs along the complete acquisition lapse time. Each photo-event is associated with an absolute time which is determined by the pulse laser. As a result, the values in this column correspond to a multiple to the laser pulses (400 ns). It growth systematically as the number of photon-events are recorded. The time is displayed in seconds.

x.lifetime It shows the arrival times of individual photons. It corresponds to the relative time between laser excitation and fluorescence photon arrival. The values are displayed in nanoseconds and range from 0 to 400 ns, corresponding to the repetition rate of the diode laser (2.5 MHz) used in the experiment.

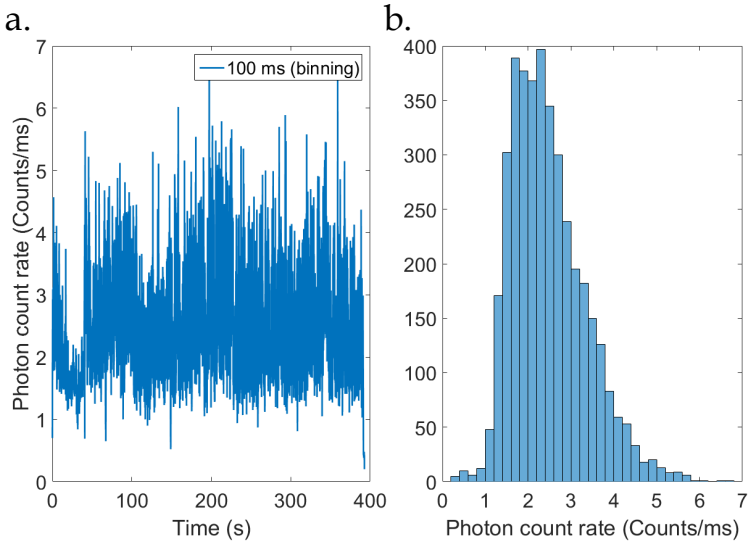

Fig. III.6 *a) Total photons count rate as a function of time of the same nanocrystal shown in Figure III.3. The nanocrystal was excited with an optical power of 850 W/cm^2 in pulsed mode. We have displayed the graph with a binning time of 100 ms. b) Histogram of the photo-events shown in a) with a binning of 0.2 counts/ms.*

The three columns on the left side of Figure III.5 shows twenty photon-events recorded by the TCSPC system registered in the photoluminescence measurements presented in section III.3. The table display the values of $x.chan$, $x.time$ and $x.lifetime$ described above. The fourth column shows the difference in $x.time$ of consecutive photo-events. We can realize that photon-events are not registered for each laser pulse. The average time between two consecutive photon-events lays in the order of milliseconds corresponding to 10^3 $counts/s$, much lower than the repetition rate of the laser. It means that, if we assume 1 ms between consecutive photon-events, the laser would have sent 2 500 pulses before the TCSPC system could have recorded another photon-event. The fifth column of Figure III.5 estimates the number of pulses between the first consecutive 20 photon-events.

For the same nanocrystal, the flux of photons is showed in Figure III.6. Figure III.6a represents the number of photo-events registered for every short intervals of 100 ms (binning) along the complete acquisition time ($T_{acq} = 392.7$ s). The Figure III.6a also shows rapid fluctuations of the number of counts, it corresponds to the fluorescence blinking of the nanocrystal. Note that the binning is 100 ms, but we have normalized the count rate to $counts/ms$. With this normalization, whatever we choose as a binning time, the count rate remains the same for a given measurement. Figure III.6b shows the histogram intensity distribution of Figure III.6a with a binning of 0.2 $couts/ms$.

Why if we excite the nanocrystal in single-photon regime with an optical power of 850 W/cm^2 and a repetition rate of 2.5 MHz, do we only collect in the avalanche photodiodes a rate of 3 kHz photons in average? There is 1 photon-event registered for every thousand

Table III.1: Budget of losses in the optical system.

Collection	Efficiency
Collection by air objective	11 %
Beam splitter (microscope)	90 %
Pinhole (100 μm)	80 %
Beam splitter (spectrometer)[1]	30 %
Lenses, mirrors	90 %
Quantum efficiency APD's	37 %
Total	0.8 %

pulses lunched by the diode laser. This considerable difference is the consequence of the overall efficiency in the experimental set-up including electronics (0.8 % from Table III.1). It is important to note that there is still a factor of 10 which is remaining to explain the proportion between excitation and detection rates. Indeed, with an excitation of 850 W/cm^2 and an absorption cross section of $\sigma = 8 \times 10^{-18}$ m^2 (following Chapter II), we know that the probability to get 1 exciton or more per pulse is close to 100 %. Therefore, for a 2.5 MHz of excitation rate and a 100 % quantum efficiency of the exciton, we should collect a photon count rate of 25 KHz. We should mention that the nanocrystal presented in this section belongs to a different batch as the one studied in Chapter II. We could have the case of a possible over estimation of the absorption cross section for this nanocrystal. It means that, the excitation of 850 W/cm^2 may not induce the excitation of at least one exciton per pulse, as it was discussed in section II.2 for a different batch. We do not discard either the presence of some defects on the nanocrystal structure which might induce a reduced quantum efficiency.

In Table III.1, we summarize the optical losses in the experimental set-up. We have included the efficiency in collection using an air objective with 0.80 NA by collecting light from the air side. This efficiency reaches only 11 % because the air-glass interface modifies the emission diagram of the nanoemitter. When the nanocrystal lays on a glass substrate, most of the fluorescence light is emitted towards the substrate side (more than 80 % of emitted power). Thus, the collection with an air objective on the air side of the interface is limited by the power emitted in this side which is nearly 11 %.

III.4.2 Decay rate curve

The fluorescence lifetime curve can be reconstructed from the row-data table (Figure III.5) by arranging the values of the third column into an histogram of times, as it is plotted in Figure III.7. This histogram is calculated from times between 0 and 400 ns. Please note that this histogram takes into account the whole number of photo-events recorded in one photodiode during the experiment. We have reduced the x-axis to the first 20 ns to distinguish the bars of the histogram. Each bar is identified as one time-channel and the width of the bar corresponds to the resolution in the TCSPC system. For the row-

[1]Normally, in conventional fluorescence measurements, the 30:70 beam splitter is not installed. We have estimated the budget of losses based on the experimental set-up of Figure III.2

data Table presented in Figure III.5, a pre-defined resolution of 256 ps was settled. This resolution can be reduced until 4 ps for a better sampling of the fluorescence decay curve, specially in short lifetimes. Nevertheless, reducing resolution of the TCSPC card doesn't assure to improve the overall response of the experimental set-up. Indeed, the temporal resolution of the optical part (laser pulse + APD resolution) is between 300 and 400 ps.

Further analysis concerning time resolution will be discussed in section III.5. where we will establish the instrument response function of the experimental set-up.

The lifetime curve shown in Figure III.7 was displayed with a binning time equal to the resolution of the TCSPC system. However, binning time could be chosen larger to increase the number of counts per channel (and improve signal to noise ratio) with the constrain of the reduction of temporal resolution. For the rest of the discussion in this thesis we will select $T_{bin} = T_{resolution} = 256$ ps.

The normalized lifetime presented in Figure III.7 was obtained within an acquisition time of $T_{ac} = 392.703$ s, which corresponds to $N_{cycle} = T_{ac}/\tau_{rep} = 9.8 \times 10^8$, where N_{cycle} corresponds to the number of laser pulses during the acquisition time. It means that, the laser have launched 9.8×10^8 pulses and only 972348 photon-events were registered (around 0.1%). The lifetime histogram of Figure III.7 can be fitted as the sum of two exponential functions and a constant noise following the model

$$\mathrm{A}_1 e^{-t/\tau_f} + \mathrm{A}_2 e^{-t/\tau_s} + \beta$$

where τ_f and τ_s are the fast and slow component of the fluorescence emission and β the noise.

We can demonstrate that the noise contribution β extracted from the fitting model corresponds to the dark counts produced by the photodiode during the measurement. The fitting model of Figure III.7 estimates a constant additive noise of $\beta = 60$ dark photon-events. In another words, 60 photon-events were registered for every time-channel of the histogram. For a resolution of 256 ps, the number of time-channels in the 400 ns interval window raise up to 1563. If we integrate the total dark photon-events in the complete 400 ns-window (that it is equivalent to multiply β by the number of time-channels), the fitting model estimates a contribution of $1563 \times 60 = 9.3 \times 10^4$ *counts*. We have then 9.3×10^4 *counts* photo-events corresponding to noise along the acquisition time T_{ac}.

The number of photo-events for each histogram is built from all the N_{cycle} during acquisition time. In order to correlate the value of β of the fitting model with the number of dark counts per second, we estimate the contribution of the noise in the photodiodes, typically ϕ/sec, along the integration time T_{ac}. Thus, the photodiode have registered 250 $\phi/sec \times T_{ac} = 9.8 \times 10^4$ photon-events corresponding to noise. This quantity is in accordance with the value of β predicted in the fitting model, described in the last paragraph.

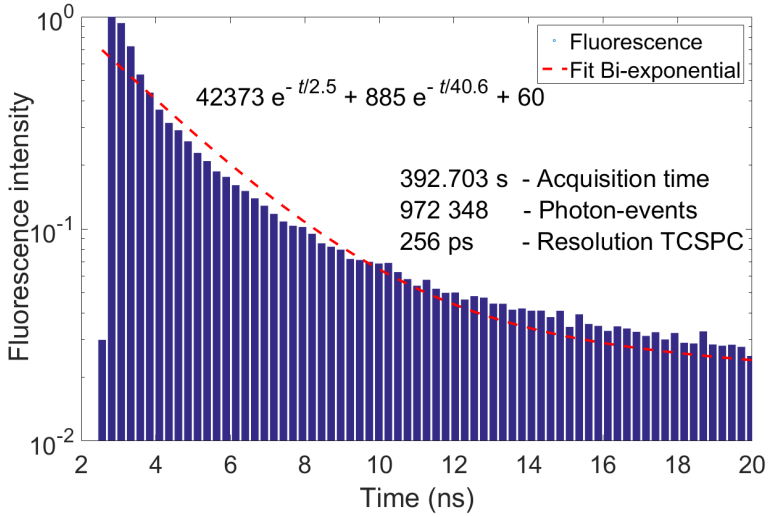

Fig. III.7 *Normalized decay rate curve extracted from the row data table of Figure III.5. We have displayed the first 20 ns to distinguish the binning (or time-channels) fixed in the TCSPC card.*

III.4.3 Second-order autocorrelation function $g^{(2)}(\tau)$

a) 2^{nd} order autocorrelation function histogram

The second-order autocorrelation function $g^{(2)}(\tau)$ is based on the conditional probability of detecting two photo-events simultaneously. This is only possible if the capabilities of the system permits to record both photo-events at the same time. However, for electronics, there is a limitation due to the characteristic deadtime of detectors and acquisition card. The limitations due to the deadtime of electronics is solved by using 2 detectors. The TCSPC card presents a typical deadtime of 90 ns. It means that, even when both photodetectors would have received a photon at the "same" time within the same window, the TCSPC can not register both photo-events. This limitation is solved by introducing a physical delay (spool cable for one photodetector) as it is depicted in Figure III.1. This cable has to be long enough so that the arrival time by this line is longer than the deadtime of the electronics. By considering this electronic delay, 2 simultaneous electrical pulses are separated by more than the deadtime of the TCSPC card, so that they can be both registered. In the optical set-up of Figure III.1, the spool cable has a length of around 100 m which introduces a delay of 480 ns between APD's.

As two successive pulses are separated by 400 ns, each single exciton recombination is separated by around 400 ns. In the case of bi-exciton radiative recombination, for which several photons originating from the same pulse will be emitted at times shorter than the deadtime, we will only keep the events corresponding 1 photon on APD1 and 1 photon on APD2. For example, in bi-exciton radiative recombination, we will lose half of the events (both photons arriving either on APD1 or on APD2).

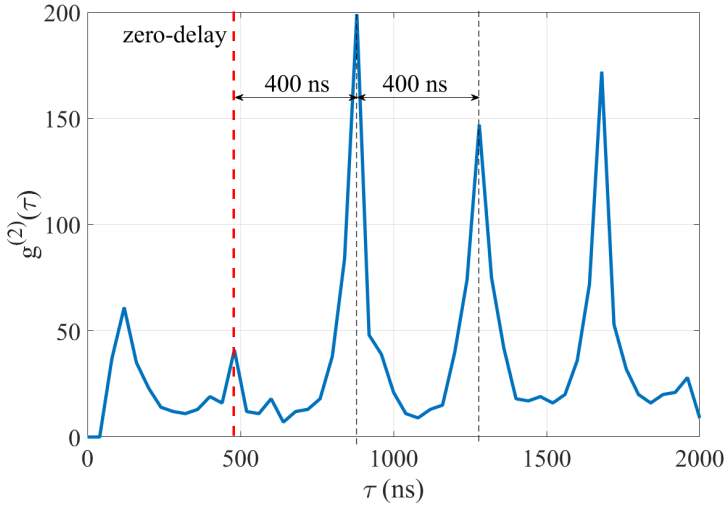

Fig. III.8 *Second-order autocorrelation function $g^{(2)}(\tau)$ with a binning time of 40 ns.*

The construction of $g^{(2)}(\tau)$ from the row data table is delimited to the number of photo-events which fulfill the following condition:

The spool cable is on APD1, so that for second order correlation function we are interested in consecutive photo-events where the first photo-event recorded corresponds to APD2 and the immediate consecutive to APD1. It means, since the earlier photodiode is APD2, after registering a photo-event by this photodiode, the following photo-event should correspond to APD1. By applying this condition, we will discard all consecutive events of the same photodiode (either APD1 or APD2) and the inverse case (first APD1 and then APD2).

The original row data table from Figure III.5 is reduced to 1797 photo-events. Each one contains an absolute arrival time that we can defined as $\mathtt{t}_1$ and $\mathtt{t}_2$ ($\mathtt{t}_1 > \mathtt{t}_2$) for APD1 and APD2, respectively. The absolute time corresponds to the sum of x.time and x.lifetime. We define the difference between these two times as $\tau = (\mathtt{t}_1 - \mathtt{t}_2)$ and define a new table with these values.

The second-order autocorrelation function $g^{(2)}(\tau)$ is shown in Figure III.8. We have limited in this plot the relative delay to $\tau = 2000$ ns and we have using a binning of 40ns. In the figure, we can note that the minimum value corresponds to 88 ns, very close to the characteristic deadtime of the TCSPC card. We have traced a red dashed line pointing out the zero-delay time (nearly $\tau = 480$ ns) when two or more photo-events are registered from the same excitation pulse. The same Figure shows the increment of coincidences every multiple of 400 ns (with respect to the zero-delay time) which corresponds to the repetition rate of the excitation diode laser 2.5 MHz. Note that the peak at 80 ns has not a physical meaning. It corresponds to the symmetric events to the first peak which has

been cut by the deadtime of the photodiode(detection on APD1 before APD2 but $t_1 > t_2$, the case of the spool cable delay).

In the following of the manuscript, we have shifted the zero-delay time at the origin of the x-axis to facilitate the interpretation of the $g^{(2)}(\tau)$ function. Additionally, we will use the $g^{(2)}(\tau)$ function without normalization in order to keep the complete information.

In Figure III.8, we note that the zero-delay peak reaches around 40 coincidences, while the right-lateral peak raised up to 200 counts. The $g^{(2)}(\tau)$ function shows the single-photon emission of the nanosource. The small counts observed at zero-delay are attributed to multi-photonic recombination of the nanocrystal. It can be found that, for low excitation power, the relative height of this central peak scales as Q_2/Q_1, where Q_2 is the radiative quantum efficiency of bi-exciton and Q_1 the radiative quantum efficiency of exciton [57]. This point has been demonstrated in section II.2.3.

The width of the peaks in the autocorrelation function $g^{(2)}(\tau)$ corresponds to the lifetime of the nanocrystal. After each laser pulse, the photons are typically emitted within the lifetime duration. In our set of data, the photoluminescence decay curve presents two components $\tau_f = 2.5$ ns and $\tau_s = 40$ ns (Figure III.7), hence the width of the peaks in $g^{(2)}(\tau)$ extends between two and three points, considering a binning of 40 ns.

b) Analysis of the height of the $g^{(2)}(\tau)$ function

From Figure III.6b, we can calculate the average photon rate of $C = 2.4 \times 10^3$ counts/s registered in both photodiodes, approximately. The average number of photo-events registered during the whole acquisition time T_{acq} raises up to

$$E_{total} = C \times T_{acq},$$

which corresponds mainly to photons emitted by the nanocrystal after excitation pulses and then collected. The number of diode laser pulses lunched during the whole measurement was

$$N_{pulses} = \frac{T_{acq}}{\tau_{rep}}, \tag{III.1}$$

where τ_{rep} is the time interval between excitation pulses ($\tau_{rep} = 400$ ns). Therefore, we can express E_{total} as

$$E_{total} = C \times N_{pulses} \times \tau_{rep},$$

and E_{pulse} is the average number of collected photons per pulse and per photodiode. In the Hanbury Brown-Twiss set-up, we use a 50:50 beamsplitter,

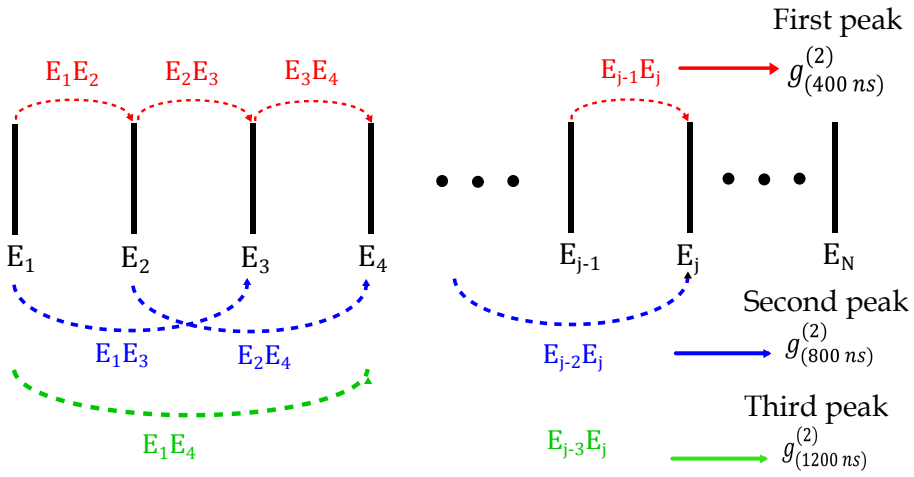

Fig. III.9 *Construction of the second-order autocorrelation function from photo-events.*

$$E_{pulse} = \frac{C \times \tau_{rep}}{2}. \tag{III.2}$$

We can now estimate the number of cross-correlation events which are represented by the second order autocorrelation function $g^{(2)}(\tau)$. We consider that each pulse gives E_j photo-events. In figure III.9 we represent the Dirac function peaks as a function of time. We define that the total number of peaks during the acquisition time is N_{pulses} with E_j a photo-event registered. The construction of the first peak (non zero-delay peak) of the second-order autocorrelation function (named as $N^1_{g_2}$), it will be composed of the multiplication of all photo-events which are distant one cycle of repetition rate

$$N^1_{g_2} = E_1E_2 + E_2E_3 + E_3E_4 + ... + E_{j-1}E_j.$$

as we represent in red arrows in Figure III.9. The total of neighbors at a distance of 1 peaks is $N-1$. The corresponding autocorrelation peak has the height of

$$N^1_{g_2} = E^2_{pulse}(N_{pulse} - 1).$$

We consider here that $\forall j,\ E_j = E_{pulse}$.

Similarly, the second peak of $g^{(2)}(\tau)$ will be composed of all photo-events distant in two cycles of repetition rate

$$N^2_{g_2} = E_1E_3 + E_2E_4 + ... + E_{j-2}E_j.$$

as we have represented as blue arrows in Figure III.9. The total of neighbors at a distance

of 2 peaks is $N-2$ and the height of the second peak will be $E^2_{pulse}(N_{pulse}-2)$.

We can perform the same demonstration up to a distance of N neighbors. Therefore, for the $j-eme$ peak in the autocorrelation function, we will obtain $N^j_{g_2}$ peaks of height $E^2_{pulse}(N_{pulse}-j)$. From a practical point of view $N_{pulse} \approx 10^9$ pulses, we never plot all the $g^{(2)}(\tau)$ correlation peaks. We restrict to display the first peaks (10 - 50 peaks with $50 \ll N_{pulse}$) of the autocorrelation function. We will start by analyzing the first peak. Thus, the first peak will raise accordingly to the probability of register an event in this photodiode.

$$N^1_{g_2} = E^2_{pulse} \times N_{pulse},$$

replacing (III.2),

$$N^1_{g_2} = \frac{C^2 \times \tau^2_{rep} \times N_{pulse}}{4},$$

we can replace N_{pulse} using (III.1), we obtain

$$N^1_{g_2} = \frac{C^2 \times \tau_{rep} \times T_{acq}}{4}. \tag{III.3}$$

The expression (III.3) represents the cross-correlation probability from the first peak. We can note that the height will dependent of the photon count rate C and the integration time T_{acq}. In such manner, extended integration times will be beneficial for the statistics of the autocorrelation function. In our example we have found $C = 2.4 \times 10^3$ $counts/s$, $\tau_{rep} = 400$ ns, $T_{acq} = 392.703$ s. Therefore, the number of values composed in the first peak of $g^{(2)}(\tau)$ (after the zero-delay peak) will raised up to $N^1_{g_2} = 226$. This value is comparable with the experimental peak shown in Figure III.8 taking into account the area under the curve. As the peaks are not Dirac functions, it is distributed along nanoseconds channels. More precisely, on the Figure III.8 with a binning of 40 ns, the first peak has a total area of 331. The second peak has a total area of 296. The third peak has a total area of 297.

We finally discuss the relative height of each peak (apart from the zero-delay). Given the fact that emission and therefore detection of photons follows a Poisson law distribution (decorrelated independent events), if the area under the curve of the peak is N, the noise is given by $\sqrt{N}$. Therefore, the relative area under the peak can fluctuate close to each other as the value of $\sqrt{N}$. For instance, when $N = 1 \times 10^3$, the relative fluctuation $\frac{\sqrt{N}}{N}$ represents $1/30 \approx 3$ % of the height. In the case when $N = 1 \times 10^2$ the relative fluctuation will increase to 10 % and for a case of poor statistics $N = 1 \times 10^1$, the fluctuations will raise up to 30 %. In this case $N \sim 200$ which means that the noise is in the order of $\frac{\sqrt{N}}{N} = 7$ %, which is a good order of magnitude with experimental results.

c) Binning time of $g^{(2)}(\tau)$

We name binning time the small period of time used for calculating the histogram of $g^{(2)}(\tau)$ function or, in another words, the time interval between points in the curve. The binning of $g^{(2)}(\tau)$ function can be modified as it is required by the experimental conditions. In the case when the number of photo-events registered is too small, the increase of binning time is helpful because it will increase the number of events in each channel and therefore increase the signal to noise ratio. On the other hand, reducing binning gives a better temporal resolution with the cost of less cross-correlation counts per binning channel and more relative noise [2].

Figure III.10 shows the same second order autocorrelation function $g^{(2)}(\tau)$ presented before, but now we have plotted with different time binning, from 1 ns to 25 ns (Figure III.10a-f). We have also included the corresponding photoluminescence decay curve in Figure III.10g. From all the curves representing $g^{(2)}(\tau)$ functions, we can see whatever the binning time is, we keep the signature of single-photon emission. In all the graphs, we can observe lower counts at the zero-delay peak ($g^{(2)}(\tau = 0)$) with respect to lateral peaks.

From Figure III.10a-f we can also note the systematic increase of the lateral peaks when the binning time increases. In fact, this increase depends on the number of events for each channel. If we use a short binning, we will have a huge quantity of channels and consequently less events per channel. For instance, if we assume that the width of the autocorrelation peak follows $2T_1$, where T_1 is the lifetime of the nanocrystal ($T_1 = 40$ ns). The number of channels is then $\frac{2T_1}{\tau_{bin}}$. In the graph plotted with $\tau_{bin} = 1$ ns (III.10a), it has 80 channels within the peak. In the case of $\tau_{bin} = 25$ ns (III.10f), there are only 3 channels, approximately, and much more events per channel. Of course, when we calculate the area under the curve, the number of events remains the same whatever the binning.

III.5 Time resolution and instrument response function

As commented before in section III.4.2, the resolution of the TCSPC card is not the element limiting the temporal resolution of the overall system. In order to resolve the fast decay rates of patch nanoantennas or multiexcitonic emission, we have to consider the three principal devices used for any time-resolve fluorescence measurement (excitation source, photodetection device and processing system). In order to determine the overall instrument response of the optical set-up, we carried out a series of experimental tests with the following components:

1. TCSPC system. A PicoHarp 300 card with 4 ps in time resolution from PicoQuant.

[2] The time binning can be reduced as lower as the time resolution of the TCSPC system. However, the precision of coincidence in $g^{(2)}(\tau)$ function will be limited by the time resolution of the photodiodes. We use MPD photodiodes with a time resolution of 250 ps. It means that, reducing the binning lower than 250 ps has not physical meaning.

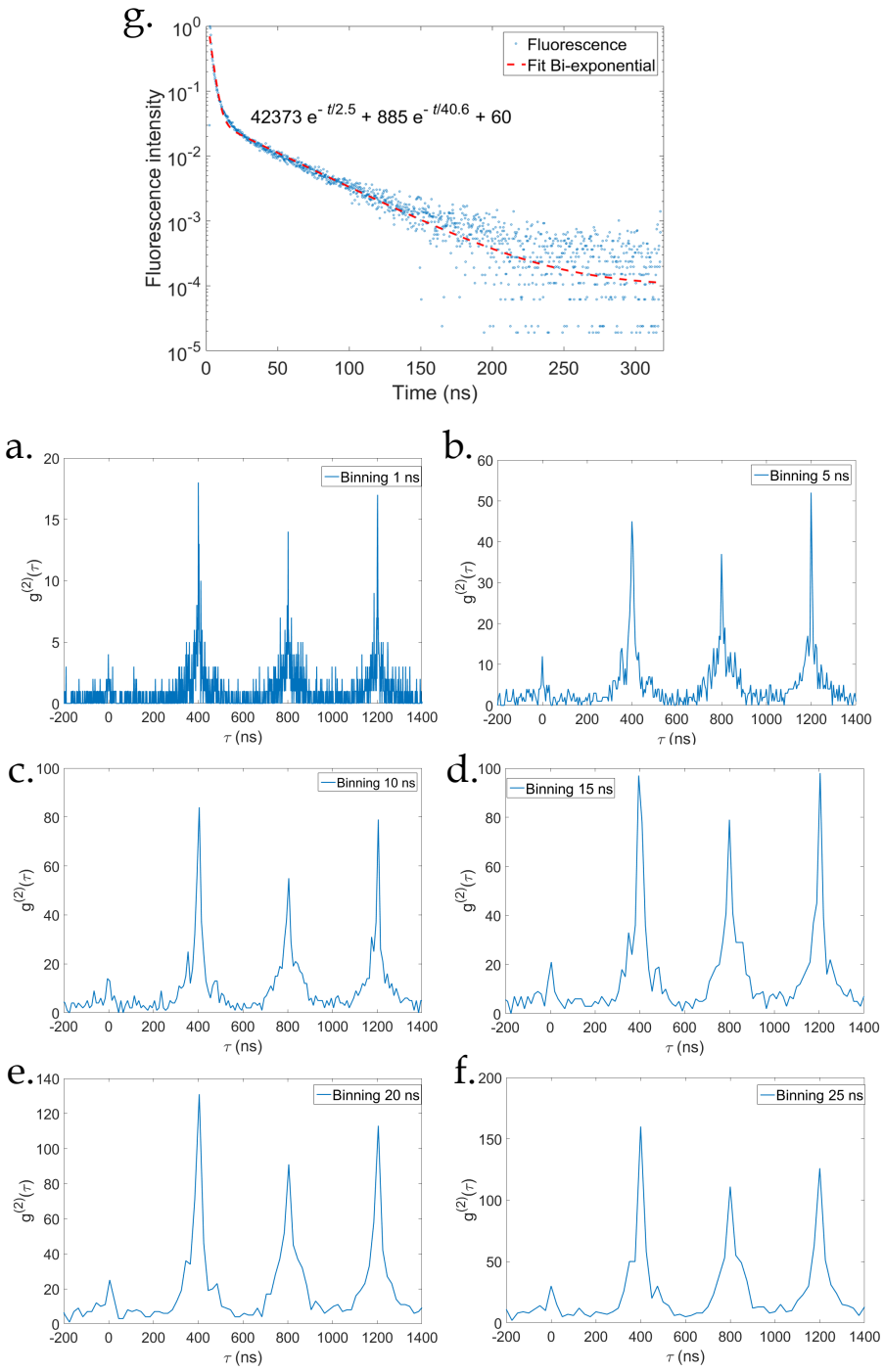

Fig. III.10 *a-f) Set of second order autocorrelation functions $g^{(2)}(\tau)$ plotted with different time binning from 1 ns to 25 ns. g) Photoluminescence decay curve.*

2. Source of excitation. A PDL 800-D unit driver with a picosecond laser diode head (LDH-D-C-405) emitting at 405 nm from PicoQuant.

3. Photon counting detector. A solid-state detector with an active area of 100 μm manufactured by Micro Photon Devices (MPD).

III.5.1 TCSPC system

The time resolution of the TCSPC system can be reduced until 4 ps. That means, the number of vertical bars shown in Figure III.7 can be as short as 4 ps. However, the TCSPC system is configured in mode T3 where a maximum of 4096 time-channels are available for each decay curve. With this constrain when setting 4 ps as time resolution we will record only the first 16 ns of the decay rate curve, which is a clear limitation for studying fluorescence of semiconductor nanocrystals whose typical lifetime extend to some tens of nanoseconds. In order to have a good sampling in time resolution from the TCSPC system, we have used 32 ps and 64 ps which extend the decay curve to 131 and 262 ns, respectively.

III.5.2 Laser source and detection

One of the most relevant components employed for time-resolved photoluminescence emission is the excitation light source. The duration of the laser pulse in the excitation can limit the time resolution of the complete experimental set-up. We used a diode laser which send narrow optical pulses between $70 - 500$ ps depending of the level in power adjustment, according to PicoQuant (http://ridl.cfd.rit.edu/products/manuals/PicoQuant/laser%20head%20specification.htm).

In order to study how the lasing threshold of the diode laser can influence the measurements of fast decay curves, we have performed intensity measurements with different excitation currents at a fixed repetition rate 2.5 MHz (400 ns period time). In the TCSPC card, we have used 64 ps as time resolution. Then, we plot with a binning of 64 ps the intensity versus time.

The Figure III.11 shows the superposition of all laser pulses for different excitation currents. From the Figure III.11 we can observe the continuous reduction of pulse width in accordance with the increase of excitation current. The shortest linewidth of the pulse is achieved for an excitation current of $I = 3.1$ in the scale of potentiometer. The duration of the pulse reaches the minimum value of 256 ps (Full Width at Half Maximum) and remains constant for the larger values from $I = 3.1$ to $I = 4.0$. It means that, for $I >> 3.1$, the laser is any more in the luminescence regime and has reached the lasing regime above threshold, corresponding to the smallest width. On the contrary, for $I = 2.57$, the laser is at threshold and the pulse width can be as long as 570 ps.

For the coming experiments we will employ the laser in the lasing regime ($I >> 3.1$) to improve the time resolution of the set-up.

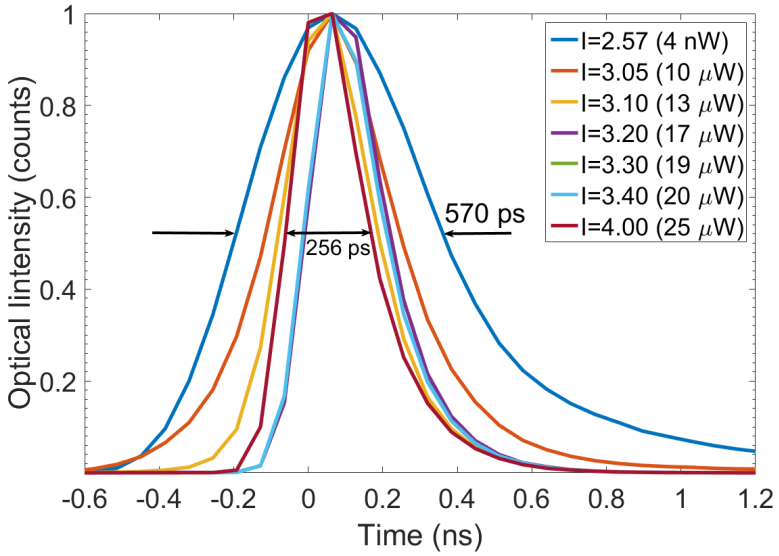

Fig. III.11 *Response of the blue diode laser for different values of excitation power. Time binning of 64 ps.*

III.6 Experimental set-up for reflectivity measurements on single nanoantenna

In addition to studies of single quantum dots, we have performed specular reflectivity measurements on single patch nanoantennas. Reflectivity measurements is a technique widely used to identify absorption properties in metallic nanostructures. It consists in illuminating (with a broadband emission source) the nanostructure to quantitatively estimate the light reflected with respect to a specific reference. In this section, we will describe the experimental set-up used to perform such measurements with a single patch nanoantenna or another individual nanostructure.

III.6.1 Illumination source

In order to perform reflectivity measurements, it is required to use a wide-spectrum source of light such as halogen lamp. This source of illumination covers an extensive spectral range including wavelengths from 350 to 800 nm, as it is shown in Figure III.12.

In the experimental set-up described in section III.3, the spatial filter (pinhole 100 μm) placed at the conjugated image plane of the sample improves the signal to noise ratio during the scanning of individual nanocrystals. For reflectivity measurements in single nanostructures, the same spatial filter will allow to collect exclusively the light coming from an area of 1 μm on the sample (the magnitude of the optical objective is 100$\times$) and block all the light outside of this region. For this reason, before performing reflectivity measurements on single nanostructures, the precise alignment of the pinhole with a diffraction-limited point-like emitter (QD) is required.

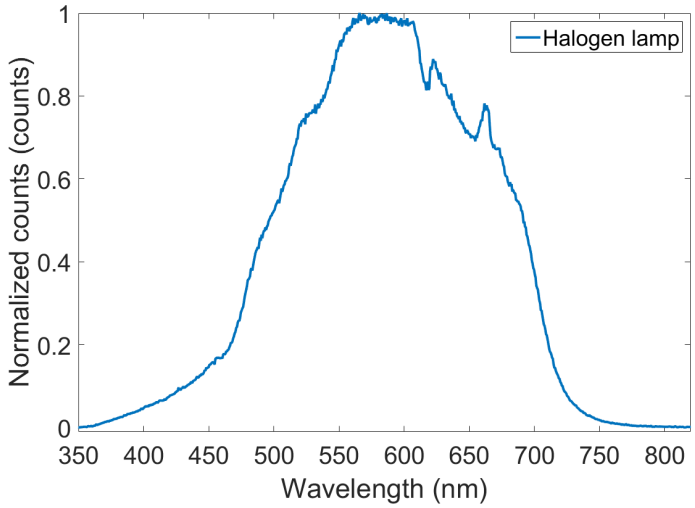

Fig. III.12 *Emission spectra of the halogen lamp.*

Our reflectivity technique starts by placing the nanoantenna inside the laser scanning area of 15×15 μm. Then, we perform a fluorescence scanning image with the laser at 405 nm to identify the metallic nano-disk along the sample. The use of fluorescence imaging helps to distinguish the Au disk around another materials around the antenna. Later on, we performed a second scanning image of some micrometers around the patch in order to increase the position precision of the nanostructure.

Figure III.13a shows a fluorescence scanning image of a single patch of 945 nm diameter. In the image we have traced a circumference of 1 μm indicating the extension of the Au nano-disk. From the same Figure III.13a we can observe fluorescence spots resulting from the dotted pattern surrounding the nanostructure (intermixing layer which will be discussed in Chapter IV). We also note a bright spot close to the border of the nano-disk which represent some dielectric residue remaining after lift-off processing. Figure III.13b shows the corresponding SEM image of the same nano-disk in the orientation presented in Figure III.13a. From both images we can correlate the bright fluorescence spot of Figure III.13a with the opaque residue dots observed in Figure III.13b. The correlation of images confirms the position of the patch.

III.6.2 Differential Reflectivity Spectroscopy (DRS)

Once the patch nanoantenna is identified and placed at the position of the laser spot, we illuminate the structure with the halogen lamp (non-polarized light). Before that, we turn off the photodiodes to avoid saturation. In Figure III.14 shows the complete experimental set-up used for reflectivity measurements on single nanoantennas. The white light is reflected by a 50:50 beam slitter then is focused by the 0.80 NA objective. In the spectrophotometer, we select an acquisition time for which the CCD camera doesn't

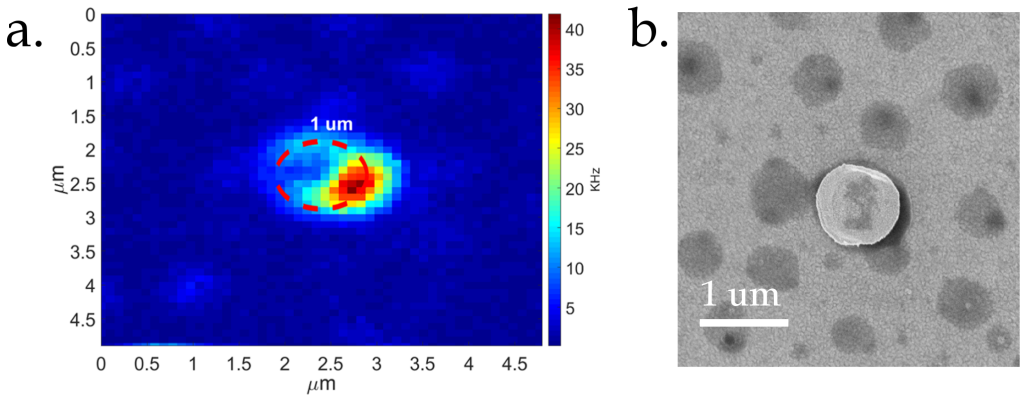

Fig. III.13 *a) Laser fluorescence scanning image of a single passive nanoantenna excited with a blue laser emitting at 405 nm. b) Scanning electron image of the same nanostructure.*

overload. We register the spectra reflected in two positions: 1) the position with the patch antenna that we will name R_{Ant}, and 2) the position some micrometers far away of the antenna labelled as R_{ref}, as it is shown in Figure III.15a. We define the differential reflectivity spectroscopy (DRS) as:

$$DRS = \frac{\Delta R_{Ant}}{R_{ref}} = \frac{R_{Ant} - R_{ref}}{R_{ref}}, \tag{III.4}$$

with R_{Ant} corresponding to the spectra reflected by the patch structure and R_{Ref} corresponding to the spectra on the gold surface that includes the dielectric layer. Differential reflectivity is a parameter that quantify the relative absorption of the Au nano-disk with respect the gold substrate including dielectric layers.

Figure III.15b shows the differential reflectivity of the passive antenna shown in Figure III.13. From the curve in Figure III.15b we observe a dip around 500 nm. At this wavelength the structure absorbed more than 20% of the incident light with respect to the flat Au substrate including PMMA layer.

III.6.3 Differential Reflectivity on passive nanoantennas

We have performed additional measurements of differential reflectivity spectroscopy of the 4×4 matrix shown on Figure III.16. All the passive antennas were fabricated using the same in-situ lithography protocol with a blue diode laser and 0.80 NA optical objective.

In Figure III.17a we show the differential reflectivity spectroscopy of seven patches from the same 4×4 matrix. We can observe that all the curves are characterized by a predominant absorption dip around 500 nm. At this wavelength the light is highly absorbed by the nanostructures reaching almost an efficiency of 50 % for some of them (Ant 4, Ant 9 and Ant 10).

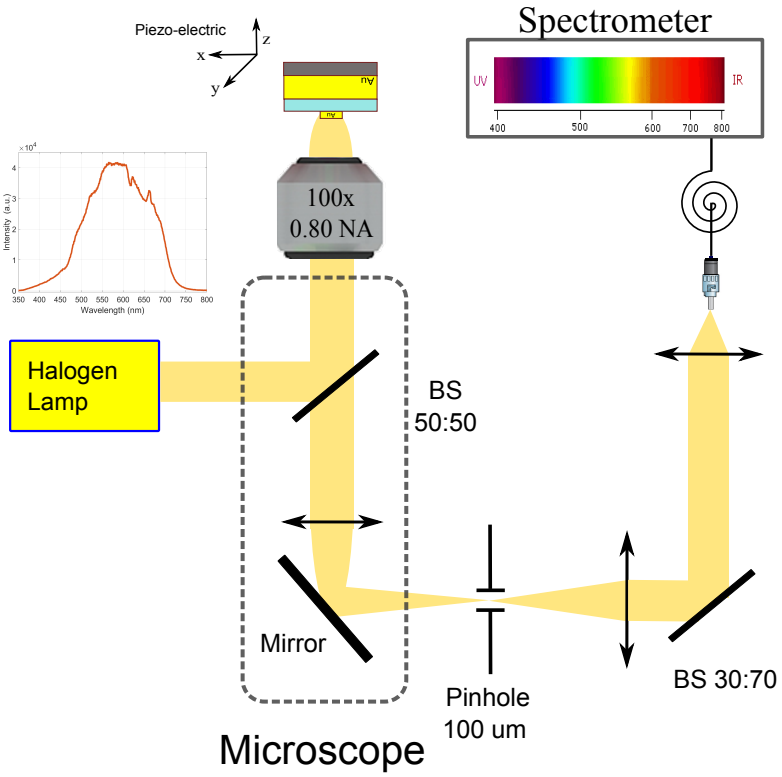

Fig. III.14 *Experimental set-up used to perform specular reflectivity measurements in a single patch antenna. We have used an halogen lamp as illumination source with non-polarized light.*

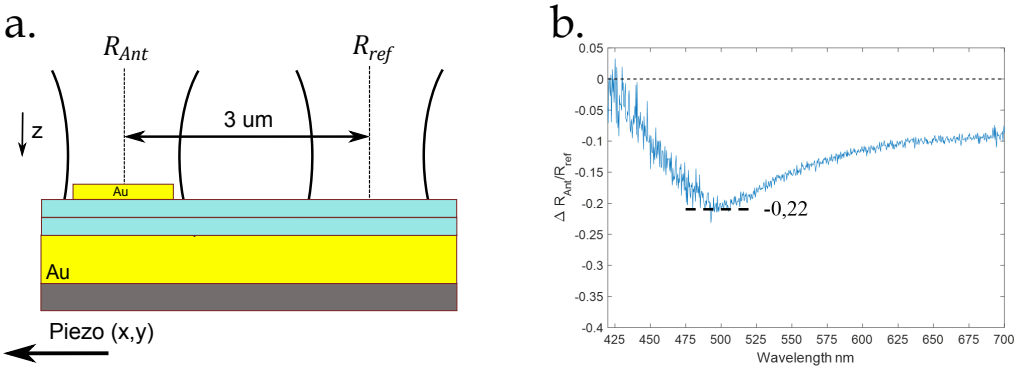

Fig. III.15 *Description of the differential reflectivity spectroscopy for a single patch antenna.*

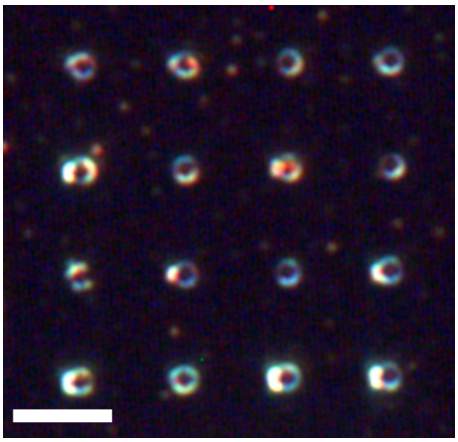

Fig. III.16 *Optical dark-field image of passive antennas subjected to reflectivity measurements. Scale bar 5 μm.*

The quantity of light absorbed by the nanostructure (or value in DRS scale) is not the same for all the patches. It can vary approximately from 0.3 to 0.5 as it is observed in Figure III.17a. In Figure III.17b we plot the wavelengths for which the minimum values in DRS scale is obtained from each antenna. The error bars on the graphs represent the standard deviation of five consecutive measurements with same experimental conditions. From the Figure III.17b we can observe that the shortest wavelength corresponding to Antenna 9 is associated with the maximum absorption of light.

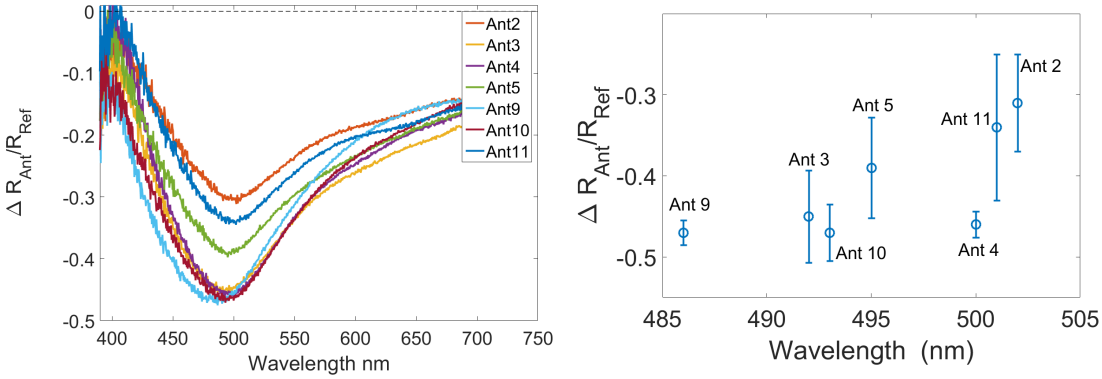

Fig. III.17 *a) Differential reflectivity curves of seven passive nano antennas belonging to the 4×4 matrix of Figure IV.33b. b) Maximum absorption wavelength of the reflectivity curves shown in a). The error bars in the graphs represent the standard deviation of five consecutive measurements with same experimental conditions.*

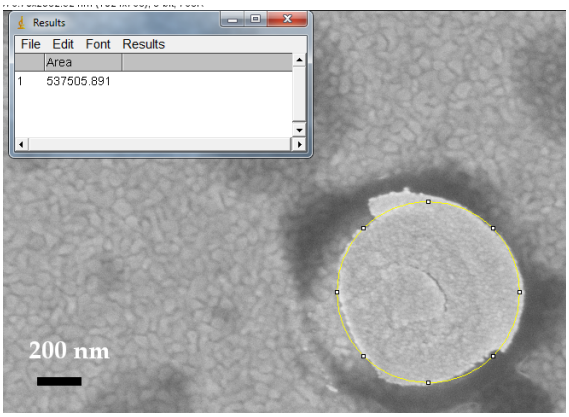

Fig. III.18 *Scanning electron image of a passive nanoantenna (Ant 9). We have estimated the effective diameter by enclosing with a yellow round trace most of the area represented by the nano-disk. We have calculated an effective diameter of* d_{eff}*= 827 nm.*

III.6.4 Effective diameter

The results shown in Figure III.17 suggest that there are some differences in morphological properties of the patch nanoantennas which may produce different maximum absorption dip. In order to examine the morphological properties of each passive antennas, we have characterized the nanostructures by Scanning Electron Microscopy. In Figure III.18 we show the scanning electron image corresponding to the Ant 9 previously discussed. From the image we can note that the disk is surrounded by an opaque dotted pattern. This pattern corresponds to the intermixing layer after lift-off processing. The opaque contrast in the SEM image confirms the presence of non-conductive materials.

In the same Figure III.18, we can note that the nano-disk is not perfectly circular. The patch has a slight asymmetry and the edge is discontinuous. Therefore we define an effective diameter (d_{eff}) in order to not take into account asymmetries and defects of the nanostructures. We have employed the following method:

From the scanning electron image, we have traced a yellow round enclosing most of the area represented by the patch, as it is showed in Figure III.18. We define as d_{eff} *the diameter of this disk.*

We can extract the effective diameter of the Ant 9 displayed in Figure III.18. The effective diameter of Ant 9 corresponds to d_{eff}= 827 nm. We have calculated the effective diameter of the rest of the passive elements subject to reflectivity analysis. In Figure III.19a we show the scanning electron image of the complete 4×4 matrix. Figure III.19b shows the effective diameters of the seven passive antennas.

In Figure III.19b we can observe that most of the passive antennas hold effective diameters around 940 nm. The smallest antenna is Ant 9 which has an effective diameter of d_{eff}= 827 nm. We can conclude then that the shortest absorption wavelength observed

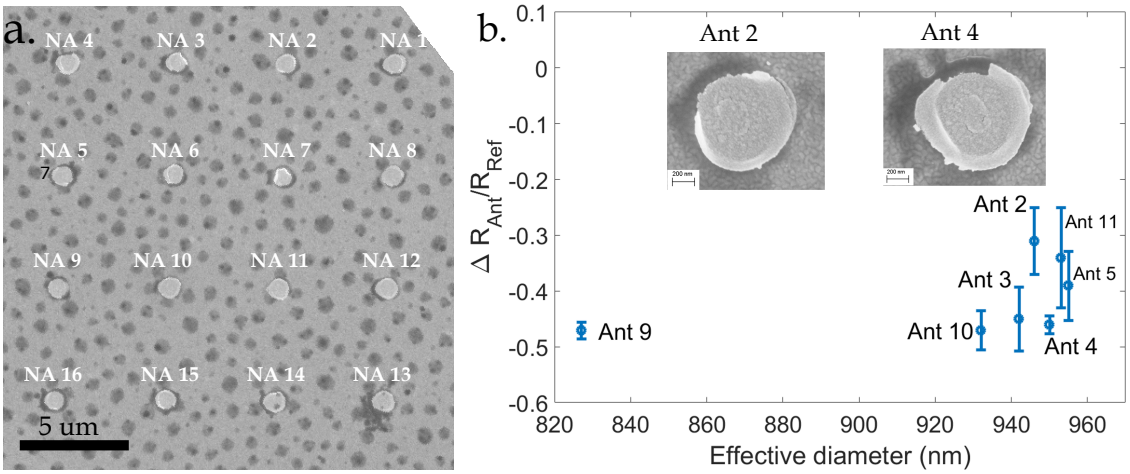

Fig. III.19 *a) Scanning electron imaging of an array of 4×4 of passive antennas. b) Estimation of the effective diameter of the antennas subject to reflectivity analysis.*

in reflectivity measurements is associated to the smallest nanostructure Ant 9.

The results on Figure III.19b showed that some passive nanoantennas exhibit similar effective diameter but substantial difference in absorption properties (DRS value). This is the case of Ant 2 and Ant 4, exhibiting respectively 30 % and 50 % of maximum values of DRS. In the same Figure III.19b, we have included insets on the graph showing the electronic images of Ant 2 and Ant 4. This shows that the effective diameter is probably not the main parameter which governs absorption. These results suggest the influence of others features such as defects on the edges which may induce hot spots and more absorption.

III.6.5 System of multiple thin layers

In a first approximation, we can reconstruct the differential reflectivity by treating the patch antenna as a system of multiple thin layers which produce multiple-beam interference. Figure III.20a shows numerical calculations of the reflectance in three different configurations: 1) bare Au substrate, 2) Au + 40 nm PMMA and 3) Au + 40 nm PMMA + 20 nm Au. The numerical results are computed with non-polarized light and normal incident illumination. Figure III.20b shows the reflectance for a second configuration with a thicker intermediate dielectric layer (60 nm PMMA). The differential reflectivity spectroscopy (DRS) for both systems is calculated according to (III.4) and plotted in Figure III.20c.

From the Figure III.20c we can note that both graphs reproduce quite well the experimental results showed in Figure III.20d. We observe a dip around 500 nm with values in differential reflectivity of $DRS = -0.3$ and $DRS = -0.8$ for 40 nm and 60 nm, respectively. By comparing both curves we can observe that the increase of the thickness in the dielectric layer modifies the amplitude of the maximum absorption dip but not

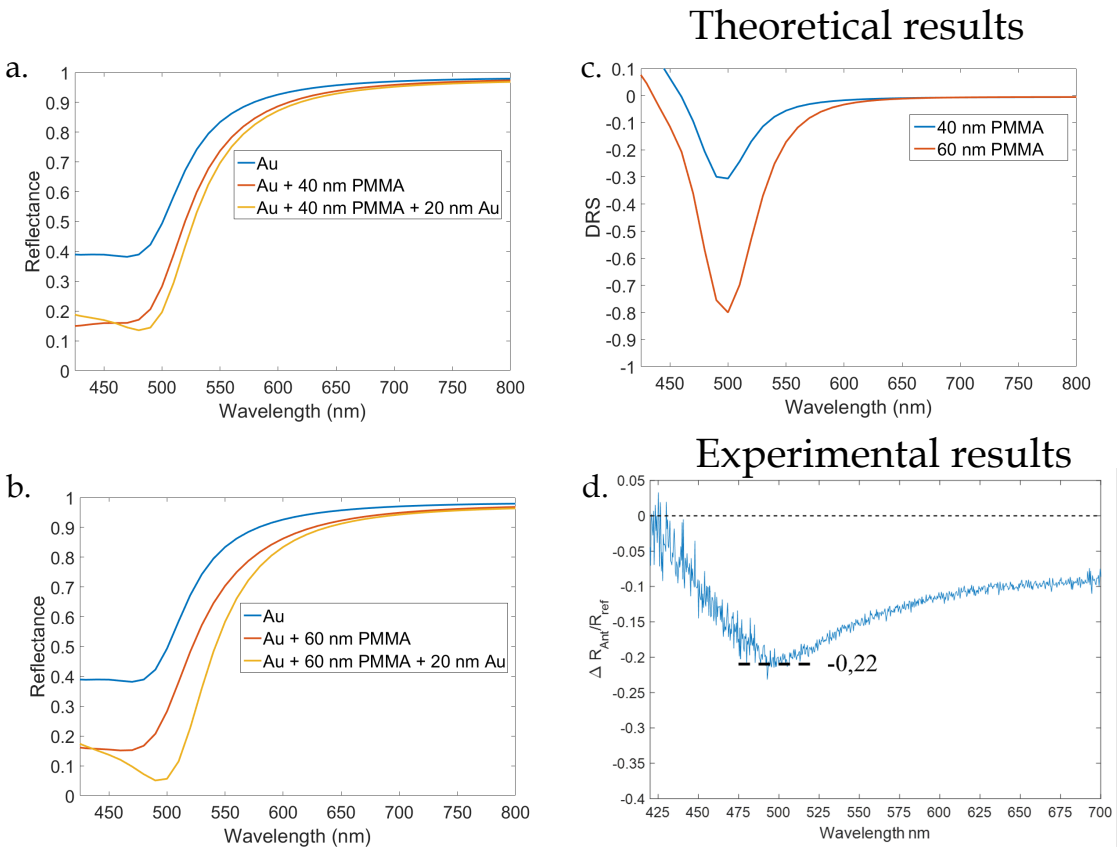

Fig. III.20 *Normal reflectivity of a) Au + 40 nm PMMA + 20 nm Au, b) Au + 60 nm PMMA + 20 nm Au, c) Differential reflectivity spectroscopy for 40 nm and 60 nm of PMMA, d) Experimental results.*

the wavelength position. At this point, we will turn our discussion towards two main questions: 1) why we have observed a dip at $\lambda = 500$ nm and 2) how can we explain such a difference between 40 and 60 nm thickness layer.

By comparing Figures III.20a and c, we can note that the position of the maximum absorption dip corresponds actually to the wavelength for which the gold becomes more absorbing. The absorption of gold changes quickly within the interval $500 < \lambda < 550$ nm. In Figure III.20a we can observe that, for $\lambda < 500$ nm, the absorption of gold is quite flat. Similar response is observed for $\lambda > 550$ nm where the variation of absorption is quite smooth. Thus, the appearance of the dip around $\lambda = 500$ nm corresponds mainly to this abruptly change in the absorption properties of the gold material.

If we now consider the reflectance curves of Figure III.20a, we can note that the absorption with 40 nm of PMMA layer is larger than bare gold. Similar characteristic is observed in Figure III.20b with 60 nm thickness layer. Then, when the 20 nm-Au layer is added to both systems, the absorption of the system with 60 nm of PMMA is larger than 40 nm. The differential reflectivity spectroscopy (DRS) estimates the relative difference

between the orange and the yellow curves. Thus, it is clear that this difference will be more important for small values in reflectance. For instance, at 500 nm the relative difference reaches $\Delta R_{Ant} = 0.08$ in the system with 40 nm of PMMA, whereas $\Delta R_{Ant} = 0.23$ for the structure with 60 nm.

In Figure III.21 we show the intensity distribution of the electric field for both systems using the commercial software "film wizard". The upper image represents the system with 40 nm PMMA layer and the bottom the corresponding 60 nm PMMA. In both images we can see that the amplitude of the electric field is maximum for a wavelength close to 500 nm on the side of the 20 nm-Au layer. It means that, the maximum absorption dip observed experimentally in Figure III.20d is associated with the maximum amplitude of the electric field inside the metallic layer. Furthermore, we can also observe that this amplitude is more important for the system with 60 nm PMMA than for the one with 40 nm PMMA. Therefore, the absorption is larger and the dip is deeper in Figure III.20c for 60 nm than for 40 nm PMMA layer.

In this section we have discussed the reflectivity properties of a single passive nanoantenna with an effective diameter of 945 nm. The numerical simulations of this section have been convenient to describe the main features in the reflectivity curve of the nanoantenna. Nevertheless, this approach assumes patch systems with infinite dielectric and metallic thin layers. The approach doesn't take into account neither the finite size of the nano disk and the morphological shape.

III.7 Conclusion

In this section we have presented the different experimental set-up employed during this thesis. The use of the photoluminescence set-up has allowed to performed spectroscopy analysis of individual nanoemitters, patch nanoantennas and materials employed for the in-situ lithography protocol. We have discussed the principal components involved in the spectral resolution of the apparatus and discussed the linewidth emission of the sources employed in photoluminescence experiments.

We have described how to retrieve the decay rate curve and the second-order autocorrelation function $g^{(2)}(\tau)$ from the row-data table registered by the TCSPC system for time-resolved fluorescence measurements. We have emphasized the role of binning time to represent photon-statistics in $g^{(2)}(\tau)$ function.

We have obtained the time resolution of the overall experimental set-up by performing systematic experiments from the excitation source to the electrical ports. We have established the time resolution (or instrument response function) of our overall experimental set-up to 116 ps when the TCSPC cards is configured with 32 ps in timing resolution and the diode laser operates above the lasing threshold ($I > 3.10$). The time resolution is limited by the pulse width of the excitation diode laser.

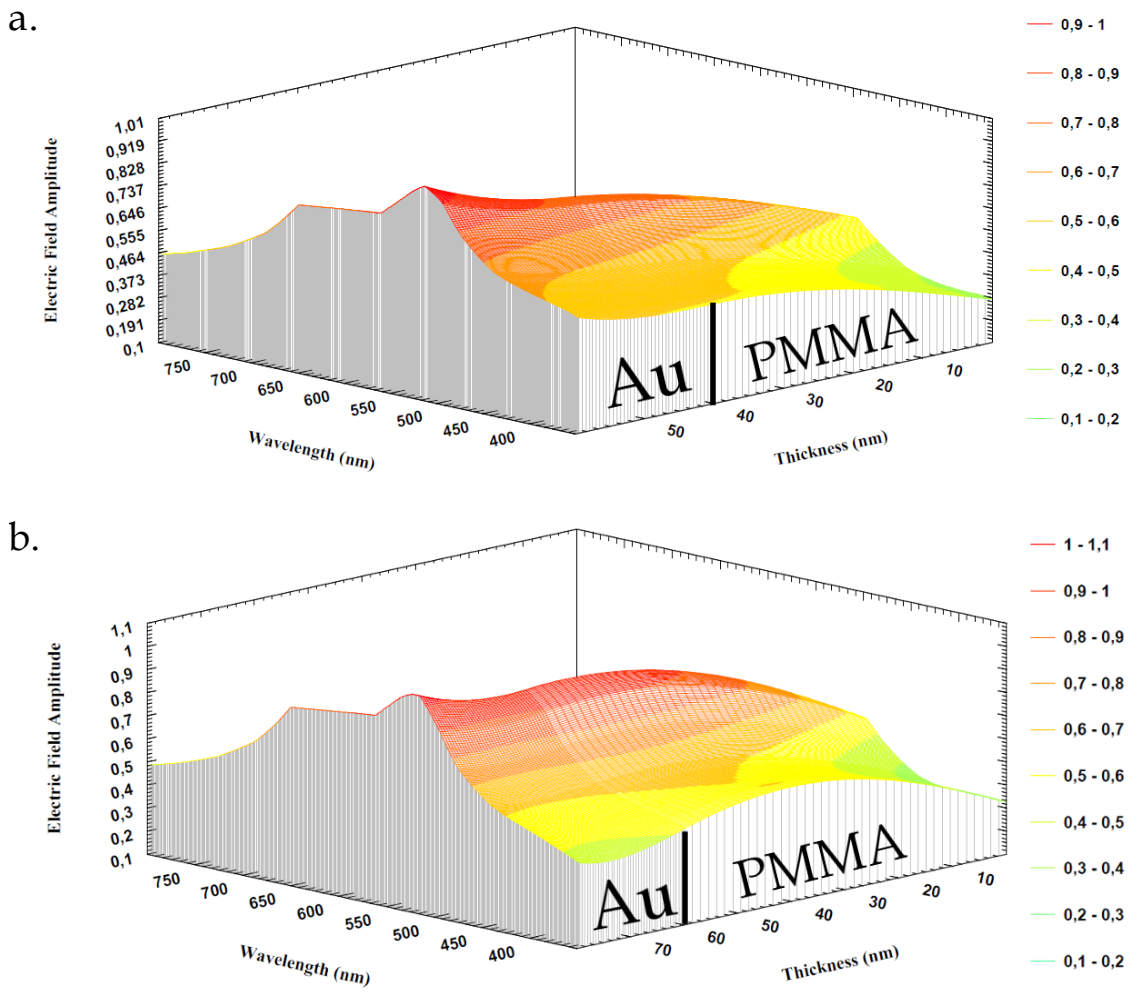

Fig. III.21 *Distribution of electric field inside the patch system for a) 40 nm thickness and b) 60 nm.*

We have described the experimental set-up used to perform reflectivity measurements on single nanoantennas. We have featured the importance of a proper source of illumination. We have defined the differential reflectivity spectroscopy which gives the absorption losses of the metallic nano-disk with respect to a given reference. We have found theoretically the strong dependence of the differential reflectivity to the dielectric gap of the nanostructure.

We have studied passive nanoantennas in terms of differential reflectivity spectroscopy (DRS). We have found that, within an array of 4×4 passive nanoantennas fabricated with exactly similar parameters, the shape, effective diameter and wavelength of maximum absorption can be different between each structure. Additionally, we have found that some patches are not completely symmetric and present some morphological defects which may induce *hot spots* in the scattering emission of light, evidenced by dark-field microscopy.

Chapter IV
Fabrication methods

IV.1 Introduction

In this chapter we will discuss mainly the fabrication methods used to fabricate deterministic antennas. All the nanostructures studied in this thesis were fabricated with the in-situ optical protocol which is based on the deterministic positioning of the nanocrystal at the middle of a single plasmonic patch antenna.

Among the several fabrication technologies currently used to realize plasmonic micro- and nano- structures, we can distinguish two of them: 1) photo-lithography with an optical laser beam (photons) and, 2) e-beam lithography where a tiny electron beam interacts with the layers of the sample. We can successively classify them in two types depending of the modifications produced in the sample. The low interaction processes the case for which the photons or electrons only modify the chemical properties of the material. For conventional photo-lithography the pattern is created in a photo-resist layer. Similarly, for e-beam lithography, the electron beam insulates a resist layer. If the interaction is now conducted in relatively high power in such a way that there exist inherently destruction on the sample to obtain the desired pattern, we can refer as Direct Laser Writing when the radiation is composed by photons and Focus Ion Beam when electron are employed in carving the target material.

In direct laser writing, the optical radiation heats, melts and evaporates the material. This mechanism is highly dependent of several parameters, such as incident power, time of exposure, wavelength of the radiation, absorption properties of the materials and substrate. This thermal process plays a key role for our in-situ lithography protocol. In that sense, it is very different from conventional photo-lithography protocols for which the photo-resist is solely exposed without removal of material.

Several techniques have been developed in the team of Nanostructures and Optics to fabricate plasmonic patch antennas, the first trials have been done by Cherif Belacel with a photoresist as an imaging resist for writing a pattern above the nanocrystal. Because the self-luminescence of the photoresist, single nanocrystal could not be observed below this imaging layer and only patch antennas with aggregates of nanocrystal were obtained.

Therefore, during the thesis of Cherif Belacel and Amit Raj Dhawan the photoresist layer has been replaced by non-luminescent layer (PMMA).

In 2013 Cherif Belacel [58] proposed the use of a diode laser emitting at 405 nm to perforate a hole on the top of PMMA layer showing the possibility to control the hole diameter from 0.50 μm to 1.36 μm by defocusing or modifying the radiation time. In spite of enormous efforts to use this source of light for the fabrication of antennas with a single nanoemitter, during the exposure process the high intensity laser photobleachs the single nanocrystal. This difficulty has been overcome during the thesis of Amit Raj Dhawan by proposing three different techniques to drill a hole in a deterministic manner without damaging the single nanocrystal. One of those techniques is based on the use of a high power supercontinuum laser which emission wavelengths can be adjusted carefully to expose the resist without photobleaching the nanocrystal.

In this chapter we will present the progress of the in-situ lithography protocol especially in the last step named "lift-off". Lift-off processing is the final stage in a sequence of nano- and micro- fabrication where all materials surrounding the nanostructure of interest are removed by means of chemical attacking or another procedures. For instance, throughout the course of this thesis, we have carried out an exhaustive study to optimize and strengthen the in-situ protocol for the fabrication of patch nanoantennas with a single nanocrystal.

In most of the lithography techniques for micro- and nano-fabrication, the find out of exposure parameters, such as time and optical intensity, are the most relevant quantities in the initial step of fabrication. These parameters also determine the resolution limit of the lithographic technique by defining shape and sizes of the future nanostructures.

IV.2 In-situ lithography protocol

We will start by introducing to the reader the procedure for depositing thin films. We have used a spin coater Karl Suss in static dispense. It means that, we firstly drop the fluid over the surface before starting the spinning of the plate holding the sample. All the thin films for in-situ protocol have been deposited by this method. We describe the general procedure for the preparation of the sample.

IV.2.1 Preparation of the sample

In a commercial silicon wafer we have deposited 5 nm-Cr followed by 200 nm-Au by thermal evaporation. The thin layer of chromium is included as an adhesion layer to stick the evaporated gold with the silicon wafer. We have then cleaned the gold surface with acetone and we have spin-coated the films as follows:

1. Deposit of first PMMA layer. We spin-coated a solution of PMMA with a concentration of 0.75 % using 4000 rpm (spin speed), 2000 rpm/s (acceleration) during 45

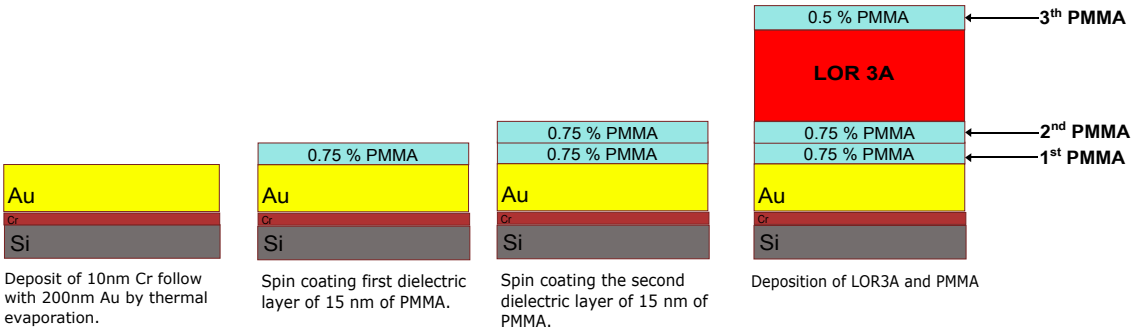

Fig. IV.1 *Procedure of thin film deposition for in-situ protocol. The combination of LOR3A layer with the third PMMA layer is called resist bi-layer.*

s (time) in the spin-coater. This procedure gives around 15 nm thickness. We have baked the layer at 150 ^{o}C during 2 min.

2. Deposit of second PMMA layer. We spin-coated the second dielectric layer with solution of similar concentration (0.75 % PMMA) and spin-coating parameters (4000 rpm, 2000 rpm/s and 45 s). The layer gives additional 15 nm in thickness. We have baked the layer at 150 ^{o}C during 2 min [1].

3. Deposit of lift-off resist LOR3A layer by spin coating. We spin-coated the resist LOR3A using 7000 rpm, 2000 rpm/s during 45 s. These parameters provide a thickness of 330 nm. We have baked the layer at 150 ^{o}C during 2 min [2].

4. Deposit of third PMMA layer. We finish the preparation of the sample with the deposition of a PMMA layer with a concentration of 0.5 % using 4000 rpm, 2000 rpm/s during 45 s. These parameters provide a thickness of 10 nm. We baked the layer at 150 ^{o}C during 2 min. The combination of LOR3A layer with the third PMMA layer is called resist bi-layer. The thickness of LOR3A layer should be at least three times larger than the thickness of the upper layer. Most of the interaction between laser light for drilling a hole occurs between these layers.

The whole procedure of thin film deposition is illustrated in Figure IV.1.

IV.2.2 In-situ optical protocol

Once the sample is coated with the resist bi-layer, we proceed with the fabrication of the nano-disk by in-situ lithography protocol. The different steps are illustrated in Figure IV.2.

1. **Hole making** . It corresponds to the process when the radiation laser creates the aperture in the resist bi-layer. From former studies [58], we know that the radiation

[1] In the final protocol with active antenna, we spin-coating nanocrystals before the second PMMA layer. Here we have skipped this step.

[2] In section IV.7.4 we will discuss more in detail the influence of baking the lift-off resist layer.

laser can not make a hole in a simple PMMA layer. Indeed, the dielectric PMMA layer is transparent for all the visible wavelengths (low absorption). On the contrary, the laser can drill easily a hole on the LOR3A layer. The radiation laser is absorbed by the LOR3A layer. When a very thin PMMA layer is covering a LOR3A layer, the high temperature of the LOR3A layer heats the PMMA layer until evaporation and makes a hole. We will concentrate our discussion on two sources of light: 1) blue diode laser emitting at 405 nm to fabricate passive patch antennas or antennas with clusters of nanocrystals and 2) Supercontinuum laser used for antennas with single nanoemitters.

2. **Development of lift-off resist LOR3A** . Development is the process in which the developer MF-319 dissolves LOR3A layer by chemical reaction removing the remaining lift-off resist on the center of the hole and creating an undercut with the upper dielectric layer. The development should be conducted with extreme precision in order to avoid the dissolution of too much LOR3A layer causing the collapsing of the upper PMMA layer (overdevelopment).

3. **Au patch deposition** . The deposition of the 20 nm-Au layer is performed by thermal vapor deposition.

4. **Lift-off processing** . It corresponds to the removal of all the materials above and surrounding the nano-disk (lift-off resist LOR3A and evaporated Au layer attached to the upper dielectric layer).

IV.3 Tracking of a single hole

As mentioned before, the optimization of the lithographic parameters implies the awareness of the modification of each dielectric and metallic layer along the in-situ protocol. We have conducted a systematic study by atomic force microscope (AFM) to analyze the modifications of the stack of layers in the development and lift-off processes. We have studied the influence of the developer MF-319 in the in-situ optical lithography for the fabrication of patch antennas.

This section contains the results in AFM and fluorescence imaging when a blue diode laser (405 nm) is used as source of radiation to make holes in the resist bi-layer. In Appendix A we present the results for similar study when the in-situ protocol is performed by the super continuum laser. The aim of both studies is to follow one single hole (future antenna) along the complete protocol in order to observe and analyze the modifications during development and liftoff stages.

IV.3.1 Laser exposure

After the preparation of the stack of layers described in IV.2.1. We have created a 3×3 matrix on the resist bi-layer using the blue diode laser pumped at maximum intensity in continuous mode (5.42 mW average optical power). We have exposed the sample during

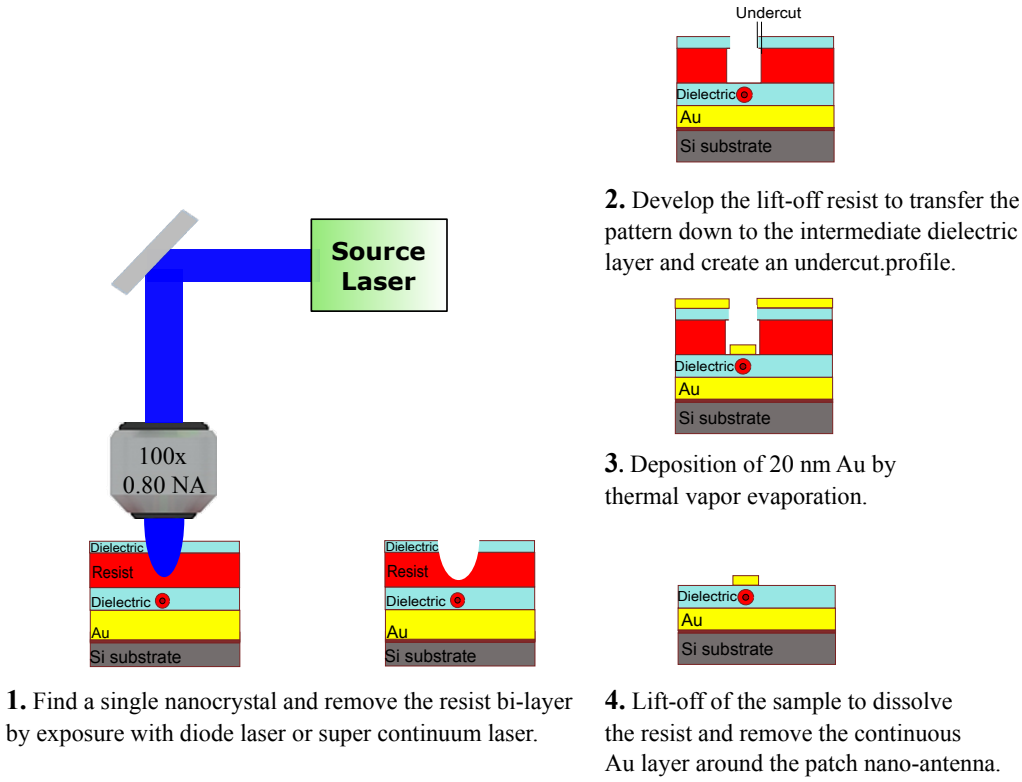

Fig. IV.2 *Schematic representation of the in-situ lithography protocol.*

2 seconds.

Figure IV.3 presents the topographic characteristics in atomic force microscopy of one hole of the matrix. From the image, we can observe how the diode laser has evaporated the resist bi-layer and created a well-defined circular hole. The lateral profile of the Figure IV.3a indicates a diameter of 1.17 μm on the top of the sample (upper PMMA layer) and a smaller diameter of 600 nm. The line profile of Figure IV.3a shows a pretty flat zone in the center of the hole, which suggests that the laser has reached a flat surface.

Figure IV.3b depicts the line traces around the hole. By averaging out all the traces we have found a depth of 190 nm. We would have expected a hole height between 300-350 nm which correspond to the sum of the upper PMMA and the LOR layer (320 nm LOR3A + 15 nm PMMA). In topographic image we observe that the height barely reaches 200 nm, much less than the total thickness expected from resist bi-layer. Several hypothesis can be considered. In the first hypothesis the power of the laser beam is not sufficient to obtain higher depth to drill a hole (due to scattering). Another hypothesis is based on the fact that the lower part of the LOR3A layer is mixed with PMMA layer which diminish the absorption properties and make it more difficult to drill. Therefore, there exist the possibility that the laser exposure has stopped in the lift-off resist layer (LOR3A) or intermediate layers, not at the very bottom.

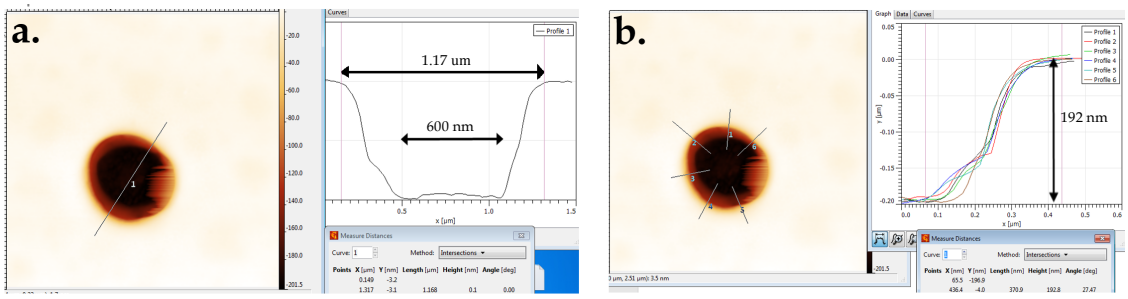

Diameter ^{PMMA}: 1.17 um Depth: 192 nm

Fig. IV.3 *Atomic Force Microscope image of one hole created with the blue diode laser during 2 seconds of exposure time. a) Diameter in PMMA layer, b) Average profile depths of the hole.*

IV.3.2 Development of lift-off resist LOR3A

We carried out the development by immersing the sample first in pure developer MF-319 during 5 seconds and introducing it immediately after in a bath of deionized water. During both baths the sample was held upside down and firmly shaken. The AFM image of the hole after development is shown in Figure IV.4.

In the topographic images of the same hole before and after development, we clearly observe the expansion of the hole on the top of the sample. The profile trace shown in Figure IV.4a indicates the diameter of the initial hole (1.18 μm). In the same Figure IV.4a, we can also observe the presence of a "nano-hill" exactly at the center of the hole. This nano-hill will be further discussed in section IV.5.

From image IV.4a, we can also distinguish the appearance of a transition zone between the initial diameter and the outer edge. This ring-shape pattern has around 900 nm width and a thickness of 20 nm, as it is shown in Figure IV.4b. In Figure IV.4c we present the profile trace of the outer diameter. We can observe that the hole has expanded from 1.18 μm to 2.07 μm, twice the initial size. In Figure IV.4d we show the transition from the ring-shape pattern to the top of the sample. It reaches approximately an height of 170 nm.

Previously, before development process, the total depth of the hole had reached 192 nm. Now, by observing Figures IV.4b and IV.4d, we can note that both depths raise to a value of 190 nm. With the finding of the initial thickness of the hole, and the fact that the developer MF-319 doesn't attack the polymer PMMA, we can conclude that the laser beam has perforated a hole in the upper PMMA layer stopping in the intermediate layer of LOR3A.

From the previous analysis we can assume now that the center nano-hill is actually composed of the same PMMA/LOR mixture dielectric layer. In Figure IV.4e we show the physical extensions, 320 nm in diameter and 12 nm in height. Because its precise position at the center of the hole, we can conclude that the nano-hill is created by the interaction of the stack of layers with the center of the gaussian beam laser during ex-

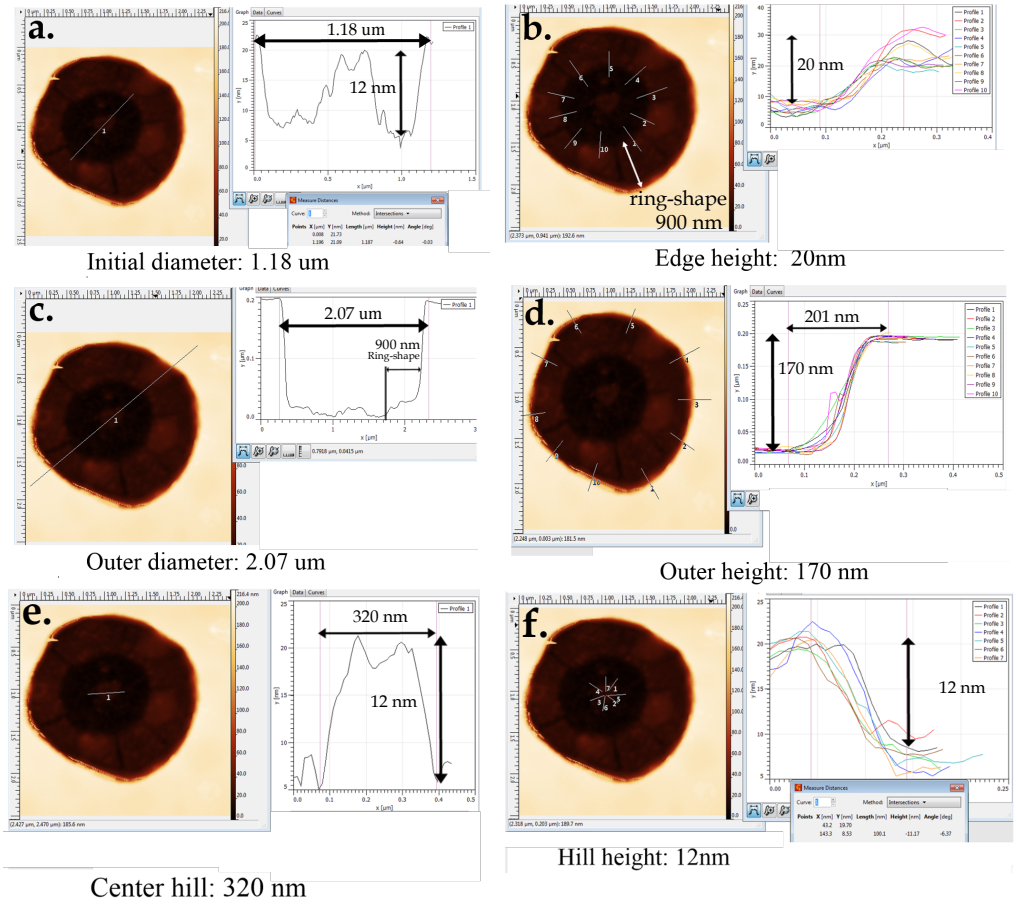

Fig. IV.4 *Atomic Force Microscope image of one hole after 5 seconds of development with pure developer MF-319. a) Traces of the initial hole, b) Profile height from the initial hole to the the ring-shape pattern, c) Traces of the complete hole, d) Profile height from the ring-shape pattern to the top PMMA layer, e) Traces of the center hill and f) Profile average height.*

posure at maximum intensity, which makes it more resistant to the attack of development.

IV.3.3 Thermal deposition of Au film

Following the in-situ protocol, we carried out the deposition of 20 nm-Au layer. In the fabrication of patch antennas, all gold layers were deposited by Physical Vapour Deposition technique (PVD). This technique deposits the material by transforming the target material from bulk-state to vapour by Joule effect. Figure IV.5 shows the general principle of such technique. The target material contained in a filament boat starts heating by passing a high current through it. The heating of the material is conducted via Joule effect that raises the temperature above the equilibrium point of the pressure chamber. The evaporated atoms travel from the filament boat to the surface of the sample where they finally condensate. The growth of the thin films is monitored by a quartz crys-

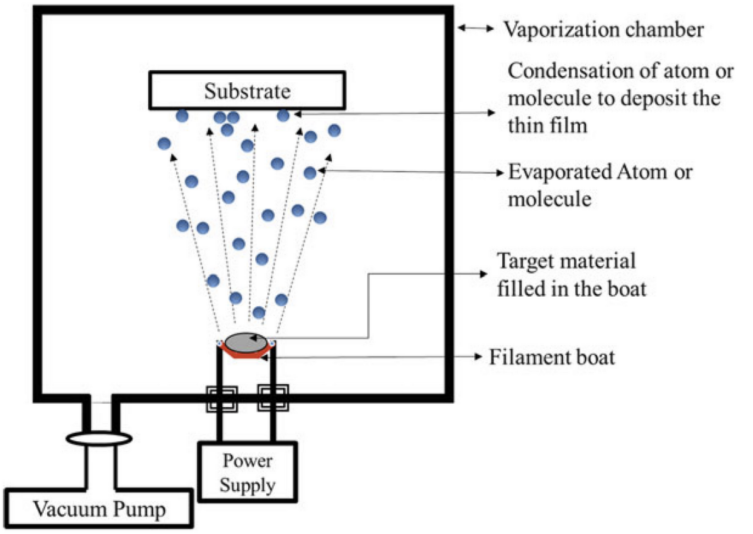

Fig. IV.5 *Schematic representation of thermal evaporation system. Figure adapted from [59].*

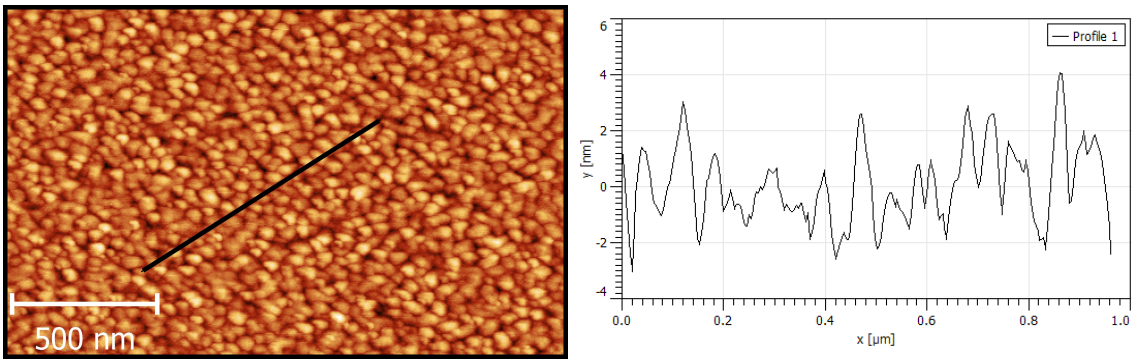

Fig. IV.6 *a) Topographic AFM imaging of 100 nm Au deposited on a substrate of silicium.*

tal microbalance whose frequency of oscillation resonance changes proportionally to the thickness of the deposited layer.

We used a thermal evaporator machine PVD-4E from VINCI technologies. The typical parameters for thermal depositions are 2.5×10^{-6} mBar of pressure in the vacuum chamber and 2.55 Å/s in deposition speed rate. As an example of the quality of the metallic microfilms fabricated with this machine, in Figure IV.6 we show a topographic AFM image of 100 nm-Au layer deposited over a Si substrate. From the Figure IV.6a we can observe that the film is densely nanostructured by nanoparticles which diameter (or grain-binning) reaches around 50 nm. In Figure IV.6b, we show the topographic trace line displaying the variation in height (peaks and valleys) on the surface. The root mean square roughness (R_q) of this film extends to 1.1 nm.

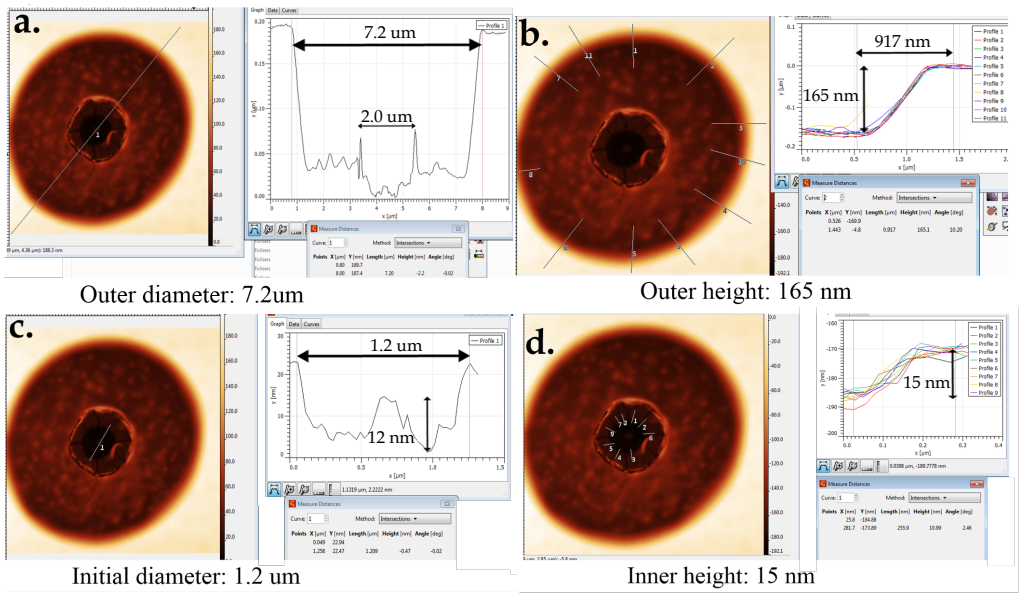

Fig. IV.7 *Atomic Force Microscope image of the same hole after 20 nm-Au deposition and lift-off processing during 50 seconds. a) Traces of the outer diameter, b) Average profile height of the top layer, c) Traces of the initial diameter and d) Profile average height with ring-shape pattern.*

The quality of the gold films deposited by PVD depends on many experimental conditions during vapour deposition. For instance, the vacuum pressure, the speed rate deposition and the supporting substrate are some of them. In a recent experimental paper describing simple rules to improve the quality of most of the metallic microfilms [60], it was emphasized the use of high deposition rates to decrease roughness in metallic thin films.

IV.3.4 Lift-off processing

We have continued with the lift-off processing of the sample. We have immersed the sample in pure MF-319 developer during 50 s. We finally washed the sample with deionized water. The AFM image of the same initial hole is shown in Figure IV.7.

From Figure IV.7a, we can observe the uniform expansion of the hole until 7.2 μm. This signature is a clear indication that the developer MF-319 has entered thorough the undercut of the resist bi-layer and it has dissolved the lift-off resist LOR3A approximately 2.5 μm around the previous hole. From the Figure IV.7a, we can note that the dissolution of the resist was isotropic but not completely homogeneous. From the topographic image we can see some hills and valleys between the limits of 2 μm and 7.2 μm hole.

Figure IV.7b estimates the outer height with respect to the top of the sample. The average of the lines indicates a difference in height of 165 nm. The difference of 5 nm with respect to the outer height found in development step (height of 170 nm in Figure IV.4d),

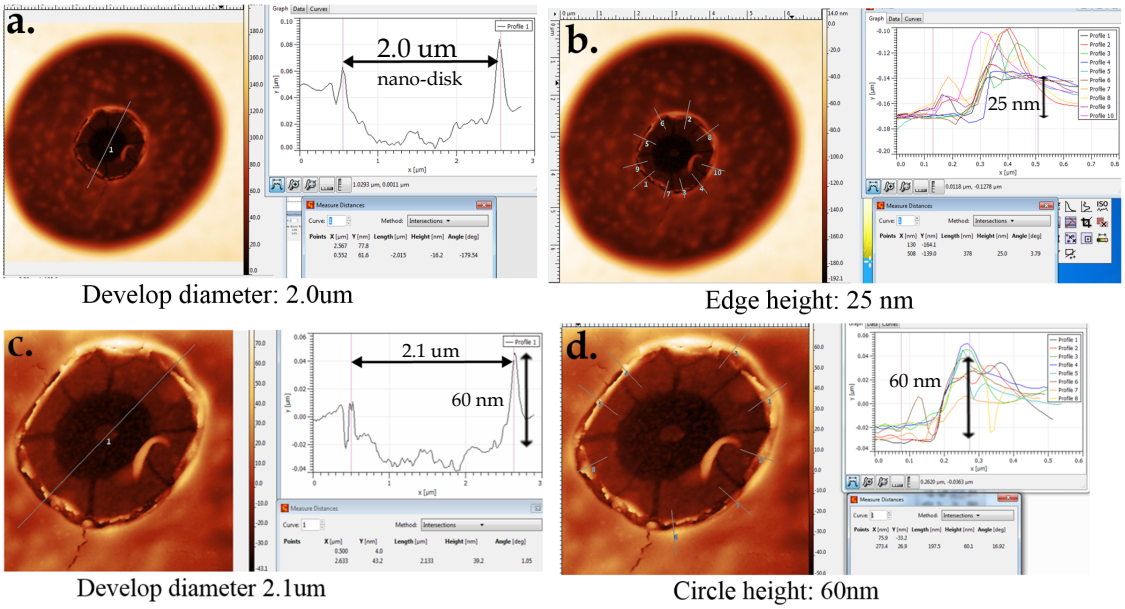

Fig. IV.8 *Atomic Force Microscope image of the same hole after 20 nm-Au deposition and lift-off processing during 50 seconds. a) Traces in the develop diameter, b) Profile average height with outer layer, c) Zoomed AFM image inside the development disk showing the nano-disk and d) Profile average height with upper layer.*

could be attributed to the irregularities due to the hills and valleys mentioned before. We can compare the features of this transition obtained before and after deposition. In the case of Figure IV.4d, the 170 nm step is obtained for 201 nm horizontal variation, whereas in Figure IV.7b, similar height is obtained for 917 nm. Therefore it shows that the deposition of gold and eventual lift-off has smoothed the step.

In Figure IV.7c, we note that the size of the inner diameter corresponds to the initial hole (1.2 μm). From the image IV.7c, we can still observe the presence of the center nano-hill discussed in the previous stage. This suggest that the deposition of the 20 nm-Au patch has followed the topography of the surface and the lift-off processing has not affected the ring-shape pattern and the nano-hill. In Figure IV.7d, we show the height of the ring-shape pattern. The average of the profile lines estimates a height of 15 nm in thickness.

Figure IV.8a shows the AFM image but now by considering the nano-disk created in the previous development process. We should remind that the final size of the nano-disk is actually delimited by development process. Thus, the patch has a diameter of 2.0 μm according to the line traced in Figure IV.8a. Figure IV.8b shows the average height profile with the outer layer. From the profile height we can observe that the 2 μm diameter patch is circled by an abruptly outline of possibly residues of lift-off resist with 25 nm height.

In order to observe the fine details of the nano-disk, we have carried out a second

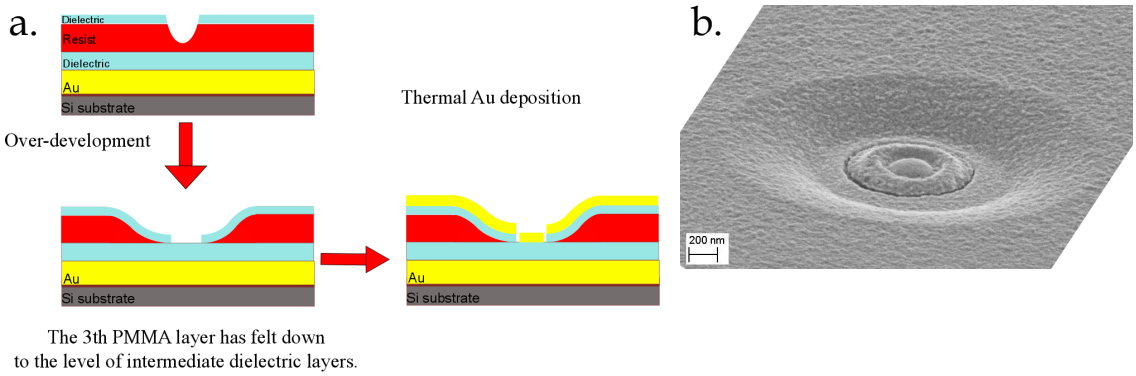

Fig. IV.9 *Over-development scenario where the upper dielectric layer has felt inside the hole. a) Schematic representation after development and thermal Au deposition. b) Scanning electron image. SEM image adapted from [61]*

topographic image zooming the center part. In Figure IV.8c we present the amplified topographic image where we can clearly distinguish the ring-shape pattern with radial cracks and the center nano-hill previously discussed. Inside the 2 μm diameter circle, we can observe the ring with radial cracks. We presume these cracks are contained inside the dielectric material which has been shielded during the metal deposition process. Therefore, we believe that it corresponds to the thin layer of PMMA. During development process, as the time of development has been too large (over-development), the lower LOR3A layer has remained and the upper PMMA layer has felt inside the hole. So, during the evaporation process both materials have been recovered by the gold layer.

In Figure IV.9 we show the case of an over-development antenna. When the development time is too large, the upper PMMA layer fall and collapse inside the hole and then, during thermal evaporation, the thin metallic layer is deposited in the continuous dielectric layer.

From the nanometric analysis in topographic images presented above, we have evidenced the different modifications in the stack of layers during the in-situ lithography protocol. We have observed that the initial hole of 1.2 μm in diameter has been expanded to 2.0 μm after development process. We have also observed the appearance of a dielectric ring-pattern with 20 nm in thickness (Figure IV.4b).

In order to discard the over-development case, we have performed the same AFM topographic analysis in a second sample reducing the development time in order to identify the origin of the ring-shape pattern and optimize the lithographic parameters for future fabrications.

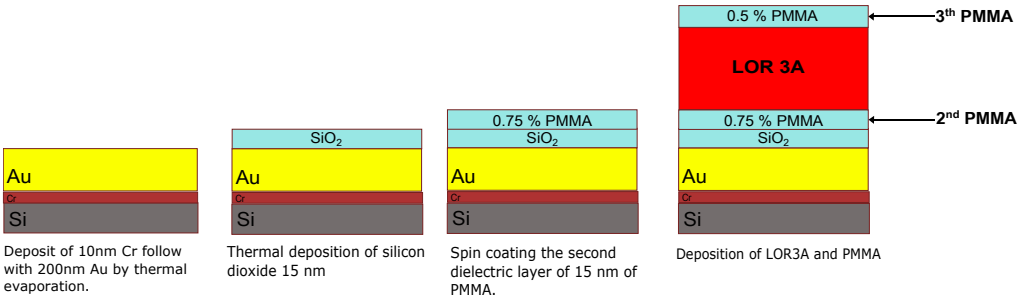

Fig. IV.10 *Schematic representation of the sample prepared for In-situ protocol.*

IV.4 Optimization of the whole process by adjusting development and lift-off processing times

The previous sample has allowed the identification of critical situations during development and lift-off processing. In the following section, we will present a second sample where we will use shorter development time for avoiding over-development and collapsing of the upper layer.

IV.4.1 Preparation of the sample

We have prepared a second sample replacing only the first dielectric layer as it is shown in the Figure A.6. The deposition of all the remaining layers was performed as follows:

1. Deposit of silicon dioxide. We deposited 15 nm of silicon dioxide by thermal vapor deposition. This layer plays the same role as the previous PMMA layer.

2. Deposit of PMMA layer. We spin-coated 0.75% of PMMA with 4000 rpm (spin speed), 2000 rpm/s (acceleration) during 45 s. This concentration gives a layer of around 15 nm thickness. We baked the layer at 150^0C during 2 min.

3. Deposit of lift-off resist layer. We spin-coated LOR3A using 4000 rpm/s, 2000 rpm/s during 45 s. These parameters provide a thickness of 330 nm thickness. We baked the sample 150 ^{0}C during 2 min [3].

4. Deposit of PMMA layer. We have successively spin-coated a solution of PMMA with 0.5% concentration. We have used the same parameters as the LOR3A layer: 4000 rpm/s, 2000 rpm/s and 45 s. The thickness of the thin dielectric layer reaches 10 nm. We have baked the layer at 150 ^{0}C during 2 min.

IV.4.2 Laser exposure

For the creation of holes, we have used the same parameters of intensity and exposure time than the previous sample (diode laser 5.4 mW in continuous mode and 2 seconds

[3] In section IV.7.4 we will discuss more in detail the influence of baking the lift-off resist layer.

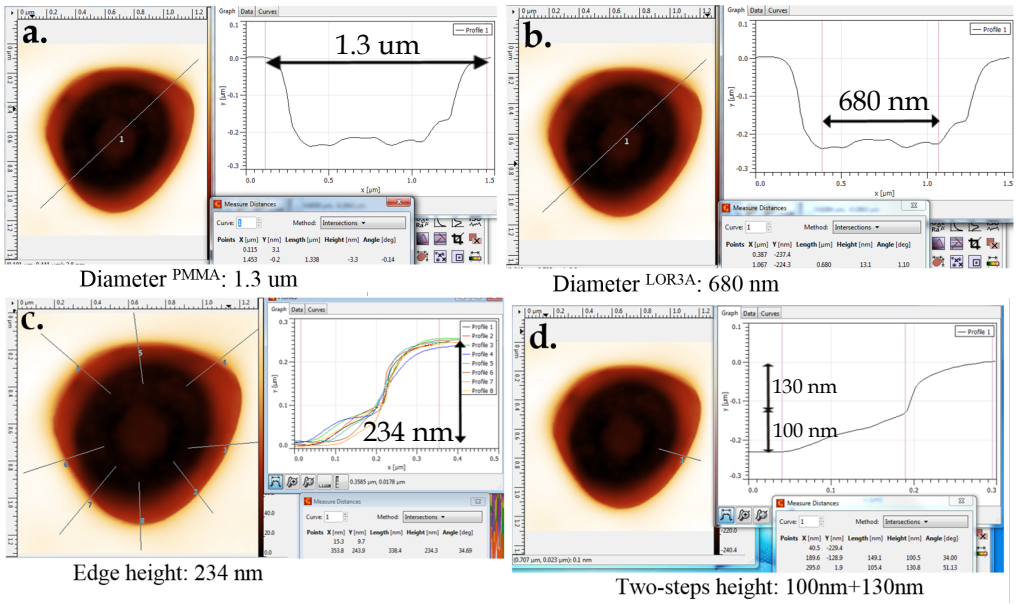

Fig. IV.11 *Atomic Force Microscope image of one hole created with the blue diode laser during 2 seconds of exposure time. a) Diameter in PMMA layer, b) Diameter in lift-off resist LOR3A, c) Traces of the center hill and d) Traces of the hill height*

exposure time). The topographic AFM image of the initial hole is shown in Figure IV.11

From the Figure IV.11a we can observe that the hole diameter on the upper PMMA layer reaches about 1.3 μm. Meanwhile, at the bottom of the hole, the diameter reduces to 680 nm (Figure IV.11b). In Figure IV.11c, we show the average height of the hole (234 nm in total height). These characteristics of the hole are very similar with respect to the previous sample, suggesting a good reproducibility during the exposure step. Figure IV.11d shows a single profile trace from the center of the hole to the top PMMA layer. We clearly note two-steps slopes between the top of the sample and the bottom of the hole. The first step comes up to the first 130 nm height. The second step reaches the remaining 100 nm. This two-steps slope may be due to the partial falling of the PMMA layer at the edge of the hole not sustained any more by the LOR3A layer beneath, which makes the first 130 nm step more thicker.

In Figure IV.12a, we show the profile trace at the center of the hole. We can identify the "center hill" observed also in the previous sample. In this case, the "center hill" has a diameter of 345 nm and a height of 20 nm. Because the symmetric characteristic of the hill and the well-defined ring surrounding it, we can certainly assure that this sub-wavelength structure is created during the high intensity exposure of the blue laser with the intermediate PMMA layer.

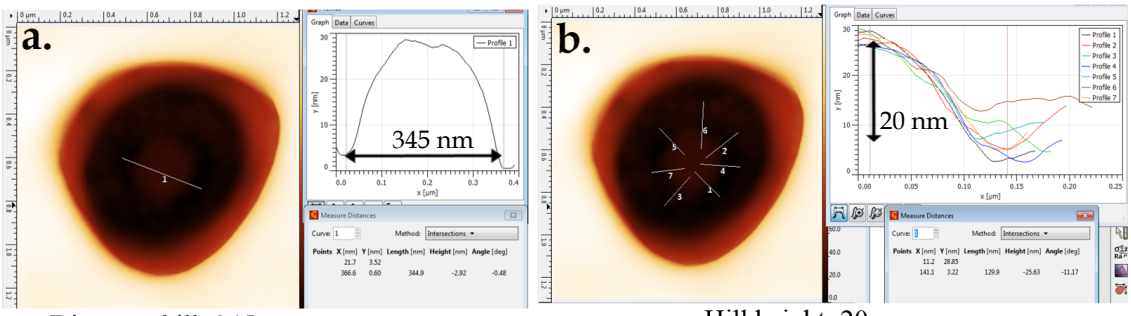

Fig. IV.12 *Atomic Force Microscope image of one hole created with the blue diode laser during 2 seconds of exposure time. a) Traces in the outer edge and b) One trace to show the two-steps height.*

IV.4.3 Development of lift-off resist LOR3A

We have continued then with the development process of the lift-off resist. Based on previous results attained with the first sample, we have now reduced the development time between 3 and 4 seconds using pure developer MF-319. The results in AFM microscopy are shown in Figure IV.13.

Figure IV.13a shows the uniform expansion of the hole from 1.3 μm to 1.8 μm. This

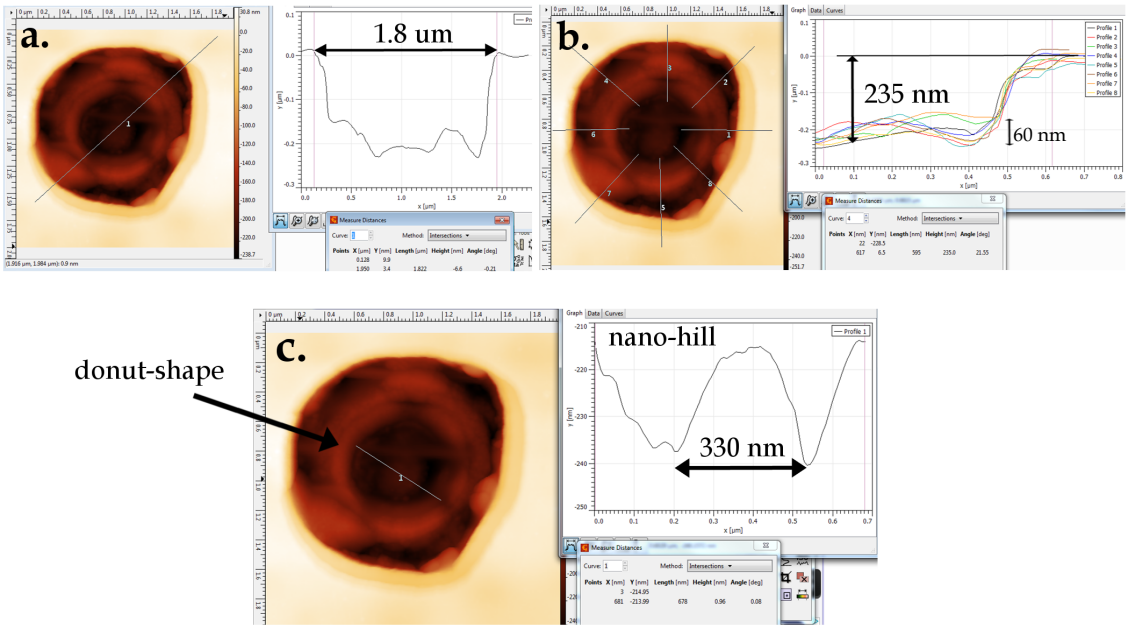

Fig. IV.13 *Atomic Force Microscope image of one hole after development process with developer MF-319 between 3-4 seconds. a) Single trace of the complete hole, b) Average of traces around the edge to estimate the height and c) Single trace with the diameter of the initial size hole in LOR3A (680 nm).*

expansion has to be compared with results of Figure IV.4 after development. In the first sample, the hole has increased from 1.18 μm to 2.07 μm (75 %). Here, the enlargement of the hole from 1.3 μm to 1.8 μm corresponds nearly 38 % of the initial size. Figure IV.13b depicts, by traces around the hole, the average depth of 235 nm, close to the initial height. Once again, the depth of the second sample is not very different from the depth reached in the first sample (190 nm). Here we can verify that the depth doesn't reach the full thickness of the LOR3A layer which is supposed to be 330 nm, approximately. Either the LOR3A layer is thinner than expected, or we have at the bottom of the layer a mixing of PMMA/LOR which make it more resistant to development.

In Figure IV.13c, we show a line trace crossing the center of the hole. From the image we can distinguish again a dielectric nano-hill with 330 nm in diameter and 24 nm height. The Figure IV.13c also shows the creation of a thick donut-shape around the nano-hill. We use the blue laser beam which is absorbed by the LOR3A layer producing a heating of the local area. This heating melts the thin upper PMMA layer and creates a hole. The maximum of energy and maximum of heating are both at the center of the laser beam. In the bottom of the LOR3A layer, assuming we have a mixing between PMMA and LOR layer, the absorption of light and consequently the hole making are more difficult. We have heated only the material in the bottom layer, specially at the center of the beam, which makes LOR3A layer more resistant to the developer MF-319. Therefore, we have a nano-hill in the center. When we compare this nano-hill with the one obtained in IV.4f, we can notice that the height is larger here. Indeed, the development time in the second sample is shorter than before, which let less time for attacking the nano-hill. In both cases, the lower diameter of the nano-hill is comparable (300 nm).

The Figure IV.13c also shows the creation of a thick donut-shape around the nano-hill. We will discuss now the origin of this pattern. As the development time in this second sample was shorter, we suppose it was not sufficient time to remove all residues remaining close to the nano-hill. Note that, for the first sample with a larger development time, this donut-pattern and residues were not observed. It means that, the heating of LOR3A tends to solidify the film (become denser) and the solvent MF-319 needs more time to dissolve the material.

In the analysis of the AFM images, we cannot assure the presence (or absence) of the undercut in the resist bi-layer. The undercut is localized beneath the upper PMMA and the LOR3A resist and therefore can not be seen by AFM microscopy. The expansion of the hole directly depends on the capacity of the solvent MF-319 to dissolve the volume of LOR3A layer. The undercut opens the way to lift-off processing.

IV.4.4 Gold deposition and lift-off processing

Continuing with the protocol we carried out the deposition of the 20 nm-Au film. Then, we have performed lift-off processing submerging the inverted sample in the developer MF-319 during 120 seconds (double time with respect to the previous sample). The AFM image is shown in Figure IV.14.

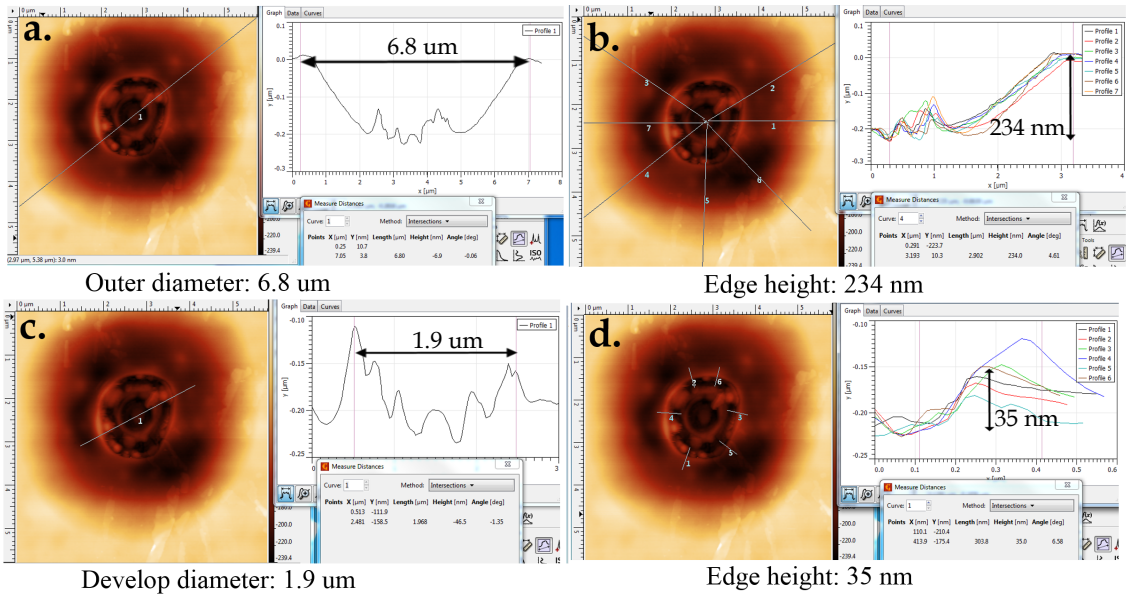

Fig. IV.14 *Atomic Force Microscope image of the same hole after 20 nm-Au deposition and lift-off processing during 120 seconds. a)Traces in the outer diameter, b) Average height of outer layer, c) Traces in the develop diameter and d) Average height with upper layer.*

From the IV.14a, we can observe the homogeneous expansion of the hole from 1.8 μm to 6.8 μm. Figure IV.14b shows the average height from the top layer to the center. This height of 234 nm is similar to the total height found after development (Figure IV.13). The image also shows the moderate slope between the top and bottom layer due to the continuous film of gold.

If we compare the expansion of the hole after lift-off processing for both samples, the first from 2.1 μm to 7.2 μm and the second from 1.8 μm to 6.8 μm, we can realize that both expansions are quite comparable, even thought the second sample was immersed for the double of time. This unexpected situation suggests that, during the lift-off processing, the upper PMMA layer not sustained by the LOR3A layer has spread in the bottom of the hole. Therefore, it has blocked the entrance of the MF319 solvent and stopped the lift-off.

Figure IV.15 compares the topographic AFM images before and after gold deposition and lift-off processing. We can observe that, after 120 seconds of lift-off processing, both the dielectric nano-hill and the residual donut-shape motifs are still present after the deposition of 20 nm-Au film. Nevertheless, as far as the donut-shape is concerned, we can clearly note that the outer part of the donut-shape has been dissolved during lift-off processing.

By observing the lower part of Figure IV.15b, we can identify some dark slashes radially aligned to the center of the hole. In Figure IV.16, we show a profile line between

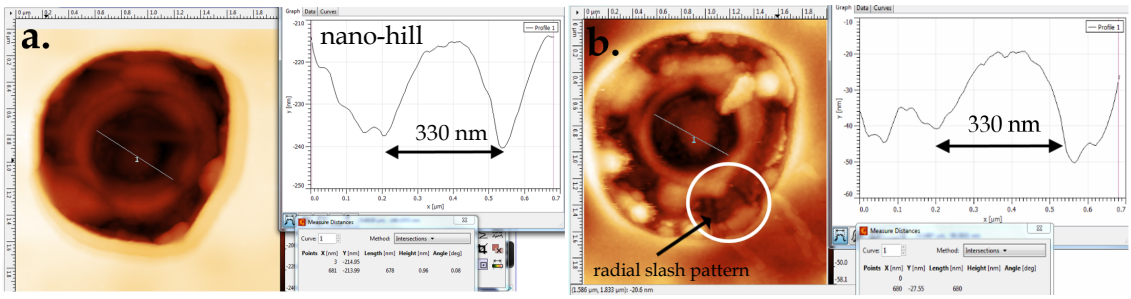

Fig. IV.15 *Atomic Force Microscope image a) After development stage, b) After 20 nm-Au deposition and liftoff (120 s). The trace was extended to the initial hole diameter in the bottom of the lift-off resist LOR3A (680 nm).*

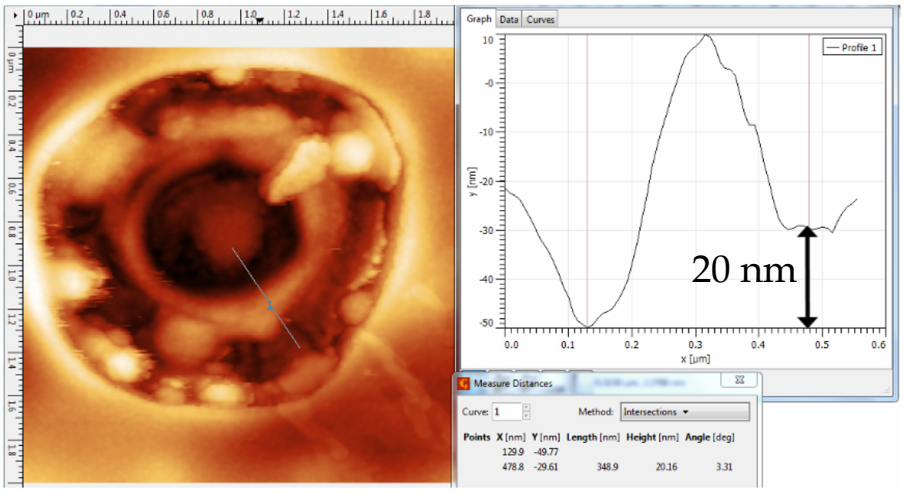

Fig. IV.16 *Atomic Force Microscope image after gold deposition (20 nm) and liftoff (120 s). c) Single trace with the difference in height from the deep dark ring to the layer containing the slash pattern.*

the center of the hole and the radial slash pattern to estimate the thickness. From the difference in height we can calculate a thickness of 20 nm corresponding to the thickness of the intermediate PMMA layer. This characteristic pattern has been detected in the previous sample after development (see Figure IV.4) and after lift-off (see Figure IV.8a and d). For the second sample, we have observed it just after lift-off. As well in the second case, on the contrary to the first one, we didn't observe those slashes after development, which may be due to the fact that the development time was shorter.

The lift-off process in both samples have demonstrated that the expected undercut was created in the resist bi-layer. The expansion of the hole during the lift-off processing was a sign that the undercut was achieved. The success of the lift-off shows that, as long the upper PMMA has not felt inside the hole and blocked the entrance to MF-319, the lift-off remains efficient.

IV.4.5 Drilling the resist bi-layer

After the tracking of one hole during the complete In-situ lithography protocol, we have found that the long exposure time of the blue laser creates the hole in the resist bi-layer. We have found similar results in the exposure with the super continuum laser (Appendix A).

In optical lithography, there is always a trade off between time and intensity power during exposure of the resist bi-layer. We can drill a hole at least in two different approaches based on the control of the main parameters, power and time. The first approach is based in the reduction of the optical power and the increase in exposure time. The second approach consists in increasing the laser power and reducing the exposure time. In the present thesis we have performed both approaches in order to control the drilling of the hole and to avoid damage of intermediate dielectric layers.

IV.5 In-situ optical lithography: dielectric nano-hill

In this section, we will reduce the optical power of the blue laser and increase the exposure time to perforate the resist bi-layer. The aim of this fabrication is to identify the minimum time for which the laser traverse solely the resist bi-layer without affecting intermediate dielectric layers.

IV.5.1 Preparation of the sample

We cleaned the surface of a glass coverslip with acetone and isopropanol. We then put the sample in ozone plasma cleaner during 30 min to remove contamination. Once we have attained the maximum cleanliness of the glass surface, we proceeded to the deposition of the dielectric thin-films as follows:

1. Deposit of quantum dots. We start by depositing single nanocrystals over the bare coverslip with a suitable dilution rate. The reason for including quantum dots was to observe the fluorescence emission of the nanocrystals through the ocular of the microscope and determine a reference plane when performing the drilling of hole during the protocol.

2. Deposit of first PMMA layer. We covered the nanocrystals with a solution of PMMA with 0.75% PMMA of concentration. This concentration gives around 25 nm thickness when it is spin-coated at speed spin of 4000 rpm, acceleration 2000 rpm/s during 45 s in the spin-coater.

3. Deposit of resist bi-layer (LOR3A + PMMA). We spin-coated first the lift-off resist LOR3A using 4000 rpm in spin speed, 2000 rpm/s as acceleration and 45 s in time.

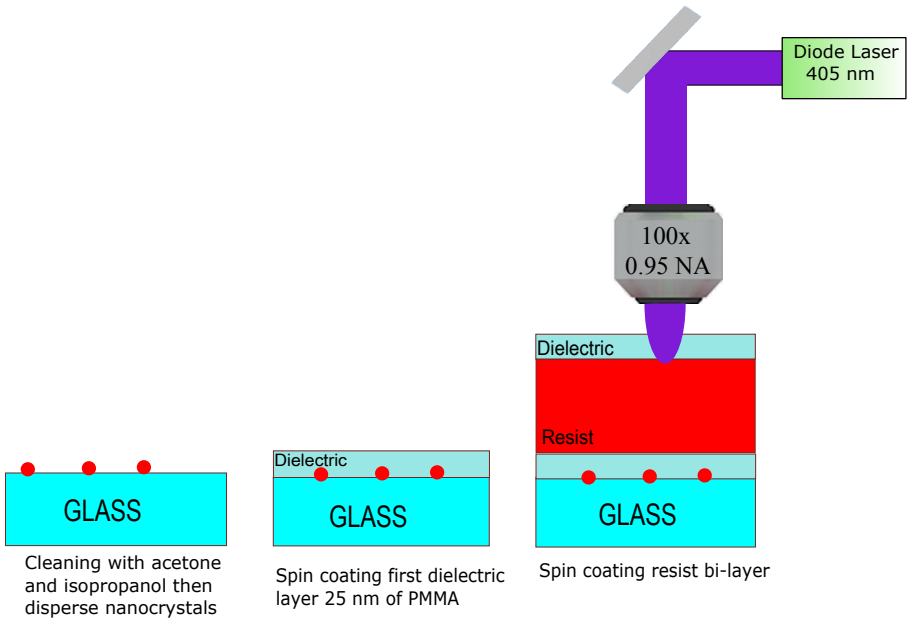

Fig. IV.17 *Schematic representation of the sample prepared for In-situ protocol.*

We baked the layer at 150 ^{o}C during 2 min [4]. We have then spin-coated with similar parameters a solution of PMMA with 0.75% of concentration. These parameters give a layer thickness of 330 nm and 25 nm for LOR3A and PMMA, respectively. The combination of both layers is called resist bi-layer. Most of the interaction between optical radiation and dielectric layers occurs on the top of these layers.

Figure IV.17 shows a schematic representation of dielectric layers on the sample and shows the principle of operation used for in-situ technique. The blue diode laser is absorbed by the lift-off resist layer which heats the upper PMMA layer and creates a well-defined circular holes on the top of the stack of layers. The drilling of holes was obtained using the blue diode laser in continuous mode with an average power of 0.71 mW measured before the microscope.

IV.5.2 Laser exposure

We have consecutively created matrices with different exposure times keeping the same focus plane on the nanocrystals. Figure IV.18a shows a color fluorescence reflection image of the sample observed through the ocular. From the image, we can distinguish the array of matrices surrounded by the red fluorescence background of the lift-off resist LOR3A. The matrices are arranged accordingly to the exposure time, from 4 s until 15 s (right to left). We can note the presence of a fluorescent ring around each hole. The higher fluorescence is due to the modification of the LOR3A layer. It is a signature of hole

[4] In previous developments of the In-situ protocol, it was found the importance of baking the resist bi-layer to avoid blending between resist and upper-layers. In section IV.7.4 we will discuss more in detail the influence that baking bring to the dielectric bottom-layers.

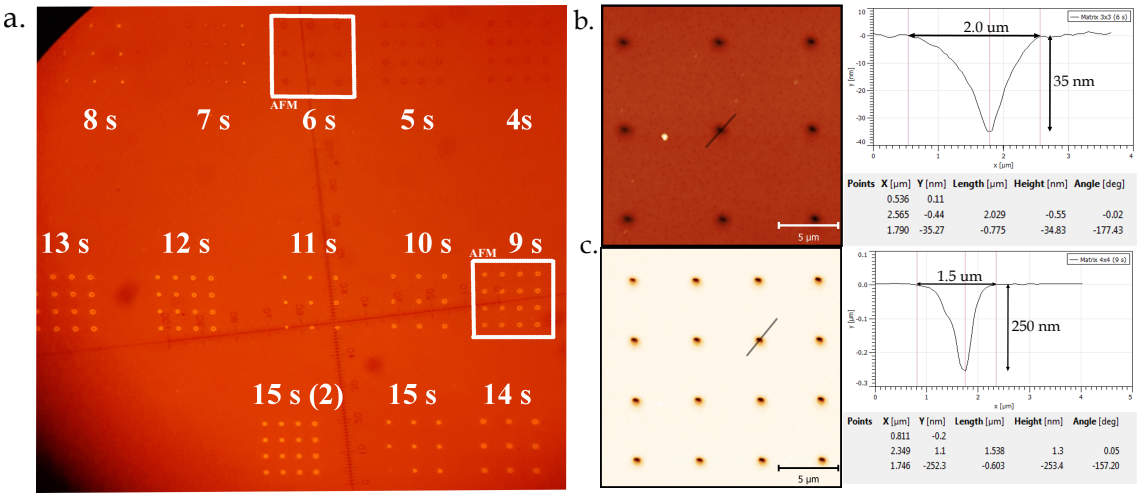

Fig. IV.18 *a) Confocal fluorescence images after hole making with diode laser using 0.71 mW and an optical objective of 0.95 NA. b) AFM imaging of the matrices* 3×3 *(6 s) and* 4×4 *(9 s) as it is shown on the fluorescence image.*

making. The first three matrices (4 s, 5 s and 6 s) don't exhibit signatures of drilling the resist bi-layer, since not fluorescence light is observed around the hole. For the rest of the matrices, the fluorescence ring is present. In conclusion, the fluorescence image of Figure IV.18a suggests that the time threshold to perforate a hole in the resist bi-layer lays between 6 and 9 seconds.

In order to confirm the drilling of the resist bi-layer when observing through fluorescence imaging, we have carried out atomic force microscopy topographic imaging in the matrices before and after the appearance of fluorescence ring around the hole. Figure IV.18b shows AFM imaging of the 3×3 matrix with 6 s, while Figure IV.18c shows for the 4×4 matrix with 9 s of exposure time.

From Figure IV.18b we can observe the line profile of an individual hole of the matrix 3×3 (6 s). The penetration depth of the hole reaches 35 nm, close to the thickness of the upper PMMA layer (25 nm). Meanwhile, the line profile of Figure IV.18c estimates a penetration depth of nearly 250 nm for the matrix 4×4 (9 s). Because the total thickness of the stack of layers reaches around 380 nm, 25 nm (0.75 % PMMA) + 330 nm (resist LOR3A) + 25 nm (0.75 % PMMA), we can then conclude that the laser has created a hole in the resist bi-layer and a portion of the lift-off resist LOR3A layer without drilling the complete stack.

IV.5.3 Development of lift-off resist

We continue with the development process of the sample by immersing it in pure MF-319 during 5 s. Figure IV.19a shows the optical reflection dark-field image of the same sample after development. From the image we can observe that, all the holes with 9 s of exposure

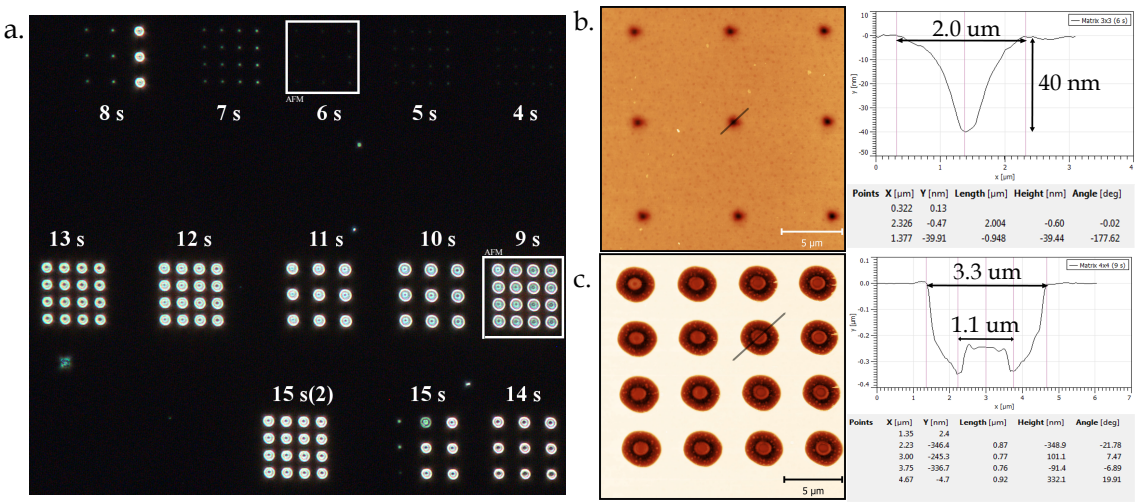

Fig. IV.19 *a) Reflection dark-field image after development in pure MF-319 during 5 s. b) Topographic AFM images of the 3×3 matrix exposed in 6 s. a) Topographic AFM image of the 4×4 matrix exposed in 9 s. At the center of the hole we observe a dielectric nano-hill with 100 nm thickness and 1.3 µm in diameter.*

time and longer times have all expanded homogeneously after development process. In the case of the matrix with 8 s of exposure time, we can note that only three holes show signatures of development. The exposure time of 8 s is close to the threshold of drilling a hole in the resist bi-layer. For some other holes of the same 8 s matrix, the expansion has not been observed, the holes are too small to let the MF-319 developer come inside. For the matrices with lower exposure time, no signature of development is observed. These results confirm our assumption that the low intensity radiation of the laser requires more than 9 s to perforate a hole in the resist bi-layer which gives entrance to the developer MF-319.

Figure IV.19b shows the AFM imaging of the 3×3 matrix with 6 s. From the image, we can observe that the height of the hole has not been affected after development. The absence of a clear entrance in the resist bi-layer has prevented the developer to attack the lift-off resist layer. On the other hand, on the Figure IV.19c corresponding to the 4×4 matrix with a exposure time of 9 s, we can note the homogeneous expansion of the holes to about 3.3 μm at the top layer. We can also note in the image, the presence of a dielectric flat nano-hill of approximately 1.1 μm in diameter and 100 nm thickness at the bottom of the initial hole.

So far, we have found the minimum exposure time to drill the upper resist bi-layer. Nevertheless, the developer has not completely removed the lift-off resist inside the hole. The appearance of a solid dielectric nano-hill in the center it seems to be very resistant to the developer. These nano-hills are obtained for all the matrices with longer exposure times. Because of their precise position in the center of the hole, we can assure that they were created by chemical modifications of the materials induce by the 405 nm diode laser.

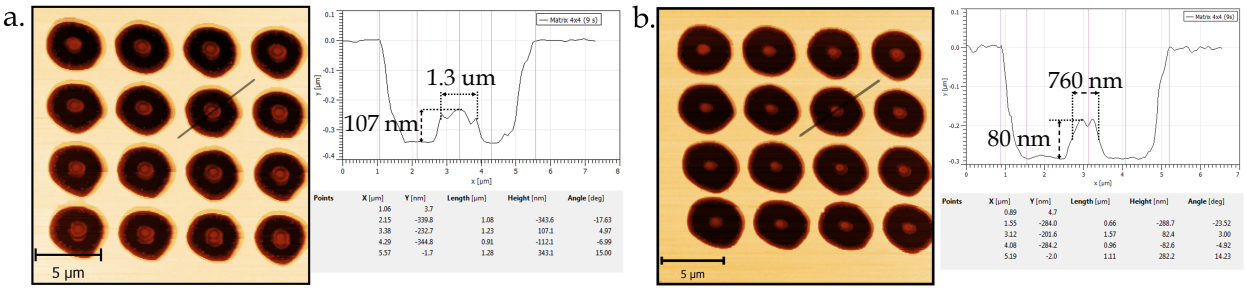

Fig. IV.20 *AFM image of the* 4×4 *matrix (9 s of exposure time) after oxygen plasma processing in a) 5 minutes and b) 10 minutes.*

The lateral resist around the nano-hill, has not suffered such chemical modification and it has been dissolved during the first development, as it is shown in the profile view of Figure IV.19c.

IV.5.4 Photopolymerization of the resist bi-layer

The irradiation with the blue laser using low power has lead to the achieving of a dielectric nano-hill after development. During the low power radiation, the lift-off resist has experienced chemical modifications becoming more dense and solid. This process is called photopolymerization. The results when exposing the resist bi-layer with the laser during several seconds has turned out to polymerize the materials resulting in dielectric nano-hills shown in Figure IV.19c.

We have proceed with a second development process using pure MF-319 during 5 s. We have then performed a treatment by oxygen plasma cleaner at 30 W of RF power. In Figure IV.20 we show topographic AFM images of the same matrix (4×4 matrix with 9 s in exposure time) after 5 minutes and 10 minutes in oxygen plasma, respectively. From the height profile in Figure IV.20a we can observed that the thickness of the nano-hill remains around 107 nm respect to the flat lateral surface. These results confirm the morphological characteristics of the nanostructure and demonstrate the high-resistance of the material after 5 minutes in oxygen plasma.

In Figure IV.20b, we show the same dielectric nano-hill after additional 10 minutes in oxygen plasma. We can observe that the diameter has been reduced to 760 nm (approximately the half of the initial size). Similarly changes have been observed in the thickness of the nano-hill which has reduced to nearly 80 nm. We demonstrated that the use of plasma oxygen cleaner opens up the possibility to control the diameter and thickness of the dielectric nanostructures.

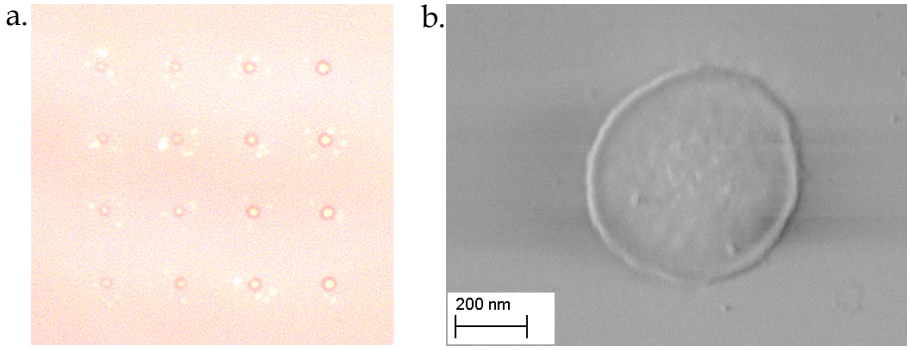

Fig. IV.21 *a) Optical brightfield image of dielectric nano-hills created during 15 s of exposure time. b) Scanning electron image of a single nano-hill belonged to the same matrix. The structure has a diameter of 596 nm.*

IV.5.5 Lift-off processing and characterization of nano-hills

We have proceed with the lift-off processing by immersing the sample into pure MF-319 during 10 min until dissolving the lift-off resist layer completely. We have characterized the dielectric nanostructures by optical reflection imaging and scanning electron microscopy. Figure IV.21a shows the reflection brightfield image of the 4×4 matrix obtained with the longer exposure time (15 s) with the blue laser. Figure IV.21b displayed the SEM image of one of these nano-hills. The diameter has extended to 596 nm.

We now consider the 3×3 matrix created with 8 s of exposure time. This matrix corresponds to the shortest time for drilling holes according to the optical image shown in Figure IV.19. We have just obtained 3 real holes over 9 in this matrix, as it is observed from the image. In Figure IV.22a, we present the optical dark-field image of such matrix after lift-off processing. From the optical image, we can observe the scattering of a blueish light coming from the three dielectric nanostructures. Figure IV.22b shows the scanning electron image of a nano-hill whose effective diameter extents to roughly 300 nm.

The 8 seconds used to expose the 3×3 matrix represents the threshold time in drilling holes on the resist bi-layer. When we work in threshold conditions, we can expect different results depending on the fluctuations in the optical laser or slight displacements of the piezo-electric stage during the exposure time. In this 3×3 matrix, we have obtained only three dielectric nano-hills of 300 nm width, as it was shown in Figure IV.22a. Nevertheless, these nanostructures represent the smallest nano-hills fabricated by this optical technique.

We have used an optical objective with 0.95 NA. The size of the laser spot registered by the CCD camera extends to approximately 460 nm, as it is shown in Figure IV.23. The diameter of the spot is clearly larger than the smallest nano-hill of 300 nm presented in Figure IV.22b. So, we can achieve dielectric nanostructures with sub-wavelength lateral sizes by performing the optical protocol presented in this section.

In conclusion, performing optical lithography at low optical power is at the origin of

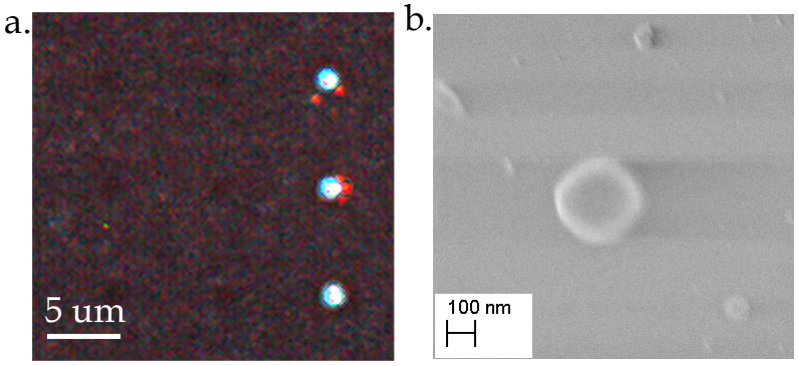

Fig. IV.22 *a) Optical dark-field image of dielectric nano-disks created during 8 s of exposure time. b) Scanning Electron Image of the middle nano-hill showing a diameter around 300 nm.*

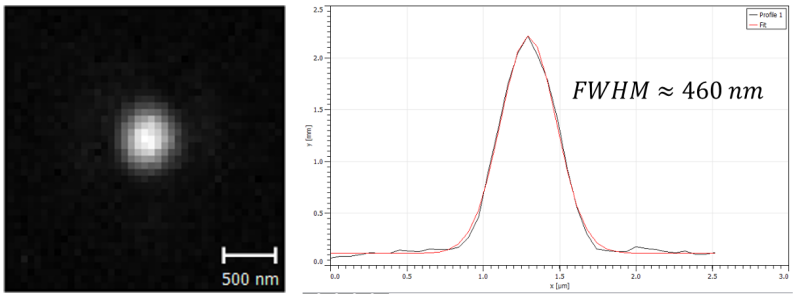

Fig. IV.23 *CCD reflection image of the spot diode laser (405 nm) using 100× objective with 0.95 NA.*

the appearance of sub-wavelengths nano-hills due to the interaction of ultra-violet light with the resist layer. This technique opens up the possibility to fabricate resistant dielectric nanostructures through photopolymerization of the materials.

The drawback of achieving a dielectric nano-hill at the center of the hole has led us to adopt another approach for drilling a hole in the upper layers: using maximum optical intensity in shorter laps time. In the following section we will address this approach emphasizing some modifications in the concentration of the developer MF-319 to achieve a better control in development processing.

IV.6 In-situ optical lithography: Au nano-disks over glass substrate

We have discussed how the in-situ protocol is based on a laser radiation process which is able to heat, melt and evaporate material of the LOR3A layer and upper PMMA layer to create a hole. In section IV.4.5, we have mentioned two different approaches of drilling a hole. In the previous studies, we have conducted the first approach at low power radiation

for long exposure time. We have found that the low radiation laser turns out to polymerize at the bottom the lift-off resist LOR3A and PMMA layers, creating high-resistant dielectric nano-hills at the center of each hole. In this section, we will discuss the second approach for which we will use high radiation laser in laps times below 1 s. We will use a blue diode laser (405 nm) at maximum optical power in continuous mode (5.2 mW). In the second approach, the interaction between the radiation laser and the resist bi-layer is reduced down to some milliseconds in order to avoid the damage of intermediate layers.

IV.6.1 Preparation of the sample

For the preparation of the glass substrate and the deposition of thin dielectric layers, we have followed exactly the same procedure described in section IV.5.1.

IV.6.2 Laser exposure

In this fabrication, we performed hole making using two optical objectives 100× with different numerical aperture and features in chromatic compensation: 1) 0.95 NA Apochromatic (https://www.olympus-ims.com/en/microscope/mplapon/#!cms[tab]=$%$2Fmicroscope$%$2Fmplapon$%$2F100x), and 2) 0.80 NA Semi-Apochromatic (https://www.olympus-ims.com/en/microscope/lmplfln/#!cms[tab]=$%$2Fmicroscope$%$2Flmplfln$%$2F100x). The exposure time was precisely controlled, ranging from 1 s to 3 ms in order to find the threshold at which the laser drill the resist bi-layer. The intensity of the laser was fixed at maximum in continuous mode operation, around 5.2 mW.

Figure IV.24a shows a confocal fluorescence image of matrices created with 0.95 NA objective for different exposure times. From the image on Figure IV.24a, we can note that every single hole is encircled with an intense fluorescent ring. This fluorescent ring is the result of some photo-chemical reactions of the PMMA material after laser radiation. The ring appears along all the holes independently of the exposure time. From the same Figure IV.24a, we can clearly note the reduction of the fluorescent ring below 10 ms of exposure time. This significant difference may have been due to the short interaction time between the laser radiation with the resist bi-layer.

In Figure IV.24b we show the fluorescence profile of a single hole of the 3×3 matrix (20 ms exposure time). From the fluorescence profile, we can discuss three different points: 1) the intense fluorescence ring around the hole, 2) the level of fluorescence background and 3) the reduction of fluorescence light at the center of the hole due to the partial removal of resist bi-layer after laser radiation (hole fluorescence contrast). The hole fluorescence contrast is observed in all the matrices exposed in times higher than 20 ms. However, for the holes created in 3 ms, 5 ms and 10 ms, it becomes difficult to observe the fluorescence contrast at the middle of the hole, even though the signature of the fluorescence ring is noticeable by fluorescence imaging.

In order to confirm the effective hole making in the 10 ms matrix, we performed AFM imaging as shown in the Figure IV.24c. The profile of the middle hole assures the partially

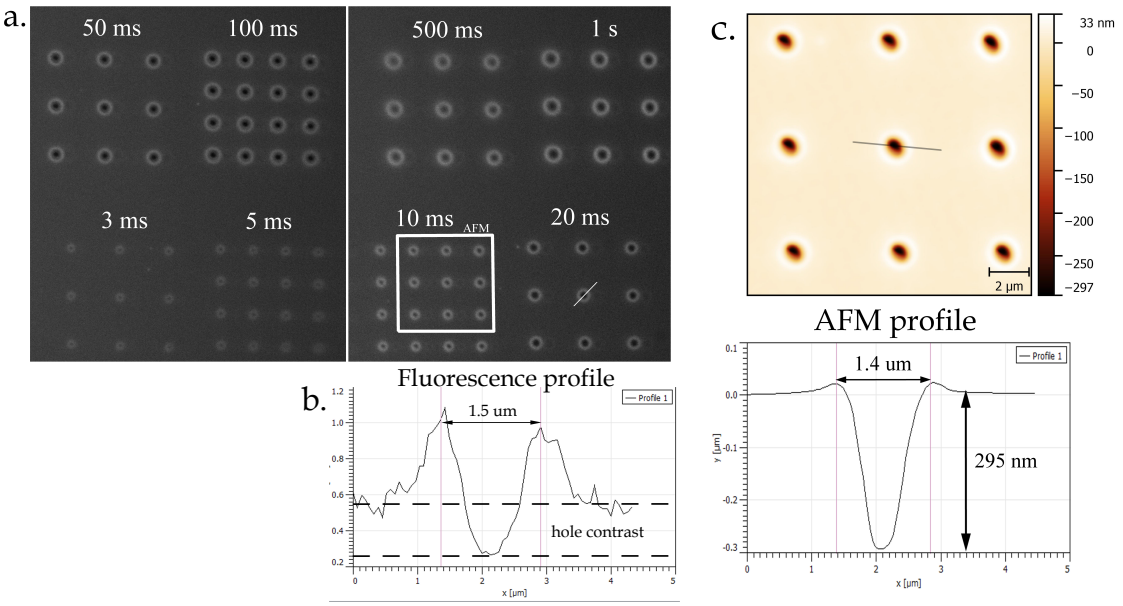

Fig. IV.24 *a) Fluorescence images after the exposure of the resist bi-layer with the blue diode laser (5.2 mW optical power) with different exposures times using an objective* 100× *and 0.95 NA. b) Topographic AFM image and profile of one hole created with 10 ms.*

removal of the resist bi-layer with a penetration depth of 295 nm, still some nanometers distance from the total thickness of the resist bi-layer (355 nm). In the AFM topography of the matrix, we can correlate the fluorescence ring with the small elevation surrounding the hole, corresponding to the contraction of the upper PMMA layer after insulation. The dimensions of this donut hill is about 20 nm higher with respect to the level of the surface and 1.45 μm in diameter (see Figure IV.24c).

In conclusion, using fluorescence and topographic AFM images, we can estimate the threshold time required by the diode laser. The threshold is of the order of 10 ms for a continuous wave laser with average power of 5.2 mW. The energy necessary for drilling a hole is then 5.2×10^{-5} J. We can compare this with the energy required in the previous fabrication. When using 0.71 mW of average power, we found a minimum exposure time of 8 s. This corresponds to an energy nearly 5.2×10^{-3} J, two orders higher than the energy required for low time case. Moreover, we can note that there is not a nano-hill in the center for short irradiation at high power. The topographic image in IV.24c shows a perfect gaussian profile along the hole when the second approach (high power illumination and low exposure time) is performed. Therefore, for fabrication of patch antennas, higher optical power and low time of exposure are preferred, as long as the illumination doesn't photobleach the nanoemitter.

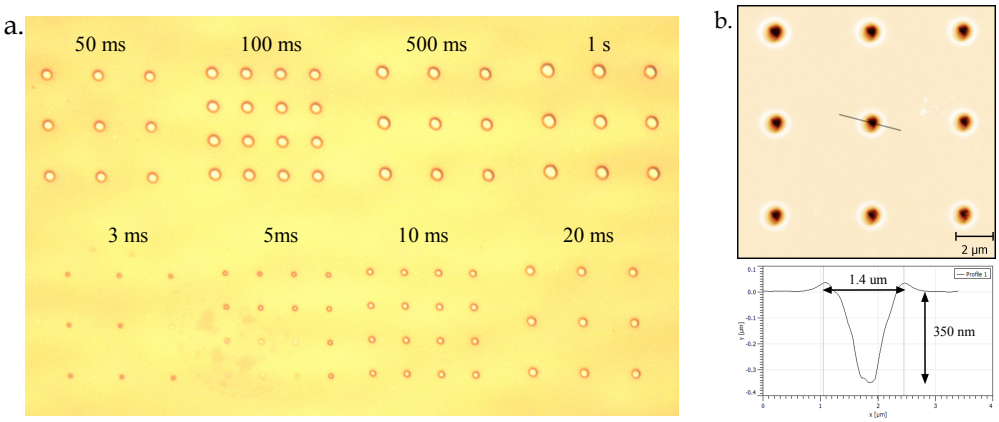

Fig. IV.25 *a) Reflection image after development process (60 s using MF-319 diluted* 1 : 3 *with deionized water) of the holes created with 0.95 NA objective. b) Topographic AFM image of the matrix exposed in 10 ms after development.*

IV.6.3 Development of lift-off resist

We continue the development processing by immersing the sample during 60 seconds into the developer MF-319 diluted with deionized water 1 : 3. It corresponds to 1 portion of pure MF-319 with 2 portions of deionized water. Figure IV.25a shows a reflection image of all matrices after development processing. From the image, we can observe that most of the holes have expanded. The developer MF-319 has attacked efficiently the lift-off resist LOR3A. From the same image, we can also identify that some of the holes were not successfully developed. These cases correspond to the matrices with 3 ms and 5 ms.

At this point we should remind that we use a PDL 800-D laser driver that switches on/off the blue diode laser by the slow gate port. The transition time of this port is around 1 ms, according to the technical specifications of the device (https://www.picoquant.com/images/uploads/downloads/pdl800-d.pdf). The threshold time for drilling a hole is very close to the control time of the electronics, so that the exact control of 1 ms remains questionable. Thus, we can expect different conditions of exposure for the holes belonging to the matrices 3 ms and 5 ms. In conclusion, from the reflection image of Figure IV.25, we can establish the limit of exposure time to 10 ms when using 5.2 mW of optical power.

Figure IV.25b displays the AFM image of the same matrix (10 ms) after development process. The profile of the hole reveals an increase in the hole depth after development of nearly 50 nm, reaching the total thickness of the resist bi-layer (330 nm lift-off resist LOR3A + 25 nm 0.75% PMMA). However, the hole diameter appears quasi constant. These results prove that the developer has selectively attacked LOR3A to the bottom of the hole and it has not affected the upper PMMA layer.

We have observed that the use of MF-319 diluted with deionized water provides a better control during development processing. Under this perspective, we can ensure that the best conditions to develop the tiny holes for matrices with 5 ms and 3 ms are em-

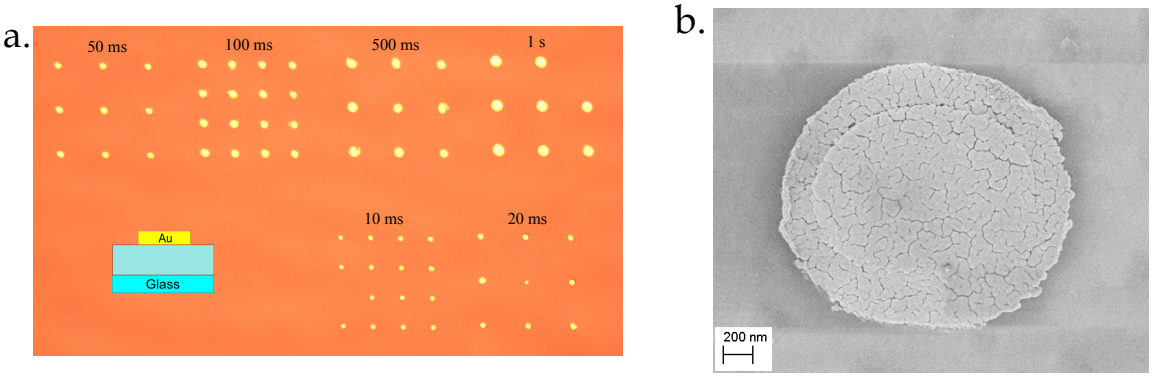

Fig. IV.26 *a) Reflection image of nano-disks over glass substrate fabricated with 0.95 NA objective b) Scanning electron micrograph of one Au nano-disk of 1.80 μm in diameter corresponding to the 3 × 3 matrix 1 s.*

ploying diluted MF-319 (diluted 1 : 3) in a more extended time (longer than 60 s, for instance). For tiny holes, the developer MF-319 will require considerably longer time to dissolve almost all the lift-off resist layer.

IV.6.4 Gold deposition and lift-off

We continue with the thermal vapour deposition, standard parameters in the vacuum chamber: pressure 4×10^{-6} mBar, deposition rate 2.0 A/s. The thickness recorded by the quartz crystal microbalance is 20.6 nm. We finally carried out the lift-off by shaking the sample face down inside pure MF-319 during 15 minutes until we observed the separation of the continuous film of gold from the glass substrate floating on the developer surface.

IV.6.5 Gold nanodisks

In Figure IV.26a, we show the reflection image of the Au nano-disks fabricated with 0.95 NA objective. From the image, we can observe the efficient lift-off processing where only two nano-disks were lost during the procedure. The image also shows the different sizes of the nanostructures respect to the time of exposure.

We characterize the Au nano-disks by Scanning Electron Microscopy (SEM). Figure IV.26b shows the image corresponding to the largest disk with 1 s in exposure time. From the SEM image of the nanodisk, we can distinguish at the center the granularity of the 20 nm thin film layer of gold. The dielectric PMMA layer that hold the nanostructure is discernible by the gray contrast on the background. The dark stripe observed on the left-side of the nano-disk corresponds to charging effects due to the scanning electron beam. These charging effects are easily observable when metallic nanostructures are supported in dielectric materials, which corresponds to our case. The nano-disks are deposited over PMMA in glass substrate, as it is shown in the inset of Figure IV.26a.

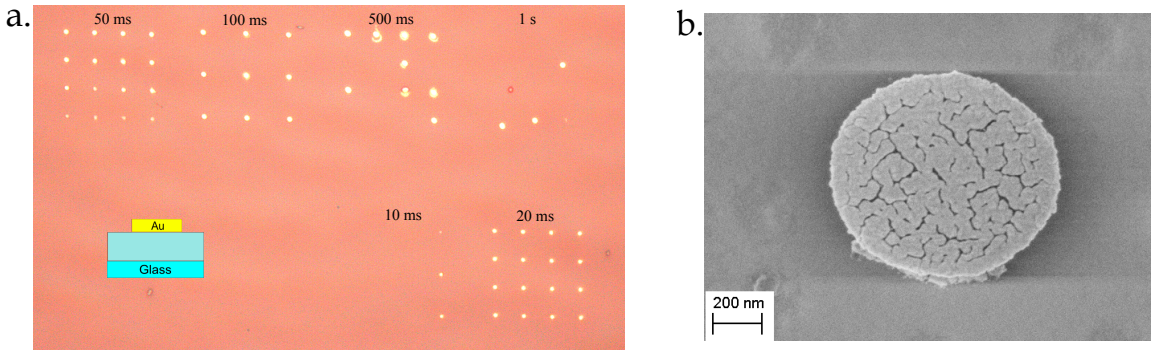

Fig. IV.27 *a) Reflection image of nano-disks over glass substrate fabricated with 0.80 NA objective b) SEM image of one Au nano-disk of 876 nm in diameter corresponding to the* 4×4 *matrix 20 ms.*

We have also characterized the Au nano-disks fabricated with 0.80 NA Semi-Apochromatic objective. In Figure IV.27a, we show the corresponding optical reflection image of the nanostructures. By comparing the results after lift-off processing for both optical objectives, we can distinguish several features in common. In both cases, the matrices exposed within 3 ms and 5 ms have gone away during lift-off processing. One of the most probable reasons is the occurrence of sub-development for such tiny holes obtained with short times of exposure. The tiny holes don't let the solvent MF-319 go inside the hole during development. In sub-developments, there is not a clear undercut below the upper PMMA layer. So that, during gold evaporation a continuous metallic film is deposited. By performing a long lift-off processing, the continuous metallic film including the gold patch, both are removed at the same time. Figure IV.27b shows the scanning electron image of one Au nano-disk of the 4×4 matrix exposed during 20 ms with 0.80 NA objective.

If we now compare the rate of lift-off success for the matrices with the longest exposure times (1 s), we can note that the performance of the 0.95 NA Apochromatic objective seems to be better than the one with 0.80 NA Semi-Apochromatic objective. In the case of 0.95 NA objective (Figure IV.26), 8/9 nano-disks remain in the 3×3 matrix. Meanwhile, in the case of 0.80 NA objective (Figure IV.27), 3/16 nano-disks have survived after lift-off processing.

Finally, for matrices corresponding to exposure times from 20 ms to 100 ms, we can observe the totality of the metallic nanostructures for both optical objectives. We can conclude that these parameters are the optimal ones in terms of laser exposure and development processing to fabricate nano-disks over glass substrate with a blue diode laser at high power and short exposure times.

The interaction between the low PMMA layer with the Au thin film is crucial to firmly maintain the Au nano-disk after lift-off processing. We have conducted a large amount of experimental studies to obtain a clean and efficient lift-off process. From most of our experimental results, we have realized that, beside the appropriate undercut below upper PMMA layer, the strong bonding interaction between the lower PMMA and the thin

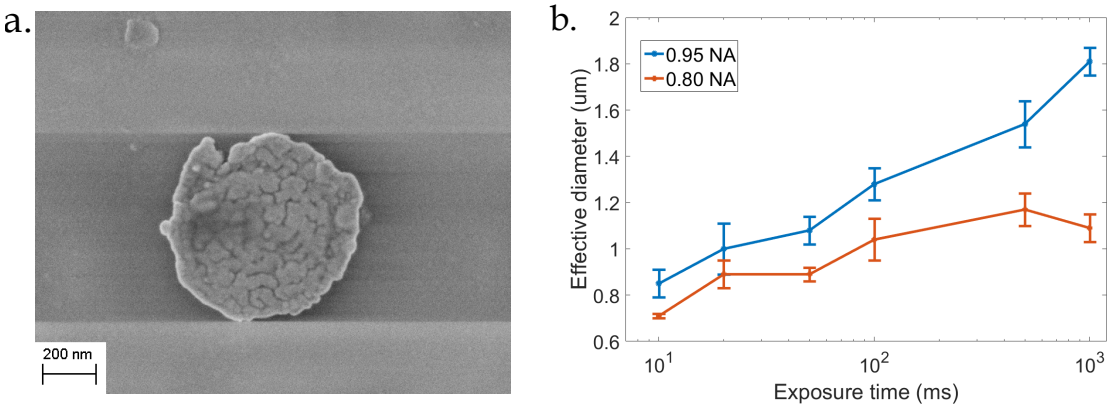

Fig. IV.28 *a) Scanning electron microscope imagining of a single nano-disk with an effective diameter of 708 nm fabricated during 10 ms of exposure time with 0.80 NA objective. b) Trace of the effective diameter for each exposure time in both objectives.*

Au patch deposited by thermal evaporation are crucial parameters for the success of the lift-off processing.

In Figure IV.28a, we show the smallest Au nano-disk obtained in this sample. The nano-disk belongs to the 3×3 matrix (10 ms of exposure time) using 0.80 NA objective. We have estimated its diameter by enclosing the area revealed by the SEM image and compare it with the area of an equivalent perfectly circular disk with the same area. The nano-disk has an effective diameter of 708 nm. This diameters is actually close to the spot size of the blue diode laser using 0.80 NA objective ($\approx$ 540 nm, approximately). Figure IV.29 shows the fluorescence scanning image of a single nanoemitter with 0.80 NA and 0.95 NA objectives. We have estimated the effective diameter for the rest of the nano-disks obtained with both optical objectives. We have calculate the mean average for each exposure time and the we have plotted in Figure IV.28b. Figure IV.28b summarizes the effective diameter per exposure time. The errorbars indicate the standard deviation for each matrix.

According to our experimental results shown in Figure IV.28b, the Apochromatic objective 0.95 NA can achieve systematically larger nano-disks by only modifying the exposure time. On the other hand, the 0.80 NA Semi-Apochromatic objective remains within nano-disks of 1 μm, approximately.

The experimental results shown in Figure IV.28b are evidently opposed to the results predicted by the diffraction theory of light. The size of the laser spot scales as $\approx \frac{\lambda}{2NA}$, with NA the numerical aperture of the objective. In Figure IV.29a and b, we show two scanning fluorescence images of a single nanoemitter using 0.80 NA and 0.95 NA objectives, respectively. From the scanning images we can clearly compare the size of the laser spots. The smaller laser spot is achieved with the 0.95 NA objective ($\approx$ 420 nm). Thus, the smallest nanostructure fabricated in this section is notably inverse with the

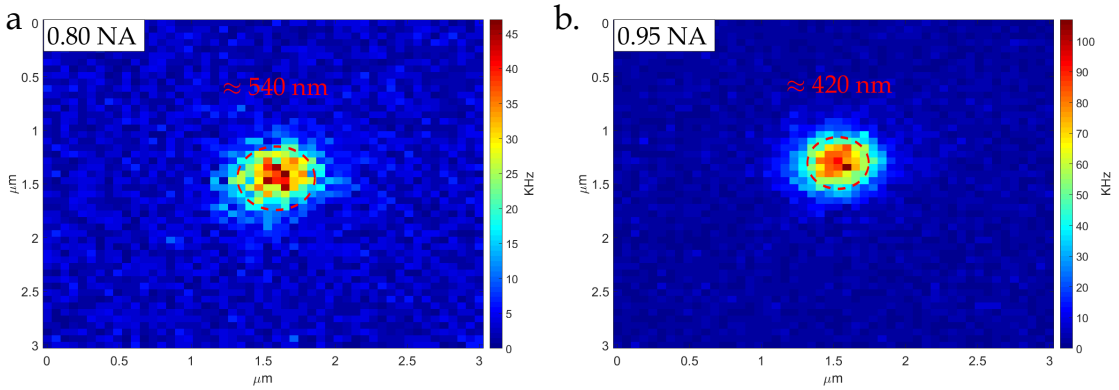

Fig. IV.29 *Scanning fluorescence image of a single nanoemitter using the blue diode laser 405 nm with a) 0.80 NA Semi-Apochromatic objective and b) 0.95 NA Apochromatic objective.*

theoretical prediction. We are not able to explain such contradictory results. We can not exclude that the numerical aperture of the objective is not the key parameter. Other parameters as the ageing of the LOR3A or PMMA solution may be for example as crucial.

So far, we have modified the parameters of the in-situ optical lithography protocol to improve the development and lift-off processing for nano-disk deposited over glass substrate. We will now apply this improvements to the protocol for the fabrication of patch antennas.

IV.7 In-situ optical lithography: passive patch nanoantennas

The patch antennas structure consists in a single Au nano-disk separated by a nanometric dielectric spacer from a gold substrate. The gold substrate has a thickness of 200 nm Au. This layer is optically opaque so the transmittance is null and almost all the visible light is reflected. In the case of the blue laser emitting at 405 nm, the reflectance is nearly 40%. In the case of a glass substrate the reflection is much lower since the glass coverslip and the PMMA are transparent to the visible light. For instance, in an air-glass interface the Fresnel reflection coefficient in intensity is only 0.04 (for each interface) at normal incidence. In the case of a gold substrate, making a hole in the resist bi-layer will be affected by the incident and reflected light from the Au mirror.

In order to find lithographic parameters now adapted to gold substrate, we have fabricated passive nanoantennas using the blue diode laser at maximum power with exposure time in the order of milliseconds.

IV.7.1 Preparation of the sample

We will start by describing the characteristics of the thin film layers deposited in this fabrication. In a commercial silicon wafer we have deposited 5 nm-Cr followed by 200 nm-Au by thermal evaporation. The thin layer of chromium is included as adhesion layer to stick the evaporated gold with the silicon wafer. Once the wafer is prepared we have proceeded with the same cleanliness procedure by flowing acetone and isopropanol during spin-coating. Finally, we have introduced the sample in a ozone plasma cleaner during 30 min to remove some micro residues of dust. We have spin-coated the following thin films:

1. Deposit of first PMMA layer. The first dielectric layer prevents the nanocystals from the direct contact with the gold layer avoiding quenching of fluorescence emission. We have spin-coated 0.5% PMMA which provides a thickness of 10 nm. After deposition, the thin layer is baked during two minutes at 150 ^{o}C in a heater plate. The baking of PMMA layer aims to solidify the material becoming more dense and resistant. The parameters for spin-coating was: 4000 rpm, 2000 rpm/s during 45 s (dispense 60 μL).

2. Deposit of nanocrystals. We have dispersed fluorescent nanoemitters with a suitable dilution rate to distinguish them individually. The purpose of including single nanoemitters in the sample is based on the fact that, after the fabrication of the stack of layers, the position of the focal plane at the different levels of the stack may be difficult to differentiate through the ocular of the microscope. The use of point-like fluorescent sources will help to precisely identify the relative focal plane on the stack and perform in-situ lithography. In this set of experiment, we do not make holes above the nanocrystal.

3. Deposit of second PMMA layer. This layer provides the second half of the gap between both metallic layers. In this fabrication we have used 0.75 % of PMMA that gives 25 nm thickness. The velocity, acceleration and laps time for spin-coating were: 4000 rpm, 2000 rpm/s and 45 s, respectively. We have baked the layer at 150 ^{o}C during 2 minutes.

4. Deposit of resist bi-layer. We have deposited first lift-off resist LOR3A and then 0.75 % PMMA using 4000 rpm, 2000 rpm/s and 45 s both. These parameters give a thickness of 330 nm of lift-off resist LOR3A and 25 nm in dielectric PMMA. We have baked each layer at 150^{0}C during 2 min [5].

Figure IV.30 shows the steps of thin film deposition for the fabrication of the stack of layers. For in-situ lithography, we have used the 405 nm diode laser at maximum optical power (5.20 mW) in continuous operation mode. We have drilled matrices with different exposure times ranging from 1 s to 10 ms with 0.80 NA and 0.95 NA optical objectives.

IV.7.2 Development time

In a first set of fabrication, we have developed the sample in two steps using MF-319 developer diluted 1:3 with deionized water. In the first development, we used 2 minutes.

[5] In section IV.7.4 we will discuss more in detail the influence of baking the lift-off resist layer.

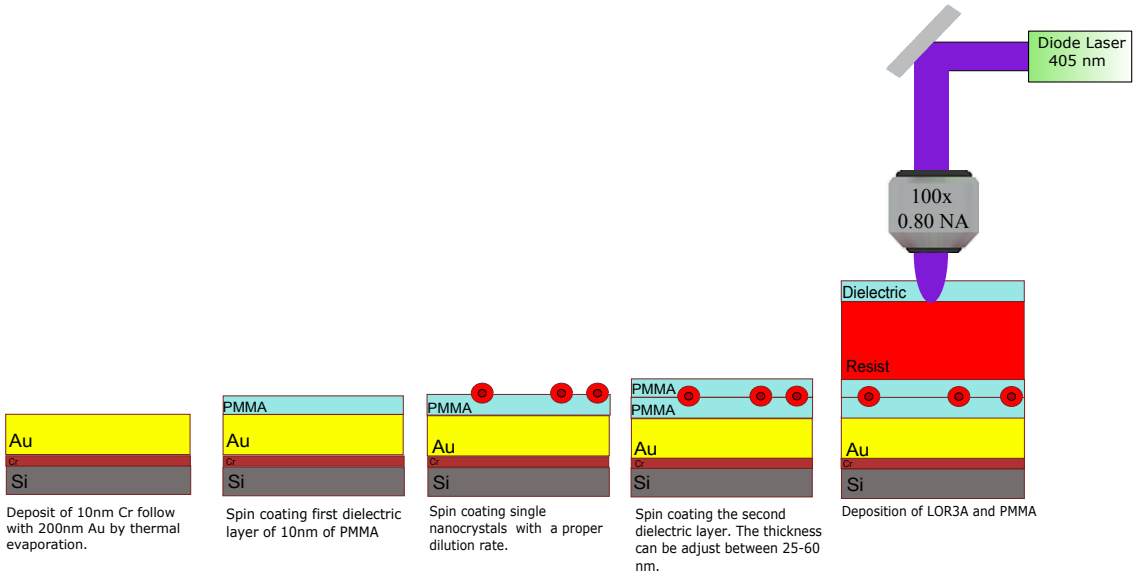

Fig. IV.30 *Preparation of the sample for in-situ lithography on gold substrate.*

After placing the sample in the fluorescence microscope, we have still observed fluorescence light at the center of the holes which indicates the presence of lift-off resist still inside. We then proceed with the second development for 1 minute more. After Au deposition and lift-off processing, most of the nano-disks went away except those fabricated with longer exposure times (1 s) with 0.95 NA objective. These results lead to the conclusion that there was not a proper undercut in the holes except for those corresponding to long exposure time. Figure IV.31a. shows one passive nanoantenna obtained in this set of fabrication.

We have then continued the development of a second sample but we have reduced the dilution of the developer to 1:2 (1 volume of pure MF-319 + 1 volume of deionized water). We have also reduced the time of development to only 20 seconds. After similar procedures in thermal gold deposition and lift-off processing, we have achieved several matrices of passive nanoantennas. The increase in the concentration of the MF-319 developer has been beneficial to the development processing and consequently to lift-off. Figure IV.31b,c shows 16 passive nanoantennas fabricated with these lithographic parameters and 0.80 NA objective. This illustrates the importance of a proper development process. If it is too short, the undercut is not made, the Au patch forms a continuous layer with the surrounding film, which inhibits the lift-off. On the other hand, if it is too long, the undercut is too large. The upper PMMA layer falls which leads to a continuous gold film after deposition, inhibiting also a proper lift-off.

In Chapter III we have discussed the passive nanoantennas fabricated in this section in terms of reflectivity analysis. In the present section, we will concentrate our discussion on the improvements of the protocol until the fabrication of nanoantennas with a single nanocrystal. So far, the realization of passive antennas has helped to find adequate lithographic parameters adapted to the configuration of patch nanoantennas.

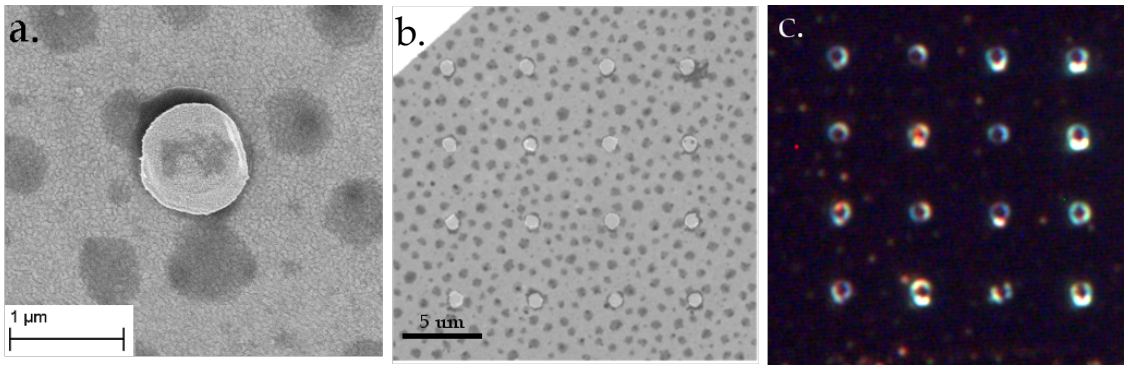

Fig. IV.31 *a) Scanning electron microscope imagining of a passive patch nanoantenna with 945 nm of diameter fabricated with the diode laser using 0.95 NA objective. b) Scanning electron microscope imagining of 16 passive patch nanoantennas fabricated with the diode laser using 0.80 NA objective. c) Optical dark-field image of b).*

IV.7.3 Intermixing layer

From the scanning electron images of both Figures IV.31a and b, we can observe a dotted pattern surrounding the passive nanoantennas. The opaque spots distributed homogeneously along the surface may correspond to different composition of dielectric materials on the surface. Figure IV.31c shows the corresponding optical dark-field image of the 16 passive nanoantennas. The dotted pattern observed by electron imaging is also observed by dark-field microscopy as small bright spots along the surface. From precedent studies, we know that MF-319 developer dissolves exclusively lift-off resist LOR3A and that it doesn't attack dielectric PMMA layer.

If at some point, there is some intermixing of PMMA and LOR3A, the lift-off will be less efficient. This final surface will be not completely homogeneous leading to a dotted pattern as well in SEM or in dark-field optical imaging.

The question is now why we have observed a dotted pattern covering all the surface of the sample when it was expected to find the homogeneous PMMA dielectric layer? The findings shown by electron imaging take us to perform the following experiment. We prepared a test sample, we first spin-coated a PMMA layer. We baked it. Then we spin-coated a layer of LOR3A without baking it. After lift-off processing using pure MF-319 we examined the sample by optical dark-field microscopy. We didn't observe any dotted pattern. We then conclude that the dotted pattern appears when the resist LOR3A is baked by the heater plate. Probably, even thought the lower PMMA has already been baked before spinning LOR3A layer, the procedure of baking the later LOR3A layer may induce some intermix between PMMA-LOR layers.

IV.7.4 Influence of no baking resist bi-layer

Initially, during the first development of the protocol established by Cherif Belacel [58], it was proposed to bake the lift-off resist LOR3A in order to avoid the intermix of LOR3A with the last third PMMA layer when they are both deposited by spin-coating. This procedure was adopted for the protocol developed by Amit Raj Dhawan during his PhD thesis [26].

Several micro- and nano- fabrication procedures recommended by MicroChem using lift-off resist LOR3A are based on baking the resist layer in order to enable a precise and reproducible control in undercut profile (http://microchem.com/pdf/PMGI-Resists-data-sheetV-rhcedi pdf). However, those procedures don't consider the influence of baking the neighboring layers. In the fabrication of patch antenna, the lift-off resist LOR3A is coated over dielectric intermediates layers (thin films of PMMA). We have found that, after baking the lift-off resist by means of a heater plate, the intermediate PMMA layer and lift-off resist LOR3A are mixed at some point. The heating creates an intermixing layer that we can distinguish as a dotted pattern along the complete sample. These findings have conducted to stop heating the lift-off resist layer (LOR3A) and the upper PMMA layer for future fabrications in order to prevent damage of the dielectric lower PMMA layer.

One consequence of no baking LOR3A layer will be the quicker dissolution during the development process. Since the heating of the resist layer tends to solidify the material (become denser and resistant), by stopping the baking process, it is very likely that the developer MF-319 will attack more quickly the lift-off resist increasing the possibility to over-development. We should then reduce the development time keeping the same concentration 1 : 2 of the MF-319 in order to achieve a suitable undercut.

IV.7.5 Differences in Au nano-disks

a) Structural properties

The quality of the metallic nanodisk depends on the different experimental conditions during the thermal deposition process and also on the substrate that holds the nanostructures. For instance, after thermal deposition of 20 nm-Au thin layer used for patch antennas, we have observed different structural properties of the metallic layer when it is deposited over 200 nm-Au thick substrate or conventional glass coverslips. In both substrates we have spin-coated a thin intermediate PMMA layer. The image IV.32 shows passive patch antennas fabricated with the in-situ optical protocol in two different substrates: 1) over a conventional glass coverslip + 25 nm PMMA (Figure IV.32a) and, 2) Au gold substrate + 35 nm PMMA (Figure IV.32b).

From the scanning electron images IV.32 we can see the size of grains forming both nano-disks. We can observe that the disk deposited on glass substrate is formed of non-regular clusters which are slightly separated. The layer is deposited just below the percolation threshold. On the other hand, the nano-disk deposited over Au substrate is much smoother. The quality of the nano-disk is notably better in terms of grain binning. These

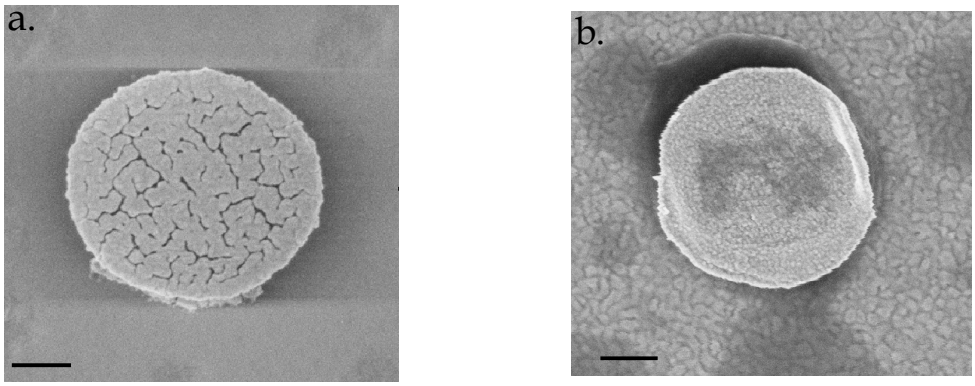

Fig. IV.32 *Scanning electron micrographs of 20 nm Au-disk deposited on PMMA layers spin coated on a) glass and b) gold substrates. Scale bar 200 nm.*

results show the influence of the supporting substrate in the thermal evaporation process. This difference is probably due to difference of temperature on the substrate for each case. We should also not exclude slight variations in the parameters of deposition in each fabrication, which could have been below percolation in one case and above in the other.

b) Scattering optical properties

We have characterized the metallic nanostructures by optical dark-field microscopy. In this technique, we observe exclusively the light scattered by the nano-disks which is highly dependent of its morphological characteristics.

We start by presenting optical dark-field images of nano-disks deposited on dielectric materials. In Figure IV.33a we show a 3×3 array of Au nano-disks deposited on a glass substrate separated by a thin dielectric layer of 25 nm of PMMA. From the dark-field image we can observe that most of the light is scattered from the circular edge of the disk. We can distinguish an intense yellowish ring enclosing the nanostructure with a notable dark spot at the center. This dark area at the center of each nano-disk indicates the flatness of the metallic layer. In Figure IV.33c we show the scanning electron image of one of those nano-disks. The effective diameter of this structure extends to D_{eff}= 960 nm, approximately. From the image we can note that the nano-disk is not perfectly circular, it has some irregularities on the borders with some release of small material. These minor defects seem to be transparent by optical dark-field illumination which shows mostly an homogeneous yellow ring around the structure.

We now present a 4×4 array of nano-disks deposited on a gold substrate. The scattering properties of these nanostructures are shown on Figure IV.33b. From the image we can observe that most of the light is also scattered from the boundary edges (similar to the nano-disks on glass substrate). However, for the structures on gold substrate, the light captured by the camera varies from bluish, whitish and brownish tones depending of the nano-disk. In Figure IV.33d we show the scanning electron image of one nano-disk

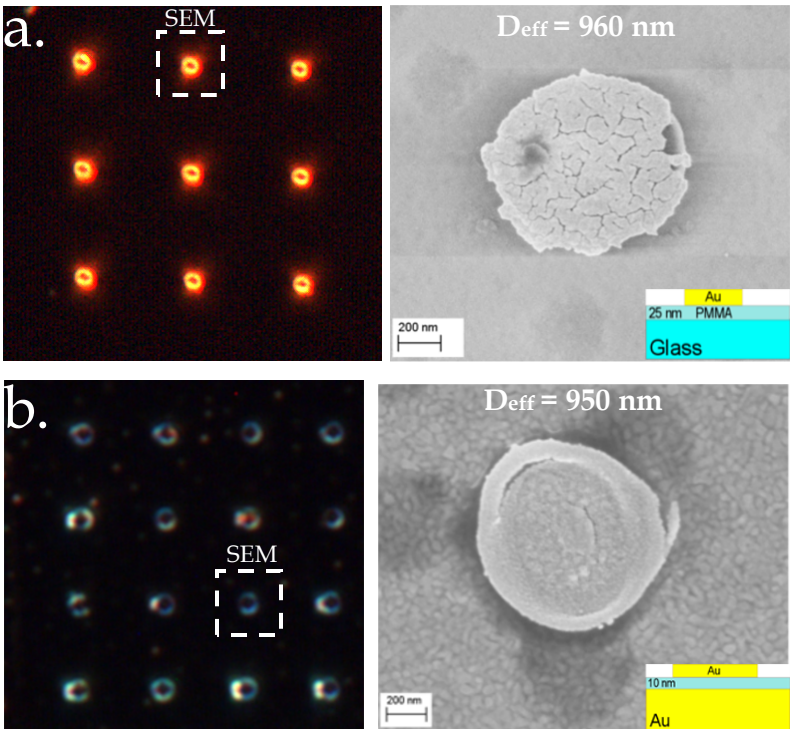

Fig. IV.33 *Optical dark-field illumination image of a) a 3 × 3 array of Au nano-disks deposited on a glass substrate + 10 nm PMMA, b) a 4 × 4 array of nano-disks deposited on a Au substrate + 10 nm PMMA.c) and d) Scanning electron images of nano-disks from a) and b), respectively.*

with an effective diameter of D_{eff}= 950 nm. From the image we can note that the edges are more defined and smooth compared with the disk on glass substrate. We can also note some small defects such as cracking or uneven surface of the thin metallic layer.

The nano-disks discussed above have been selected with similar effective diameters in order to compare the scattering properties of the nanostructures obtained with different supporting substrates and different dielectric spacer.

c) Shape of patch antennas

In the analysis of optical dark-field imaging of Figure IV.33b, we have seen that some patches are surrounded with rings of different tones and colors. More precisely, the presence of bright white spots emerging on the left-side of some passive elements of Figure IV.33b seems to be the consequence of different morphological defects.

In order to further investigate the 4×4 matrix of passive antennas, we have correlated optical dark-field images with scanning electron micrographs. In Figure IV.34 we show such correlation for three passive antennas which have showed bright white spots (Ant 10,

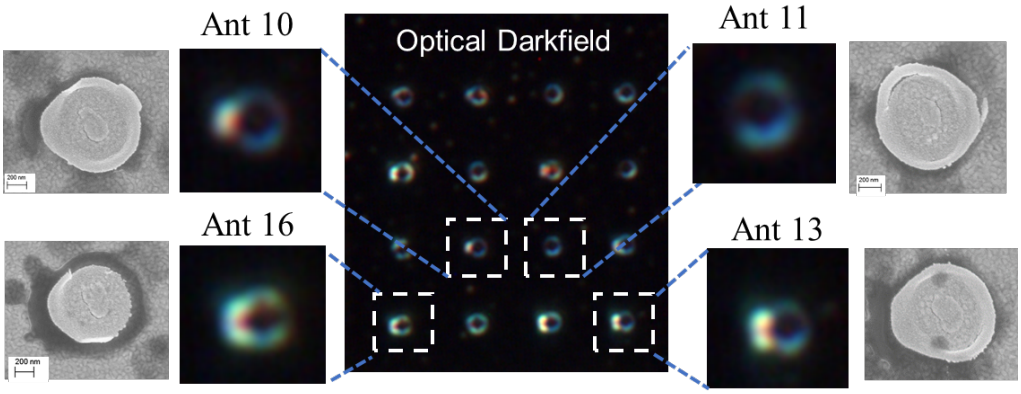

Fig. IV.34 *Correlation between scanning electron imaging and optical dark-field microscopy of four patches exhibiting asymmetric defects (Ant 10, Ant 16 and Ant 13) with one antenna with quasi circular shape (Ant 11).*

Ant 16, Ant 13). From the Figure IV.34 we can directly correlate the bright white spot observed in dark-field illumination with the elongation on the left side of the nano-disk. The pronounced sharpness on the left side of the nano-disk turns out to concentrate the electromagnetic field on the extreme edge-tip, becoming observable by dark-field illumination. In Figure IV.34 we have also included the dark-field image of the nano-disk shown in the previous section (Figure IV.33b, Ant 11). In this case the blueish ring surrounding the structure has a homogeneous distribution.

Even though the passive antennas of the same 4×4 matrix were fabricated with exactly the same lithographic parameters, the characterization of passive antennas by electron imaging has revealed important morphological difference between the structures. We have found that some patches are slightly elongated (asymmetric defects). These defects can be observed by optical dark-field microscopy.

IV.8 Improvement in lift-off process

Until now, the lift-off processing is not optimized as the rate of success is low. If the lift-off time is too short, the flat gold around the patch is not lifted. On the other hand, if the lift-off time is too long, we loose the patch which is lifted at the same time with the gold layer. We have to define a new strategy. The problem comes from the fact that the only entrance of the resist bi-layer to the developer is the hole at the position of the patch. Therefore, the developer attacks mainly the patch and the very close part of the resist around the hole.

In order to remove a larger part of the flat gold layer around the patch, we need a long time in lift-off processing which is detrimental for patch antenna. The new strategy is to open new entrances for MF-319 developer in order to lift-off the flat gold without attacking the patch.

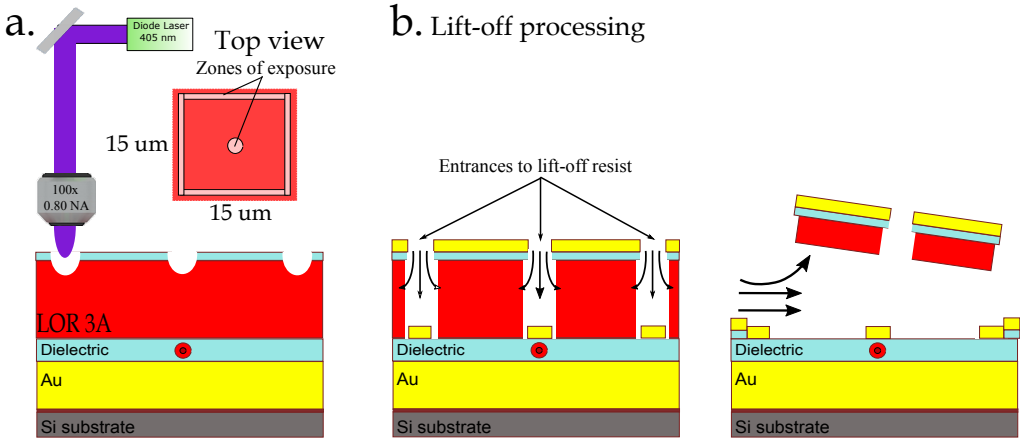

Fig. IV.35 *Additional square writing in the resist bi-layer to have access to LOR3A layer.*

IV.8.1 Additional Square writing

Similarly as drilling a hole in the position of the nanocrystal, we create a square-shape aperture in the resist bi-layer in order to get new entrances for the MF-319 liquid during lift-off processing which will attack mainly the region of the flat gold layer and not the patch region. The square entrances will allow to dissolve the resist LOR3A from the lateral sideways of the patch antenna. The writing of the square is performed after the initial hole and around it. The square writing is made with the blue diode laser drilling the resist bi-layer. The piezo-electric controls the displacement of the sample so that we get a square, as it is shown in Figure IV.35a.

In Figure IV.35b we show a schematic diagram during lift-off processing. The several entrances on the resist bi-layer allow to the MF-319 product to dissolve the resist LOR3A layer inside the square. After some minutes (5 minutes, approximately) most of the resist LOR3A layers is dissolved and the 20nm-Au thin layer with the upper PMMA layer is ejected from the sample, as it is represented in the Figure IV.35b. The improved lift-off processing is then beneficial to reduce the risk of loosing the nano-disk caused by the flow of the liquid. The rate of success is very high, reaching more than 90 %.

IV.8.2 SEM characterization

Figure IV.36a shows a scanning electron imaging of one passive patch nanoantenna fabricated with the supercontinuum laser and square lift-off processing. In the image, we can observe the patch at the center of the 15 μm square and the homogeneous dielectric PMMA layer that supports the patch. Outside the square we can distinguish the 20 nm-Au layer. In Figure IV.36b, we show the passive patch antenna with a diameter of 845 nm.

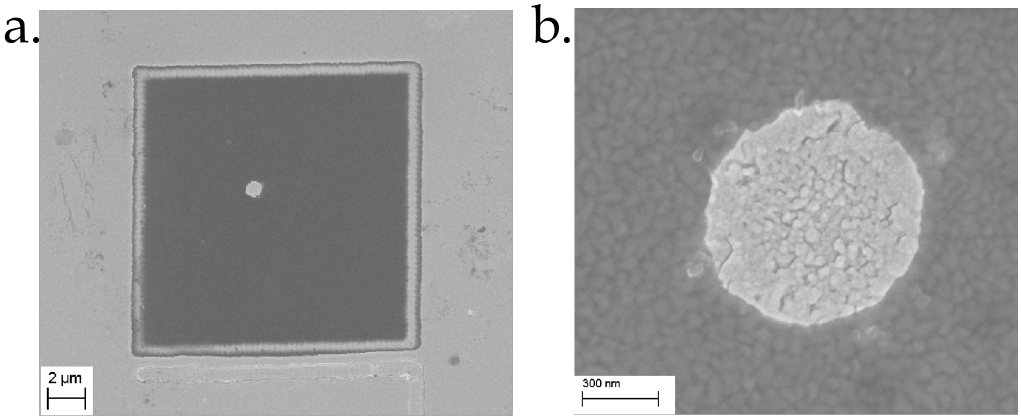

Fig. IV.36 *a) Scanning electron image of one passive nanoantenna fabricated with the supercontinuum laser and square lift-off processing. b) Amplified SEM image showing a nano-disk of 845 nm in diameter.*

The nano-disk shown in Figure IV.36b holds a quasi circular shape. From previous studies conducted by topographic AFM imaging using super continuum laser (Appendix A), we have found that the exposure of the resist bi-layer by this source creates irregular holes in the resist. We have attributed these asymmetries due to the chromatic effects of the optical objective. Since we use from 550 nm to 605 nm wavelengths of the super continuum source, when the laser beam is focused by the objective, the light is slightly dispersed along the optical axis for the different wavelength. This dispersion creates nano-holes with irregular diameters and shapes, as observed in Appendix A. The nano-disk shown in Figure IV.36b suggests that, in spite of these chromatic effects caused by the optical objective, the hole seems to recover a quasi circular shape during development process.

IV.8.3 In-situ protocol with square writing for active antenna

This section aims to explain the in-situ optical protocol including square lift-off step. We have prepared the stack of layers as described in section IV.7.1 (without baking the resist LOR3A and the upper PMMA layer). We then performed the in-situ protocol including the writing of the square. We have to face here another difficulty which has been solved during Amit Raj Dhawan thesis. During the drilling of the hole, we have to assure that the nanocrystal is not photobleached by the exposure. Unfortunately, the exposure with 405 nm leads to the photobleaching of the nanocrystal. On the contrary, with a super continuum laser (optical power 20 mW, repetition rate 80 MHz, range of wavelengths 550-605 nm), we can drill a hole without photobleaching the nanocrystal. The choose of the wavelength range is a trade off between the efficiency in hole drilling and survival of the nanocrystal.

A Hole making with supercontinuum laser. The fluorescence emission of a single nanocrystals is higher than the background fluorescence of the resist bi-layer, so

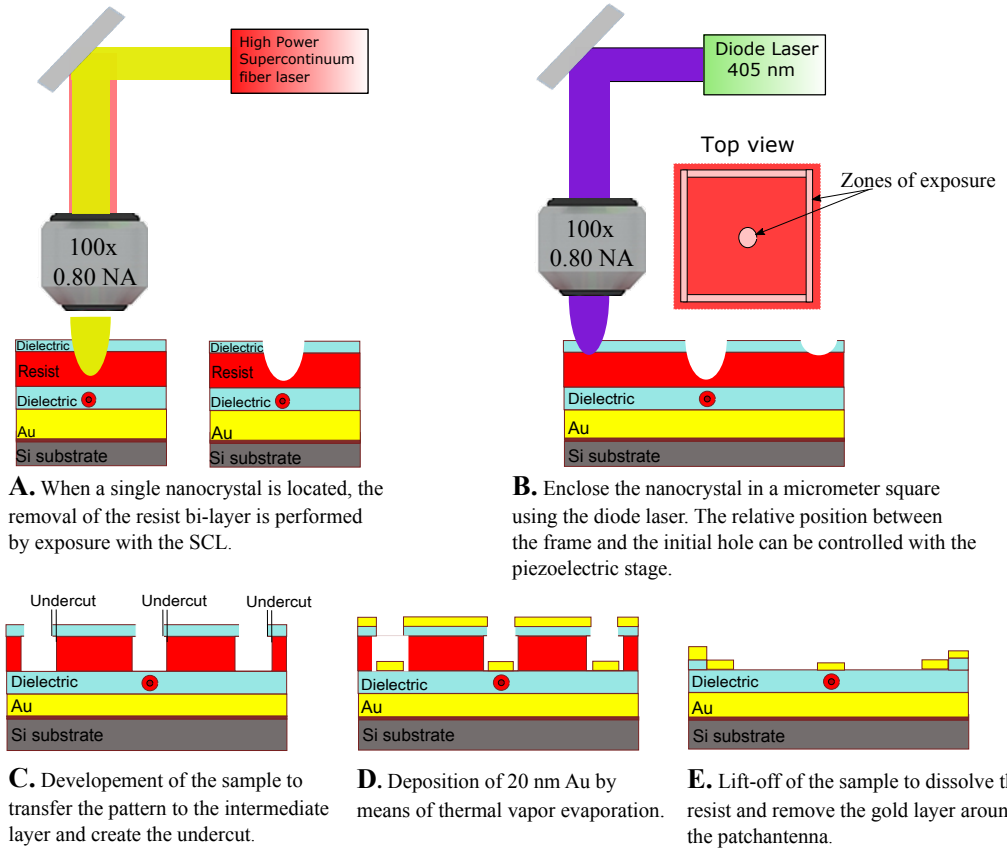

A. When a single nanocrystal is located, the removal of the resist bi-layer is performed by exposure with the SCL.

B. Enclose the nanocrystal in a micrometer square using the diode laser. The relative position between the frame and the initial hole can be controlled with the piezoelectric stage.

C. Developement of the sample to transfer the pattern to the intermediate layer and create the undercut.

D. Deposition of 20 nm Au by means of thermal vapor evaporation.

E. Lift-off of the sample to dissolve the resist and remove the gold layer around the patchantenna.

Fig. IV.37 *In-situ optical lithography including the developments for lift-off processing.*

that single nanocrystals can be detected beneath the resist bi-layer. The hole is drilled with the high intensity supercontinuum laser (pulse duration 300 ps, repetition rate 80 MHz, optical power 20 mW, range of wavelengths 550-605 nm). The exposure with the supercontinuum laser in a reduced laps of time will remove PMMA and partially LOR3A layers by the same precess as discussed before. The hole entrance created in this step will define the shape and size of the future patch nanoantenna.

B Square with blue laser. We create a micrometer square by exposing the resist bi-layer using the blue diode laser at maximum intensity (5.3 mW). We enclose the initial hole within the micrometer square to improve lift-off processing. The square is realized with 50 ms of exposure time to drill solely the resist bi-layer. The writing of the square is operated with the same Labview routine used for laser scanning. Therefore, the size of the square and relative position with respect to the initial hole can be adjusted with nanometric precision.

C Development of the sample. In the development of the sample, the lift-off resist LOR3A will be dissolved isotropically meanwhile PMMA layers are unaffected. The undercut will create a discontinuity in the metallic film that will help during lift-off.

The development process is highly sensitive to the time and concentration of the developer.

D Au deposition. Thermal evaporation of 20 nm-Au thin layer.

E Square Lift-off. In this process, similarly as development, the MF-319 developer will start attacking the resist LOR3A starting from the entrances on the top resist bi-layer.

Figure IV.37 displays the in-situ optical protocol with the improvements for lift-off processing. When performing the writing of the square in the resist bi-layer, it is crucially important that all the lines (borders) of the square intersect each other in order to facilitate the removal of the flat metallic layer.

In this fabrication, we have performed the development process during 10 seconds using the conventional developer MF-319 (diluted 2:1 with deionized water). The square discontinuity created by the diode laser will let to the developer liquid pass through the resist bi-layer and dissolve the lift-off resist inside the square, as it is shown in Figure IV.37c. After deposition of 20 nm-Au thin layer by thermal evaporation process, we finally performed the lift-off by holding the sample (inverted) in pure MF-319 during 5 minutes and then in deionized water for cleaning. The lift-off process in 5 minutes is long enough to dissolve the resist LOR3A beneath the 15 μm square and get rid of the metallic thin film and the PMMA layer around the nanoantenna without attacking the gold patch.

IV.8.4 Optical characterization

In Figure IV.38 we show two optical reflection images with white light illumination of the sample. On the left image we can observe four squares of 15×15 μm size where the first three have an opaque circular spot at the center. The dark spots correspond to the gold nano-disks. The yellowish color that enclose the disks corresponds to the light reflected by the 200 nm-Au substrate supporting the nanostructures. In the 4th one, we can see that the lift-off didn't succeed. This is probably because the lines didn't intersect completely.

The right image of Figure IV.38 corresponds to the same part of the sample but using dark-field microscopy. When imaging by dark-field microscopy, we can improve the contrast of small particles since the background is dark and the objects are bright. In dark-field microscopy only the light scattered by the nanoparticles is detected. The information about the scattering properties of small nano-objects or discontinuities in thin films are easily observed. From the right image of Figure IV.38 we can note the scattering light emitted by the three nano-disks with proper lift-off. In the case of the fourth nano-disk, which has not been completely lifted, the scattering properties of the nano-disk is significantly affected by the film around the nanostructure.

Although the dark-field microscopy is limited by optical diffraction, the optical technique provides substantial information related to the scattering properties of the patch nanoantennas.

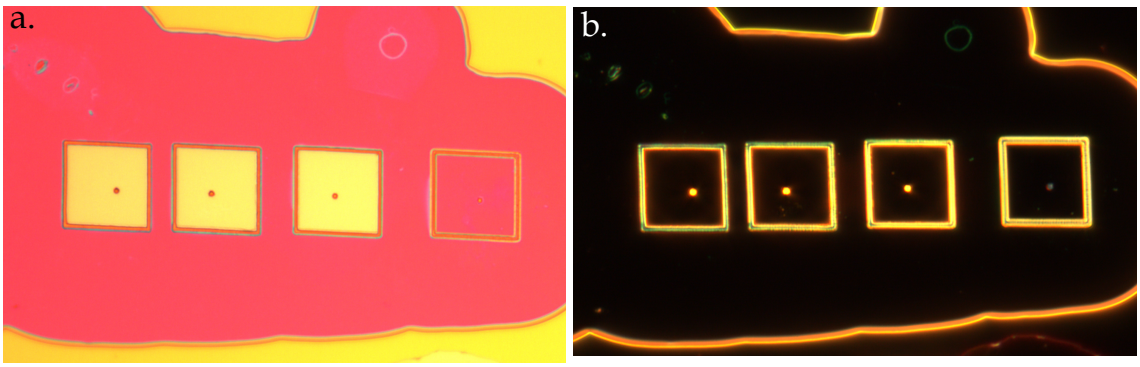

Fig. IV.38 *Optical reflection images of passive patch antennas at the center of a 15 μm square after lift-off processing during 5 minutes in pure developer MF-319. a) Brightfield illumination, b) Dark-field illumination. Objective with 100× and 0.90 NA.*

IV.8.5 Interference colors

In Figure IV.38, we can observe that, in the proximity of the squares, the presence of a pinkish region which expands over some micrometers around the squares. In Figure IV.39 we show the same squares but using an objective with 20× and 0.45 NA. From the image we can note that the pinkish zones are indeed localized all around the array of squares. These zones represent the expansion of the product MF-319 during lift-off processing. The liquid MF-319 attacks the lift-off resist LOR3A by the entrances created by the borders of the 15×15 μm squares, inside and outside the square.

In the square, the liquid attacks the resist LOR3A and reduces the thickness of the layer, as it is shown in Figure IV.39. The pinkish zones indicates where the light is transmitted by the thin gold layer and then reflected by the lower thick gold layer. This is at the origin of interferences, which results in this colourful patterns. The color is an indication of the thickness of the dielectric layer between the two metallic layers and, at the same time is an indication of the efficiency during lift-off processing. Outside of the pinkish zones, we can distinguish an extensive domain with a slightly different yellowish tone with respect to the color inside the squares. These larges domains represent the part of the sample where the product MF-319 hasn't reached the resist LOR3A beneath the gold film and, consequently, there are not modifications of the LOR3A thickness.

The Figure IV.39 also shows another colorful zones such as blueish, greenish localized along the surface. In 2018, during the stage of Mme Hajar Amyar at the INSP [62], she demonstrated that different colors observed in the sample after lift-off processing are attributed to the difference in thickness of the resist LOR3A layer. By calculating the normal reflectance of the complete stack of layers at difference thickness in resist LOR3A layer, it is possible to compute the RGB parameters via a transformation matrix [63]. When an halogen lamp illuminates the sample, the changes in the thickness of LOR3A layer will produce different coordinates in RGB scale. Figure IV.40a shows the colors obtained at specific thickness of the resist from 300 nm to 0 nm. We can observe the

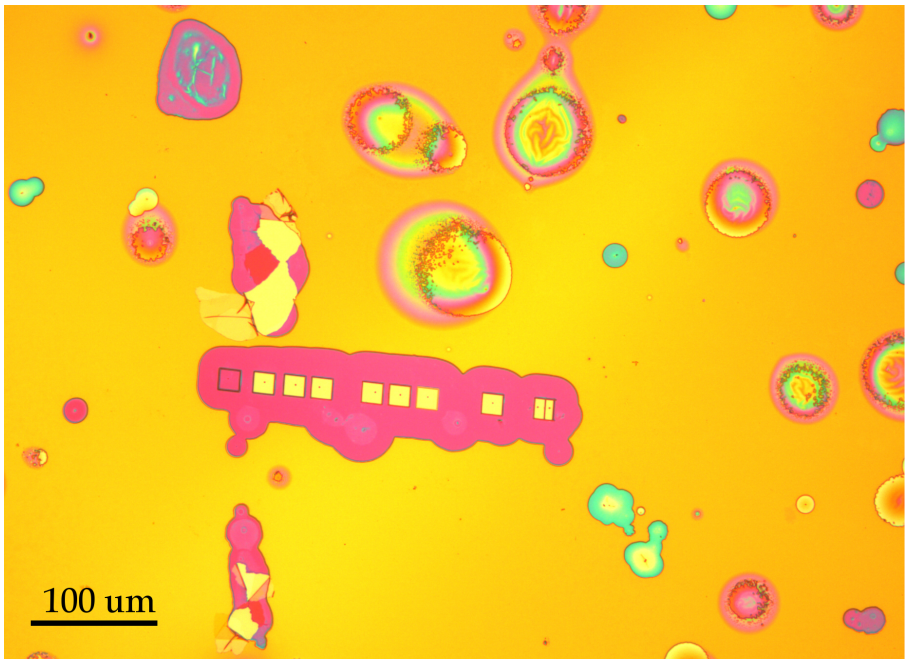

Fig. IV.39 *Optical reflection image taken with a 20× and 0.45 NA objective of an arrays of 15×15 μm squares after lift-off processing during 5 minutes in pure developer MF-319.*

large variety of colors that can be result for a given thickness changing from pinkish to yellowish and purple in some nanometers.

In Figure IV.40b we show the RGB color obtained with the same procedure for Au substrate with 49 nm of dielectric layer. This image helps to differentiate with the case when the resist LOR3A is completly dissolved, as it was shown above in Figure IV.40a. This technique developed in [62] is very convenient to estimate the residual thickness of the LOR3A layer beneath the metallic film.

IV.9 In-situ optical lithography: active patch nanoantennas

So far, we have established the lithographic parameters for the fabrication of passive antennas. We will now apply this protocol including colloidal single nanoemitters. For instance, before starting the in-situ protocol, it is absolutely necessary to perform two principal tests on the nanocrystals: 1) Temperature test with the heater plate at 150^{o}C during 5 minutes, and 2) Gold deposition test by evaporating the 20 nm-Au layer over the second dielectric layer. These tests should be conducted before the in-situ optical protocol and with exactly the same characteristics of dielectric thin films. The objective here is to check that the nanocrystals remains fluorescent after both tests.

In this section, we will discuss how the in-situ protocol has to be adapted in the fab-

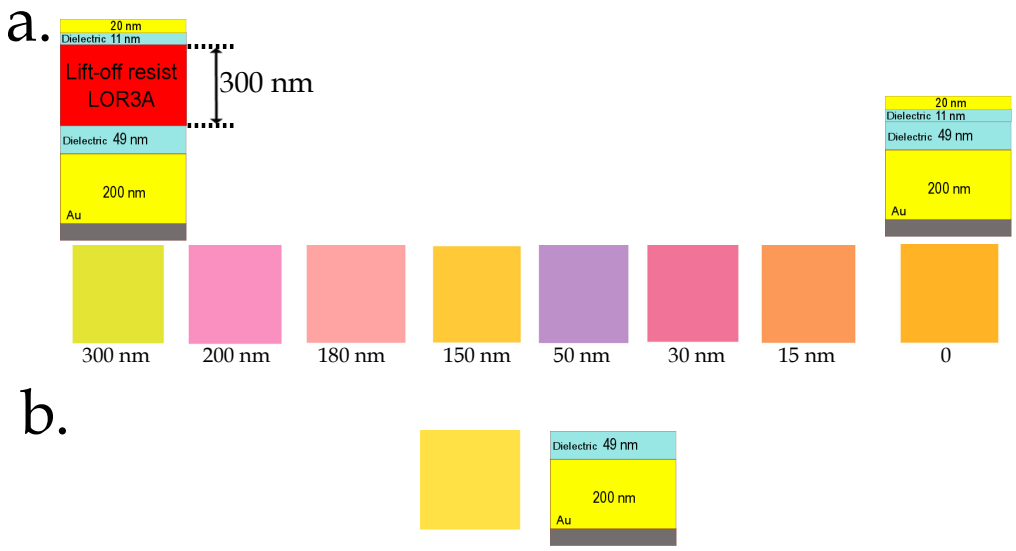

Fig. IV.40 *a) Colors obtained in RGB coordinates from the reflection of an halogen lamp at different thickness of resist LOR3A layer. Thickness from 300 nm to 0 nm (from left to right). b) Color obtained with 200 nm Au substrate + 49 nm of dielectric layer (PMMA). Adapted from [62].*

rication of active antennas instead of passive ones.

IV.9.1 Controlling thickness of dielectric layers

Controlling the gap thickness between the gold mirror and the thin patch is one of the main parameters for efficient coupling between the single nanoemitter and the plasmonic modes. Herein, we will explain how to prepare dilutions of polymethyl methacrylate (PMMA) to obtain thin dielectric films. The thickness of the films depend of the characteristics of the powder material. In this procedure we have used powder of Poly(methyl methacrylate) which has a molecular weight of $M_w = 101000$. We will start by selecting the desire concentration. We will chose 0.75%, for example. The procedure for diluting PMMA is described as follows:

1. We first calculate the total mass when preparing a dilution in a volume of 10 mL. The density of toluene is $0.8669\frac{g}{mL}$. Therefore, in 10 mL of liquid we will have $m_{\text{toluene}} = 8.67$ g.

2. With the pre-define concentration of 0.75 %, we calculate the mass of PMMA who satisfy the following expression:

$$\frac{m_{\text{PMMA}}}{m_{\text{PMMA}} + m_{\text{toluene}}} \times 100\% = 0.75\%$$

3. For a concentration of 0.75 % we will need 65.51 mg of powder of PMMA. Using a high resolution microbalance to measure the quantity of material, we proceed to

Table IV.1: Concentration and thickness of PMMA diluted in 10 mL of toluene. The values were obtained by spin coating the dilution of PMMA in a glass substrate using a speed spin of 4000 rpm, acceleration of 2000 rpm/s during 45 s.

%	m_{PMMA}	Thickness
1.5%	132.01 mg	60 nm
1.0%	87.56 mg	35 nm
0.75%	65.51 mg	25 nm
0.50%	43.56 mg	10 nm

incorporate the powder into the toluene and we leave the container in a warm bath at 60 ^{o}C during 24 hours.

From the method described above, we were able to prepare dilutions which provide different thickness of PMMA layers. Table IV.1 summarizes some values for different concentrations and thickness measured by DEKTAK profilometer in the period of the present thesis. It is important to mention that, because of the evaporation of the solvent inside the solution, the layer will be thicker for a solution diluted months or years before than for a fresh solution.

IV.9.2 Preparation of the sample

The preparation of the sample including single colloidal nanocrystals is presented as follows:

1. Deposit of the first PMMA layer. The first dielectric layer prevents the nanocrystals to stay directly in contact with the gold substrate avoiding quenching of fluorescence emission. We spin coating 0.5 % PMMA which provides a separation of 10 nm from the metallic layer (measured by DEKTAK profilometer). The parameters used for spin-coating deposition are: 4000 rpm, 2000 rpm/s, 45 seconds. The layer is baked during 2 minutes at 150^{o}C.

2. Deposition of nanocrystals. The method to dilute nanocrystals consists in mixing two different substances in terms of volume units. The dilution factor is represented as A:B. A represents the quantity of the solute (nanocrystals) in volume units. B represents the total volume of the dilution (solute + solvent). For the dilution of CdSe/CdS nanocrystals, we have used hexane as solvent, normally starting with 1:1000 as dilution factor followed by a second dilution of 1:1000 to reach 1:1000000. The final dilution is one over one million times from the mother concentration. For such dilutions the nanocrystals are separated by a few micrometers. The parameters for spin-coating are: 4000 rpm, 2000 rpm/s during 40 seconds.

3. Deposition of the second PMMA layer. This layer provides the second half of the gap between both metallic layers. The second dielectric layer can be adjusted depending of mainly two parameters: 1) the thickness has to be higher than the dimensions of the nanocrystal and, 2) the thickness should be large enough to protect them from

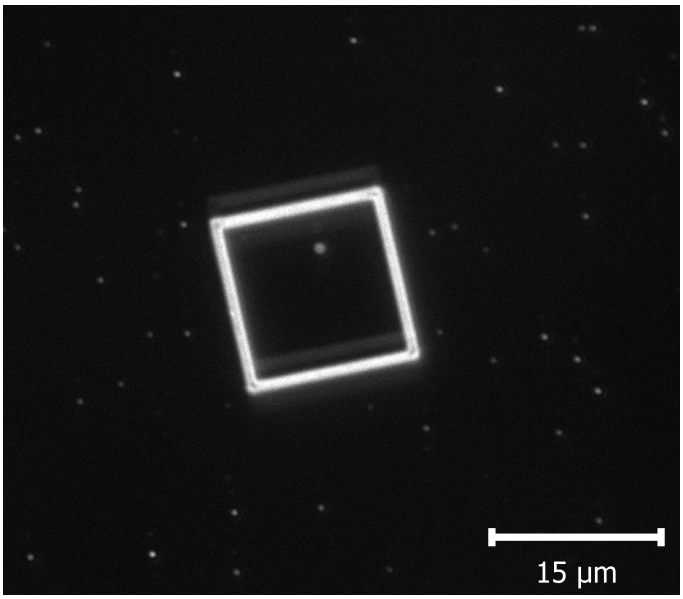

Fig. IV.41 *In-situ optical lithography including the development for lift-off processing.*

thermal deposition process and avoid photobleaching [6]. In this fabrication we have used a concentration that provides 35 nm thickness. The second dielectric layer is spin-coated with similar parameters and heated at 150^{o}C during 2 minutes.

4. Deposit resist LOR3A and third PMMA layer. We have successively deposited lift-off resist LOR3A and 0.5% PMMA, both spin coated using 4000 rpm, 2000 rpm/s and 45 s. These parameters give a thickness of 330 nm in resist LOR3A and 10 nm in dielectric PMMA.

After the preparation of the stack of layers, we performed the in-situ optical protocol on the sample, as it is described in section IV.8. In Figure IV.41 we present a fluorescence microscopy image after the writing process. From the image we can distinguish single nanocrystals dispersed homogeneously on the sample. We observe also a 15 μm square created in the resist bi-layer by means of the blue diode laser (405 nm). Inside the square, usually in the middle, we can see a hole created with the super continuum laser at the position of a single nanocrystal.

IV.10 Conclusion

In this chapter, we have presented the developments of the in-situ optical lithography protocol for the fabrication of patch antennas with single nanoemitters. We have followed the evolution of a single hole for drilling a hole in the resist bi-layer. We have

[6] During the thesis of Amit Raj Dhawan, it was found that using a dielectric layer of 1.5% PMMA (35 nm) photobleaching is avoided

demonstrated that the perforation of the resist bi-layer can be conducted by two different approaches. We have found that each approach brings different results in terms of nanofabrication. When the resist bi-layer is exposed at low optical intensity during an extended time (several seconds), the interaction of the radiation laser with the resist bi-layer induces photopolymerization of the materials, leading the fabrication of dielectric nano-hills at the center of the hole. We have found that these dielectric nanostructures are composed of a very resistant material which remains even after 15 min of attacking with oxygen plasma cleaner.

On the other hand, in the second approach, when the exposition of the resist bi-layer is performed at high power in milliseconds laps-time, the cumulative thermal effects are reduced leaving well-define holes on the resist bi-layer without damaging intermediate dielectric layers. We have realized the importance of controlling the exposure time in the order of milliseconds to not damage the intermediate layers. We have found that, the development process is a critical factor during the protocol. The development time establishes the morphological characteristics of the patch antenna and, in a proper undercut process, it helps to achieve a suitable lift-off process.

We have fabricated gold nano-disks supported in a gold substrate (passive antennas) with the blue diode laser. After the removal of the 20 nm-Au layer, we have observed by scanning electron microscopy, the intermixing layer produced by the baking of the resist bi-layer during the preparation of the sample. We have stopped baking the resist bi-layer. We have re-adjusted the parameters in development process.

We have proposed the incorporation of a micrometer square in the writing process to improve the lift-off processing. The writing of the micrometer square is performed with the blue diode laser and the piezo electric stage around the hole created above the nanocrystal with the super continuum laser.

The resistance of the nanocrystals to the baking temperature and the thermal vapour deposition of the thin disk are two tests very important to perform before starting the protocol.

In conclusion, we have here optimized the protocol in the fabrication of a patch antenna with a single nanocrystal.

Chapter V

Active nanoantennas characterization

V.1 Introduction

In this chapter we will discuss some results obtained with active antennas fabricated in this thesis. Each active antenna exhibits different behaviour in terms of photodynamic emission. We will discuss mostly two antennas emphasizing two aspects: 1) the modification of LDOS in antennas with over-development condition, and 2) some antennas which have exhibited photon emission described as super-poissonian distribution.

In the first antenna, we will show the progressive acceleration of fluorescence emission during the fabrication protocol. Then we will discuss the statistics of emission of active antennas. We will evidence an interference fringe pattern associated to the emission of one antenna.

V.2 Active patch nanoantenna and modification of LDOS

Several theoretical studies have demonstrated that metal-insulator-metal structures can support two plasmonic modes, short- and long- range plasmon modes according to their propagation length [64], [65], [66]. In a patch nanoantenna, short-range plasmons modes are efficiently excited [23], [27]. These modes are confined inside the dielectric gap better than at the outer interface of the metal. In a finite patch structure, the surface plasmons excited at both metallic-dielectric interfaces are reflected from the edges creating a stationary electromagnetic wave distributed along the cavity.

Beside the relative position of the nanoemitter with respect the nano-disk, the orientation of the emitting dipole plays a key role in the emission dynamics. Theoretical studies performed in patch systems have demonstrated that the orientation of the dipole source represents one of the crucial parameters in the excitation of surface plasmons [27], [67]. The fluorescence emission of single semiconductor nanocrystals CdSe/CdS is well described as the emission of 2D orthogonal, incoherent dipoles. Therefore, in a random dropped deposition, there is some probability of having a vertical dipole whose light emission can be coupled efficiently into surface plasmons of both metallic dielectric interfaces.

First of all, we start by defining the factor F_{Ant} which takes into account the modification of fluorescence emission dynamics of a nanocrystal before and after the deposition of the gold nano-disk. In other words,

$$F_{Ant} = \frac{\Gamma_{Ant}}{\Gamma_{Au}},$$

where Γ_{Ant} is the decay rate after the coupling with the nanoantenna and Γ_{Au} is the decay rate of the same nanocrystal deposited on Au substrate. The factor F_{Ant} represents the acceleration $F_{Ant} > 1$ provided by the coupling of the nanocrystal emission with the plasmonic antenna.

V.2.1 Coupling the nanocrystal emission to patch-antenna

a) Acceleration of emission

Since the work of Drexhage in 1970 [68], it is well-known that the decay rate of fluorescence molecules is modified in the vicinity of a metallic surface. The acceleration of emission is directly proportional to the modification of LDOS provided by the planar nanostructure. The position of a single nanoemitter at few nanometers from the metallic surface can also conduct to quenching of fluorescent light. Quenching is the phenomenon when non-radiative recombination channels are predominant respect to radiatives. At very low distance, the quenching is mainly due to the short distance coulomb interaction. Quenching is characterized by the acceleration of decay rate but reduction of fluorescence intensity (brightness). It is associated to the excitation of lossy surface modes at the metal interface.

In order to avoid quenching by the flat gold surface, we have spin-coated a thin dielectric layer of 10 nm (measured by Dektak profilometer) in all the antennas fabricated in this thesis. With this separation between the single nanocrystals and the metallic surface, the contribution of quenching in fluorescence emission is reduced to less than 5 %, according to numerical simulations reported in [27].

We start by discussing the the modification of fluorescence emission in an active antenna which has experienced an over-development process. In the over-development case, the resist LOR3A layer is removed during the development step around the hole by some micrometers causing the collapsing of the PMMA layer. By lift-off processing the MF-319 solvent can not enter so that the lift-off is inefficient. We can see in scanning electron image of Figure V.1a that the gold has covered the PMMA layer by this smooth transition. From the image we can observe that the nano-disk lays at the bottom of the transition surrounded by the metallic thin film. In the same Figure V.1a, we can note that there is a nanometric separation between the nano-disk and the metallic layer.

When the patch antenna has experienced over-development, there is no chance that the MF-319 solvent dissolves the resist beneath the thin metallic layer. In the case of over-developed antennas we have overcame this limitation by using the ultrasonic cleaner.

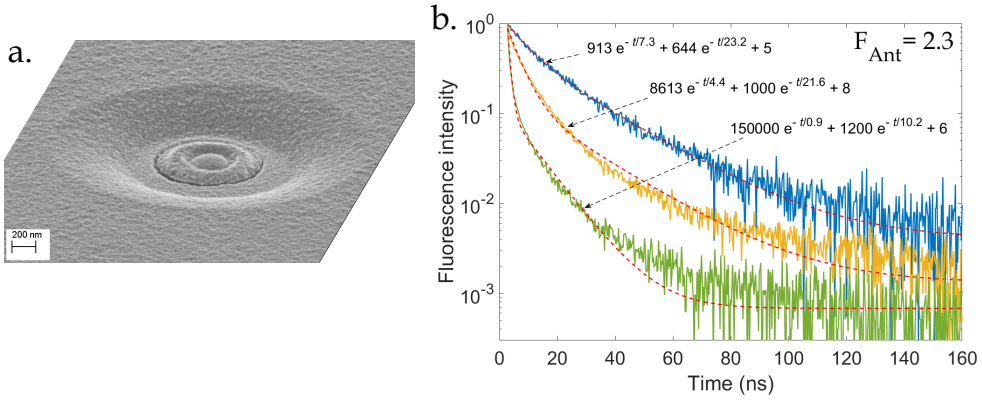

Fig. V.1 *a) Scanning electron image of an antenna with over-development processing. b) Photoluminescence decay curves of the same emitter at different conditions during fabrication. The nanocrystal over Au substrate (blue curve). Same nanocrystal after gold deposition in over-development case (yellow curve). Same emitter after lift-off processing (green curve).*

The ultrasonic cleaner generates ultrasonic waves which agitate the liquid in such as way that the delicate 20-nm layer is instantly broken. The rupture of the layer allows to the MF-319 product to dissolve the resist layer and get rid of the metallic/dielectric residues around the antennas. Of course, the ultrasonic bath was exceptionally used on these over-developed antennas and it is not recommended for conventional square lift-off processing. Indeed, the risk of removing as well the gold patch by ultrasonic operation is quite high.

In Figure V.1b, the fluorescence decay curves of the single nanocrystal are presented for three different conditions. In the first case, we present the lifetime of the nanoemitter laying 10 nm above the flat gold layer (blue curve in Figure V.1b) before development. By fitting the blue decay curve we can distinguish a fast and long component corresponding to $\tau_f = 7$ ns and $\tau_s = 22$ ns, respectively. The second decay rate curve (the yellow one), corresponds to the same nanocrystal after gold deposition in over-development case, as it has been discussed before and shown on Figure V.1a. In this situation we can observe that the patch disk provides a first acceleration of emission, especially in the fast component. Finally, the green decay curve represents the case when the patch antenna has been isolated from the lateral Au film. In such case, the fluorescence emission is found that accelerate both components. The successful lift-off processing has provided the maximum acceleration of the emission with an antenna factor of F_{Ant}=2.3.

The active nanoantenna presented above has been fabricated using a dielectric spacer of 70 nm. Numerical results performed in patch systems have demonstrated that the Purcell factor decrease as the thickness of the dielectric spacer increase [27]. The reduction of the dielectric layer may provide better confinement of the electromagnetic field and achieve important Purcell factors. Nevertheless, as the deposition of the metallic nanodisk is made by thermal vapour deposition, the nanocrystals could be damaged during the evaporation process if the dielectric layer is not thick enough to protect them.

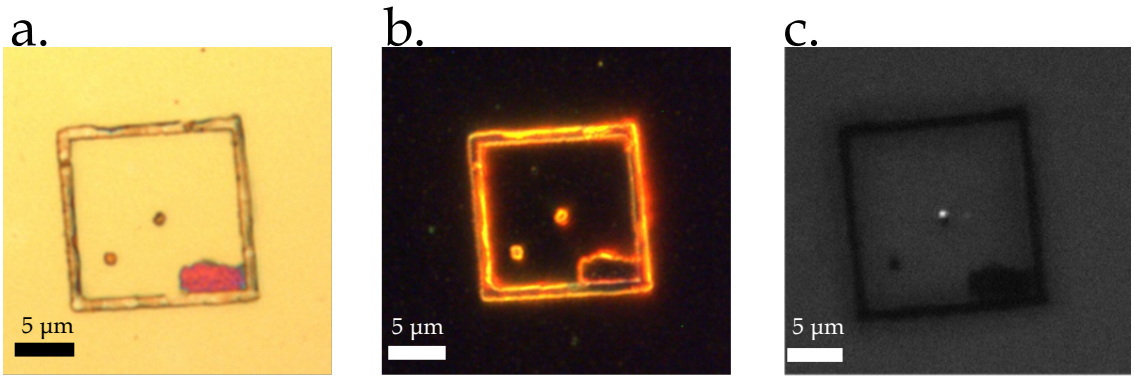

Fig. V.2 *a) Bright-field and b) Dark-field optical image of a patch nanoantenna after proper lift-off. c) Fluorescence microscope imaging of the same antenna (integration time 800 ms).*

To overcome this limitation and improve the confinement of the electromagnetic field, Arnaud Choux from the INSP is currently exploring another approach to fabricate gap antennas based on the fabrication of thin Au flakes.

b) Optical and fluorescence imaging characterization

We have characterized the active nanoantenna presented before in terms of optical microscopy techniques. In Figure V.2 we show optical bright-field, optical dark-field and confocal fluorescence microscope imaging of the active antenna after the complete lift-off processing.

Figure V.2a shows color reflection optical image of two gold patches framed by a gold-square. The center patch corresponds to an active antenna. At a distance of 5 μm in the left-bottom side we have a passive nanoantenna fabricated by similar conditions. In the same image V.2a we can observe some residues of the 20 nm-Au layer remaining inside the frame gold-square after lift-off processing. These residues are far enough to neglect any interaction with the active and passive antennas.

Figure V.2b corresponds to the dark-field optical image of the sample showing the light scattered by the edges of the nanostructures. In Figure V.2c we show the corresponding fluorescence image. From Figure V.2c, we can observe that all the metallic zones with 20 nm-Au thickness (frame of the square, residue inside and passive nanoantenna) show significant less fluorescence than the active antenna at the center. The combination of optical bright-field, dark-field and fluorescence imaging in Figure V.2 helps to illustrate the successful coupling between the metallic nanoantenna and the single nanocrystal.

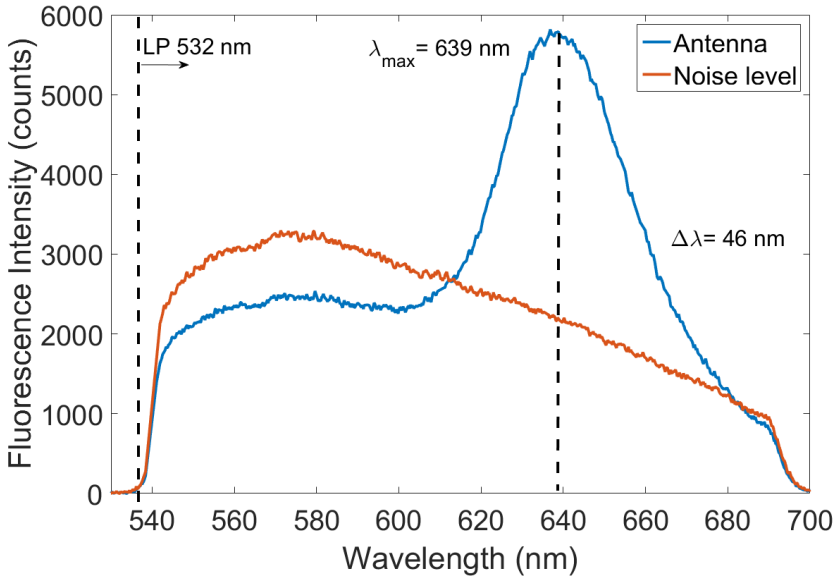

Fig. V.3 *Photoluminescence emission spectra of the antenna and the level of the noise around 5 μm distant from the antenna. Integration time 20 s.*

c) Photoluminescence spectra

We have characterized the active antenna by photoluminescence emission spectra. For the excitation of the antenna we have used a diode laser emitting at 470 nm in continuous mode. In the experimental set-up, we have installed two fluorescence filters: 1) a long-pass Semrock filter LP 532 nm to suppress the excitation laser and 2) a band-pass Semrock filter FF01-609/152 to select the light emitted by the nanoantenna. We have measured two photoluminescence spectra, one on the position of the patch antenna and the second some micrometers aside using exactly the same parameters in excitation and collection (20 s integration time in the spectrometer).

In Figure V.3 we show the photoluminescence emission spectra of the antenna (blue curve) and the level of the noise some micrometers far away from the nanoantenna (orange curve). The last spectra corresponds to the luminescence of the lift-off resist (combined with the dielectric layers used for the fabrication of the antenna). From Figure V.3 we observe that the antenna emission spectrum exhibits a maximum emission peak around λ_{max} = 639 nm with linewidth of $\Delta\lambda$ = 46 nm (Full Width at Half Maximum). We can note that the emission spectra of the nanoantenna is closed to the emission spectra of a single nanocrystal at λ_{max} = 639 nm. However, the low-wavelength part of antenna emission spectrum has the same shape than the luminescence of the resist layer. Therefore, in the antenna emission spectrum we can identify one part coming from the luminescence of the LOR3A layer and one part due to the luminescence of the nanocrystal.

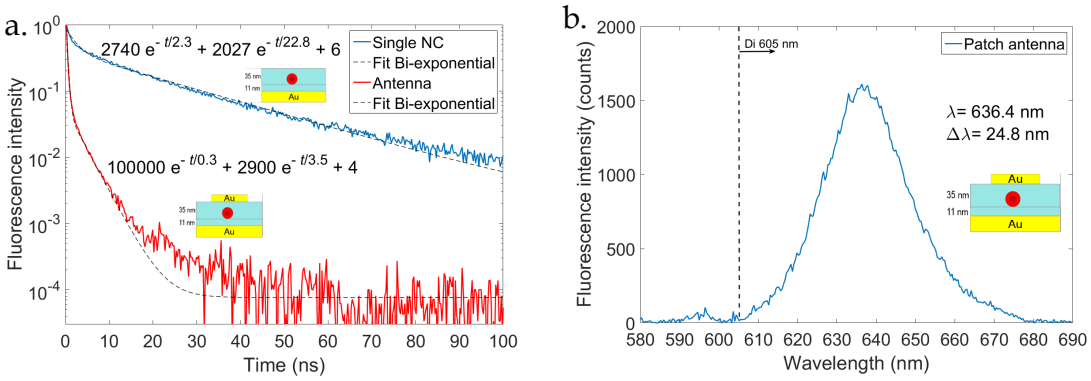

Fig. V.4 *a) Photoluminescence decay curve of a single nanocrystal before and after the coupling with the patch antenna. b) Emission spectra of the patch antenna.*

V.3 Antenna with super-poissonian emission

V.3.1 Acceleration of emission

The antennas fabricated during this thesis have shown different effects depending of the dipole orientation and fabrication parameters. We have seen in section II.1.7 that single nanocrystals allow radiative multi-exciton recombination which can be identified in the fast component of the decay curve. More precisely, the bi-excitonic recombination can be suppressed by using a post-processing temporal filter. In this section, we will discuss the case of an active patch antenna when a temporal filter is used.

In Figure V.4a we show the photoluminescence decay curves of the nanocrystal before and after the deposition of the nano-disk. This antenna has shown an antenna acceleration factor of $F_{Ant} = 6$. When the decay curve is fitted using a two-terms exponential model we calculate a fast and a slow component of $\tau_f = 0.3$ ns and $\tau_s = 3.5$ ns, respectively. In Figure V.4b we show the fluorescence emission spectra of such antenna. From the Figure V.4b we can estimate the maximum emission wavelength centered at λ= 636 nm with an emission linewidth of $\Delta\lambda$= 25 nm, approximately.

In Figure V.5a we show the photoluminescence decay curve of the nanocrystal laying on the flat gold layer and coated by the thin PMMA layer (35 nm thickness). The blue curve represents the complete events obtained during the measurement while the the orange curve is obtained after filtering the first 2.0 ns. In Figure V.5b and c we show the corresponding second-order autocorrelation functions, $g^{(2)}(\tau)$. From Figure V.5b (without any temporal filter), the multi-excitonic contribution calculated by the ratio of the zero-delay peak area and the lateral peak area is approximately $\frac{g^{(2)}(0)}{g^{(2)}(\tau_{rep})} = 0.5$.

On the other hand, from the second-order autocorrelation function $g^{(2)}(\tau)$ obtained after removing the first 2.0 ns in the decay curve (Figure V.5c), we can observe that the contribution of the multi-excitonic emission has been reduced to a value of $\frac{g^{(2)}(0)}{g^{(2)}(\tau_{rep})} = 0.3$.

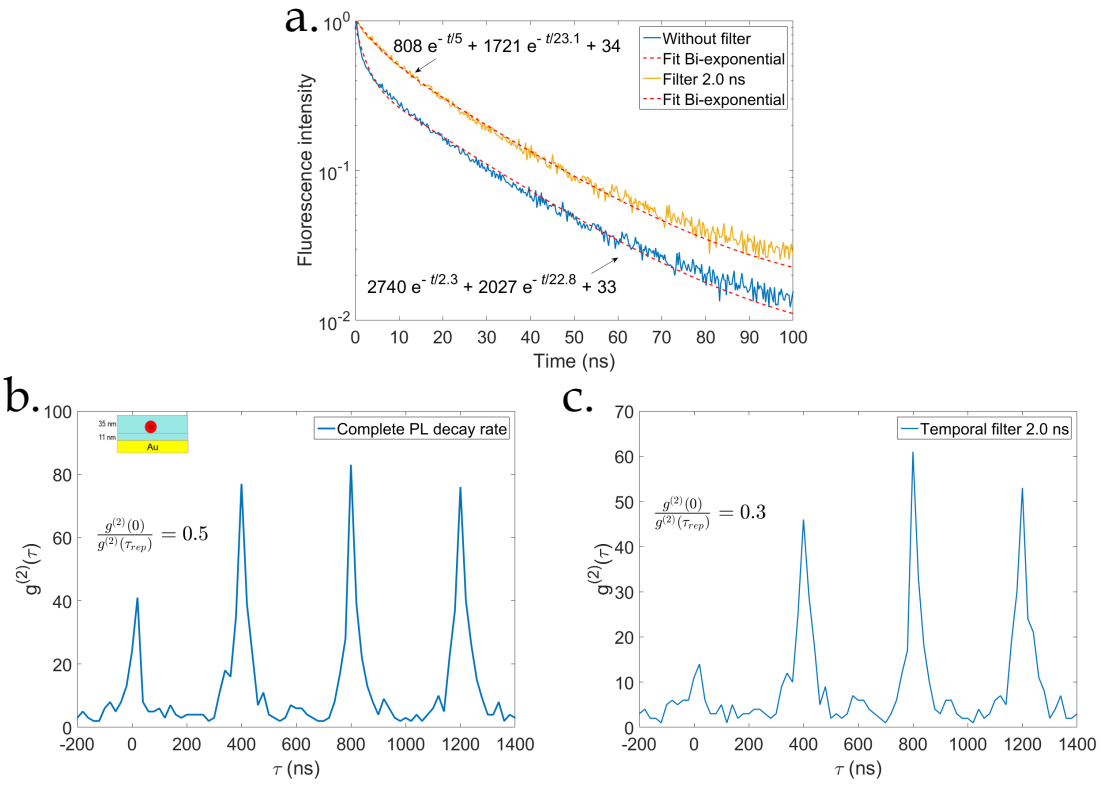

Fig. V.5 *a) Photoluminescence decay curve of the single nanocrystal without filter (blue line) and filtered during the first 2.0 ns (orange line). b) Second-order autocorrelation function $g^{(2)}(\tau)$ without filter. c) Second-order autocorrelation function $g^{(2)}(\tau)$ after 2.0 ns filter. The autocorrelation functions were plotted using 20 ns as binning time. Integration time: 140 s.*

The multi-excitonic processes have been filtered with the post-processing filter, the remaining events in the decay curve corresponds mostly to the excitonic recombination of a single-photon source.

Thanks to the antenna, the change of the local density of photonic states leads an acceleration of spontaneous emission. As Auger processes become less efficient, the recombination of multi-excitons becomes radiative. In Figure V.6a, we represent the decay curve and the bi-exponential fit corresponding to the antenna. The fast and slow component are $\tau_f = 0.3$ ns and $\tau_s = 3.5$ ns, respectively. In Figure V.6b, we show the second order autocorrelation function $g^{(2)}(\tau)$ of the patch antenna without filter. The peak at zero-delay is a signature of radiative multi-excitonic recombination in a single nanocrystal.

If we now apply the same 2 ns temporal filter (removal of the first 2 ns) to separate fast and slow component, we should recover the single-photon feature of the nanocrystal inside the patch antenna. In Figure V.6c, we show the second-order autocorrelation function after the subtraction of the first 2.0 ns in the photoluminescence decay curve

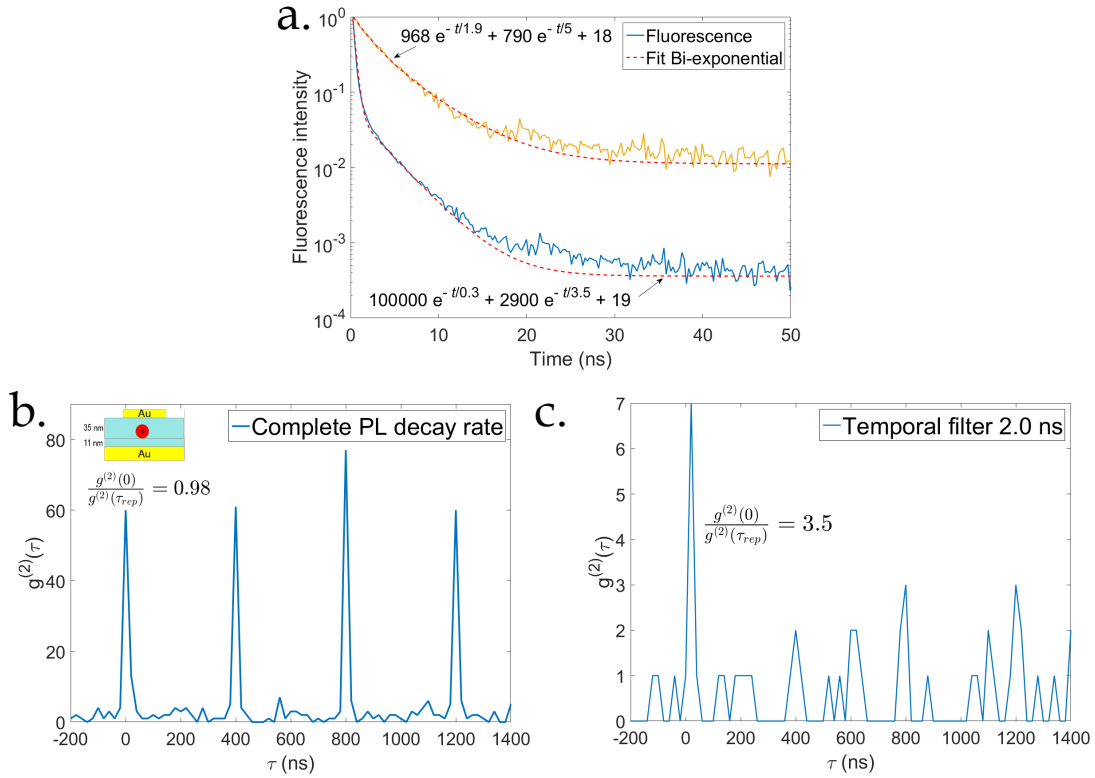

Fig. V.6 *a) Photoluminescence decay curve of the patch antenna without filter (blue line) and filtered during the first 2.0 ns (orange line). b) Second-order autocorrelation function $g^{(2)}(\tau)$ without filter. c) Second-order autocorrelation function $g^{(2)}(\tau)$ with 2.0 ns filter. The autocorrelation functions were plotted using 20 ns as binning time. Integration time: 90 s.*

of the nanoantenna. From the Figure V.6c, we can observe that the ration $\frac{g^{(2)}(0)}{g^{(2)}(\tau_{rep})}$ has raised to a value above the unity $\frac{g^{(2)}(0)}{g^{(2)}(\tau_{rep})} = 3.5$. The zero-delay peak, which represents the probability of emitting two or more photons at the same time in the same excitation pulse, has raised well above the shot noise limit.

From the perspective of photon statistics, when $\frac{g^{(2)}(0)}{g^{(2)}(\tau_{rep})} > 1$, it corresponds to a super-poissonian distribution. The probability of detecting two or more photons at the same time is higher than a classical poissonian distribution. It means that, if we detect a photon at time $\tau = 0$, there is a higher probability of detecting a second photon at short times (picoseconds timescale) than at longer times. The photons arrive to the photodiodes in compact groups, commonly said bunched of photons.

In this antenna we have found that the temporal distribution of photon presents a super-poissonian signature $g^{(2)}(0) > g^{(2)}(\tau_{rep})$ when we apply a post-processing temporal filter.

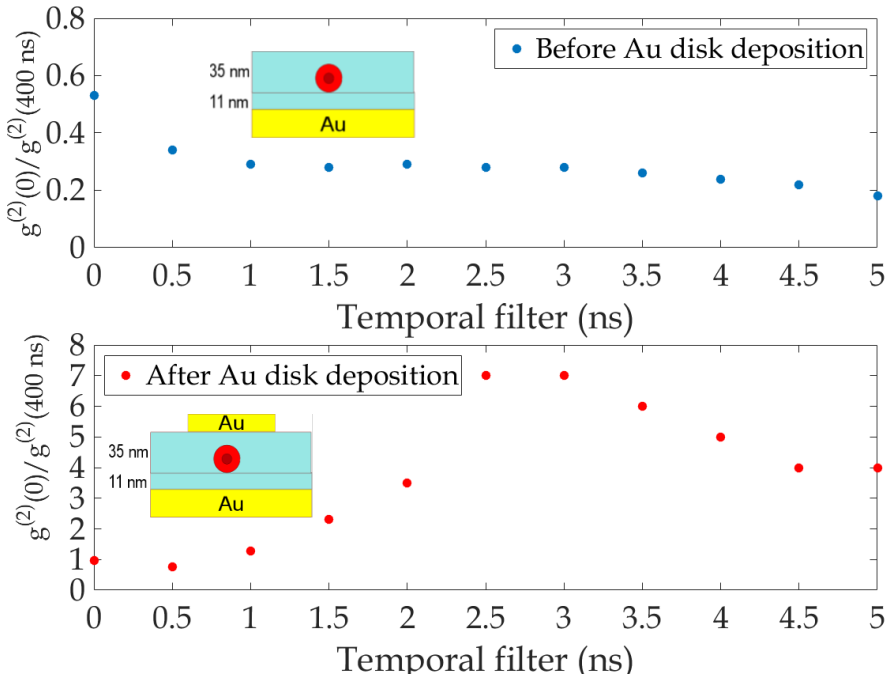

Fig. V.7 *Ratio of the zero-delay peak with respect to the first peak at 400 ns ($g^{(2)}(0)/g^{(2)}(400ns)$) for different cut-off times for the same nanocrystal. a) Before depositing gold patch, b) inside antenna.*

V.3.2 Temporal filter before and after coupling with nano-disk

In order to analyse the different phenomena observed by filtering the fast component, in Figure V.7, we have traced the value of $g^{(2)}(0)/g^{(2)}(\tau_{rep})$ as a function of the temporal filter (with different cut-off times). The upper graph shows the case when the single nanocrystal is coupled to the Au substrate (no antenna $\tau_{fast} = 2.3$ ns and $\tau_{slow} = 23$ ns). The bottom graph shows the results obtained with the same nanocrystal inside the plasmonic antenna. In the upper graph we can see that the temporal filter tends to reduce the zero-delay peak $g^{(2)}(0)/g^{(2)}(\tau_{rep})$ as the filter gradually removes the fast component. From Figure V.7a, we observe that most of the multi-excitonic emission is reduced almost to the half after filtering 1 ns in the decay curve. Indeed, we know from Figure II.10 that the lifetime of the bi-exciton is $\tau_{BX} = 500$ ps approximately. After this cut-off time, the contribution of multi-excitonic emission continues decreasing and the peak at zero-delay decreases until $g^{(2)}(0)/g^{(2)}(400ns) = 0.26$ at 3.5 ns. We have extended the temporal filter to 10 ns and we have found that the zero-delay peak is as small as 0.12 times the adjacent peak (no shown in the graph). This corresponds to the fact that we have removed the bi-excitonic contribution.

On the other hand, in the case of the patch antenna ($\tau_{fast} = 0.3$ ns and $\tau_{slow} = 3.5$ ns), the zero-delay peak increases with the cut-off time. For a cut-off time equal to 3.0 ns, $g^{(2)}(0)/g^{(2)}(400ns)$ reaches its maximum value of 7. Then, for longer cut-off times, $g^{(2)}(0)/g^{(2)}(400ns)$ starts to decrease. Indeed, 3.5 ns corresponds to the lifetime of exciton

recombination inside the antenna. By applying a temporal filter longer than 3.5 ns we mainly record noise which has a $g^{(2)}(0)/g^{(2)}(\tau_{rep}) \sim 1$.

In summary, by applying a post-processing temporal filter, for a single nanocrystals close to a gold surface, the zero-delay peak goes close to 0. With this filtering, we have removed the fast multi-excitonic recombination of the decay curve. Meanwhile, for the nanocrystal embedded in the patch antenna, the zero-delay peak increases with the use of the same temporal filter until reaching a maximum of 7 for a cut-off time of 3.0 ns (corresponding to the exciton lifetime). This effect has been observed in three antennas. The values of $g^{(2)}(0)/g^{(2)}(\tau_{rep}) > 1$ is a sign of a super-poissonian emission. The origin of this super-poissonian emission is not understood until now.

V.3.3 Temporal filter with different binning time

In this section we will show that the super-poissonian distribution of photons is independent of the binning time which is used to displayed the second-order autocorrelation function $g^{(2)}(\tau)$. We start by presenting in Figure V.8 the set of graphs used to construct Figure V.7. All the graphs were plotted with a binning time of 20 ns with a cut-off time between 0.5 ns and 3.0 ns. From the figure we can note, for the antenna, the continuous increase of the zero-delay peak as the filter cut-off time increase.

We now check tha this behaviour is not dependent of the binning. In Figure V.9 we show the same set of autocorrelation functions but now with a binning time of 10 ns. We can note that all the peaks are about half smaller than with the 20 ns binning. Indeed, in the 10 ns binning the number of events is divided by two whereas the number of time channels is multiplied by two. From Figure V.9 we can observe that for the antenna the zero-delay peak compared to the lateral peaks raises to higher values when the cut-off time increase.

In conclusion, the signature of super-poissonian distribution of photons after the post-processing of the second-order autocorrelation function is independent of the binning time used to plot the graphs.

V.4 Fringe pattern

Several studies have demonstrated the capacity of the patch nanoantenna to direct light on specific solid angles [27], [23]. The calculated radiation pattern for a point emitter presents several highly directional lobes. The direction of emission of these lobes are defined by two principal features:

- The morphological shape of the patch antenna. The angular direction of the lobes increases as the diameter of the patch is reduced. This property of emission is commonly understood following the diffraction theory of light which states that the diffraction of incident light depends on the size aperture.

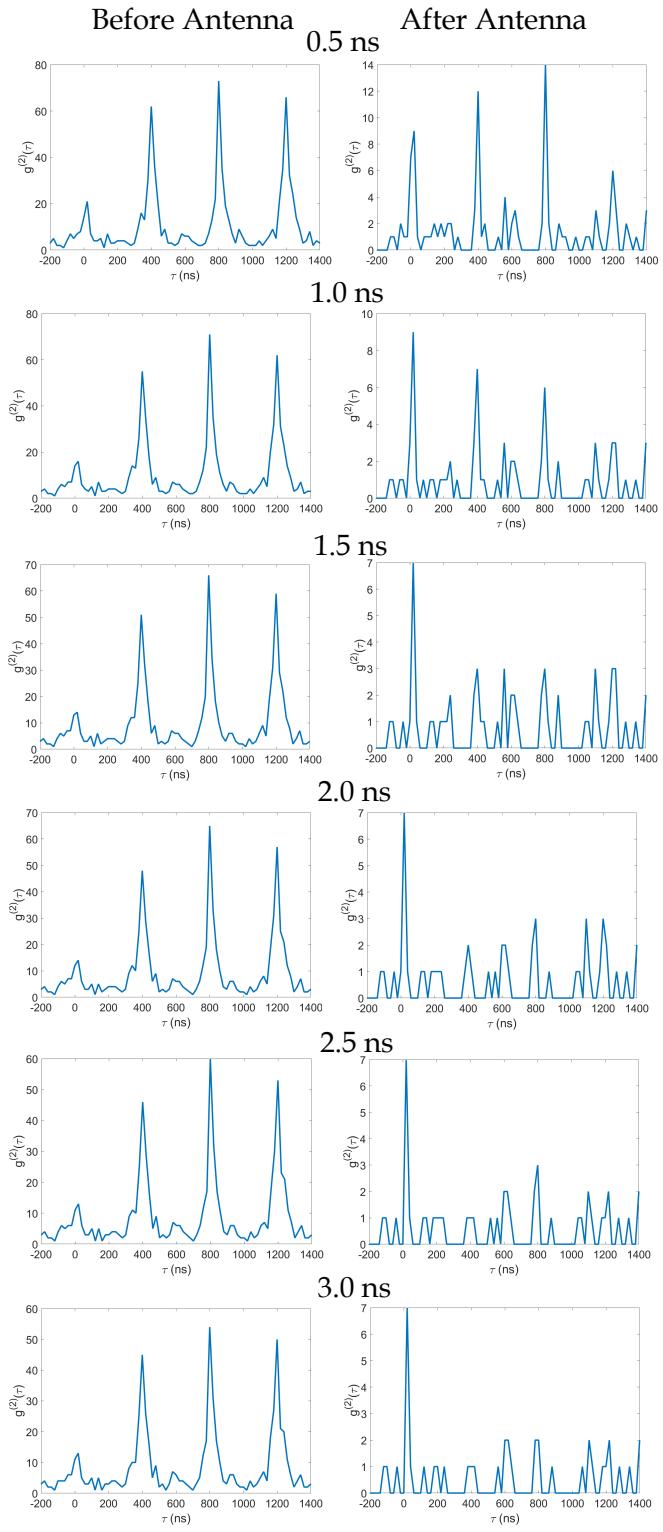

Fig. V.8 *Second-order autocorrelation function $g^{(2)}(\tau)$ before antenna (left graphs) and after antenna (right graphs) for different cut-off times with binning time of 20 ns.*

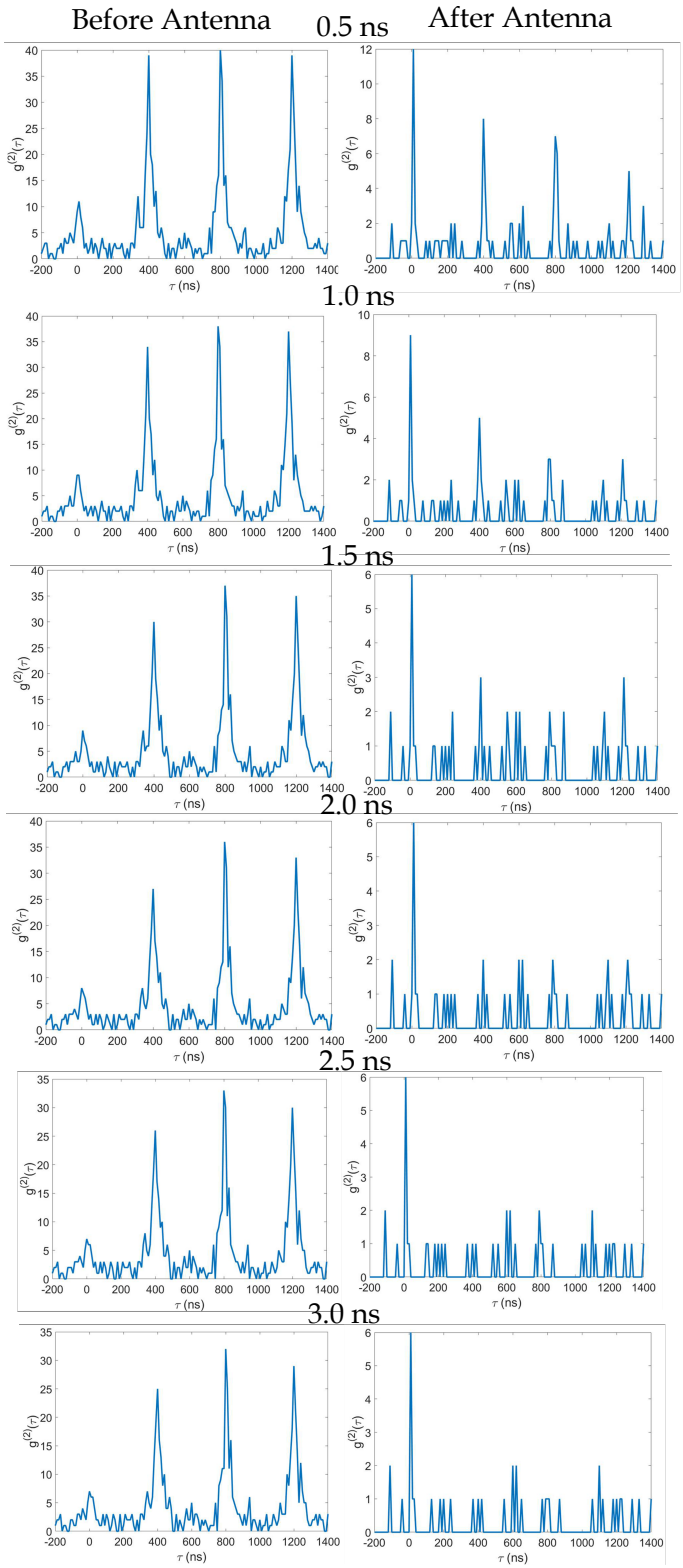

Fig. V.9 *Second-order autocorrelation function $g^{(2)}(\tau)$ before antenna (left graphs) and after antenna (right graphs) for different cut-off times with binning time of 10 ns.*

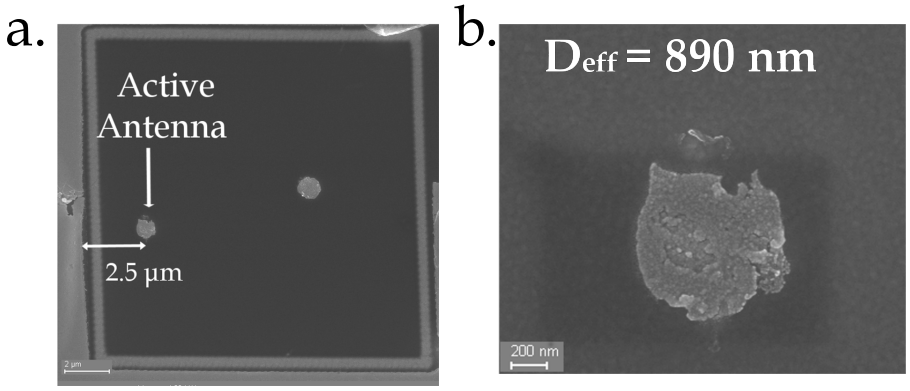

Fig. V.10 *a) Scanning electron image of the 15×15 µm square containing two patch antennas. One active antenna at 2.5 µm from the lateral edge (left one) and one passive antenna at the center of the square. b) Amplified electron image showing the active antenna with an effective diameter of D_{eff} = 890 nm.*

- The relative position of the single nanoemitter below the nano-disk. When the single emitter is positioned at the center of the patch, the emission pattern holds symmetry with respect to the perpendicular axis. However, for some misalignment of the emitter (off-center), asymmetries on the radiation pattern can be expected.

In this section we will discuss the emission pattern of the patch antenna that we have already discussed and corresponding to super-poissoninan emission. In Figure V.10a, we present the scanning electron image of a 15×15 μm square containing two nanoantennas. The active nanoantenna corresponds to the left one on the electron microscope image. In Figure V.10b, we present the morphological characteristics of the active antenna with an effective diameter of D_{eff} = 890 nm, approximately. The antenna is positioned 2.5 μm from the left metallic edge of the square.

We have characterized the emission of the patch antenna in terms of Fourier imaging technique. In Figure V.11 we show the experimental set-up. The nanoantenna is placed at the focal plane of the air objective (100× magnification and 0.95 NA). Our fluorescence microscope is composed of two lenses in confocal geometry, the objective lens (f_{obj}) and the tube lens (f_{tube} = 180 cm). The image of the object is reconstruct at the image plane with an magnifying factor of $g = 1/G = 1/100$.

At the output of the microscope, we have installed another optical lens (Fourier lens $f_{Fourier}$) with a distance f_F = 150 mm from the image plane. Finally, we have settle the EM-CCD camera at the same distance f_F from the Fourier lens as it is shown in the schematic representation of Figure V.11. On the camera sensor, the position x (with respect to the optical axis) corresponds to the direction $\beta = x/f_F$. This direction β corresponds to the Fourier transform component of the image, which is directly linked to α the corresponding Fourier transform component (or the direction of the emitted light) of the object by $\beta = g\alpha$. We have used an EM-CCD camera iXon Ultra 897 manufactured by ANDOR technology. The sensor is composed of 512×512 pixels with pixel size of 16×16

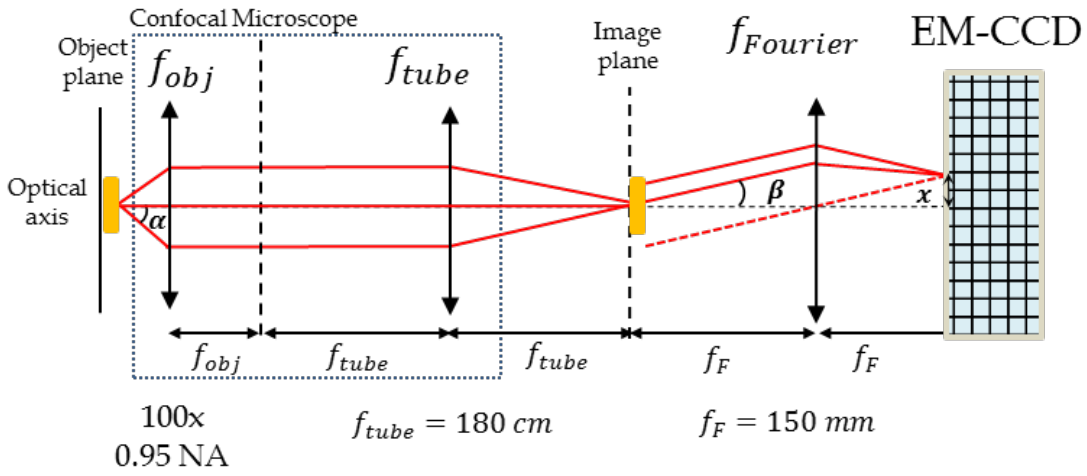

Fig. V.11 *Experimental set-up used to image the emission pattern of the patch nanoantenna.*

μm.

In Figure V.12a we show the emission diagram of the patch antenna. We have integrated during 40 s of acquisition time. From the Figure V.12a we can observe that the emission pattern is not symmetric along the optical axis. The maximum emission is slightly deflected from the center of the Fourier plane. This asymmetry can be attributed to a possible off-center alignment of the single nanoemitter with respect to the perpendicular axis of the nano-disk, as numerical calculations suggest [27].

Beside the deflection of light emission in Figure V.12a, we can also observe the presence of a fringe pattern on the Fourier image. We have traced a red line along the fringes to estimate the contrast (or visibility) and periodicity of the pattern. In Figure V.12b we show the intensity profile of the line. The visibility of the pattern reaches ν= 0.11 and the period between consecutive maximums is equal to Δ_{Max}= 24 px (384 μm). This interfering in Fourier plane is associated to the corresponding angle $\beta_{interfering} = \frac{\Delta_{max}}{f_F}$.

Given the periodicity of the pattern we can estimate the distance at which two hypothetical point sources can produce such interference pattern. The distance between consecutive maximums (Δ_{Max}) is proportional to the difference in the optical path light. We express this as interference fringe. Following the formalism of Young for two emitting points separated by a distance a, constructive interference can occur in far-field for direction $\alpha_{interfering} = \frac{\lambda}{a}p$, where p is an entire number. By associating interference pattern in the Fourier plane, we can state that

$$\alpha_{interfering} = \beta_{interfering} \times G, \tag{V.1}$$

$$\frac{\lambda}{a} = \frac{\Delta_{Max}}{f_F} \times G \Rightarrow \quad a = \frac{\lambda f_F}{\Delta_{max} \times G}.$$

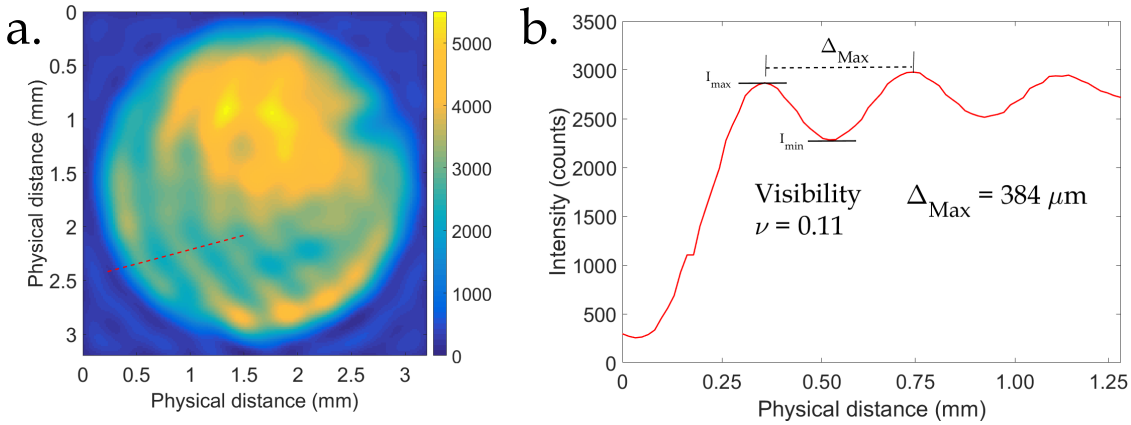

Fig. V.12 *a) Fourier imaging of the plasmonic patch antenna b) line trace showing the periodicity of the fringe pattern. Distance between maximums* Δ_{Max} = *384 μm, visibility* ν= *0.11.*

By calculating the distance a with expression (V.1) we obtained $a = 2.5$ μm, approximately. Indeed, this value corresponds to the distance between the active antenna and the metallic board edge of the square, as it is shown in the scanning electron image of Figure V.10a. We then conclude that the interference pattern is produced by the interference between the light emitted at the position of the patch antenna and the light scattered by the metallic edge after propagation $a = 2.5$ μm.

From the several antennas fabricated in this thesis, this antenna was the only which has produced an interference fringe pattern. The rest of the antennas have been fabricated nearly at the center of the lift-off square and none fringes were observed. For those antennas, the average distance between the gold nano-disk and the metallic edges extends to 7 μm. We may assume that the propagation length of the surface plasmon is not so long that it is absorbed before reaching the edges. The observation of the interference fringe pattern in far-field evidence the plasmonic coupling of the single nanoemitter with surface plasmons on both metal-dielectric interfaces.

For a fringe pattern to be observed, the two waves need to be in phase with each other. It means that, the distance between the sources has to be lower than the coherence length. The linewidth emission of $\Delta\lambda = 24.8$ nm corresponds to a coherence length of $L_c = 15$ μm. Therefore, the two train waves can exhibit interference only when they are not extended more than L_c. Indeed, the distance of 2.5 μm between antenna and metallic edge is smaller than L_c.

V.5 Conclusion

With the active antennas discussed in this chapter, we have shown how the modification of local density of photonic states between both metallic layers can accelerate the fluorescence emission of a single nanocrystal. We have quantified the direct modification of LDOS by defining an antenna factor F_{ant} corresponding to the photoluminescence decay rates before and after the coupling of the patch and the single nanocrystal emission.

In section V.2.1 we have discussed the acceleration of emission of the quantum dot in the case of an over-developed antenna. We have found that, when the nanoantenna is over-developed, there is a first moderate acceleration of fluorescence emission. Then, for a complete lift-off processing, the maximum acceleration of emission is achieved.

We have evidenced super-poissonian distribution ($g^{(2)}(0) > 1$) of light emitted by an active antenna containing a single nanocrystal. The use of a temporal filter in the photoluminescence decay curve has permitted to identify such super-poissonian statistics of light.

For a specific antenna, close to the edge of the metallic squared, the emission pattern presents some fringes due to interferences between patch antenna emission and scattering on the edge.

Chapter VI
General conclusion

Spectroscopy analysis on single nano-emitters

We have carried out experimental studies on single colloidal nanocrystals CdSe/CdS. We have evidenced mono-exciton, bi-exciton and multi-exciton radiative recombination in such nanocrystals. We have developed an experimental set-up which allows to analyze fluorescence dynamics with emission spectra simultaneously at room temperature.

In the case of bi-exciton recombination, we have implemented a temporal post-processing filter to separate fast and slow recombination processes from the photoluminescence decay curve. This temporal filter allows to retrieve single-photon emission in the particular case of bi-excitonic recombination.

We have developed a theoretical model for describing the fluorescence intensity of the emitter. Our model is based on the number of excitons (electron-hole pairs) created inside the nanocrystal at different excitation powers. The model takes int account a maximum of bi-exciton radiative recombination and has a good agreement with experimental results for moderate excitation power. With our model, we have estimated the quantum efficiency of bi-exciton emission of $\eta = 0.21$.

Optical In-situ lithography protocol

We have carried out topographic studies using Atomic Force Microscopy imaging to improve development and lift-off processes during the fabrication of patch antennas with in-situ lithography protocol. The analysis of the topographic images in each process has allowed to improve the overall performance of the protocol and determine lithographic parameters for passive and active patch nanoantennas with single emitters. The robustness of the in-situ protocol has permitted to fabricate antennas in a systematic way.

We have proposed the incorporation of an intermediate step in the in-situ protocol to improve the efficiency during lift-off processing. This technique consists in writing a micrometer square after the initial hole to increase the solvent entrances into the resist bi-layer.

Reflectivity spectroscopy measurements

In chapter III, we have described the experimental set-up used to perform reflectivity measurements on individual patch antennas. We have defined the differential reflectivity spectroscopy (DRS) as a factor which accounts for the absorption properties of the metallic structures. We have found that, for some antennas, the differential reflectivity factor can reach nearly $DRS = 0.5$ (50% of absorption with respect to Au surface including PMMA). The DRS value is an indicator of the capacity of the nanostructure to efficiently absorb incident light and transform it into another relaxation mechanisms, for example ohmic losses characteristic in metallic structures. We have found that, within an array of 4×4 passive nanoantennas fabricated with exactly similar parameters, the shape, effective diameter and wavelength of maximum absorption can be different between each other. The reflectivity technique developed in this thesis can be adapted to nanostructures holding arbitrary shapes and/or sizes.

Coupling of quantum dots with patch nanoantennas

In Chapter V, we have studied the photoluminescence properties of two active antennas in terms of acceleration of spontaneous emission (Purcell factor) and photon emission statistics. We have first discussed the importance of the lift-off processing in the acceleration of spontaneous emission. The maximum acceleration has been reached when the thin gold layer was removed from the vicinity of the nanoantenna with a complete lift-off process.

Then, in the second active antenna, we have discussed the modification of emission in terms of photon statistics properties of a single nanocrystal before and after the coupling with the patch gold disk. We have shown that active antennas can produce super-poissonian distribution of photons $\left(\frac{g^{(2)}(0)}{g^{(2)}(\tau_{rep})} > 1\right)$ when we use a temporal filter to separate slow and fast recombination processes and keep the fast ones. This antenna has shown $\frac{g^{(2)}(0)}{g^{(2)}(\tau_{rep})} = 7$ for a cut-off filter time corresponding to the lifetime of the exciton.

We have measured the emission diagram of the active antenna. We have found an interfering fringes pattern with a visibility $\nu = 0.11$. We have found that the interferences are associated to nanoantenna emission and the scattering of its emission on the lift-off square edge.

Appendix A

In-situ protocol: supercontinuum laser

A.1 Results in testing the Development and liftoff of LOR3A

Parallel with the topographic studies using the blue diode laser, we have carried out topographic imaging of one hole created with super continuum laser in a resist bi-layer.

A.1.1 Preparation of the sample

The preparation of the sample was described in section IV.2.1. Figure A.1 recovers the information of thin dielectric layers deposition.

A.1.2 Laser exposure

The exposure of the resist bi-layer was performed using a supercontinuum laser in a range from 550 to 605 nm, repetition rate of 80 MHz and average optical power of 16.82 mW (measured at 577 nm). We create a hole during 2 seconds of exposure time.

In Figure A.2 we show the topographic AFM image of the initial hole. From the line profiles of Figure A.2a and b, we can distinguish two different diameters associated to the upper PMMA and LOR3A layer. We clearly note the smallest size corresponds to the bottom part of LOR3A layer (around 227 nm) and this value is three times smaller than

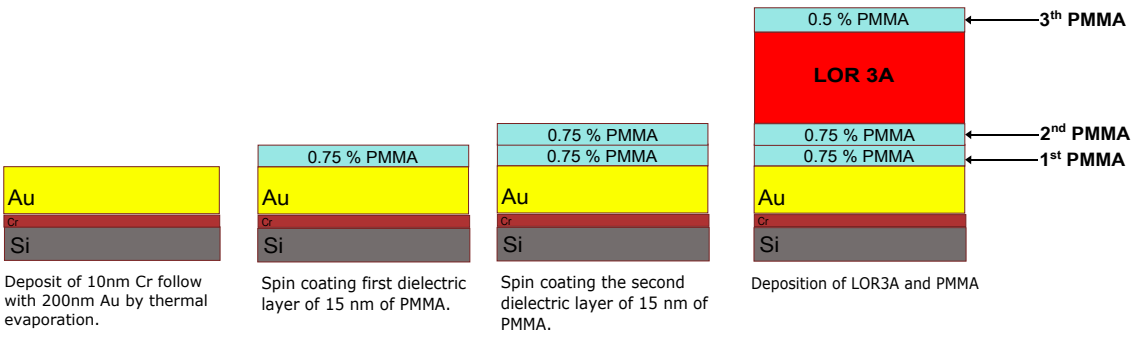

Fig. A.1 *Procedure of thin film deposition for in-situ protocol.*

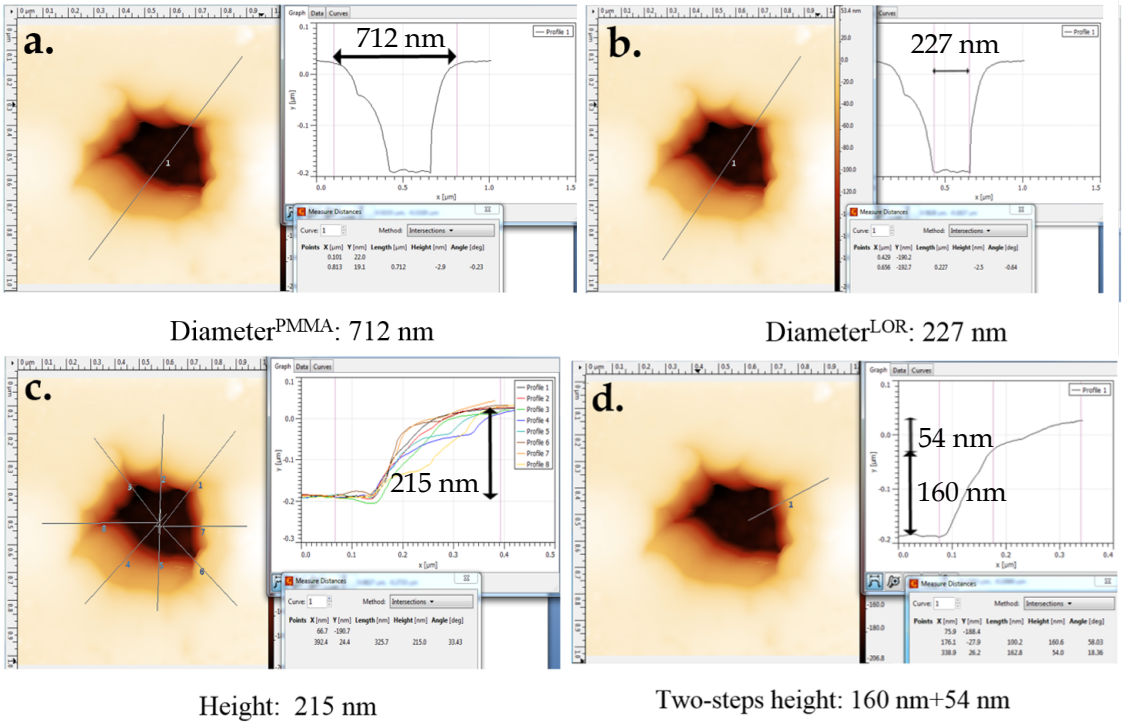

Fig. A.2 *Hole created with supercontinuum laser with 2 seconds of exposure.*

the holes produced with the blue diode laser.

In Figure A.2, we can observe profile line around the hole which estimate a height of 215 nm. In Figure A.2d we show the characteristic of the edge hole described as two-step transition from the center of the hole to the upper PMMA layer.

A.1.3 Development lift-off resist LOR3A

We carried out the development of the sample using pure developer MF-319 during 5 seconds. The topographic results are showed in Figure A.3. From the image we can observe the homogeneous expansion of both LOR3A and upper PMMA layers. In the case of the diameter in the resist bi-layer the expansion was from 227 nm to 1.3 um, more than 5 times. The depth of the hole after development process is close to the height before (with respect Figure A.2c).

From Figures A.3a we can note a blurry outline enclosing the perimeter of the hole. This feature has been observed before and it corresponds to an artifact of the microscope tip. This limitation of the resolution prevents to distinguish the details at the center. However, the image is clear enough to estimate the diameter and height of the hole. From the same Figure A.3a, we can also distinguish some residues of LOR3A remaining inside the hole close to the edges, especially on the left side part.

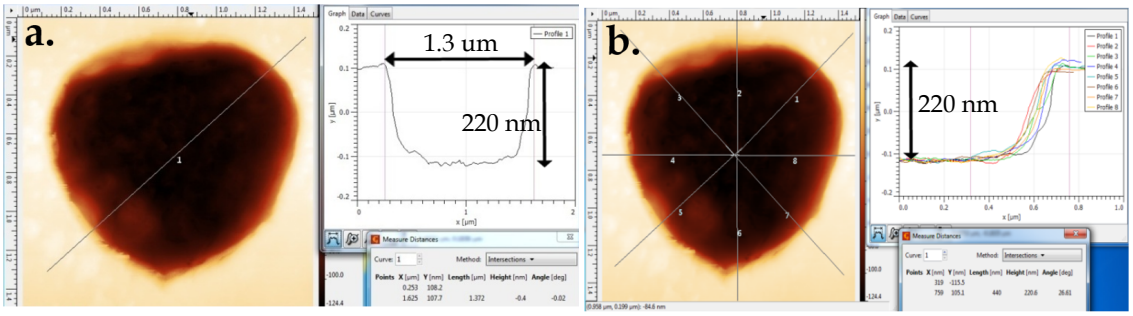

Fig. A.3 *Same hole after development in pure MF-319 during 5 seconds.*

A.1.4 Thermal deposition of Au film and lift-off processing

We carried out the thermal gold deposition of 20 nm thickness layer. We then performed lift-off processing by submerging the sample 50 seconds in pure developer MF-319. In Figure A.4 we show the results in topographic surface microscope.

From Figure A.4a we clearly note the hole expansion from 1.3 to 3.3 μm diameter. The difference in height from the center of the hole to the external surface is about 223 nm, very close to the precedent value (Figure A.3b).

In Figure A.4c we show the diameter size of what it would be the disk of the patch antenna (1.3 μm). If we observe carefully on the edge of the disk in Figure A.4c, we can note a high contour surrounding the antenna. Figure A.4d shows the profile height from this raised border (around 50 nm high) to the center of the hole. This characteristic was observable as well in the analysis of the protocol using blue diode laser.

In Figure A.5 we show a topographic image at the center of the hole where we can examine in detail the modifications of the layers. From Figure A.5a, it is possible to distinguish at less three lines which are aligned radially to the center. In Figure A.5b we show the difference in height from the center hole to the layer which comprises this pattern. The profile line estimates a height of 15 nm, approximately. This value is close to the thickness of the upper PMMA layer.

A.2 Optimization of development and lift-off processing

We prepared a second sample modifying the first dielectric layer as it is showed in the stack of layers of Figure. The deposition of all the remaining layers was performed as described in IV.4.1. We used the same parameters of thin film deposition as the first sample. The creation of the hole in the resist bi-layer was performed using the supper-continuum laser with an optical power of 15.11 mW.

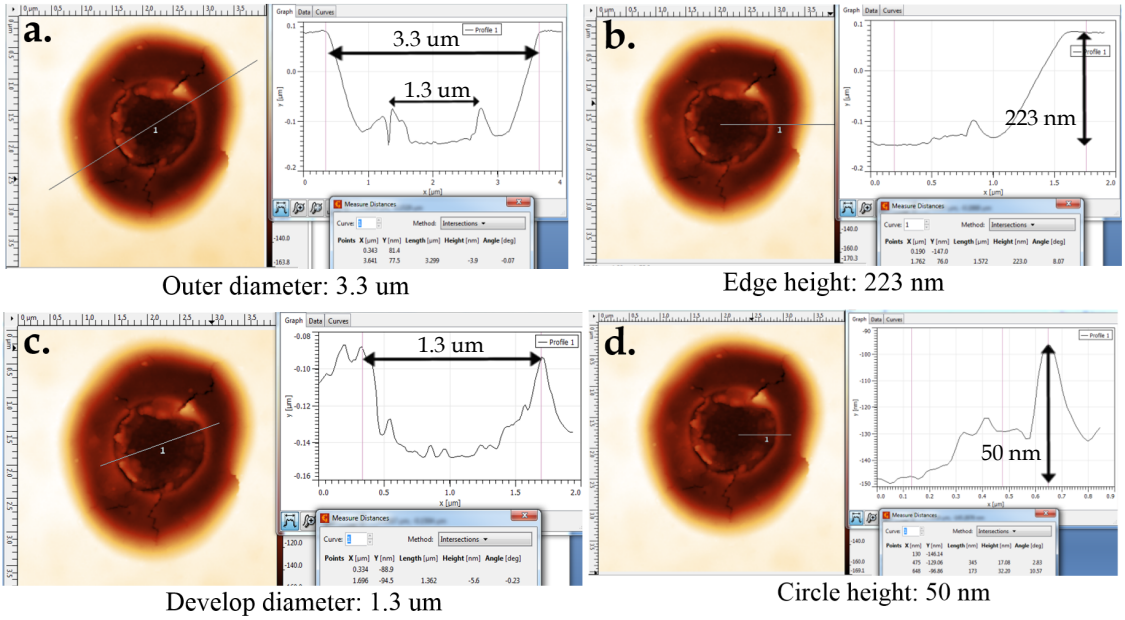

Fig. A.4 *Hole after thermal vapor deposition and lift-off processing during 50 seconds in pure developer MF-319.*

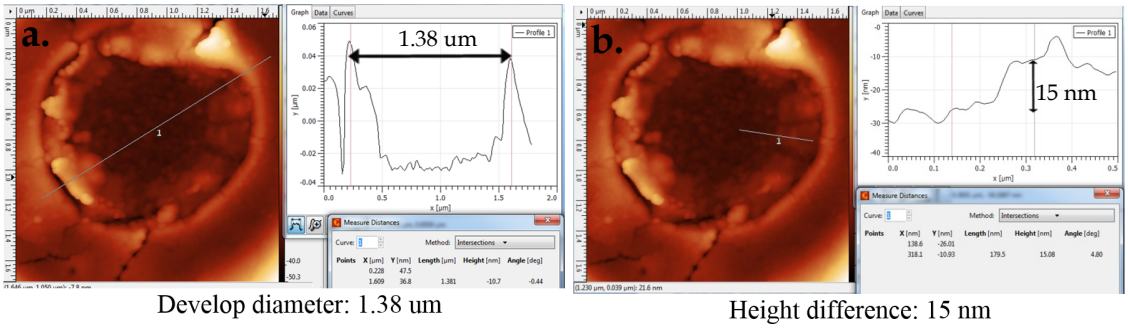

Fig. A.5 *AFM image showing the center of the hole. a) Trace line indicating the develop diameter around 1,38 um. b) Trace line showing the differential in height from the center hole to the layer which comprise the radial pattern.*

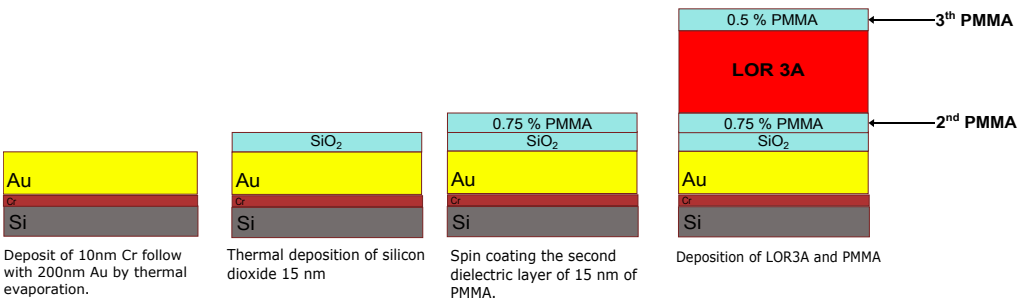

Fig. A.6 *Schematic representation of the sample prepared for In-situ protocol.*

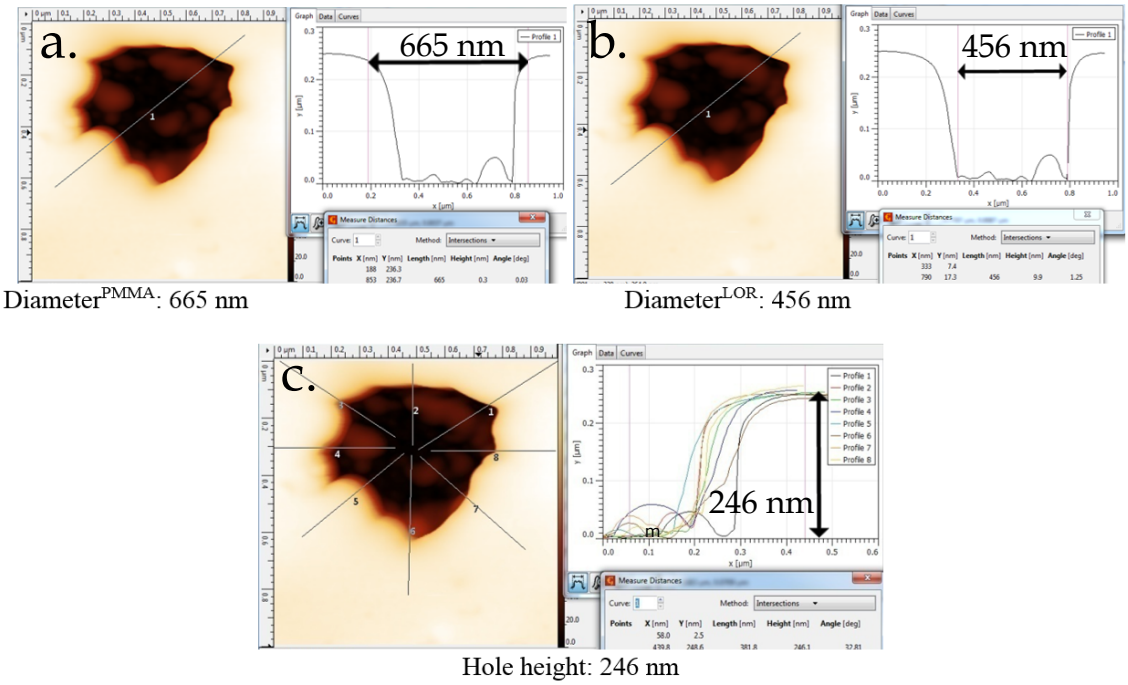

Fig. A.7 *AFM images of one hole created with supercontinnum laser during 2 seconds of exposure time. a) Diameter in PMMA layer, b) Diameter in LOR layer, c) Average of depth*

A.2.1 Laser exposure

In Figure A.7 we show the results of the initial stage. From the image we can note that the characteristics in size and shape of the hole are very different from the findings of the first sample. This fact is comprehensible since the creation of the hole is base on the multi-wavelength radiation combine with focusing technique of the microscope.

From the Figure A.7a and b, we can distinguish two hole diameters 665 nm and 456 nm corresponding to the upper PMMA layer and LOR3A resist layers, respectively. In Figure A.7 we show the depth of the hole which is around 246 nm. This depth is lower than the expected from the complete stack of layers (15 nm PMMA + 330 LOR3A + 10 nm upper PMMA). From the images we can also note some remaining residues of resist LOR3A.

A.2.2 Development lift-off resist LOR3A

We performed the development stage, in this occasion we submerged the sample inside pure developer MF-319 between 3 and 4 seconds. The results are showed in Figures A.8.

From the Figure A.8 we can note the expansion of the hole from 456 nm to 1.3 um, almost three times the original size. Once again, the depth of the hole is about 246 nm, similar as the initial phase, confirming that the super continuum laser has created a hole

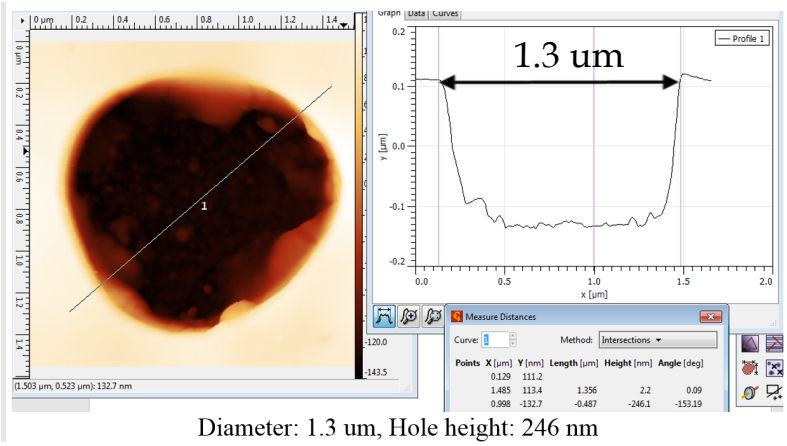

Fig. A.8 *AFM images after development 3-4 seconds inside MF-319. a) Single trace in the complete hole.*

in the resist bi-layer. The resolution of the topographic image allows to distinguish the border of the hole and and roughness of the bottom layer at the center. For this sample, we have not found the slash pattern at the center of the hole, meaning that the PMMA layers was not affected during the exposure. In the same images we can note some residues of resist close to the border.

A.2.3 Thermal deposition of Au film and lift-off processing

We carried out the deposition of 20 nm of gold film and we performed the lift off process submerging the sample in the pure MF-319 during 120 seconds. The results in AFM imagining are showed in Figure A.9.

In Figure A.9a we observe that the hole has expanded from 1.3 to 4.5 um. In Figure A.9b we show the height of the hole from the bottom center to the upper layer. This height reaches around 247 nm, close to the initial depth. In Figure A.9c we show the develop diameter and Figure A.9d the contour surrounding the develop diameter. From the image we can observe that the contour reaches some hundred nanometers.

In this study we have observed the evolution of one single hole (future patch antenna) during the complete in-situ lithography protocol using a super continuum laser. We have experimentally observed the expansion of the initial hole size after development process and we have noted how it affects the following stages.

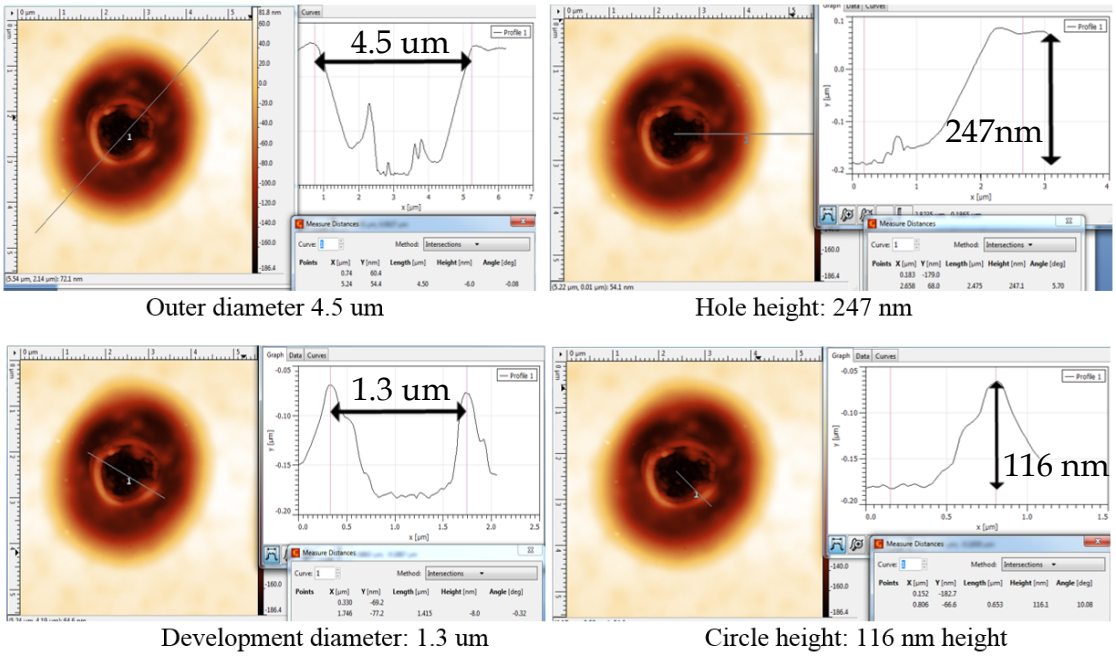

Outer diameter 4.5 um | Hole height: 247 nm

Development diameter: 1.3 um | Circle height: 116 nm height

Fig. A.9 *AFM images after gold deposition (20 nm Au layer) and liftoff processing with pure MF-319 during 120 s. a) Profile line in the outer diameter, b) Height from the center of the hole to the upper layer. c) Profile line in the develop diameter and c) in the contour surrounding the develop diameter.*

Appendix B

Spectroscopic signatures of materials

It is well-known that dielectric or metallic materials surrounding the nanocrystal can introduce fluorescence noise during the fine measurements in single nanocrystals. In this section we will present the fluorescence spectroscopic signatures of poly(methyl methacrylate) PMMA, conventional glass coverslip and flat Au surface which are materials commonly used as support substrates in photoluminescence measurements with nanocrystals. In order to identify the fluorescence of PMMA material with respect to the nanocrystal under study, we proceed with the preparation of the following sample. In a clean coverslip we deposited a thin dielectric layer 2% PMMA that gives roughly 45 nm thickness (measured with profilometer Dektak). We created a linear discontinuity by removing the PMMA film with a metallic tweezers. Figure B.1 displays the transverse step-height profile of the micrometer groove along the glass surface.

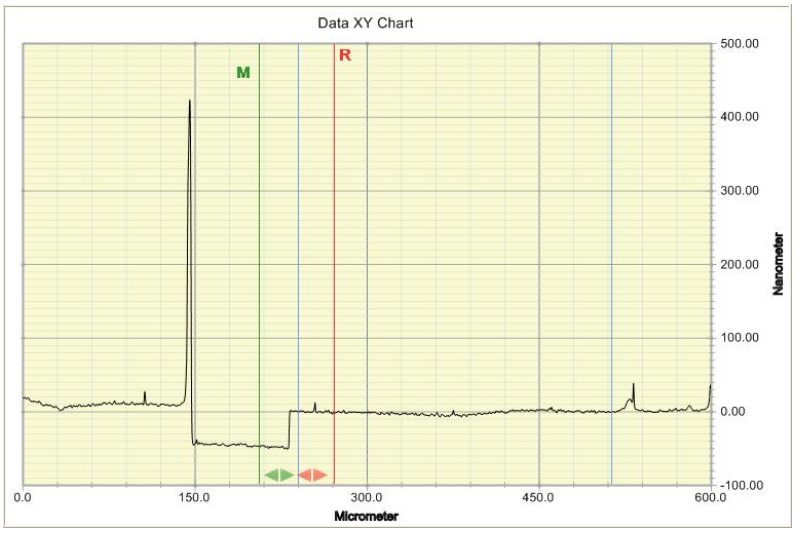

Fig. B.1 *Graph displaying the step-height profile to determine the highness of the groove. Image directly obtained from the profilometer Dektak after a single trace.*

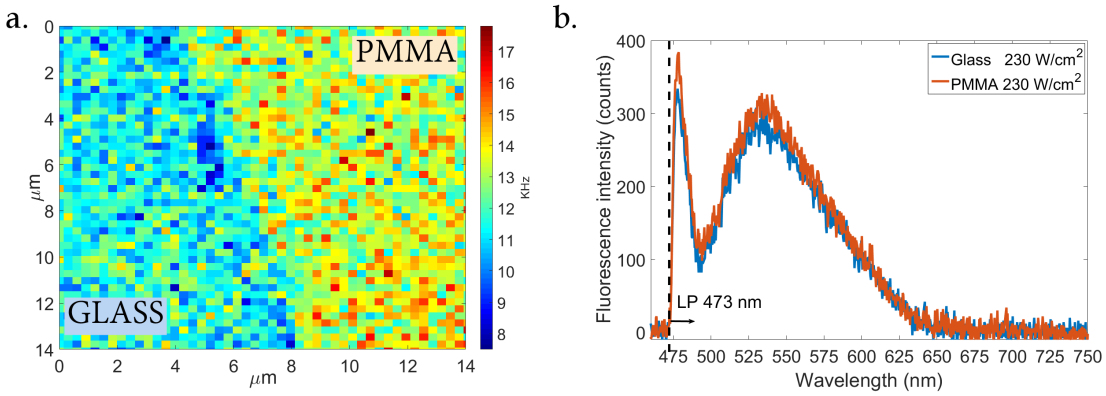

Fig. B.2 *a) Fluorescence scanning image in the interface between PMMA and glass substrate. b) Photoluminescence spectros corresponding to glass and PMMA zones of image a.*

B.0.1 Fluorescence of dielectric materials: PMMA, glass coverslip

Using the sample with the discontinuity layer of PMMA coated in glass coverslip showed on Figure B.1. We positioned the border of the discontinuity groove in the 15×15 μm scanning area in the fluorescence microscope and we excited the interface between PMMA and bare glass using the blue laser 405 nm in continuous mode at 230 W/cm^2. Using the same experimental set-up as described in section III.3, we obtained the scanning fluorescence image showed in Figure B.2a. From the image we can distinguish two parts, one having more fluorescence than the other one. As expected, the emission in PMMA is slightly higher with respect to bare glass. The down-left (bluish) zone corresponds mostly to the emission of the glass substrate and the upper-right (greenish) zone belongs to PMMA layer. By means of the piezo-electric stage, we positioned the laser spot separately in the two zones of the scanning image to extract the photoluminescence signatures for each material.

Figure B.2b display the signatures for each zone PMMA and bare glass. The signature in both material is almost identical. In both signatures we can note the sharp cut of fluorescence by the Semrock LP filter 473 nm. We also observe the presence of a wide emission extended from 500 nm to 650 nm.

Quantitatively speaking, the contribution close to the cut-edge wavelength around 475 nm seems to be more significant than the large emission around 540 nm. In all multiphotonic spectra measured with the maximum excitation power, this spurious signal from dielectric materials was not even notice, confirming its negligible contribution.

B.0.2 Luminescence of Au film

Evaporated gold is another material widely used in the interaction with single nanoemitters. In nanophotonics, high-quality gold is extensively employed in the fabrication of

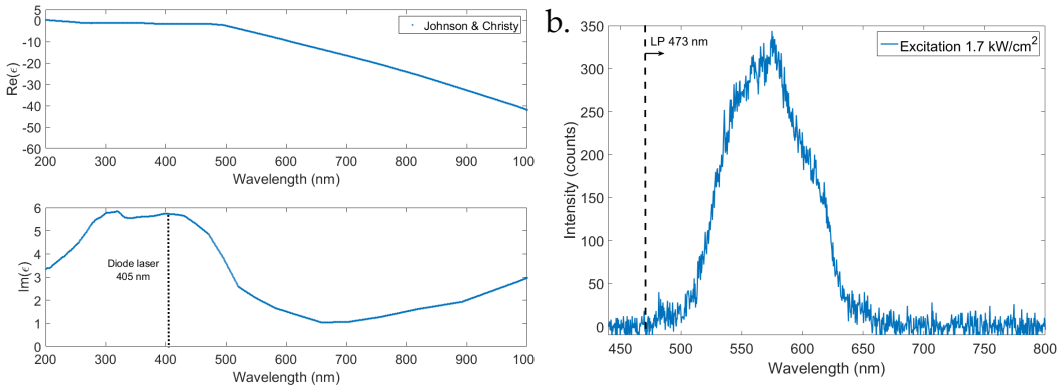

Fig. B.3 *a) Dielectric function ϵ of bulk gold obtained by Johnson and Christy [70]. b) Photoluminescence emission spectra of 200 nm Au film. We have excited with an optical power of 1.7 kW/cm^2 in continuous mode using a diode laser emitting at 405 nm. The integration time in the spectrometers was 60 s.*

plasmonic nanostructures. The recent development of techniques in nanofabrication like e-beam lithography or Focus Ion Beam (FIB) allow to fabricate different nanostructures of sophisticate shapes and sizes. In this section we will present the photoluminescence properties of a thick-Au film fabricated by thermal vapor deposition at the INSP.

The first observation of photoluminescence emisison in metallic materials was reported in 1969 by Mooradian using a high intensity argon ion laser [69]. The luminescence of metallic material may bring an extra source of background noise during laser scanning and also in spectroscopic measurements of patch-antennas. In this section, we will present the photoluminescence spectra measured in a thick Au layer deposited by thermal evaporation.

In noble metals, such as gold and silver, they have bands of absorption associated to inter-band transition of electrons in low energies bands (d-band). In gold bulk material, these bands start appearing in the near ultraviolet frequencies. Figure B.3a shows the real part (upper graph) and imaginary part (lower graph) of the dielectric function $\epsilon(\omega)$ measured by Johnson and Christy in 1972 [70]. From the lower graph, we can note that the imaginary component (associated to the absorption properties of the bulk material) starts increasing below 600 nm reaching maximum close to the emission linewidth of the blue diode laser at 405 nm. The same imaginary component of the dielectric function shows that the absorption of gold is minimum around 650 nm, nearly in the emission linewidth of colloidal nanocrystals. Therefore, the luminescence of the noble metal would become important within excitation with the laser at 405 nm.

In order to identify the luminescence signature of gold, we have used a sample containing 200 nm Au thickness fabricated by thermal vapor deposition. We have increased the optical power of the diode laser 405 nm (working in continuous mode) until 1.7 kW/cm^2 to be able to collect the fluorescence signal from bare gold. Figure B.3b shows the pho-

toluminescence spectra of the gold surface after 60 s of integration time. We can observe that the emission extends over a range from 500 nm to 650 nm, approximately. This range overlay partially the fluorescence emission of single CdSe/CdS nanocrystals as we can note from the Figure II.13 described in section II.2.

In laser scanning fluorescence imaging, part of the incident energy is absorbed by these d-band electrons whose mechanisms of relaxation can lead to the emission of luminescence in the visible spectrum range. However, the fluorescence emission of nanocrystals laying on gold substrate is several times more higher than the luminescence of the background gold.

Bibliography

[1] A. V. Akimov, A. Mukherjee, C. L. Yu, D. E. Chang, A. S. Zibrov, P. R. Hemmer, H. Park & M. D. Lukin; «Generation of single optical plasmons in metallic nanowires coupled to quantum dots»; Nature **450**, p. 402–406 (2007). 2

[2] R. Kolesov, B. Grotz, G. Balasubramanian, R. J. Stöhr, A. A. L. Nicolet, P. R. Hemmer, F. Jelezko & J. a. Wrachtrup; «Wave–particle duality of single surface plasmon polaritons»; Nature Physics **5**, p. 470–474 (2009). 2

[3] M.-C. Dheur, E. Devaux, T. W. Ebbesen, A. Baron, J.-C. Rodier, J.-P. Hugonin, P. Lalanne, J.-J. Greffet, G. Messin & F. Marquier; «Single-plasmon interferences»; Science Advances **2** (2016). http://advances.sciencemag.org/content/2/3/e1501574; http://advances.sciencemag.org/content/2/3/e1501574.full.pdf.

[4] B. Vest, M.-C. Dheur, E. Devaux, A. Baron, E. Rousseau, J.-P. Hugonin, J.-J. Greffet, G. Messin & F. Marquier; «Anti-coalescence of bosons on a lossy beam splitter»; Science (2017). ISSN 0036-8075. http://science.sciencemag.org/content/early/2017/05/24/science.aam9353; http://science.sciencemag.org/content/early/2017/05/24/science.aam9353.full.pdf.

[5] L. Novotny & N. van Hulst; «Antennas for light»; NATURE PHOTONICS **5**, p. 83–90 (2011). ISSN 1749-4885. 2, 3

[6] A. Badolato, K. Hennessy, M. Atatüre, J. Dreiser, E. Hu, P. M. Petroff & A. Imamoğlu; «Deterministic Coupling of Single Quantum Dots to Single Nanocavity Modes»; Science **308**, p. 1158–1161 (2005). ISSN 0036-8075. http://science.sciencemag.org/content/308/5725/1158; http://science.sciencemag.org/content/308/5725/1158.full.pdf. 2

[7] A. G. Curto, G. Volpe, T. H. Taminiau, M. P. Kreuzer, R. Quidant & N. F. van Hulst; «Unidirectional Emission of a Quantum Dot Coupled to a Nanoantenna»; Science **329**, p. 930–933 (2010). ISSN 0036-8075. http://science.sciencemag.org/content/329/5994/930; http://science.sciencemag.org/content/329/5994/930.full.pdf. 2

[8] C. Ropp, Z. Cummins, S. Nah, J. T. Fourkas, B. Shapiro & E. Waks; «Nanoscale imaging and spontaneous emission control with a single nano-positioned quantum dot»; NATURE COMMUNICATIONS **4** (2013). ISSN 2041-1723. 2

[9] S.-H. Gong, J.-H. Kim, Y.-H. Ko, C. Rodriguez, J. Shin, Y.-H. Lee, L. S. Dang, X. Zhang & Y.-H. Cho; «Self-aligned deterministic coupling of single quantum emitter to nanofocused plasmonic modes»; Proceedings of the National Academy of Sciences **112**, p. 5280–5285 (2015). ISSN 0027-8424. http://www.pnas.org/content/112/17/5280; http://www.pnas.org/content/112/17/5280.full.pdf. 3

[10] A. Cuche, O. Mollet, A. Drezet & S. Huant; «"Deterministic" Quantum Plasmonics»; Nano Letters **10**, p. 4566–4570 (2010). 3

[11] A. Huck, S. Kumar, A. Shakoor & U. L. Andersen; «Controlled Coupling of a Single Nitrogen-Vacancy Center to a Silver Nanowire»; Phys. Rev. Lett. **106**, p. 096 801 (2011). https://link.aps.org/doi/10.1103/PhysRevLett.106.096801. 3

[12] A. Kinkhabwala, Z. Yu, S. Fan, Y. Avlasevich, K. Müllen & W. E. Moerner; «Large single-molecule fluorescence enhancements produced by a bowtie nanoantenna»; Nature Photonics **3**, p. 654–657 (2009). 2

[13] S. Morozov, M. Gaio, S. A. Maier & R. Sapienza; «Metal–Dielectric Parabolic Antenna for Directing Single Photons»; Nano Letters **18**, p. 3060–3065 (2018). 3

[14] P. Bharadwaj, B. Deutsch & L. Novotny; «Optical Antennas»; Adv. Opt. Photon. **1**, p. 438–483 (2009). http://aop.osa.org/abstract.cfm?URI=aop-1-3-438. 3

[15] H. A. Atwater & A. Polman; «Plasmonics for improved photovoltaic devices»; NATURE MATERIALS **9**, p. 205–213 (2010). ISSN 1476-1122. 3

[16] J. A. Schuller, E. S. Barnard, W. Cai, Y. C. Jun, J. S. White & M. L. Brongersma; «Plasmonics for extreme light concentration and manipulation»; NATURE MATERIALS **9**, p. 193–204 (2010). ISSN 1476-1122. 3

[17] A. J. Haes, W. P. Hall, L. Chang, W. L. Klein & R. P. Van Duyne; «A Localized Surface Plasmon Resonance Biosensor: First Steps toward an Assay for Alzheimer's Disease»; Nano Letters **4**, p. 1029–1034 (2004). https://doi.org/10.1021/nl049670j; https://doi.org/10.1021/nl049670j. 3

[18] T. A. Taton, C. A. Mirkin & R. L. Letsinger; «Scanometric DNA Array Detection with Nanoparticle Probes»; Science **289**, p. 1757–1760 (2000). ISSN 0036-8075. http://science.sciencemag.org/content/289/5485/1757; http://science.sciencemag.org/content/289/5485/1757.full.pdf. 3

[19] J. Chen, D. Wang, J. Xi, L. Au, A. Siekkinen, A. Warsen, Z.-Y. Li, H. Zhang, Y. Xia & X. Li; «Immuno Gold Nanocages with Tailored Optical Properties for Targeted Photothermal Destruction of Cancer Cells»; Nano Letters **7**, p. 1318–1322 (2007). https://doi.org/10.1021/nl070345g; pMID: 17430005; https://doi.org/10.1021/nl070345g. 3

[20] C. Loo, A. Lowery, N. Halas, J. West & R. Drezek; «Immunotargeted Nanoshells for Integrated Cancer Imaging and Therapy»; Nano Letters **5**, p. 709–711

(2005). https://doi.org/10.1021/nl050127s; pMID: 15826113; https://doi.org/10.1021/nl050127s. 3

[21] X. Huang, I. H. El-Sayed, W. Qian & M. A. El-Sayed; «Cancer Cell Imaging and Photothermal Therapy in the Near-Infrared Region by Using Gold Nanorods»; Journal of the American Chemical Society **128**, p. 2115–2120 (2006). https://doi.org/10.1021/ja057254a; pMID: 16464114; https://doi.org/10.1021/ja057254a. 3

[22] S. I. Bozhevolnyi & T. Søndergaard; «General properties of slow-plasmon resonant nanostructures: nano-antennas and resonators»; Opt. Express **15**, p. 10 869–10 877 (2007). http://www.opticsexpress.org/abstract.cfm?URI=oe-15-17-10869. 4

[23] R. Esteban, T. V. Teperik & J. J. Greffet; «Optical Patch Antennas for Single Photon Emission Using Surface Plasmon Resonances»; Phys. Rev. Lett. **104**, p. 026 802 (2010). https://link.aps.org/doi/10.1103/PhysRevLett.104.026802. 4, 113, 122

[24] C. Belacel, B. Habert, F. Bigourdan, F. Marquier, J.-P. Hugonin, S. Michaelis de Vasconcellos, X. Lafosse, L. Coolen, C. Schwob, C. Javaux, B. Dubertret, J.-J. Greffet, P. Senellart & A. Maitre; «Controlling Spontaneous Emission with Plasmonic Optical Patch Antennas»; Nano Letters **13**, p. 1516–1521 (2013). PMID: 23461679. 4

[25] A. Dousse, L. Lanco, J. Suffczyński, E. Semenova, A. Miard, A. Lemaître, I. Sagnes, C. Roblin, J. Bloch & P. Senellart; «Controlled Light-Matter Coupling for a Single Quantum Dot Embedded in a Pillar Microcavity Using Far-Field Optical Lithography»; Phys. Rev. Lett. **101**, p. 267 404 (2008). https://link.aps.org/doi/10.1103/PhysRevLett.101.267404. 4

[26] A. R. DHAWAN; *Deterministic lithographic fabrication of single emitter plasmonic patch nanoantennas, and their characterization*; Thèse de doctorat (2016); thèse de doctorat dirigée par Maitre, Agnes, Institut des Nano Sciences de Paris. 4, 99

[27] B. Habert; *Contrôle de la fluorescence par des nanoantennes plasmoniques*; Thèse de doctorat (2014). http://www.theses.fr/2014IOTA0003; thèse de doctorat dirigée par Greffet, Jean-Jacques Physique Palaiseau, Institut d'optique théorique et appliquée 2014. 5, 113, 114, 115, 122, 126

[28] C. Sinito; *Magneto-optical properties of single CdSe nanocrystals at low temperature*; Theses; Université de Bordeaux (2014). https://tel.archives-ouvertes.fr/tel-01194873. 7, 20

[29] M. Manceau; *Single CdSe/CdS dot-in-rods fluorescence properties*; Theses; Université Pierre et Marie Curie - Paris VI (2014). https://hal.archives-ouvertes.fr/tel-01101939. 7

[30] X. Brokmann; *Fluorescence properties of single CdSe nanocrystals*; Theses; Université Pierre et Marie Curie - Paris VI (2004). https://tel.archives-ouvertes.fr/tel-00007873. 7

[31] B. O. Dabbousi, J. Rodriguez-Viejo, F. V. Mikulec, J. R. Heine, H. Mattoussi, R. Ober, K. F. Jensen & M. G. Bawendi; «(CdSe)ZnS Core-Shell Quantum Dots: Synthesis and Characterization of a Size Series of Highly Luminescent Nanocrystallites»; The Journal of Physical Chemistry B **101**, p. 9463–9475 (1997). 8

[32] M. Nasilowski; *Synthesis and optical spectroscopy of thick-shell semiconductor nanoparticles : applications to biological imaging*; Thèse de doctorat (2015). http://www.theses.fr/2015PA066432; thèse de doctorat dirigée par Dubertret, Benoît Physico-Chimie des Matériaux Paris 6 2015. 8

[33] M. Nasilowski, P. Spinicelli, G. Patriarche & B. Dubertret; «Gradient CdSe/CdS Quantum Dots with Room Temperature Biexciton Unity Quantum Yield»; Nano Letters **15**, p. 3953–3958 (2015). PMID: 25990468. 8, 9

[34] C. A. Leatherdale, W.-K. Woo, F. V. Mikulec & M. G. Bawendi; «On the Absorption Cross Section of CdSe Nanocrystal Quantum Dots»; The Journal of Physical Chemistry B **106**, p. 7619–7622 (2002). 8, 38

[35] D. NORRIS, A. SACRA, C. MURRAY & M. BAWENDI; «MEASUREMENT OF THE SIZE-DEPENDENT HOLE SPECTRUM IN CDSE QUANTUM DOTS»; PHYSICAL REVIEW LETTERS **72**, p. 2612–2615 (1994). ISSN 0031-9007. 8

[36] S. A. Empedocles, D. J. Norris & M. G. Bawendi; «Photoluminescence Spectroscopy of Single CdSe Nanocrystallite Quantum Dots»; Phys. Rev. Lett. **77**, p. 3873–3876 (1996). https://link.aps.org/doi/10.1103/PhysRevLett.77.3873. 8

[37] C. B. Murray, D. J. Norris & M. G. Bawendi; «Synthesis and characterization of nearly monodisperse CdE (E = sulfur, selenium, tellurium) semiconductor nanocrystallites»; Journal of the American Chemical Society **115**, p. 8706–8715 (1993). 8

[38] M. A. Hines & P. Guyot-Sionnest; «Synthesis and Characterization of Strongly Luminescing ZnS-Capped CdSe Nanocrystals»; The Journal of Physical Chemistry **100**, p. 468–471 (1996). 8

[39] Y. Chen, J. Vela, H. Htoon, J. L. Casson, D. J. Werder, D. A. Bussian, V. I. Klimov & J. A. Hollingsworth; «"Giant" Multishell CdSe Nanocrystal Quantum Dots with Suppressed Blinking»; Journal of the American Chemical Society **130**, p. 5026–5027 (2008). 8

[40] V. I. Klimov, D. W. McBranch, C. A. Leatherdale & M. G. Bawendi; «Electron and hole relaxation pathways in semiconductor quantum dots»; Phys. Rev. B **60**, p. 13 740–13 749 (1999). https://link.aps.org/doi/10.1103/PhysRevB.60.13740. 8

[41] Y. D. Kim, M. V. Klein, S. F. Ren, Y. C. Chang, H. Luo, N. Samarth & J. K. Furdyna; «Optical properties of zinc-blende CdSe and $Zn_xCd_{1-x}Se$ films grown on GaAs»; Phys. Rev. B **49**, p. 7262–7270 (1994). https://link.aps.org/doi/10.1103/PhysRevB.49.7262. 9

[42] J. Li & L.-W. Wang; «First principle study of core/shell structure quantum dots»; Applied Physics Letters **84**, p. 3648–3650 (2004). https://doi.org/10.1063/1.1737470; https://doi.org/10.1063/1.1737470. 9, 10

[43] C. Javaux, B. Mahler, B. Dubertret, A. Shabaev, A. V. Rodina, A. L. Efros, D. R. Yakovlev, F. Liu, M. Bayer, G. Camps, L. Biadala, S. Buil, X. Quelin & J.-P. Hermier; «Thermal activation of non-radiative Auger recombination in charged colloidal nanocrystals»; NATURE NANOTECHNOLOGY **8**, p. 206–212 (2013). ISSN 1748-3387. 11

[44] P. Spinicelli, S. Buil, X. Quélin, B. Mahler, B. Dubertret & J.-P. Hermier; «Bright and Grey States in CdSe-CdS Nanocrystals Exhibiting Strongly Reduced Blinking»; Phys. Rev. Lett. **102**, p. 136 801 (2009). https://link.aps.org/doi/10.1103/PhysRevLett.102.136801. 11

[45] C. Galland, Y. Ghosh, A. Steinbrück, M. Sykora, J. A. Hollingsworth, V. I. Klimov & H. Htoon; «Two types of luminescence blinking revealed by spectroelectrochemistry of single quantum dots»; Nature **479**, p. 203–207 (2011). https://link.aps.org/doi/10.1103/PhysRevLett.22.185. 11, 12, 13

[46] J. Laverdant, W. D. de Marcillac, C. Barthou, V. D. Chinh, C. Schwob, L. Coolen, P. Benalloul, P. T. Nga & A. Maitre; «Experimental Determination of the Fluorescence Quantum Yield of Semiconductor Nanocrystals»; MATERIALS **4**, p. 1182–1193 (2011). ISSN 1996-1944. 13

[47] R. H. BROWN & R. Q. TWISS; «Correlation between Photons in two Coherent Beams of Light»; Nature **177**, p. 27–29 (1956). 14, 15

[48] H. J. Kimble, M. Dagenais & L. Mandel; «Photon Antibunching in Resonance Fluorescence»; Phys. Rev. Lett. **39**, p. 691–695 (1977). https://link.aps.org/doi/10.1103/PhysRevLett.39.691. 14

[49] R. Loudon; *The quantum theory of light* (Clarendon Press) (1973). https://books.google.fr/books?id=OHspAQAAMAAJ. 15

[50] A. L. Efros, V. Kharchenko & M. Rosen; «Breaking the phonon bottleneck in nanometer quantum dots: Role of Auger-like processes»; Solid State Communications **93**, p. 281 – 284 (1995). ISSN 0038-1098. http://www.sciencedirect.com/science/article/pii/0038109894007608. 18

[51] V. I. Klimov, A. A. Mikhailovsky, D. W. McBranch, C. A. Leatherdale & M. G. Bawendi; «Quantization of Multiparticle Auger Rates in Semiconductor Quantum Dots»; Science **287**, p. 1011–1013 (2000). ISSN 0036-8075. http://science.sciencemag.org/content/287/5455/1011; http://science.sciencemag.org/content/287/5455/1011.full.pdf. 18

[52] C. Sinito, M. J. Fernée, S. V. Goupalov, P. Mulvaney, P. Tamarat & B. Lounis; «Tailoring the Exciton Fine Structure of Cadmium Selenide Nanocrystals with Shape Anisotropy and Magnetic Field»; ACS Nano **8**, p. 11 651–11 656 (2014). 20

[53] Y. Louyer, L. Biadala, J.-B. Trebbia, M. J. Fernée, P. Tamarat & B. Lounis; «Efficient Biexciton Emission in Elongated CdSe/ZnS Nanocrystals»; Nano Letters **11**, p. 4370–4375 (2011). 20

[54] N. Chowdhury; «Single CdSe/CdS fluorescent nanocrystals under low and high excitation intensities.»; (2017)A Dissertation Submitted to ESIEE, Paris In partial Fulfillment of the Requirements for the Degree of International Master of Electronics. 31, 38

[55] Y.-S. Park, A. V. Malko, J. Vela, Y. Chen, Y. Ghosh, F. García-Santamaría, J. A. Hollingsworth, V. I. Klimov & H. Htoon; «Near-Unity Quantum Yields of Biexciton Emission from CdSe/CdS Nanocrystals Measured Using Single-Particle Spectroscopy»; Phys. Rev. Lett. **106**, p. 187 401 (2011). https://link.aps.org/doi/10.1103/PhysRevLett.106.187401. 38

[56] PicoQuant; «User's Manual PDL 800-D Picosecond Pulsed Diode Laser.»; (2007)Version 0.2. 42

[57] G. Nair, J. Zhao & M. G. Bawendi; «Biexciton Quantum Yield of Single Semiconductor Nanocrystals from Photon Statistics»; Nano Letters **11**, p. 1136–1140 (2011). https://doi.org/10.1021/nl104054t; pMID: 21288042; https://doi.org/10.1021/nl104054t. 49

[58] C. Belacel; *Emission de nanocristaux semi-conducteurs dans une antenne patch plasmonique*; Thèse de doctorat (2013). http://www.theses.fr/2013PA066715; thèse de doctorat dirigée par Maître, Agnès et Senellart, Pascale Physique de la particule à la matière condensée Paris 6 2013. 66, 67, 99

[59] S. B. K. Moorthy; *Thin Film Structures in Energy Applications*; Series on tools and techniques for computer typesetting; 1re édition (Springer International, Cham, Heidelberg, New York, Dordrecht, London) (2015); ISBN 978-3-319-14773-4. 72

[60] K. M. McPeak, S. V. Jayanti, S. J. P. Kress, S. Meyer, S. Iotti, A. Rossinelli & D. J. Norris; «Plasmonic Films Can Easily Be Better: Rules and Recipes»; ACS Photonics **2**, p. 326–333 (2015). 73

[61] T. AOUDJIT; «Optimisation d'Antennes Optiques.»; (2017)Stage de Master1. Specialite : Physique Appliquée. 75

[62] H. AMYAR; «Fabrication et Caracterisation des Antennes patch plasmoniques.»; (2018)Stage effectué à l'Institut des NanoSciences de Paris. 107, 108, 109

[63] J. Henrie, S. Kellis, S. M. Schultz & A. Hawkins; «Electronic color charts for dielectric films on silicon»; Opt. Express **12**, p. 1464–1469 (2004). http://www.opticsexpress.org/abstract.cfm?URI=oe-12-7-1464. 107

[64] H. Raether; *Surface plasmons on smooth and rough surfaces and on gratings*; numéro v. 111 dans Springer tracts in modern physics (Springer) (1988); ISBN 9783540173632. https://books.google.fr/books?id=ZLwrAAAAYAAJ. 113

[65] C. F. Bohren & D. Huffman; *Absorption and scattering of light by small particles*; Wiley science paperback series (Wiley) (1983); ISBN 9780471293408. https://books.google.fr/books?id=S1RCZ8BjgN0C. 113

[66] P. Berini; «Plasmon-polariton waves guided by thin lossy metal films of finite width: Bound modes of symmetric structures»; Phys. Rev. B **61**, p. 10 484–10 503 (2000). https://link.aps.org/doi/10.1103/PhysRevB.61.10484. 113

[67] C. Vion, P. Spinicelli, L. Coolen, C. Schwob, J.-M. Frigerio, J.-P. Hermier & A. Maître; «Controlled modification of single colloidal CdSe/ZnS nanocrystal fluorescence through interactions with a gold surface»; Opt. Express **18**, p. 7440–7455 (2010). http://www.opticsexpress.org/abstract.cfm?URI=oe-18-7-7440. 113

[68] K. Drexhage; «Influence of a dielectric interface on fluorescence decay time»; Journal of Luminescence **1-2**, p. 693 – 701 (1970). ISSN 0022-2313. http://www.sciencedirect.com/science/article/pii/0022231370900827. 114

[69] A. Mooradian; «Photoluminescence of Metals»; Phys. Rev. Lett. **22**, p. 185–187 (1969). https://link.aps.org/doi/10.1103/PhysRevLett.22.185. 141

[70] P. B. Johnson & R. W. Christy; «Optical Constants of the Noble Metals»; Phys. Rev. B **6**, p. 4370–4379 (1972). https://link.aps.org/doi/10.1103/PhysRevB.6.4370. 141

Juan Uriel ESPARZA VILLA **19 avril 2019**

Sujet : Fabrication et caractérisation d'antennes patch plasmoniques

Résumé : Nous étudions l'interaction lumière-matière d'un nanocristal CdSe/CdS individuel et une antenne patch plasmonique. Les études réalisées dans le cadre de ce travail peuvent être visualisées en deux parties. En première, nous avons caractérisé les propriétés de photoluminescence d'un nanocristal individuel en termes de la dynamique et la spectroscopie à différents conditions d'excitation. Les nanocristaux semi-conducteurs sont des sources de photon-unique à température ambiante. Néanmoins, l'émission multi-excitonique de ces émetteurs est possible lorsque la recombinaison de deux ou plus excitons devient radiative. Nous avons développé un modèle analytique qui permet de décrire le nombre de photons émis en fonction du nombre moyen d'excitons créés par une impulsion laser. Le modèle nous a permis d'estimer le rendement quantique de la transition bi-excitonique. La deuxième partie est consacrée à l'optimisation d'un protocole de fabrication d'antennes patch. Nous avons établi un protocole de lithographie optique qui permettre de coupler un nanodisque d'or avec un nanocristal individuel de manière déterministe. En première temps, nous avons fabriqué antennes passives afin d'analyser les propriétés de réflectivité de la structure, puis nous avons fabriqué des antennes couplées à une boite quantique. Nous avons montré la modification de l'émission spontanée due au couplage avec l'antenne. Nous avons mis en évidence une émission super-poissonnienne de l'antenne après un filtrage temporel, ainsi que l'émission de lumière partialement cohérente.

Mots clés : Nanoantenne, plasmonique, nanocristaux semiconducteurs, lithographie optique, fluorescence, effet Purcell.

Subject : Fabrication and characterization of plasmonic patch nanoantennas

Abstract: In this thesis, we exploit light-matter interaction between a single semiconductor CdSe/CdS nanocrystal and a plasmonic patch antenna. This work can be divided in two main parts. We have first characterized the photoluminescence dynamics and spectroscopic signatures of single nanocrystals at different excitation powers. High quality CdSe/CdS nanocrystals are single-photon sources at room temperature. Nevertheless, multiexcitonic emission occurs when two or more excitons are recombining radiatively. We have developed an analytical model which describes the number of photons emitted by a nanocrystal as a function of the mean number of excitons created in one excitation pulse. With this model, we can calculate the quantum efficiency of the bi-exciton recombination. The second part is devoted to the development and optimization of an optical lithography protocol for patch antennas. We have stablished a protocol that allows us to couple a thin Au nano-disk above a single nanocrystal in a deterministic way. We have first fabricated passive nanoantennas in order to study reflectivity spectroscopic properties in the plasmonic structure. Later on, we have fabricated several active patch nanoantennas coupled with single CdSe/CdS nanocrystals. We have demonstrated the acceleration of spontaneous emission thanks to the coupling with the plasmons nanodisk. For some antennas, we have evidenced a super-poissonian emission signature when a post-processing temporal filter is applied. Finally, we have evidenced the emission of light partially coherent of one antenna in the proximity of the metallic square edge.

Keywords : Nanoantenna, plasmonics, semiconductor nanocrystals, optical lithography, fluorescence, Purcell effect.